Grain Size Evolution and Strain Localization in Deformed Marbles

by

Nicholas James Austin

Submitted to the Department of Earth, Atmospheric and Planetary Sciences
in partial fulfillment of the requirements for the degree of

Doctor of Philosophy

at the

MASSACHUSETTS INSTITUTE OF TECHNOLOGY

September 2008

©2008 Massachusetts Institute of Technology. All rights reserved

Signature of Author: ……
Department of Earth, Atmospheric and Planetary Sciences
July 10, 2008

Certified by:……..
J. Brian Evans
Professor of Geophysics
Thesis Supevisor

Accepted by:…….
Maria Zuber
E.A. Griswold Professor of Geophysics
Department Head

Grain Size Evolution and Strain Localization in Deformed Marbles

by
Nicholas James Austin
Submitted to the Department of
Earth, Atmospheric and Planetary Sciences
on June 26th, 2008 in partial fulfillment of
the requirements for the degree of
Doctor of Philosophy

Abstract

In the lithosphere, strain is frequently accommodated along localized shear zones, the rheology of which are inextricably linked to their microstructural characteristics. Shear zones in orogenic belts frequently form in calcite-rich lithologies due to the relatively low strength of these rocks, especially when compared to quartz- and feldspar-rich lithologies. This dissertation addresses the kinetics of microstructural evolution during deformation of calcite-rich rocks, and the coupling between the rheological properties of deforming rocks and such microstructural characteristics as grain size and crystallographic preferred orientation (CPO) by combining laboratory studies with field based observations. In Chapter 2, a scaling relationship for recrystallized grain size is derived based on a balance between the rate that mechanical work is done during deformation and the rate that this energy can be dissipated. This suggests that recrystallized grain size reflects the product of stress and strain rate rather than stress alone. When this scaling relationship is applied to measured calcite grain sizes from the Morcles nappe, in the Swiss Helveitc Alps, where the microstructure is unaffected by second phases, the geologically estimated regional strain rates are successfully reproduced, and when it is applied to samples collected along a transect perpendicular to the thrust contact, the results suggest strain became progressively localized (Chapter 3). This calculation is consistent with the increased CPO intensity which is observed in the finest grained mylonites closest to the thrust contact. In Chapter 4, laboratory deformation experiments are used gain insight into the kinetics of microstructural evolution in calcite-rich rocks. The grain size evolution rates measured in experiments correlate well with the product of the measured stresses and strain rates, consistent with the scaling relationship presented in Chapter 2. These experiments also suggest that, with increasing strain, strain rates will increase at constant stress, and there is a correlation between this weakening and the formation and intensification of CPO, consistent with the observations in the Morcles nappe. Rocks are seldom composed of a single mineral phase. The influence of rigid second phases on the strength, CPO, and grain size of deforming marbles is investigated through a combination of hydrostatic, compression, and torsion experiments performed in the laboratory, which are presented in Chapters 5&6. Both the volume fraction and geometry of rigid second phases have a dramatic effect on the mechanical strength, the CPO, and the grain size. In samples deformed to high strains in torsion, where the recrystallized grain size resulting from deformation is finer than the grain size due to pinning of grain boundaries by the rigid inclusions, the scaling relationship derived in Chapter 2 successfully predicts the measured recrystallized grain size. Thus, this scaling relationship is consistent with both grain size evolution rates and stabilized grain sizes measured in the laboratory, and with field constraints on the strain rates in the Morcles nappe.

Thesis Supervisor: J. Brian Evans
Title: Professor of Geophysics

Acknowledgements

First and foremost, I would like to thank my advisor, Brian Evans. Throughout my time at MIT, Brian has given me the academic freedom to follow my interests, and has always been more than willing to provide his immense insight to my many questions. This dissertation would not have been possible without Brian's guidance.

I was privileged to work with many brilliant scientists and amazing people throughout my time at MIT. This thesis would not have been possible without their help. Greg Hirth, Peter Kelemen, Tim Grove, Bill Durham, and Clark Burchfiel were all kind enough to be on my thesis and/or General Exam committees. More importantly, their doors were always open, and they were all more than willing to sit down and discuss my research. I was fortunate to have the opportunity to work with Marco Herwegh and Andreas Ebert at Bern University. Marco and Andreas were both incredibly patient with me while I learned the many complexities of the geology of the Swiss Alps. Michaela and Kamil Ustaszewski were kind enough to allow me to stay with them during my visits to Bern. Georg Dresen, Erik Rybacki, and Michael Naumann devoted a significant amount of their time during my visit to the GFZ-Potsdam, and David Kohlstedt and Mark Zimmerman were kind enough to teach me the intricacies of furnace design during my visit to the University of Minnesota. Before coming to MIT, I was fortunate enough to work with an amazing group of scientists and friends at UBC. In particular, I want to thank Lori Kennedy, Kelly Russell, Greg Dipple, Steve Quane, and Steve Israel.

During my many long hours in the lab at MIT, Xiaohui Xiao, Uli Mok, and Jock Hirst were always available to help me out. Without their help, I would have spent far more time puzzling over how to fix lab equipment, and far less time running experiments. I must also thank Louie Kerr for his willingness to answer my many questions about the SEM. Outside of the lab, I must thank Carol Sprague, Vicki McKenna, Jean Danek, and Kerin Willis for making sure I didn't miss any major deadlines, especially when I frequently forgot to read my email.

During my time at MIT, I have been fortunate to meet and work with many amazing people. In particular, numerous discussions with Chris Studnicki-Gizbert, Eric Hetland, Luc Mehl, Jessica Warren, Einat Lev, Brian deMartin, Lili Xu, Jay Barr, and Matt Rioux motivated a significant portion of this work. Chris Studnicki-Gizbert, Luc Mehl, Adam Pidlisecky, Chris Zibailo, Tim O'Dea, Todd Cunningham, and the rest of the Superstition crew have all been more than willing to drag me away from work whenever the snow fell, the wind was blowing, or it wasn't too cold to ride a bike.

Finally, I want to thank my family. My parents, Ian and Jane, have always supported me in everything I have attempted. I don't know where I would have been without their support. My time at MIT was made all the more enjoyable by having my sister, Sarah, in Boston at the same time. Tom and Gina Tupper and Jen Tupper and Brett Habijanac have all been incredibly supportive throughout all the fun and stressful times. Lastly, and most importantly, I want to thank my wife, Brie. No matter how stressful things got, Brie was always there. I couldn't have done this without her love and support.

Contents

Chapter 1 11
Introduction
1. Introductory Statement 11
2. Thesis Overview 14
3. References 17

Chapter 2 21
***PaleoWattmeters*: A scaling relation for dynamically recrystallized grain size**
Abstract 21
1. Introduction 22
2. Scaling between power and grain size 23
3. Comparison to other models of dynamic recrystallization 25
4. Comparison with experimental data 27
5. Extrapolation to the conditions of natural deformation 28
6. Data from natural shear zones 29
7. Conclusions 30
8. Acknowledgements 30
9. References 31
10. Figures 34

Chapter 3 39
Strain Localization in the Morcles Nappe (Helvetic Alps, Switzerland)
Abstract 39
1. Introduction 40
2. Regional geology 41
3. Outcrop-scale structures 43
4. Microstructures within the Morcles nappe 43
5. Methodology of new observations 44
   5.1. Sampling 44
   5.2. Grain size and second-phase content 45
   5.3. Analysis of crystallographic preferred orientation 46
6. Microstructural observations 47
   6.1. Matrix grain size 47
   6.2. Second phases 48
   6.3. Crystallographic preferred orientation (CPO) 48
7. Discussion 49
   7.1. Deformation mechanisms 49
   7.2. Pore fluids 51
   7.3. Power dissipation and strain-rate estimates 52
      7.3.1. From grain-size to strain-rate: The paleowattmeter 52
      7.3.2. Are microstructures indicative of deformation conditions? 54
      7.3.3. Stresses and strain rates along the inverted limb of the Morcles nappe 55

7.3.4. Stress and/or strain rate variations normal to the thrust contact 57
7.4. Estimating the temporal and spatial evolution of strain 60
7.5. Implications for the emplacement of the Helvetic nappes 61
8. Conclusions 62
9. Acknowledgements 63
10. References 64
11. Tables 71
12. Figures 75

Chapter 4 89
The Kinetics of Microstructural Evolution During Deformation of Calcite
Abstract 89
1. Introduction 90
1.1. Previous Grain Size Evolution Models 91
1.2. The Paleowattmeter 98
1.3. Comparison of Grain Size Evolution Models 101
2. Methodology 102
2.1. Sample Material and Preparation 102
2.2. Static Grain Growth Experiments 102
2.3. Deformation Experiments 103
2.4. Microstructural Analysis 104
3. Results 106
3.1. Mechanical Data 106
3.2. Static Grain Growth 106
3.3. Grain-size Evolution during Deformation 107
3.3.1. Low Stress 107
3.3.2. High Stress 108
3.4. Crystallographic Preferred Orientation 108
4. Discussion 109
4.1. Mechanical Evolution 109
4.2. Kinetics of coarsening during triaxial and hydrostatic loading 110
4.3. Grain-Size Reduction Kinetics 112
4.4. Grain Size Stabilization During Deformation 116
4.5. Microstructural Evolution and Rheological Weakening 117
5. Conclusions 118
6. Acknowledgements 119
7. References 119
8. Tables 124
9. Figures 131

Chapter 5 147
Strength Evolution and the Development of Crystallographic Preferred Orientation During Deformation of Poly-Phase Marbles
Abstract 147
1. Introduction 148
2. Methodology of Laboratory Experiments 150

2.1. Sample Materials 150
2.2. Deformation Experiments 150
2.2.1. Compression 150
2.2.2. Torsion 152
2.3. Grain-Size Analysis 155
2.4. Crystallographic Preferred Orientation 155
3. Laboratory Results 156
3.1. Mechanical Results 156
3.1.1. Compression 156
3.1.2. Torsion 157
3.1.3. Strength Comparison: Compression vs. Torsion 158
3.2. Microstructural Evolution During Torsion Deformation 159
3.3. Crystallographic Preferred Orientation 160
4. Polycrystalline CPO Calculations 162
5. Slip System activity and the strength of two-phase marbles 165
5.1. Pure Samples and 1 vol.% Spheres 166
5.2. 10 vol.% Splinters 167
5.3. 10 vol.% Spheres 167
6. Discussion 168
7. Conclusions 172
8. Acknowledgements 173
9. References 174
10. Tables 178
11. Figures 182

Chapter 6 197
Grain Size Evolution During Deformation of Poly-Phase Marbles
Abstract 197
1. Introduction 198
2. Experimental Methodology 200
2.1. Sample Materials 200
2.2. Grain-Size Analysis 201
3. Microstructural Observations 201
3.1. Hydrostatic Grain Growth 201
3.2. Microstructural Evolution During Deformation 203
4. Discussion 204
4.1. Pinning of Grain Boundaries by Second Phases 204
4.2. Recrystallized vs. Pinned Grain Sizes 205
4.3. Comparison to Natural Data 208
5. Conclusion 211
6. Acknowledgements 211
7. References 212
8. Tables 216
9. Figures 218

Chapter 1

Introduction

1. Introductory Statement

The localization of strain is ubiquitous within the lithosphere. For well over a hundred years, structural geologists have recognized that significant lateral displacements are accommodated in shear zones with widths of centimeters to meters (Heim 1878; Bertrand 1884; Peach & Horne 1884; Boullier & Quenardel 1981; Milton & Williams 1981; Harris et al. 1983; Siddans 1983; Groshong Jr et al. 1984). More recently, geodetic data have shown that, globally, tectonic strains are accommodated in relatively few discrete zones (Kreemer et al. 2000; Kreemer et al. 2003). Cumulatively, these observations suggest that the mechanics of shear zones and the mechanisms controlling the distribution of strain in the lithosphere are important elements of geodynamics. However, the mechanisms of strain localization are still being debated. Theoretical considerations suggest that, under most circumstances, system weakening is necessary for strain localization to occur (Poirier 1980; Hobbs et al. 1990; Burg 1999; Montesi & Zuber 2002). Potential candidates for weakening mechanisms include changes in the geometry of the shear zone; local changes in the pressure or temperature conditions; or material softening. During non-dilatant deformation, in the absence of significant geometric effects, some sort of material (rheological) weakening is required (Hobbs et al. 1990).

Laboratory, field, and theoretical studies all suggest that a rock's rheological properties are intimately linked its microstructural characteristics, which include elements such as grain size and crystallographic preferred orientation (CPO). In particular, dynamic recrystallization, and

concomitant grain size evolution, may lead to weakening in several ways. For example, grain size reduction may cause a switch in deformation mechanism from dislocation creep to diffusion creep (White 1977), or dynamic recrystallization may lead to the production of new, relatively "soft", strain free grains (Tullis & Yund 1985; Urai et al. 1986). If a crystallographic preferred orientation is developed (Pieri et al. 2001; Barnhoorn et al. 2004), or if chemical reactions occur (Stünitz 1998; Holyoke & Tullis 2006), these may also have a significant effect on a rock's mechanical properties.

Despite its significance, the rate of change of grain size during deformation is relatively poorly constrained. During dislocation creep, previous experimental work has demonstrated that mineral grains often evolve to a stable size, dictated by the deformation conditions. Early work suggested that this stable grain size was inversely related to the differential stress (Twiss 1977) and, thus, mylonite grain sizes have been used to infer paleostresses. More recent studies have suggested additional variables such as strain rate or temperature may also influence the dynamically recrystallized grain size (Derby & Ashby 1987; Derby 1991, 1992; Kameyama et al. 1997; De Bresser et al. 1998; Shimizu 1998; De Bresser et al. 2001b; Hall & Parmentier 2003). Some of these studies focus on the mechanisms of dynamic recrystallization (Derby & Ashby 1987; Derby 1991, 1992; Shimizu 1998), and many consider this problem in terms of the relative rates of grain size reduction and grain growth (Kameyama et al. 1997; Braun et al. 1999; Hall & Parmentier 2003). However, there is little data in the literature with which to compare many of these models and scaling relationships, particularly with regards to measurements of the rates of microstructural evolution during deformation. Most of the data that do exist suggest that the stable recrystallized grain size is inversely related to differential stress, in agreement with Twiss' (1977) proposal (Karato et al. 1980; Schmid et al. 1980; Van Der Wal et al. 1993; Rutter

1995; Stipp et al. 2001). However, several authors have recently suggested that stresses estimated from recrystallized grain sizes in marbles may not be consistent with mechanical data inferred from laboratory studies (De Bresser et al. 2001a; Herwegh et al. 2005). If grain size is inversely related to stress and independent of strain rate and temperature, then the progressive reduction in recrystallized grain size that is frequently observed towards the core of shear zones implies that the most highly deformed rocks have seen the highest stresses which, under certain boundary conditions, is in contradiction to localization theory (Hobbs et al. 1990).

It is apparent that the coupling between a rock's microstructure and the deformation conditions must be understood in order to interpret the mechanics of natural deformation. This coupling is usually investigated either by field based studies, laboratory experiments, theoretical considerations, or numerical models. However, few studies investigate the distribution of strain through a multi-faceted approach combining more than one of these techniques. In this dissertation, I address the evolution of microstructure, the coupling between microstructure and rheology, and the implications of this coupling on the distribution of strain through a combination of laboratory and field based studies on deformed limestones and marbles.

Calcite-rich rocks were chosen for this study as they have been well studied in the laboratory, enabling specific aspects of their microstructural evolution to be investigated within a well controlled rheological framework. For example, the dominant slip systems which accommodate strain during dislocation creep, and their relative strengths, have been determined experimentally over the course of more than 70 years (Griggs 1938; Turner 1953; Turner et al. 1954; Turner & Heard 1965; Goetze & Kohlstedt 1977; Paterson 1979; De Bresser & Spiers 1990, 1993; De Bresser & Spiers 1997), although questions still remain regarding the exact form the constitutive relationship(s) relating stress and strain rate (De Bresser et al. 2001a; Renner & Evans 2001; De

Bresser 2002; Renner et al. 2002). Both the dislocation and diffusion creep regimes are also readily accessible under laboratory deformation conditions (Rutter 1974; Schmid et al. 1977; Walker et al. 1990; Renner et al. 2002; Herwegh et al. 2003).

In addition to the wealth of laboratory data, calcite-rich rocks also accommodate significant strains in many orogenic belts, due to their relatively low strength, especially compared to quartz- and feldspar-rich rocks. This is particularly true when these orogenic belts result from closing of marine basins containing massive limestone deposits, such as in the Himalayan-Alpine orogeny. In particular, the tectonic setting and the geologic structures in many of the limestone-hosted shear zones within in the Swiss Alps have been extensively studied. In fact, arguably the first example in the geologic literature of large-scale, sub-horizontal displacements was the "double fold" of Glarus (Heim 1878), which was later re-interpreted as the Glarus Thrust (Bertrand 1884). Since the revolutionary work of Albert Heim (1878) and Marcel Bertrand (1884), the kinematics and tectonic histories of thrusts throughout the Swiss Alps have been mapped in exquisite detail. The precise geologic and tectonic constraints that have been placed on these shear zones allow for the interpretation of microstructures within a known geodynamic framework, thus enabling laboratory results to be extrapolated to, and tested against, field based observations.

2. Thesis Overview

This dissertation consists of 5 individual chapters (Chapters 2-6), which are designed to be read independently, however, all address the overall themes discussed above. Cumulatively, these investigate the kinetics of microstructural evolution during deformation of calcite, and the coupling between various microstructural elements and the rheology of deforming limestones.

In Chapter 2, I derive a scaling relationship for recrystallized grain size based on a balance between the rate that mechanical work is done during deformation and the rate that this energy can be dissipated. This relationship is consistent with both recrystallized grain sizes measured in the laboratory in calcite, quartz, and olivine and with field constraints from a range of shear zones. As a result, I propose that recrystallized grain size relates to the rate that mechanical work was done, or the product of stress and strain rate, rather than stress alone. Thus, recrystallized grain size is a *"paleowattmeter*"

In Chapter 3, I apply the scaling relationship derived in Chapter 2 to deformed marbles in the Morcles nappe, in the Swiss Helvetic Alps. This shear zone was chosen as it has been well studied at the regional scale (Badoux 1972; Trümpy 1973; Pfiffner 1981; Ramsay 1981, 1989; Escher et al. 1993; Pfiffner 1993) thus providing well bounded constraints on the finite strain, strain rates, and peak metamorphic temperatures: it has accommodated 10-12 km of displacement in a zone with a thickness less than ~50 m, at peak metamorphic temperatures between 572 and 668 K (Frey et al. 1980; Pfiffner 1993; Kirschner et al. 1995; Goy-Eggenberger 1998; Burkhard & Goy-Eggenberger 2001; Ebert et al. 2007). Further, the shear zone is hosted exclusively within limestones, containing between 0 and 50% non-calcite phases. When the scaling relationship derived in Chapter 2 is applied to measured calcite grain sizes in samples with a microstructure unaffected by second phases, the estimated regional strain rates, based on geologic constraints, are successfully reproduced. When this relationship is applied to samples collected along a transect perpendicular to the thrust contact, the results suggest strain became progressively localized. This calculation is consistent with the increase in CPO intensity observed in the finest grained mylonites closest to the thrust contact.

In Chapter 4, grain size evolution rates measured during deformation experiments on synthetic calcite-rocks are presented. One of the limitations of laboratory deformation studies performed in axial compression or in shear is that the maximum finite strain is limited to orders of magnitude below that reached in many shear zones, thus leading some authors to question assumptions regarding the attainment of steady state. To get around this problem in interpreting the recrystallized grain sizes that develop during laboratory deformation experiments, I measure the rate of evolution of mean grain size, which correlates well with the product of the measured stress and strain rate, consistent with the derivation in Chapter 2. These experiments also suggest that, with increasing strain, strain rates will increase at constant stress, and there is a correlation between this weakening and the formation and intensification of CPO, consistent with the observations made on the Morcles nappe in Chapter 3.

In shear zones, rocks frequently consist of more than one mineral phase. The final two chapters investigate the influence of rigid second phases on the strength and CPO evolution (Chapter 5), and grain size evolution (Chapter 6) of deforming marbles through a combination of hydrostatic, compression, and torsion experiments performed in the laboratory. In Chapter 5, I conclude that the shape of the second phase particles has a dramatic effect on both the strength and the CPO, even at similar volume fractions. However, in all cases, the measured bulk strength is consistent with the strength of the slip systems whose activity is suggested by crystallographic orientations. The data reported in Chapter 6 suggest that, in samples deformed to high strains in torsion, where the recrystallized grain size resulting from deformation is finer than the grain size due to pinning of grain boundaries by the rigid inclusions, the relationship derived in Chapter 2 successfully predicts the measured recrystallized grain size. On the other hand, if the mean free spacing is finer than the deformation controlled grain size, the distribution of the pinning phase

dictates the measured grain size. These observations from laboratory experiments are consistent with those from deformed limestones in the Morcles nappe that have a second phase effected microstructure (Chapter 3). Overall, the relationship derived in Chapter 2 is found to be consistent with both grain size evolution rates and stabilized grain sizes measured in the laboratory, and with field constraints on the strain rates in the Morcles nappe.

Although this dissertation focuses predominantly on calcite-rich rocks, many of the conclusions that are drawn, and questions that are raised, are of broader significance both for the microstructural evolution of shear zones, and the rheological controls on the distribution of strain. It is my hope that these conclusions and questions will motivate future studies aimed at reconciling laboratory, field, and theoretical observations pertaining to the microstructural evolution of shear zones and the driving forces for strain localization.

3. References

Badoux, H. 1972: Tectonique de la nappe de Morcles entre Rhône et Lizerne: Matériaux pour la Carte Géologique de la Suisse. Nouvelle Série **143**: 1–74.

Barnhoorn, A., Bystricky, M., Burlini, L.&Kunze, K. 2004: The Role of Recrystallization on the Deformation Behaviour of Calcite Rocks: High Strain Torsion Experiments on Carrara Marble. Journal of Structural Geology **26**: 885–903.

Bertrand, M. 1884: Rapports de structure des Alpes de Glarus et du Bassin houllier du Nord. Bull Soc. Geol. France **3**(XII): 318-330.

Boullier, A.&Quenardel, J. 1981: The Caledonides of northern Norway: relation between preferred orientation of quartz lattice, strain and translation of the nappes. Geological Society London Special Publications **9**(1): 185-195.

Braun, J., Chéry, J., Poliakov, A., Mainprice, D., Vauchez, A., Tomassi, A.&Daignières, M. 1999: A simple parametrization of strain localization in the ductile regime due to grain size reduction: A case study for olivine. Journal of Geophysical Research **104**(B11): 25167-25182.

Burg, J. 1999: Ductile structures and instabilities: their implication for Variscan tectonics in the Ardennes. Tectonophysics **309**(1): 1-25.

Burkhard, M.&Goy-Eggenberger, D. 2001: Near vertical iso-illite-crystallinity surfaces cross-cut the recumbent fold structure of the Morcles nappe, Swiss Alps. Clay Minerals **36**(2): 159-170.

de Bresser, J.&Spiers, C. 1990: High-temperature deformation of calcite single crystals by r+ and f+ slip. Geological Society London Special Publications **54**(1): 285-298.

de Bresser, J.&Spiers, C. 1993: Slip systems in calcite single crystals deformed at 300–800 C. Journal of Geophysical Research **98**(B4): 6397-6409.

de Bresser, J., Peach, C., Reijs, J.&Spiers, C. 1998: On dynamic recrystallization during solid state flow: Effects of stress and temperature. Geophysical Research Letters **25**(18): 3457-3460.

de Bresser, J., Evans, B.&Renner, J. 2001a: On estimating the strength of calcite rocks under natural conditions. Geological Society London Special Publications **200**(1): 309.

de Bresser, J., Ter Heege, J.&Spiers, C. 2001b: Grain size reduction by dynamic recrystallization: can it result in major rheological weakening? International Journal of Earth Sciences **90**(1): 28-45.

de Bresser, J. 2002: On the mechanism of dislocation creep of calcite at high temperature: inferences from experimentally measured pressure sensitivity and strain rate sensitivity of flow stress. Journal of Geophysical Research **107**(B12): doi:10.1029/2002JB001812.

de Bresser, J. H. P.&Spiers, C. J. 1997: Strength characteristics of the r, f, and c slip systems in calcite. Tectonophysics **272**(1): 1-23.

Derby, B.&Ashby, M. 1987: On Dynamic Recrystallization. Scripta Metallurgica et Materialia **21**(6): 879-884.

Derby, B. 1991: The Dependence of Grain Size on Stress During Dynamic Recrystallization. Acta Metallurgia et Materialia **39**(5): 955-962.

Derby, B. 1992: Dynamic recrystallisation. The steady state grain size. Scripta Metallurgica et Materialia **27**(11): 1581-1586.

Ebert, A., Herwegh, M., Evans, B., Pfiffner, A., Austin, N.&Vennemann, T. 2007: Microfabrics in carbonate mylonites along a large-scale shear zone (Helvetic Alps). Tectonophysics **444**(1-4): 1-26.

Escher, A., Masson, H.&Steck, A. 1993: Nappe geometry in the Western Swiss Alps. Journal of Structural Geology **15**(3-5): 501-509.

Frey, M., Teichmüller, M., Teichmüller, R., Mullis, J., Künzi, B., Breitschmid, A., Gruner, U.&Schwizer, B. 1980: Very low-grade metamorphism in external parts of the Central Alps: Illite crystallinity, coal rank and fluid inclusion data. Eclogae Geologicae Helvetiae **73**: 173–203.

Goetze, C.&Kohlstedt, D. 1977: The dislocation structure of experimentally deformed marble. Contributions to Mineralogy and Petrology **59**(3): 293-306.

Goy-Eggenberger, D. 1998: Faible métamorphisme de la nappe de Morcles: minéralogie et géochimie, Université de Neuchâtel.

Griggs, D. T. 1938: Deformation of single calcite crystals under high confining pressures. American Mineralogist **23**(1): 28-33.

Groshong Jr, R., Pfiffner, O.&Pringle, L. 1984: Strain partitioning in the Helvetic thrust belt of eastern Switzerland from the leading edge to the internal zone. Journal of Structural Geology **6**(1): 5-18.

Hall, C.&Parmentier, E. 2003: Influence of grain size evolution on convective instability. Geochemistry, Geophysics, Geosystems **4**(3): doi:10.1029/2002GC000308.

Harris, L., Burg, J.&Sauniac, S. 1983: Strain distribution within the Pardailhan Nappe(Montagne Noire, France) and structure of its basal thrust zone: implications for events associated with nappe emplacement. Journal of Structural Geology **5**(3-4): 431-440.

Heim, A. 1878: Untersuchungen Uber Den Mechanismus Der Gebirgsbildung. Benno Schwabe, Basel.

Herwegh, M., Xiao, X.&Evans, B. 2003: The effect of dissolved magnesium on diffusion creep in calcite. Earth and Planetary Science Letters **212**(3-4): 457-470.

Herwegh, M., de Bresser, J.&ter Heege, J. 2005: Combining natural microstructures with composite flow laws: an improved approach for the extrapolation of lab data to nature. Journal of Structural Geology **27**(3): 503-521.

Hobbs, B., Muhlhaus, H.&Ord, A. 1990: Instability, softening and localization of deformation. Geological Society London Special Publications **54**(1): 143-165.

Holyoke, C.&Tullis, J. 2006: The interaction between reaction and deformation: an experimental study using a biotite+ plagioclase+ quartz gneiss. Journal of Metamorphic Geology **24**(8): 743-762.

Kameyama, M., Yuen, D.&Fujimoto, H. 1997: The interaction of viscous heating with grain-size dependent rheology in the formation of localized slip zones. Geophysical Research Letters **24**(20): 2523-2526.

Karato, S., Toriumi, M.&Fujii, T. 1980: Dynamic recrystallization of olivine single crystals during high-temperature creep. Geophysical Research Letters **7**(9): 649-652.

Kirschner, D., Sharp, Z.&Masson, H. 1995: Oxygen isotope thermometry of quartz-calcite veins; unraveling the thermal-tectonic history of the subgreenschist facies Morcles Nappe (Swiss Alps). Bulletin of the Geological Society of America **107**(10): 1145-1156.

Kreemer, C., Haines, J., Holt, W., Blewitt, G.&Lavallee, D. 2000: On the determination of a global strain rate model. Earth Planets Space **52**(10): 765-770.

Kreemer, C., Holt, W.&Haines, A. 2003: An integrated global model of present-day plate motions and plate boundary deformation. Geophysical Journal International **154**(1): 8-34.

Milton, N.&Williams, G. 1981: The strain profile above a major thrust fault, Finnmark, N Norway. Geological Society London Special Publications **9**(1): 235.

Montesi, L.&Zuber, M. 2002: A unified description of localization for application to large-scale tectonics. J. Geophys. Res **107**(B3): doi: 10.1029/2001JB000465.

Paterson, M. 1979: Deformation Mechanisms in Carbonate Crystals. Physics of Materials (A festschrift for Dr. Walter Boas), CSIRO and University of Melbourne, Melbourne: 199-208.

Peach, B.&Horne, J. 1884: Report on the geology of the north-west of Sutherland. Nature **31**: 31–35.

Pfiffner, O. 1981: Fold-and-thrust tectonics in the Helvetic Nappes (E Switzerland). Geological Society London Special Publications **9**(1): 319-327.

Pfiffner, O. 1993: The structure of the Helvetic nappes and its relation to the mechanical stratigraphy. Journal of Structural Geology **15**(3-5): 511-521.

Pieri, M., Kunze, K., Burlini, L., Stretton, I., Olgaard, D., Burg, J.&Wenk, H. 2001: Texture development of calcite by deformation and dynamic recrystallization at 1000K during torsion experiments of marble to large strains. Tectonophysics **330**(1): 119-140.

Poirier, J. 1980: Shear localization and shear instability in materials in the ductile field. Journal of Structural Geology **2**(1-2): 135–142.

Ramsay, J. 1981: Tectonics of the Helvetic Nappes. Geological Society London Special Publications **9**(1): 293.

Ramsay, J. 1989: Fold and fault geometry in the western Helvetic nappes of Switzerland and France and its implication for the evolution of the arc of the western Alps. Geological Society London Special Publications **45**(1): 33-45.

Renner, J.&Evans, B. 2001: Do calcite rocks obey the power-law creep equation? Geological Society London Special Publications **200**(1): 293.

Renner, J., Evans, B.&Siddiqi, G. 2002: Dislocation creep of calcite. Journal of Geophysical Research **107**: 1-16.

Rutter, E. 1974: The influence of temperature, strain rate and interstitial water in the experimental deformation of calcite rocks. Tectonophysics **22**(3-4): 311-334.

Rutter, E. 1995: Experimental study of the influence of stress, temperature, and strain on the dynamic recrystallization of Carrara marble. Journal of Geophysical Research **100**(B12): 24651-24664.

Schmid, S., Boland, J.&Paterson, M. 1977: Superplastic flow in fine-grained limestone. Tectonophysics **43**(3-4): 257-291.

Schmid, S., Paterson, M.&Boland, J. 1980: High temperature flow and dynamic recrystallization in Carrara marble. Tectonophysics **65**: 245-280.

Shimizu, I. 1998: Stress and temperature dependence of recrystallized grain size: A subgrain misorientation model. Geophysical Research Letters **25**(22): 4237-4240.

Siddans, A. 1983: Finite strain pattern in some Alpine nappes. Journal of Structural Geology **5**(3-4): 441-448.

Stipp, M., Stunitz, H., Heilbronner, R.&Schmid, S. 2001: Dynamic recrystallization of quartz: correlation between natural and experimental conditions. Geological Society London Special Publications **200**(1): 171-190.

Stünitz, H. 1998: Syndeformational recrystallization-dynamic or compositionally induced? Contributions to Mineralogy and Petrology **131**(2): 219-236.

Trümpy, R. 1973: The timing of orogenic events in the Central Alps. Gravity and Tectonics"(De Jong, K. & Scholten, R.).-Wiley, New York: 229-251.

Tullis, J.&Yund, R. 1985: Dynamic recrystallization of feldspar; a mechanism for ductile shear zone formation. Geology **13**(4): 238-241.

Turner, F., Griggs, D.&Heard, H. 1954: Experimental deformation of calcite crystals. Bulletin of the Geological Society of America **65**(9): 883-933.

Turner, F.&Heard, H. 1965: Deformation in calcite crystals at different strain rates. Geol. Sci. Publ. Univ. Calif. Los Angeles **46**: 103-126.

Turner, F. J. 1953: Nature and dynamic interpretation of deformation lamellae in calcite of three marbles. American Journal of Science **251**(4): 276-298.

Twiss, R. 1977: Theory and applicability of a recrystallized grain size paleopiezometer. Pure and Applied Geophysics **115**(1): 227-244.

Urai, J., Means, W.&Lister, G. 1986: Dynamic recrystallization of minerals. AGU Geophysical Monograph **36**: 161-199.

van der Wal, D., Chopra, P., Drury, M.&Fitzgerald, J. 1993: Relationships between dynamically recrystallized grain size and deformation conditions in experimentally deformed olivine rocks. Geophysical Research Letters **20**(14): 1479-1482.

Walker, A., Rutter, E.&Brodie, K. 1990: Experimental study of grain-size sensitive flow of synthetic, hot-pressed calcite rocks. Geological Society London Special Publications **54**(1): 259.

White, S. 1977: Geological significance of recovery and recrystallization processes in quartz. Tectonophysics **39**(1-3): 143-170.

Chapter 2

PaleoWattmeters: A scaling relation for dynamically recrystallized grain size

Nicholas Austin
Brian Evans

Abstract

During dislocation creep, mineral grains often evolve to a stable size, dictated by the deformation conditions. We suggest that grain-size evolution during deformation is determined by the rate of mechanical work. Provided that other elements of microstructure have achieved steady-state and that the dissipation rate is roughly constant, then changes in internal energy will be proportional to changes in grain boundary area. If normal grain growth and dynamic grain-size reduction occur simultaneously, then the steady-state grain size is determined by the balance of those rates. A scaling model using these assumptions, and published grain-growth and mechanical relations, matches stress-grain size relations for quartz and olivine rocks with no fitting. For marbles, the model also explains scatter not rationalized by assuming that recrystallized grain size is a function of stress alone. When extrapolated to conditions typical for natural mylonites, the model is consistent with field constraints on stresses and strain rates.

Published as:

Austin, N.J., & Evans, B. (2007): *Paleowattmeters*: A scaling relation for recrystallized grain size. *Geology*, **35;4**, 343-346. doi: 10.1130/G23244A.1

1. Introduction

Reduced grain size is a common and striking feature of mylonites. Creep experiments indicate that the recrystallized grain size evolves to a stable value (d_s) determined by the deformation conditions. Early work suggested that d_s was inversely related to stress (σ) (Twiss, 1977), and, thus, mylonite grain sizes have been used to infer paleostresses (e.g., Stipp and Tullis, 2003):

$$d_s = A\sigma^{-m} \tag{1}$$

where A and m are empirically determined. The application of this idea was clouded by evidence of independent influence of metamorphic conditions (Etheridge and Wilkie, 1981). More recent workers suggest that d_s is also a function of temperature or strain rate (Poirier and Guillopé, 1979; de Bresser et al., 1998, 2001; Drury, 2005). At present, there is no universally accepted theory to explain the relationship between d_s and the deformation conditions, but factors to be considered are transitions in the recrystallization mechanism (Poirier and Guillopé, 1979; Rutter, 1995), stabilization of the grain size at values balancing diffusion and dislocation creep (de Bresser et al., 1998, 2001), subgrain nucleation and grain growth rates (Shimizu, 1998), and nucleation site density (Sakai and Jonas, 1984).

Field observations of nominally single phase rocks often indicate a gradation in recrystallized grain size from protomylonite to ultramylonite (eg. de Bresser et al., 2002 and references therein). If stress is the only parameter determining d_s, then one may infer that the most highly deformed rocks have seen the highest stresses, in contradiction to localization theory for non-dilating materials (eg. Hobbs et al., 1990). Clearly, a theoretical understanding of recrystallization is necessary to interpret natural microstructures.

2. Scaling between power and grain size

During deformation, external forces do work (per unit volume) at a rate of $\dot{W}_{tot} = \sigma\dot{\varepsilon} + \dot{\sigma}\varepsilon$, where a dot denotes a time derivative; σ and ε are differential stress and incremental strain. For simplicity, we consider uniaxial stress and coaxial strain. If σ varies less rapidly than grain size, then, on some timescale, $\dot{\sigma} = 0$, and $\dot{W}_{tot} = \sigma\dot{\varepsilon}$. The rate that work is done equals the rate of increase in internal energy, $\dot{E}_{\text{int}}$, plus the rate of energy dissipation, $\dot{\theta}_{irr}$, including heat production and any other irreversible increases in entropy (Poliak and Jonas, 1996; Bercovici and Ricard, 2005). If the stored energy associated with free dislocations rapidly attains steady state, then, the rate of change of internal energy is proportional to the rate of change of grain boundary area:

$$\dot{E}_{\text{int}} = \frac{-c\gamma}{d^2}\dot{d}_{red} \tag{2}$$

where *c* is a geometric constant, *d* the grain size at time *t,* and γ the average specific grain boundary energy. Then,

$$\dot{W}_v = \sigma\dot{\varepsilon} = \frac{-c\gamma}{d^2}\dot{d}_{red} + \dot{\theta}_{irr} \tag{3}$$

Grain growth rates in calcite rocks during diffusion creep do not differ from normal, static growth rates (Walker et al., 1990; Austin and Evans, 2005), so we postulate that the mechanical work done by diffusion creep, $\dot{W}_{diff} = \sigma\dot{\varepsilon}_{diff}$, is completely dissipated. Part of the work done on the material by dislocation creep, $\dot{W}_{disl} = \sigma\dot{\varepsilon}_{disl}$, is also dissipated, but a fraction, λ, is responsible for increases in internal energy owing to grain boundary area. If the total strain rate can be

partitioned between dislocation and diffusion creep, then $\beta = \dot{W}_{disl} / \dot{W}_{tot}$, and the dissipation rate is

$$\dot{\theta}_{irr} = (1-\beta)\sigma\dot{\varepsilon} + (1-\lambda)(\beta)\sigma\dot{\varepsilon} \tag{4}$$

Incorporating 4 into 3 and rearranging yields

$$\sigma\dot{\varepsilon} = \frac{-c\gamma}{\beta\lambda d^2}\dot{d}_{red} . \tag{5}$$

The stable grain size is often posited to occur when grain growth and reduction rates are equal (de Bresser et al., 1998; Hall and Parmentier, 2003). When no mechanical work is done, the total grain size evolution rate must equal the static growth rate. Lacking any specific information on how (or if) growth and reduction processes couple, we assume they are linearly independent: $\dot{d}_{tot} = \dot{d}_{red} + \dot{d}_{gr}$.

Thus,

$$\sigma\dot{\varepsilon} = \frac{-c\gamma}{\beta\lambda d^2}\left(\dot{d}_{tot} - \dot{d}_{gr}\right) \tag{6}$$

Assuming that deformation does not modify normal grain growth kinetics, then the rate of growth is $\dot{d}_{gr} = K_g \exp\left[-Q_g / RT\right] p^{-1} d^{1-p}$, where p is the exponent in the normal grain growth law. The total grain size evolution rate is

$$\dot{d}_{tot} = -\frac{\beta\lambda\sigma\dot{\varepsilon}d^2}{c\gamma} + K_g \exp\left(\frac{-Q_g}{RT}\right) p^{-1} d^{1-p} . \tag{7}$$

The steady-state grain size occurs when the total evolution rate is zero:

$$d_s^{1+p} = \frac{K_g \exp\left(\frac{-Q_g}{RT}\right) p^{-1} c\gamma}{\beta\lambda\sigma\dot{\varepsilon}} \tag{8}$$

into which β may be substituted, yielding:

$$d_s^{1+p} = \frac{K_g \exp\left(\frac{-Q_g}{RT}\right) p^{-1} c\gamma}{\lambda\sigma\dot{\varepsilon}_{disl}} \tag{9}$$

and finally, if the rock deforms by power law creep, $\dot{\varepsilon} = \dot{\varepsilon}_o \sigma^n \exp\left(\frac{Q_{disl}}{RT}\right)$, then

$$d_s = \kappa \cdot \sigma^{-m'} \cdot \exp\left[\frac{Q'}{RT}\right] \tag{10}$$

where $\kappa = \left[\frac{c\gamma K_g}{\lambda p \varepsilon_o}\right]^{\frac{1}{p+1}}$, $m' = \left(\frac{n+1}{p+1}\right)$, and $Q' = \frac{Q_g - Q_{disl}}{(p+1)}$.

Eqs. 8–9 suggest that the stable grain size during dynamic recrystallization scales with the rate of mechanical work done by dislocation creep. Thus, recrystallized grain size, rather than being a paleo-piezometer, is likely a *paleo-wattmeter*.

3. Comparison to other models of dynamic recrystallization

Because this treatment includes neither the exact physics of the grain size reduction process (eg. Derby, 1991, 1992), nor the kinetics of nucleation (e.g., Shimizu, 1998), this wattmeter is properly called a scaling relation, rather than a kinetic law. The model contains several explicit assumptions:

1. Other elements of microstructure have achieved steady-state or do not influence the partitioning of work into the stored boundary energy.

2. The rate of production of new boundary area is proportional to the rate of work done on the material.

3. Grain growth and reduction processes operate independently and, at steady-state, balance each other.

4. The growth mechanism is governed by an equation similar to that for normal grain growth.

5. During diffusion creep, the grain size reduction rates are small compared with grain growth rates.

6. Diffusion and dislocation creep operate as linearly independent processes.

These assumptions arise either because of lack of contrary evidence (3, 4, and 6), or because of positive experimental evidence, albeit fragmentary (1 and 5). The constant of proportionality in the second assertion, (λ), might conceivably depend on the dislocation density and/or the recrystallization mechanism. For example, Hirth and Tullis (1992) suggest that three distinct recrystallization regimes exist for quartz rocks. If so, λ might not simply be a numerical constant over all conditions; it would, of course, be bounded by $0<\lambda<1$. Assertion 4 is based on experimental observations for olivine (Karato, 1989) and calcite rocks (Walker et al., 1990; Austin and Evans, 2005), but may not be true for all materials. If not, Eqs. 5–7 could be modified to include modifications to the grain size evolution rate. Likewise, if solute drag or additional phases influence either the grain size evolution kinetics or the power dissipation, the appropriate equations may be modified accordingly.

Previous treatments of dynamic recrystallization also predict relations similar to Eq. 10 (de Bresser et al., 1998; Derby, 1992; Derby and Ashby, 1987; Drury, 2005; Shimizu, 1998). In

common with those models, the paleowattmeter suggests a modest temperature dependence of the d_s-σ relation, involving the difference between Q_g and Q_{disl} (cf. Eq. 10). Such a correlation between recrystallized grain size and temperature can be seen for rocks deformed at constant $\sigma\dot{\varepsilon}$ (Fig. 1). The exponents, *m'*, predicted by particular models, although differing in details, are similar in magnitude: e.g., *m'* is predicted to be 1.5 (Derby); 1.25–1.33 (Shimizu); 1.0 (Field Boundary), and 1.33 (wattmeter taking n = 3, p = 2). Additional data and observations will be necessary for validation of one model or another. However, notice that, unlike the de Bresser field boundary model, the wattmeter does not constrain the grain size to lie at the boundary between creep mechanisms (Figs. 2, 3).

4. Comparison with experimental data

In Fig. 2, we compare the wattmeter to stress-grainsize data reported from deformation experiments on calcite (Schmid et al., 1980; Rutter, 1995; Barnhoorn et al., 2004), quartz (Stipp and Tullis, 2003), and olivine (Karato et al., 1980; Van der Wal et al., 1993) rocks. Inserting material parameters from published creep and grain-growth laws without fitting, the wattmeter predicts recrystallized grain sizes in remarkably good agreement with data (Fig. 2a,c,d). Slight misfits could be explained by variations in grain-boundary mobility owing to differences in water fugacity, porosity, or solute impurities. For example, for olivine rocks (Fig. 2d), Karato (1989) used hot-pressed powders to study grain growth kinetics. This technique invariably results in small amounts of porosity, which reduces grain boundary mobility. Conversely, Karato et al. (1980) and Van der Wal et al. (1993) used olivine single crystals and natural samples, respectively. These probably have lower porosity and, thus, higher grain boundary mobility. If the pre-exponential in the grain growth equation is adjusted to account for experimental differences, the resulting agreement is striking (Fig. 2d).

For calcite, we also inverted the piezometric data using Eq. 8, assuming that β was constant (Fig. 2b). The inverted value for p (4.9) is significantly larger than that observed in experiments (Evans et al., 2001). However, it is striking that this three parameter fit reconciles laboratory data that are discrepant with any of the empirical piezometers (i.e., Eq. 1). The elevated p value might indicate that β includes a grain-size dependence, perhaps reflecting an increased component of diffusion creep for smaller grain sizes.

5. Extrapolation to the conditions of natural deformation

Extrapolation from laboratory conditions to natural deformation of rocks requires knowledge of the effects of stress, temperature, and strain rate. The empirical piezometers (Eq. 1) are temperature and strain rate independent, whereas kinetic balance models, such as the paleowattmeter or the field boundary model may contain temperature dependence. Extrapolations to natural conditions are shown in Fig. 3.

For calcite, our paleowattmeter predicts stresses lower than the piezometer of Rutter (1995), and different from that of Schmid et al. (1980). For example, for a grain size of 10 μm (common in both natural shear zones and experiments), predicted paleostresses are 105 MPa (Rutter, 1995) and 46 MPa (Schmid et al., 1980), regardless of temperature; the paleowattmeter predicts 75 MPa at 573 K, a temperature consistent with many calcite-hosted shear zones (A. Ebert, personal comm.). In a recent study of the Helvetic Nappes, Herwegh et al. (2005) noted that stresses predicted by Rutter's (1995) piezometer are much greater than the expected lithostatic pressure, perhaps suggesting the actual shear stresses along these faults were lower. For quartz rocks, the paleowattmeter also predicts consistently lower stresses for lower temperature deformation. For example, for a grain size of 10 μm, the Stipp and Tullis (2003) piezometer predicts a stress of 110 MPa, while our paleowattmeter predicts stresses of 130 MPa and 44 MPa at 1373K and

773K, respectively. For olivine, there is very little difference between our paleowattmeter (K_g = 7.0e16 μm^p s^{-1}) and the paleopiezometric calibration of Van der Wal et al. (1993). The temperature dependence for this material is small because activation energies for dislocation creep (530 kJ/mole; (Hirth and Kohlstedt, 2003) and for grain growth (520 kJ/mol; Karato, 1989) are similar.

6. Data from natural shear zones

When studying natural shear zones, two of the most readily available pieces of information are grain size and temperature. Average recrystallized grain size often correlates with inverse temperature, as shown in Fig. 4 for mylonites hosted within calcite and quartz rocks. For a given strain rate, both power and flow stress will correlate with inverse temperature. Recently, de Bresser et al. (2002) found consistent discrepancies between paleopiezometers and stresses inferred from currently available flow laws. In Fig. 4, we compare the predicted power for natural shear zones as a function of temperature. Using the parameters shown in Fig. 2(b,c), we see that both lab and natural data are parallel to lines of constant $\sigma\dot{\varepsilon}$ (Figs. 1, 4), with the natural data being shifted to coarser grain sizes. For calcite, the natural samples span an immense range of $\sigma\dot{\varepsilon}$, with most protomylonites lying on contours that are essentially static (e.g., $\sigma\dot{\varepsilon} << 10^{-14}$ MPa s^{-1}). However, virtually all the calcite ultramylonites are consistent with power levels necessary for strain rates of $10^{-12} < \dot{\varepsilon} < 10^{-6}$ s^{-1}. The grain size – temperature relationship for quartz rocks of Stipp et al. (2002) is consistent with $\sigma\dot{\varepsilon} < 10^{-12}$ MPa s^{-1}.

The paleowattmeter may also explain the progressive reduction in recrystallized grain size from shear-zone margin to core (i.e., from proto- to ultra-mylonite). If the average grain size at a given position in the shear zone is a function of stress only, then the stress within the shear zone

is inferred to increase toward the core. If grain size reflects the local power dissipated then, for constant stress conditions, those regions with higher strain rates will have smaller grain sizes.

7. Conclusions

We propose that the rate of recrystallization is proportional to the difference between the rate of work done during deformation and the rate of energy dissipation. In this view, a steady-state value of the average dynamically recrystallized grain size will occur when growth and reduction processes balance, and, therefore will depend on temperature if the two processes have different kinetics. The paleowattmeter successfully reproduces experimentally measured recrystallized grain sizes in calcite, quartz, and olivine rocks by accounting for the experimental conditions, and using published kinetic laws. When extrapolated to natural conditions, the paleowattmeter produces results consistent with temperatures, stresses, and strain rates inferred from field observations.

Many interesting questions remain concerning the relations between microstructure and strength, particularly involving the exact physics and kinetics of grain size modification. None the less, the paleowattmeter seems consistent with both natural and experimental data; thus, it may provide an intuitive framework for further progress in understanding dynamic recrystallization.

8. Acknowledgements

We benefited from discussions with G.Hirth, J. Renner, H. deBresser, M. Herwegh,, J. ter Heege, and L. Mehl. X.-h. Xiao was an invaluable resource in the laboratory. J. Tullis and an anonymous reviewer provided constructive reviews which greatly improved this manuscript. This work was supported by the NSF (EAR 030915) and GSA, Graduate Student Research Grant (7586-04).

9. References

Austin, N., and Evans, B., 2005, The role of deformation on the microstructural evolution of calcite: EOS, Trans. Amer. Geophysical Union, v. 86, p. Fall Meet. Suppl. Abstract V21A–0586.

Barnhoorn, A., Bystricky, M., Burlini, L., and Kunze, K., 2004, The role of recrystallisation on the deformation behaviour of calcite rocks: large strain torsion experiments on Carrara marble: Journal of Structural Geology, v. 26, p. 885–904, doi: 10.1016/j.jsg.2003.11.024.

Bercovici, D., and Ricard, Y., 2005, Tectonic plate generation and two-phase damage: Void growth versus grain size reduction: Journal of Geophysical Research, v. 110, B03401, doi: 10.1029/2004JB003181

Covey-Crump, S., 1986, Grain Growth Kinetics of Calcite Aggregates: MSc Thesis, Univ. London.

de Bresser, H., Evans, B., and Renner, J., 2002, Estimating the strength of calcite rocks under natural conditions, in de Meer, S., Drury, M.R., de Bresser, J.H.P., and Pennock, G., eds., Deformation Mechanisms, Rheology, and Tectonics: Current Status Future Perspectives, Volume Spec. Vol. 200: London, UK, Geological Society, p. 293–307.

de Bresser, J.H.P., Peach, C., Reijs, J., and Spier, C., 1998, On dynamic recrystallization during solid state flow: Effects of stress and temperature: Geophysical Research Letters, v. 25, p. 3457–3460, doi: 10.1029/98GL02690.

de Bresser, J.H.P., Ter Heege, J.H., and Spiers, C.J., 2001, Grain size reduction by dynamic recrystallization: can it result in major theological weakening?: International Journal of Earth Sciences, v. 90, p. 28–45, doi: 10.1007/s005310000149.

Derby, B., 1991, The dependence of grain-size on stress during dynamic recrystallization: Acta Metallurgica et Materialia, v. 39, p. 955–962, doi: 10.1016/0956-7151(91)90295-C.

Derby, B., 1992, Dynamic recrystallisation: The steady state grain size: Scripta Metallurgica et Materialia, v. 27, p. 1581–1585, doi: 10.1016/0956-716X(92)90148-8.

Derby, B., and Ashby, M.F., 1987, On dynamic recrystallisation: Scripta Metallurgica, v. 21, p. 879–884, doi: 10.1016/0036-9748(87)90341-3.

Drury, M., 2005, Dynamic recrystllization and strain softening of olivine aggregates in the laboratory and the lithosphere, in Gapais, D., Brun, J.P., and Cobbold, P.R., eds., Deformation, Mechanisms, Rheology, and Tectonics: from Minerals to the Lithosphere, Volume Spec. Pub. 243: London UK, Geological Society, p. 143–158.

Etheridge, M.A., and Wilkie, J.C., 1981, An assessment of dynamically recrystallized grain size as a palaeopiezometer in quartz-bearing mylonite zones: Tectonophysics, v. 78, p. 475–508, doi: 10.1016/0040-1951(81)90025-1.

Evans, B., Renner, J., and Hirth, G., 2001, A few remarks on the kinetics of static grain growth in rocks: International Journal of Earth Sciences, v. 90, p. 88–103, doi: 10.1007/s005310000150.

Hall, C.E., and Parmentier, E.M., 2003, The influence of grain size on a convective instability: Geochemistry, Geophysics, Geosystems, v. 4, doi: 10.1029/2002GC000308.

Herwegh, M., Xiao, X., and Evans, B., 2003, The effect of dissolved magnesium on diffusion creep in calcite: Earth and Planetary Science Letters, v. 212, p. 457–470, doi: 10.1016/S0012-821X(03)00284-X.

Herwegh, M., de Bresser, J.H.P., and ter Heege, J.H., 2005, Combining natural microstructures with composite flow laws: an improved approach for the extrapolation of lab data to nature: Journal of Structural Geology, v. 27, p. 503–521, doi: 10.1016/j.jsg.2004.10.010.

Hirth, G., and Tullis, J., 1992, Dislocation creep regimes in quartz aggregates: Journal of Structural Geology, v. 14, p. 145–159, doi: 10.1016/0191-8141(92)90053-Y.

Hirth, G., and Kohlstedt, D.L., 2003, Rheology of the Mantle Wedge, in Eiler J. ed., Inside the Subduction Factory, Geophysical Monograph, 138, AGU, Washington DC, p 83–105.

Hirth, G., Teyssier, C., and Dunlan, W.J., 2001, An evaluation of quartzite flow laws based on comparisons between experimentally and naturally deformed rocks: International Journal of Earth Sciences, v. 90, p. 77–87, doi: 10.1007/s005310000152.

Hobbs, B.E., Muhlhaus, H.-B, and Ord, A., 1990, Instability, softening, and localization of deformation, in Knipe., R.J., and Rutter, E.H. eds., Deformation mechanisms, rheology, and tectonics, Volume Spec. Vol. 54: London, UK, Geological Society, p. 143-165.

Karato, S.-I., 1989, Grain growth kinetics in olivine aggregates: Tectonophysics, v. 168, p. 255–273, doi: 10.1016/0040-1951(89)90221-7.

Karato, S.-I., Toriumi, M., and Fujii, T., 1980, Dynamic recrystallization of olivine single crystals during high temperature creep: Geophysical Research Letters, v. 7, p. 649–652.

Poirier, J.P., and Guillopé, M., 1979, Deformation induced recrystallization of minerals: Bulletin de la Société minéralogique de France., v. 102, p. 67–74.

Poliak, E.I., and Jonas, J.J., 1996, A one parameter approach to determining the critical conditions for the initiation of dynamic recrystallization: Acta Materialia, v. 44, no. 1, p. 127–136, doi: 10.1016/1359-6454(95)00146-7.

Renner, J., Evans, B., Siddiqi, G., 2002, Dislocation creep of Calcite: Journal of Geophysical Research, 107;B12, 2364, DOI:10.1029/2001JB001680.

Rutter, E.H., 1995, Experimental study of the influence of stress, temperature, and strain on the dynamic recrystallization of Carrara marble: Journal of Geophysical Research-Solid Earth, v. 100, p. 24651–24663, doi: 10.1029/95JB02500.

Rutter, E.H., and Brodie, K.H., 2004, Experimental grain-size sensitive flow of hot pressed Brazilian quartz aggregates: Journal of Structural Geology, v. 26, p. 2011–2023, doi: 10.1016/j.jsg.2004.04.006.

Sakai, T., and Jonas, J.J., 1984, Overview No-35 - Dynamic Recrystallization - Mechanical and Microstructural Considerations: Acta metall., v. 32, p. 189–209.

Schmid, S.M., Paterson, M.S., and Boland, J.N., 1980, High temperature flow and dynamic recrystallization in Carrara marble: Tectonophysics, v. 65, p. 245–280, doi: 10.1016/0040-1951(80)90077-3.

Shimizu, I., 1998, Stress and temperature dependence of recrystallized grain size; a subgrain misorientation model: Geophysical Research Letters, v. 25, p. 4237–4240, doi: 10.1029/1998GL900136.

Stipp, M.S., Heilbronner, R., and Schmid, S.M., 2002, Dynamic recrystallization of quartz: correlation between natural and experimental conditions, in de Meer, S., Drury, M.R., de Bresser, J.H.P., and Pennock, G., eds., Deformation Mechanisms, Rheology, and Tectonics: Current Status Future Perspectives, Volume Spec. Vol. 200: London, UK, Geological Society, p. 171–190.

Stipp, M., and Tullis, J., 2003, The recrystallized grain size piezometer for quartz: Geophys. Res. Lett., v. 30.

Tullis, J., and Yund, R.A., 1981, Grain growth kinetics of quartz and calcite aggregates: The Journal of Geology, v. 90, p. 301–318.

Twiss, R.J., 1977, Theory and applicability of a recrystallized grain size palaeopiezometer: Pure and Applied Geophysics, v. 115, p. 227–244, doi: 10.1007/BF01637105.

Van der Wal, D., Chopra, P., Drury, M., and Fitzgerald, J., 1993, Relationship between dynamically recrystallized grain size and deformation conditions in experimentally deformed olivine rocks: Geophysical Research Letters, v. 20, no. 14, p. 1479–1482.

Walker, A.N., Rutter, E.H., and Brodie, K.H., 1990, Experimental study of grain-size sensitive flow of synthetic, hot pressed calcite rocks, in Knipe, R.J., and Rutter, E.H., eds., Deformation Mechanisms, Rheology Tectonics, Volume 54, Geolog. Society Special Publication, p. 259–284.

Wightman, R.H., Prior, D.J., and Little, T.A., 2006, Quartz veins deformed by diffusion creep accommodated grain boundary sliding during a transient, high strain rate event, in the Southern Alps, New Zealand: Journal of Structural Geology, v. 28, p. 902-918, doi: 10.1016/j.jsg.2006.02.008

10. Figures

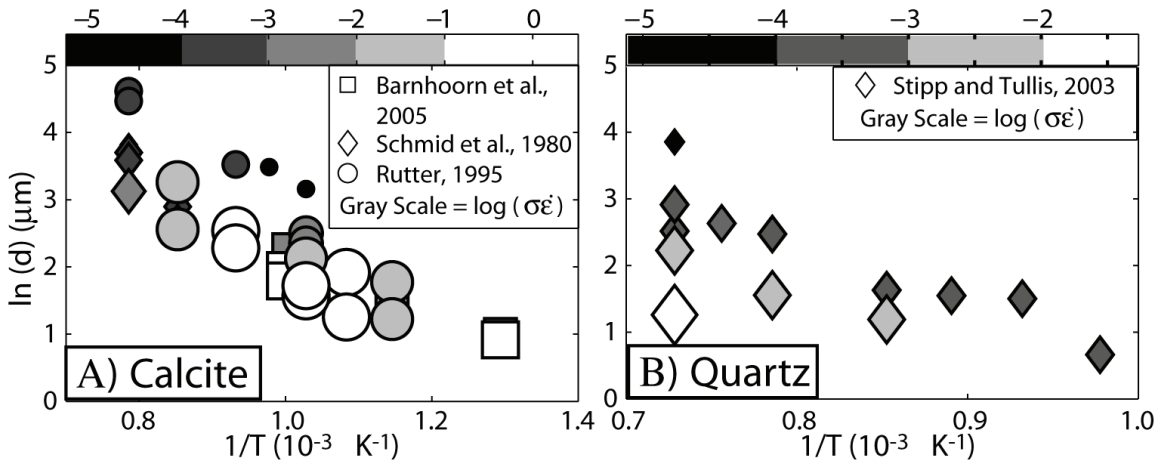


Figure 1) The relationship between temperature and grain size for A) calcite and B) quartz . See legend for data sources. The gray scale and symbol size both scale with the log of the power in each experiment.

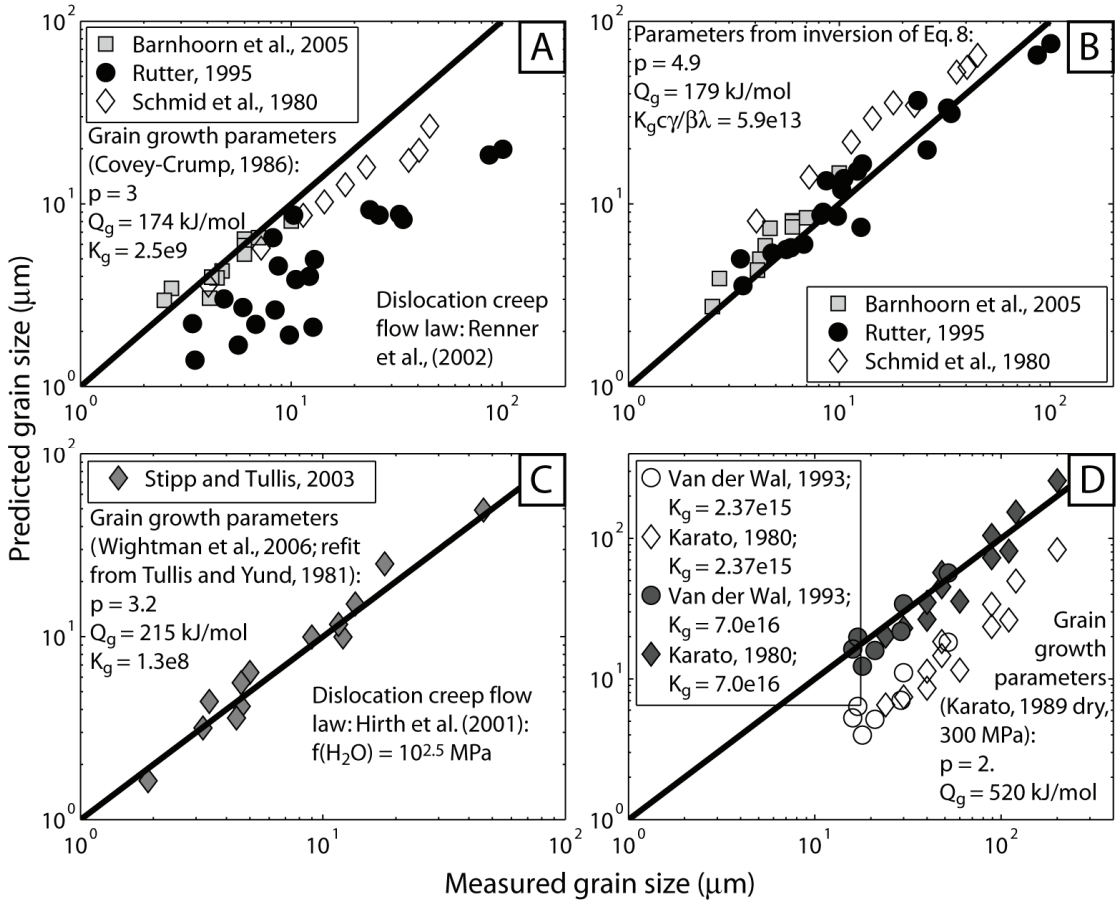


Figure 2) Grain size predicted from the paleowattmeter (Eq. 8 or 9) compared to that measured during dynamic recrystallization of A) calcite, using the dislocation creep flow law of Renner et al. (2002), and grain-growth parameters from Covey-Crump (1986); B) calcite, using an inversion of Eq. 8; C) quartz using the dislocation creep flow law of Hirth et al. (2001) and grain growth parameters from Wightman et al. (2006); D) olivine, using the dislocation creep flow law of Hirth and Kohlstedt (2003) and grain-growth parameters from Karato (1989).

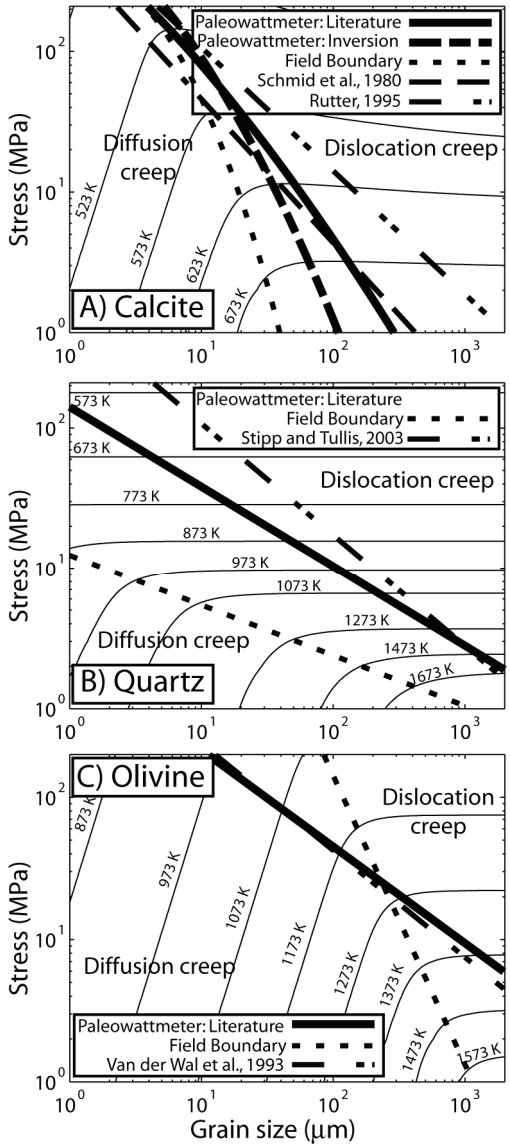


Figure 3) Deformation mechanism maps at $\dot{\varepsilon}$ =1e-12 s-1 for A) calcite, B) quartz, and C) olivine, with stress – grain size relationships from the paleowattmeter, empirical paleopiezometric calibrations (see respective legends), and the field boundary hypothesis (de Bresser et al., 1998, 2001). For olivine, Kg was taken as 7.0e16 μm^p s^{-1}. The dislocation and diffusion creep laws used are, respectively: A) calcite: Renner et al., 2002 ; Herwegh et al., 2003; B) quartz: Hirth et al., 2001; Rutter and Brodie, 2004; C) olivine: Hirth and Kohlstedt, 2003.

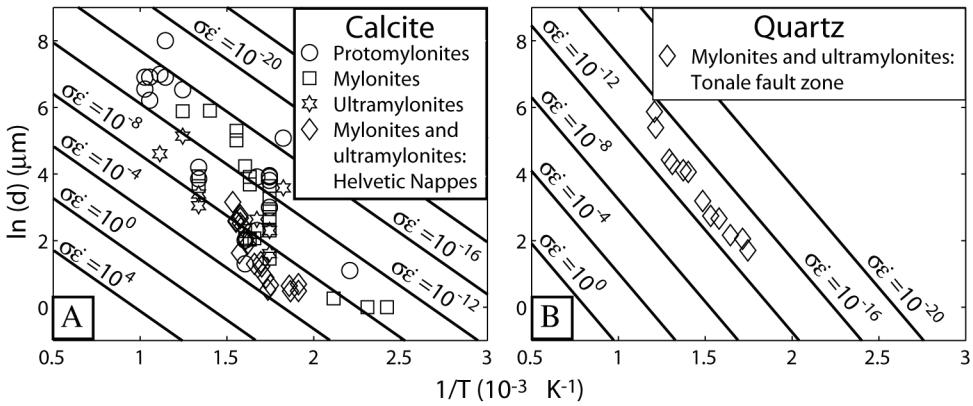


Figure 4) Grain size versus temperature relationships for samples from natural shear zones. A) calcite (cf. Herwegh et al., 2005; de Bresser et al., 2002 and references therein) and B) quartz (Stipp et al. 2002). Contours are for constant $\sigma\dot{\varepsilon}$ calculated using A) Eq. 8 with the parameters from the inversion (Fig. 2B), and B) Eq. 9 using the same parameters as in Fig. 2C, assuming deformation is completely accommodated by dislocation creep (β=1).

Chapter 3

Strain Localization in the Morcles Nappe (Helvetic Alps, Switzerland)

Nicholas Austin
Brian Evans
Marco Herwegh
Andreas Ebert

Abstract

Deformation in orogenic belts is frequently accommodated in calcite-rich lithologies, owing to their relatively low strength, particularly compared to quartz-rich rocks. Here, we investigate the coupling between calcite grain size, the presence and mineralogy of second phases, and crystallographic preferred orientation (CPO) in a transect through deformed limestones, perpendicular to the dominant foliation in the inverted limb of the Morcles nappe of the Swiss Helvetic Alps. Calcite grain size becomes progressively finer as the thrust contact is approached, and there is a concomitant increase in CPO intensity, with the strongest CPO's in the finest-grained, quartz-rich limestones, nearest the thrust contact. To understand the distribution of strain and the extent of strain localization, we compared the paleowattmeter and calcite flow laws from laboratory studies to previously published observations of microstructure at a range of locations, with varying peak metamorphic temperatures, along the Morcles nappe. The strain-rates predicted by extrapolation of these laboratory relationships agree well with the geologic constraints. We then applied the same approach to the samples from the present study. The results indicate that strain became progressively localized towards the thrust contact of the Morcles nappe, leading to an increase in strain rate of >1 order of magnitude in a zone <0.50 m thick. For localization to occur system and/or material softening is necessary. If dislocation activity is positively correlated with CPO, then softening cannot have occurred by a complete transition to diffusion creep in the finest grained samples. Rather, softening may have resulted from the formation of CPO, possibly coupled with effects related to the distribution of second phases and the overall geometry of the shear zone.

Published as:
Austin, N., Evans, B., Herwegh, M., & Ebert, A. (2008): Strain Localization in the Morcles Nappe (Helvetic Alps, Switzerland). *Swiss Journal of Geosciences* doi: 10.1007/s00015-008-1264-2

1. Introduction

Inelastic strains in lithospheric rocks, deformed during tectonic processes, are often accommodated along narrow faults and shear zones. For example, geodetic data show that global strains are largely accommodated along a few localized features (Kreemer et al. 2000; Kreemer et al. 2003). Similarly, at the field scale, structural geologists often conclude that lateral displacements of up to several kilometers have been accommodated in shear zones with widths of centimeters to meters (Boullier & Quenardel 1981; Milton & Williams 1981; Harris et al. 1983; Siddans 1983; Groshong Jr et al. 1984). Thus, the mechanics of shear zones are an important element in geodynamics (Poirier 1980; Hobbs et al. 1990; Burg 1999; Rutter 1999; Montesi & Zuber 2002; Burlini & Bruhn 2005).

Owing to the relatively low strength of calcite-rich rocks, deformation during orogenic events is frequently localized within limestones and marbles, particularly where these lithologies are juxtaposed with quartz- and feldspar-rich rocks (Groshong Jr et al. 1984; Pfiffner 1993; Kennedy & White 2001). The Helvetic zone in western Switzerland is a useful location for investigating the rheology of naturally deformed limestones. The nappes that comprise this region are composed of Jurassic to Cretaceous sediments that Burkhard (1988) attributed to basins within the Alpine Tethys, which were closed and inverted during the Alpine orogeny, resulting in the formation of highly localized shear zones in the limestones of the overturned limbs of the nappes.

Motivated by the regional scale observations of Ebert et al. (2007a), in this study, we undertook a dense and systematic sampling of calcite mylonites in an ~12m section of the inverted limb of Morcles nappe, in the Helvetic Alps of Switzerland near Saillon, just above the thrust contact with the autochthonous cover of the Aiguille Rouge Massif (Fig. 1). Earlier studies provide substantial constraints on the stratigraphy, geometry, and deformation history of

the Morcles nappe and its eastern pendant, the Doldenhorn nappe, at a regional scale (Badoux 1972; Ramsay 1981; Ramsay et al. 1983; Dietrich & Durney 1986; Burkhard & Kerrich 1988; Coward & Dietrich 1989; Dietrich & Casey 1989; Ramsay 1989; Escher et al. 1993; Pfiffner 1993; Crespo-Blanc et al. 1995; Kirschner et al. 1995; Kirschner et al. 1996; Burkhard & Goy-Eggenberger 2001; Bucher et al. 2003; Herwegh & Pfiffner 2005). Detailed studies of the microstructures of deformed marbles from a range of locations along the nappe also exist (Schmid et al. 1981; Dietrich 1986; Ebert et al. 2007a) (Figs. 1,2). Laboratory and field studies provide further insight into the coupling between strength and such microstructural elements as grain size and crystallographic preferred orientation (CPO) (Herwegh et al. 1997; Pieri et al. 2001a; Barnhoorn et al. 2004; Herwegh et al. 2005). By observing the matrix microstructure, matrix CPO, and the geometry and distribution of second phases at this particular location, we aim to identify and constrain the deformation mechanisms that operated, and to understand the spatial and temporal distribution of strain and strain rate in the shear zone.

2. Regional geology

The Helvetic nappes in western Switzerland are a stack of folds that include, moving structurally upwards, the Morcles, the Diablerets, and the Wildhorn nappes. This stack, in turn, is overlain by the Ultrahelvetic nappes (Escher et al. 1993). The Helvetic nappes were emplaced from top to bottom, and, thus, the thrust surfaces of the upper folds were bent during the emplacement of the lower ones (Trümpy 1973; Ramsay 1981). The Morcles nappe, itself, is a NW-verging recumbent fold, consisting primarily of Jurassic and Cretaceous shallow-water limestones with intercalated shales and marls (Badoux 1972; Epard 1990). The lower limb of this fold was inverted during the Alpine orogeny (Pfiffner 1981; Ramsay 1981, 1989; Pfiffner 1993). During the period from early Oligocene to Miocene, the recumbent-fold structure, which

roots in the Mont Blanc massif, was thrust >10 km over the Aiguille Rouge Massif and its cover of siliciclastic sediments and flysch units (Goy-Eggenberger 1998). The overturned limb of the nappe has been extensively sheared, resulting in axial ratios up to and exceeding 90:1 (Badoux 1972; Ramsay 1981; Siddans 1983; Dietrich 1989; Dietrich & Casey 1989; Kirschner et al. 1996). In addition, there was a late stage of brittle faulting and kinking associated with uplift. The total displacement accommodated in the inverted limb of the Morcles nappe varies from a maximum of 10-12 km in the root zone, to zero at the front of the nappe (Pfiffner 1993; Panien et al. 2005; Ebert et al. 2007a).

The peak metamorphic temperature at the toe of the nappe was approximately 200 ºC, with temperatures increasing linearly down-dip to greater than 350 ºC in the root zone (Frey et al. 1980; Kirschner et al. 1995; Burkhard & Goy-Eggenberger 2001; Ebert et al. 2007a) (Fig. 2). Folding of the sediments began before diagenesis was complete, resulting in the expulsion of significant volumes of fluids (Kirschner et al. 1995). Rapid burial to depths of 6-8 km occurred between 29 and 24 Ma, producing peak metamorphic conditions, which were accompanied by northward thrusting (Loup 1992; Kirschner et al. 1999). As the nappe deformed, the shear zone narrowed, resulting in a highly localized region of deformation (Ramsay et al. 1983), accommodated, wholly or in part, by crystal-plastic mechanisms (Schmid et al. 1981; Dietrich 1986; Ebert et al. 2007a), until ~16 Ma. Thermal modeling suggests that temperatures dropped by ~30-50 ºC during thrusting (Kirschner et al. 1995; Kirschner et al. 1996), and the last stages of deformation, during exhumation, were probably accommodated by brittle faulting (Burkhard & Kerrich 1988; Herwegh & Pfiffner 2005). Some fluids flowed along the thrust contact during deformation, but there is little evidence of fluid transport within the internal portions of the nappe (Kirschner et al. 1999).

3. Outcrop-scale structures

Three distinct lithologies outcrop at the study location (Swiss Coordinates 578.950/113.500), where the peak metamorphic temperature has been estimated as 358 ±15 ºC (Dietrich & Casey 1989; Marquer et al. 1994; Kirschner et al. 1995; Burkhard & Goy-Eggenberger 2001; Ebert et al. 2007a) (Figs. 1-3). The structurally highest lithology considered here is the limestone of the lower Urgonian. Rocks in this formation are gray and, on average, consist of greater than 95 vol% calcite. Below this unit are outcrops of upper Urgonian limestone, ~5 m thick, containing greater than 95 vol% calcite, which are distinguished from the lower Urgonian by their white colour. Structurally below this is a section of Gault limestone, >7 m thick, green in colour, and containing up to 50 vol% quartz and chlorite. The autochtonous Triassic cover sediments of the Aiguille Rouge massif do not outcrop at this location. Throughout the study area, stratigraphic layering is parallel to the dominant foliation, which dips at 35-40º towards the ESE.

Oblique to the main foliation are progressive generations of meso-scale shear zones (denoted by "loc" in Table 1), resulting in imbrication of (a) lower Urgonian and upper Urgonian (Fig. 3b,c), and (b) upper Urgonian and Gault (Fig. 3d). Progressive generations of these features cross-cut each other (Fig. 3b,c), and are associated with isoclinal folding of the main foliation (Fig. 3c), indicating that these features formed while distributed deformation was still occurring throughout the shear zone, and thus, are probably not related to brittle deformation associated with uplift.

4. Microstructures within the Morcles nappe

Heavily sheared marbles in the lower limb of the Morcles nappe show clear evidence that crystal-plastic mechanisms operated (Ramsay 1981; Schmid et al. 1981; Ramsay et al. 1983; Dietrich & Song 1984; Dietrich 1986; Ebert et al. 2007a): coarse vein calcite is heavily twinned and recrystallized; matrix calcite exhibits elongation (Schmid et al. 1981) and shows

characteristic recrystallization microstructures (Ebert et al. 2007a). In addition, near the thrust contact, the matrix calcite contains a distinct CPO, with c-axes oriented normal to the main foliation, which parallels the shear-zone boundary, consistent with formation during shear, rather than during initial folding (Schmid et al. 1981; Dietrich 1986; Ebert et al. 2007a). Calcite grain sizes decrease non-linearly from the root zone of the Morcles nappe to the fold hinge, even when there is no evidence that additional phases influence the matrix grain size (Ebert et al. 2007a). In addition, CPO intensity decreases as peak temperature decreases. The presence of second phases (i.e. minerals other than calcite) results in reduced matrix grain size, but this effect is more pronounced for samples containing sheet silicates than for those containing rounded quartz grains (Ebert et al. 2007a). CPO is also weaker in samples containing large volume fractions of second phases (Ebert et al. 2007a). Those authors found elevated dislocation densities in calcite grains in the vicinity of sheet silicates, in samples with a weak CPO, compared to calcite grains distal to sheet silicates in rocks with strong CPO.

5. Methodology of new observations

5.1. Sampling

Specimens were collected along a transect normal to the primary foliation, over a distance of 12.55 m. When heterogeneity in the formation existed, additional samples were selected from regions that were cut by the meso-scale shear zones or that contained anomalously high or low second-phase contents, to supplement those from nearby regions apparently homogeneously deformed. In total, 27 samples have been analyzed as part of this study (Table 1). Although the autochthonous Triassic cover of the Aiguille Rouge Massif does not outcrop at the study location, we believe that the structurally lowest sample (MOG18N1) is <<1 m from the contact between the inverted limb of the Morcles nappe and the Triassic, based on the thickness of Gault at this location and on the foliation intensity of that sample. All distances are given relative to

sample MOG18N1, and are considered estimated distances to the thrust contact. Oriented sections were prepared parallel to the dominant lineation and perpendicular to the primary foliation (i.e. the shear plane), and were etched in dilute hydrochloric acid and acetic acid in order to highlight grain boundaries and create relief between the calcite grains and second phases (Herwegh 2000).

5.2. Grain size and second-phase content

Calcite grain sizes were determined using the linear-intercept method on reflected-light micrographs of the oriented, etched samples. Average intercept lengths were measured both parallel and perpendicular to the foliation. A factor of 3/2 was used to correct the average intercepts (Underwood 1970; Exner 1972). The average grain sizes we obtained using this technique are consistent with those obtained by area weighting equivalent circular diameters of measured grain areas on samples from the outcrop we are investigating (Ebert et al. 2007a). The size and area of second-phase grains were determined by tracing regions of high relief, as observed in reflected light, and measuring the tracings using NIH ImageJ®. When second–phase grains were in direct contact, they were treated as a single grain, because we were primarily interested in the influence of second phases in pinning matrix grain boundaries. We characterized the dispersion of second phases by calculating a Zener parameter (Z) (Smith 1948; Nes et al. 1985; Olgaard & Evans 1986; Humphreys & Ardakani 1996)

$$Z = \frac{d_2}{f_2^k} \qquad 1)$$

Here, d_2 refers to the grain or aggregate size of second phases, and f_2 refers to the areal fraction of those phases. The exponent, k, varies between 0.33 and 1 depending on details of the dispersion of pinning phases. Based on extensive microstructural observations, Ebert et al.

(2007a) suggested that $k=1$ is the appropriate exponent for calcite mylonites in the Morcles nappe. But even withstanding that conclusion, Z should serve as a relative measure of the dispersion of the second phases, for which purpose it is used here. Second-phase mineralogy was determined by observation in both transmitted and reflected light. Wherever possible, observations were made in adjacent bands of nominally "pure" and "impure" matrix.

5.3. Analysis of crystallographic preferred orientation

Crystallographic preferred orientation (CPO) was measured by Electron Back Scatter Diffraction (EBSD) on the oriented sections previously used for measurement of matrix grain size and second-phase content. In many samples, several areas within a given section were analyzed for both CPO and grain size. Analyses were performed using a JEOL JSM 840 SEM with HKL Channel 5+ software at the Woods Hole Oceanographic Institution (WHOI), with an accelerating voltage of 15kV, tilt of 70º, and working distance of 23mm. The beam current was varied between 3e-7 and 3e-8 A. For each region of investigation, ~200 individual grains were manually selected by ensuring that the diffraction pattern was significantly different than neighboring analyses. Each analysis was indexed using the HKL software, accepting only fits with a mean angular deviation (MAD) < 1.3. In addition, each indexed pattern was manually checked. Analyses from 200 individual grains have been shown to be sufficient to quantify texture intensity (Skemer et al. 2005). Several samples were also analyzed using a Zeiss EVO 50 SEM with TSL-EBSD system (OIM 4.5 software) and automated data acquisition of >1000 points (step sizes 1-5 μm), at the University of Bern. The resulting crystallographic orientations were indistinguishable from those obtained manually at WHOI. Pole figures were created using the program PFch5 (D. Mainprice, pers. comm., 2007). They are presented as lower hemisphere projections with Gaussian smoothing of 8.5º, and are contoured for each multiple of a uniform

distribution (MUD) up to global maximum of 15. The texture intensity is quantified with the M-Index (Skemer et al. 2005).

6. Microstructural observations

6.1. Matrix grain size

Three distinct trends in grain size are observed in the deformed marbles in the inverted limb of the Morcles nappe (Figs. 4-6). Most striking is the reduction in calcite grain size (D_{cc}) with decreasing distance to the thrust contact (Fig. 6a). Secondly, it is well known that second-phase content may influence the matrix grain size, and this effect has been copiously documented in naturally deforming rocks (Mas & Crowley 1996; Krabbendam et al. 2003; Herwegh & Berger 2004; Herwegh et al. 2005; Ebert et al. 2007a; Ebert et al. 2007b). In this study, samples from all three units appear to cluster into one of two groups, those with Z greater than or less than 500 μm, respectively (Fig. 6). Note that Ebert et al. (2007a) suggested that the transition from a pinned to unpinned microstructure should occur at Z~200 μm at our study location, although this boundary is not sharply defined. Apparently, chemical variations between lithologies do not influence the calcite grain size, and, in fact, Ebert et al. (2007a) found no measurable difference in calcite chemistry (e.g. Mn, Mg, Fe, and Sr concentrations) between the Gault and the lower Urgonian at the location of this study. There is, however, substantial local variation in the calcite grain size in samples within the Urgonian, at distances greater than 7 m from the thrust contact and with Z>500 μm, sometimes even when there are no readily apparent second phases (Fig 6b, Z=2000 μm samples). Finally, samples from the meso-scale shear zones (Fig. 3) within the upper Urgonian have a reduced grain size compared to the host rock (<0.01 m away) (Fig. 4c-d, Fig. 6a-b, samples labeled “loc”), and compared to the grain size predicted by the Zener relation (eq. 1, Fig. 6b).

6.2. Second phases

The mineralogy and distribution of second phases varies as a function of primary lithology, and thus also distance to the thrust contact. In the upper and lower Urgonian, second phases are sheet silicates (Fig. 4a-d), with minor quartz (Fig. 5e-f). Second phases may be rare and broadly spaced (e.g., Fig. 4c), or closely spaced and aligned with the primary foliation (e.g. Fig. 4b). Along the boundaries of the meso-scale shear zones, within the upper Urgonian, sheet silicates are often interconnected at the thin-section scale (Fig. 4d). Within the Gault, second phases are predominantly quartz and chlorite (Fig. 5a-d), frequently occurring as fine-grained elongate aggregates, parallel to, and often defining, the primary foliation. The sample closest to the thrust contact (MOG18N1: Fig. 4e,f) is unique in that it contains quartz but no chlorite. In this sample, quartz is either homogeneously mixed with the calcite (Fig. 4f), segregated into bands (Fig. 4e), or present as large porphyroblasts, around which the calcite clearly flows (Fig. 5b). Some layers within this sample are the most quartz rich of any studied (Fig. 4f) whereas other layers contain very little visible quartz (Fig. 4e). In the Gault, coarse-grained quartz porphyroblasts exhibit undulose extinction (Fig 5b,d,f), but, in both the Gault and the Urgonian, fine-grained quartz embedded in a calcite matrix frequently shows uniform extinction (Fig. 5a,e). Proximal to the thrust contact, coarse-grained quartz porphyroblasts also appear to be fractured (Fig 5b).

6.3. Crystallographic preferred orientation (CPO)

In all samples, calcite c-axes are preferentially oriented approximately normal to the thrust contact, and a-axes form a girdle in the shear plane (Fig. 4). Samples from the upper and lower Urgonian, with a range of second-phase contents, display back rotation of the calcite c-axes and a-axes with respect to the shear direction (Fig. 4a,b). Such rotations are not seen in finer-grained calcite near the thrust contact (Fig. 4e,f). The r-poles are moderately inclined to the shear plane, and are sometimes evenly distributed around the c-axes (Fig. 4a,e,f), but in those samples with

the strongest preferred orientation (MOG18N1), they form 3 distinct point maxima (Fig. 4e,f). These patterns are similar to those observed by Bestmann et al. (2000) in deformed marbles on Thassos, Greece.

The samples taken from closest to the thrust contact have a stronger preferred orientation, quantified using the M-Index (Figs. 4,7a) compared to all samples from distal to the thrust contact. The degree of preferred orientation is reduced with decreasing calcite grain size (Fig. 7b). However, there are two distinct trends: (a) the samples from <1.05 m above the thrust contact, and (b) all remaining samples. The former gives rise to the increase in CPO intensity proximal to the thrust contact. In samples distal to the thrust contact, the fine-grained regions bounding the meso-scale shear zones have a reduced CPO intensity compared to the coarser-grained calcite which hosts them (Fig. 4c,d). The trend of these features on a plot of M-Index vs. calcite grain size (Fig. 7b) is similar to that for all samples distal to the thrust contact. The sample from closest to the thrust contact, and that from 0.8 m away, also exhibit reduced CPO intensity with decreasing grain size (Fig. 4e,f, 7b). However, despite having grain sizes similar to the fine-grained regions bounding the meso-scale shear zones (Fig. 6b, 7b), these samples have dramatically stronger CPO's (M-Index up to 0.5 compared to <0.05 for the samples from the meso-scale shear zones) (Fig. 4,7). Note that the sample from 0 m (MOG18N1) contains quartz, but no sheet silicates, whereas all other fine-grained samples contain sheet silicates (including chlorite) ± quartz (Fig. 7).

7. Discussion

7.1. Deformation mechanisms

At the Saillon cave, at all distances from the thrust contact of the Morcles nappe, matrix-calcite grains have crystallographic preferred orientations (CPO) with c-axis maxima normal to, or slightly antithetically rotated from, the shear plane, and with a-axes distributed within the shear

plane. Antithetic rotation of calcite c-axis maxima has also been observed in the Morcles nappe, near Saillon, by Schmid et al. (1981), a pattern that has been attributed to e-twinning, resulting in the alignment of calcite c-axes with the greatest compressive stress (σ_1)(Schmid et al. 1987). Pieri and coworkers (Pieri et al. 2001a; Pieri et al. 2001b) suggested that calcite c-axes progressively rotate during shear deformation, becoming perpendicular to the shear plane with increasing strain. Grains with c-axis maxima normal to the shear plane are preferentially oriented for basal slip (Barber & Wenk 1979; Paterson 1979; De Bresser & Spiers 1993; De Bresser & Spiers 1997; Bestmann et al. 2000; Barber et al. 2007), and the spread of a-axes within the shear plane may be caused by duplex slip in the basal plane (De Bresser & Spiers 1997; Bestmann et al. 2000; Barber et al. 2007). The strong preferred orientation of r-poles (particularly in sample MOG18N1; Fig. 4) can result from simultaneous activation of all three of c-slip, r-slip, and e-twinning as observed in calcite single crystals deformed in both compression and torsion (Wenk et al. 1973; Paterson 1979; De Bresser & Spiers 1990; Wang et al. 1996; Barber et al. 2007). However, we did not quantify the densities of twins, which are not common, particularly in the finest-grained samples (Fig. 4e).

There are two trends of CPO intensity: at a given distance from the thrust contact, M-Indices increase with increasing grain size, particularly in samples distal to the thrust contact and from rocks bearing sheet silicates (Fig. 6). As the distance from the thrust contact varies, the M-Indices, while quite scattered, are roughly constant, except for samples closest to the thrust contact, which exhibit M-Indices between 0.25 and 0.5. The former trend may indicate that a greater proportion of the bulk strain rate was accommodated by grain-boundary sliding in finer grains, that the fine grains, on average, record smaller strains, or that the correlation between total strain and M-Index differs between coarse and fine-grained rocks. In close proximity to the

thrust contact, the carbonates are quartz-bearing; and these, the finest-grained rocks, have the highest CPO intensities. If dislocation activity and CPO intensity are positively correlated (Rutter et al. 1994; Barnhoorn et al. 2004; Warren & Hirth 2006; Mehl & Hirth 2008), deformation within the finest-grained rocks cannot be supposed to have been dominated by diffusion creep, however, we cannot rule out some component of grain-boundary sliding (e.g. Schmid et al. 1987). Measurements of misorientation between neighbouring grains may be used to gain insight into the role of grain-boundary sliding, as well as active slip systems (Bestmann & Prior 2003), but owing to the fine grain size of the Morcles samples, we were unable to perform correlated misorientation measurements.

7.2. Pore fluids

To this point, we have neglected the role of pore fluids. As has been well documented by Kirschner et al. (1999), fluid flow was focused along the thrust contact of the Morcles nappe for most of its deformation history. Several authors suggest that water fugacity has little influence on the kinetics of dislocation creep in calcite, both in the laboratory (Rutter 1972; De Bresser et al. 2005) and in natural mylonites (Schenk et al. 2005). But high water pressures will influence pressure solution/fluid-assisted mass-transfer processes (Paterson 1995). At the Saillon cave, the role of fluids likely influenced the formation of the meso-scale shear zones (Fig. 4c,d), which are frequently associated with variably recrystallized veins, have elevated concentrations of sheet silicates, and have the lowest CPO's we observe. Mass transfer in fluids also occurred near the thrust contact, as both quartz and calcite veins are present in the Gault. However, the strong CPO's near the thrust contact at our study location probably indicate that dislocation creep, rather than pressure solution, was the dominant deformation mechanism.

7.3. Power dissipation and strain-rate estimates

7.3.1. From grain-size to strain-rate: The paleowattmeter

Grain-size responds to thermodynamic driving forces through the processes of dynamic recrystallization, normal and abnormal grain growth, and chemically induced grain-boundary migration (Urai et al. 1986; Atkinson 1988; Drury et al. 1989; Humphreys & Hatherly 1995; De Bresser et al. 1998; Evans et al. 2001). Many studies suggest that the average grain size at steady state during dynamic recrystallization (d_s) is indirectly related to differential stress (σ) to a power (q) that is of order of unity (Table 2, eq. S1980, R1995SG) (Twiss 1977; Twiss & Sellars 1978; Guillope & Poirier 1979; Karato et al. 1980; Schmid et al. 1980; Gleason et al. 1993; Rutter 1995; Stipp et al. 2001). The mechanism by which steady state is achieved is a topic of some discussion (Guillope & Poirier 1979; Karato et al. 1980; Etheridge & Wilkie 1981; Sakai & Jonas 1984; Urai et al. 1986; Derby & Ashby 1987; Derby 1991, 1992; Van Der Wal et al. 1993; Rutter 1995; De Bresser et al. 1998; Shimizu 1998; De Bresser et al. 2001; Ter Heege et al. 2002; Hall & Parmentier 2003; Montesi & Hirth 2003; Ter Heege et al. 2005). Some authors have suggested that the stable average grain size represents a balance between the rates of reduction by dynamic recrystallization and of normal grain growth (Derby & Ashby 1987; Derby 1991, 1992; Kameyama et al. 1997; Shimizu 1998; Braun et al. 1999; Shimizu 1999; Hall & Parmentier 2003). De Bresser and coworkers (De Bresser et al. 1998; De Bresser et al. 2001) concluded that this balance might cause the aggregate grain-size to stabilize at a value for which the strain rates owing to dislocation creep and to diffusion creep are equal.

Recently, Austin & Evans (2007) suggested that the grain-size reduction rate during deformation is controlled by the rate that mechanical work is done, and the ability of the rock to either dissipate or store this energy. During deformation, the rate that mechanical work is done per unit volume (power) is the product of stress and strain rate (note that “stress” refers to

"differential stress"). The rate of energy input into the system must be balanced by the rate of increase in the internal energy of the system plus the rate that energy is dissipated, which is largely related to heat production and/or other increases in entropy. Because decreased grain size implies increased stored interfacial free energy, Austin & Evans (2007) suggested that the magnitude of $\dot{d}_{reduction}$ is proportional to the rate of mechanical work done on the deforming rock. The existing laboratory data, although sparse (e.g. Karato et al. 1980; Walker et al. 1990) suggest that all of the power input during diffusion creep is completely dissipated, whereas some fraction of the power input during dislocation creep (λ) is stored in the material. Grain-size reduction rates will be enhanced by the increased efficiency of storage, as well as by the relative partitioning of the total strain rate between dislocation creep and diffusion creep. As suggested previously (Kameyama et al. 1997; Braun et al. 1999; Hall & Parmentier 2003), we assume a balance between the rates of static grain growth and reduction by dynamic processes: $\dot{d}_{total} = \dot{d}_{growth} - \dot{d}_{reduction}$, where $\dot{d}_{reduction}$ is explicitly negative. The scaling relationship that results, a paleowattmeter, predicts a stabilized grain size (Table 2, eq. AE07) that is a function of: γ, the specific grain-boundary energy, β, the fraction of the work partitioned into dislocation creep $\left(\sigma\dot{\varepsilon}_{dis}/\sigma\dot{\varepsilon}_{tot}\right)$; λ, the fraction of that mechanical work stored as internal energy; and K_g, Q_g, p, the constants in the normal grain-growth law ($d^p - d_o^p = K_g \exp\left[\frac{-Q_g}{RT}\right]\Delta t$, Table 2)(Evans et al. 2001; Austin & Evans 2007).

Thus, in this model, recrystallized grain sizes provide information regarding the rate that mechanical work is done during deformation, or the product of stress and strain rate, rather than stress alone. By incorporating the appropriate flow laws into the paleowattmeter (Table 2, eq. AE07), stress and strain rate are simultaneously obtained from the measured grain sizes and

measured/estimated thermal conditions during deformation. When published grain-growth laws and dislocation creep flow laws are incorporated into the paleowattmeter, grain sizes obtained in laboratory deformation experiments on calcite, quartz, and olivine are successfully predicted. In the following sections, we will test predictions from the paleowattmeter and paleopiezometers against our observations from the Morcles nappe.

7.3.2. Are microstructures indicative of deformation conditions?

For samples deformed in the laboratory at high temperatures, it is sometimes difficult to distinguish microstructures formed during static grain growth from those formed during deformation. So, before applying the paleowattmeter and paleopiezometers to the natural microstructure data, we consider the possibility that grain sizes have been influenced by annealing and grain growth after deformation. Fine recrystallized grains are universally present, particularly in the coarsest-grained samples (Fig. 4a,c). Further, Herwegh and coworkers (Herwegh & Berger 2003; Herwegh et al. 2005; Ebert et al. 2007b) argue that the grain size of rocks with varying second-phase content, if annealed at similar conditions, will exhibit a positive slope in $d_s - Z$ space (where d_s is the stable grain size), for all Z values, because grains will grow until they interact with a pinning phase. The average grain size of our samples and those of Ebert et al. (2007a) from this study location, do not vary with Z when Z>500 μm (Fig. 6b). However, we cannot rule out the possibility that some coarsening related to annealing occurred; thus, incomplete coarsening might be responsible for some of the scatter observed in calcite grain size for samples with no visible second phases (Fig. 6b, Z=2000 μm). Such coarsening, if present, did not, however, proceed to the fully pinned state. The strong correlation between grain size and distance to the thrust contact also indicates that there has not been extensive annealing.

An additional possibility is that the matrix grain size has not reached a steady state, due to incomplete recrystallization. However, two lines of evidence suggest that the measured

recrystallized grain sizes are representative of the deformation conditions. First, where calcite veins are present they exhibit incomplete recrystallization, with recrystallized grains having the same grain size as the matrix calcite (Fig. 5). Herwegh et al. (2005) made similar observations on the Doldenhorn nappe and Gellihorn and Wildhorn nappes, and drew the same conclusion as we do here: measured grain sizes are indicative of deformation conditions. Further, in the fine-grained, micritic limestones of the Doldenhorn nappe (the eastern extension of the Morcles nappe) grain growth seems to have occurred in the matrix as grains in nearby veins were reduced with both reaching similar final grain sizes (Herwegh et al., 2005). The suggestion is that, not only are microstructures indicative of the deformation conditions, but also that these microstructures result from competing grain-growth and grain-size reduction processes; an inherent assumption of the paleowattmeter. Second at all distances from the thrust contact, the primary foliation is approximately parallel to the shear zone, consistent with the observations of Ramsay (1981), Schmid et al. (1981), and Ebert et al. (2007a) that all of the limestones in the inverted limb of the Morcles nappe are highly sheared, frequently exhibiting axial ratios of >90:1. Based on laboratory studies (Pieri et al. 2001a; Pieri et al. 2001b; Barnhoorn et al. 2004), we expect to find complete recrystallization at shear strains greater than ~10, well below the minimum strains in all of our samples. From these constraints, we infer that variations in calcite grain size correspond to variations in the conditions of deformation.

7.3.3. Stresses and strain rates along the inverted limb of the Morcles nappe

We applied the paleowattmeter and paleopiezometers (Eqs.AE07, S1980, R1995SG, Table 2) to the data from samples with Z>500 μm from the upper Urgonian at various positions along the Morcles nappe (Ebert et al. 2007a) (Figs. 2 and 8a). We limit our analysis to flow laws for fine-grained carbonates (Schmid et al. 1977; Walker et al. 1990; Renner et al. 2002; Herwegh et al. 2003) (Table 3), as these are most applicable to the microstructures observed in the Morcles

nappe. Note that the parameters in these flow laws were obtained from experiments run to relatively low strains in triaxial compression: we will address the role of strain softening, as observed by Barnhoorn et al. (2004) during high-strain torsion experiments on coarse-grained Carrara marble, in the next section.

If grain-growth parameters from Covey-Crump (1997) and dislocation creep flow laws for synthetic marbles (Renner et al. 2002) (Table 3, Rp) or for Solnhofen limestone (Schmid et al. 1977) (Table 3, Sdis) are used, equation AE07 predicts values of $\sigma\dot{\varepsilon}_{dis}$ consistent with strain rates from dislocation creep between 10^{-10} and 10^{-12} s^{-1} (Fig. 8a,b). The total strain rate may be estimated by using diffusion creep and dislocation creep laws, and the assumption that $\dot{\varepsilon}_{tot} = \dot{\varepsilon}_{dif} + \dot{\varepsilon}_{dis}$ (Ter Heege et al. 2004; Herwegh et al. 2005). For the dislocation and diffusion creep flow laws in table 3, the strain-rate profiles in figure 8b are predicted for the length of the nappe. The predicted strain rates are slightly faster (~10^{-11} s^{-1}), but still roughly consistent with values constrained by the field structural data (Ebert et al., 2007a; 10^{-11} to 10^{-13} s^{-1}). The dislocation creep flow laws of Renner et al. (2002) (Rp) and Schmid et al. (1977) (Sdis), when coupled with a diffusion creep flow law for the same material, Herwegh et al. (2003) (Hdif) and Schmid et al. (1977) (Sdif), respectively, both suggest that the total strain rate is dominated by dislocation creep (Fig. 8c), consistent with the CPO observations of Ebert et al. (2007a), particularly in the higher temperature portions of the shear zone. But, if the diffusion creep parameters from Walker et al. (1990) (Wdif) are used with either dislocation creep flow law, diffusion creep is predicted to dominate.

The paleowattmeter suggests that the power increased from the root zone, reached a peak at distances of 12-14 km from the fold hinge, and then progressively decreased towards the hinge (Fig. 8b). Field relations indicate that the total displacement accommodated across the inverted

limb of the Morcles nappe decreased progressively from ~12km at the Saillon cave to 0 km at the fold hinge, and that the shear zone narrows. Thus, strain rates are believed to remain roughly constant along the shear zone (Ebert et al. 2007a). But, without denser sampling along the shear zone, it is difficult to be more precise.

At the lower temperatures estimated near the toe of the nappe, it may be that deformation occurred, at least in part, by other mechanical processes, e.g., granular flow, fracture, or pressure solution. None of these processes are included in the paleowattmeter or the composite flow law that we have considered, so their presence might be responsible for the apparent decrease in power and strain rate as recorded in the grain sizes. CPO intensities also decrease towards the frontal portions of the nappe (Ebert et al. 2007a), as might be consistent with partitioning of strain into cataclastic mechanisms; however, this decrease might also be caused by variations in total strain. Also note that, at the temperatures and grain sizes investigated in the Morcles nappe, the paleopiezometer calibrations of Schmid et al. (1980) and Rutter (1995) bound the predictions of the paleowattmeter, when the dislocation creep flow law of Renner et al. (2002) (Rp) is used. Variations in the stress predicted by the several piezometers may arise owing to differences in technique used to the measure grain size (Rutter 1995; De Bresser 2002). In this study, we simply use the reported grain-size values, without attempting to resolve differences in techniques.

7.3.4. Stress and/or strain rate variations normal to the thrust contact

At the Saillon cave, in carbonate samples where grain-boundary pinning is unlikely (Z>500 μm), the paleowattmeter suggests that significantly more power was dissipated near the thrust contact (Fig. 9a). The fine-grained samples nearer to the thrust contact also have the strongest CPO's of any samples we investigated (Fig. 4e,f, 7a), and, on average, the highest quartz contents (Fig. 4-6). The reduced grain size, and increased power closest to the thrust contact can

be explained in two ways: 1) there may have been temporal and spatial variations in stress, or 2) the limestones nearest the thrust contact may have strain weakened, resulting in progressive strain localization and increased strain rates at constant stress.

Using any of the flow laws (Table 3) and the paleowattmeter, we predict both elevated stresses and strain rates in the finest-grained rocks closest to the thrust contact (Figs. 9b,c). If this scenario is correct, stress must have varied temporally, as mechanical considerations preclude contemporaneous stress variations normal to the thrust contact in a simple thrusting geometry. Stress variations may have occurred if there were significant variations in the orientation of the lithological contact between the inverted limb of the Morcles nappe and the Triassic cover of the Aiguille Rouge massif, however, in outcrop we see no evidences of any deviation from a simple, relatively flat, thrust-fault geometry.

As with the variations along the inverted limb of the Morcles nappe, the stresses along a profile normal to the thrust contact predicted by the paleowattmeter and the dislocation creep flow law of Renner et al. (2002) (Rp) are bound by the predictions of the paleopiezometers of Schmid et al. (1980) (S1980) and Rutter (1995) (subgrain: R1995SG). If, instead, the paleowattmeter, and the dislocation creep flow law from Schmid et al. (1977) (Sdis) are used, stresses are approximately a factor of 2-3 higher. Rutter's grain boundary migration piezometer (Rutter 1995) (not shown) predicts stresses of ~180 MPa in the upper Urgonian, and stresses >450 MPa closest to the thrust contact, in the Gault.

The limestones nearest the thrust contact are quartz-rich. Experimental studies have shown that the addition of as little as 5 vol% uniformly dispersed quartz to fine-grained calcite aggregates increases the strength of the material (Dresen et al. 1998; Rybacki et al. 2003; Xiao & Evans 2003; Renner et al. 2007). However, it is difficult to envision this strength variation resulting in

contemporaneous stress variations across the shear zone, when quartz-rich limestones (Gault) are juxtaposed with pure limestones (Urgonian).

Temporal variations in loading geometry are mechanically admissible. An alternative explanation might be that stresses increased as temperature decreased (Kirschner et al. 1996). Ebert et al. (2007a) have suggested that progressive localization occurred under retrograde conditions. However, again considering the juxtaposition of relatively pure and impure limestones, we would expect elevated stresses to be recorded in all microstructures, particularly in the pure limestones of the Urgonian. Thus stress variations of a factor of ~3 recorded over a spatial scale of less than 15 m seem unlikely.

We now consider a second, more plausible, scenario: the increase in power closest to the thrust contact resulted from strain weakening of the material, leading to an increase in strain rate at constant stress. This hypothesis is consistent with theoretical and experimental considerations of strain localization (Hobbs et al., 1990; Rutter, 1999). If we assume that stresses were constant in sections normal to the thrust contact, then a >10-fold enhancement in strain rate in the rocks closest to the thrust contact would be required to explain the power predictions from the paleowattmeter (Fig. 9a), regardless of which dislocation creep flow law is chosen. For example, if the stress was 35 MPa throughout the shear zone, the paleowattmeter predicts strain rates nearly equivalent to those labelled AE07RpHdif in figure 9c, whereas if the stress was 125 MPa, the predicted strain-rate distribution is closer to that labelled AE07SdisSdif.

Multiphase materials might weaken, particularly if the stronger phase reorganizes into a foliation plane (Handy 1990, 1994; Ji et al. 2004; Barnhoorn et al. 2005), or if a strong CPO is formed (Pieri et al. 2001a; Pieri et al. 2001b; Barnhoorn et al. 2004). In those studies on coarse-grained marbles, a 20-25% weakening was observed at constant strain rate, equivalent to a 3-4-

fold enhancement of strain rate under constant stress conditions. The rocks in the Morcles nappe have undergone at least 5-10 times more total strain than even the highest-strain experiments in the studies discussed above, and considering the strength of the CPO's in the samples from closest to the thrust contact of the Morcles nappe, a 10-fold strain-rate enhancement may not be unreasonable (Fig. 7a).

Based on the assumption that strong CPO's indicate deformation was dominated by dislocation creep, weakening cannot have been related to a switch in deformation mechanism from dislocation creep to diffusion creep, associated with grain-size reduction. Both sets of flow laws we investigated also suggest that deformation was dominated by dislocation creep (Fig. 9d) even withstanding any assumptions regarding geometric weakening.

7.4. Estimating the temporal and spatial evolution of strain

If the shear zone initially had a thickness of 50 m, and was deforming at a strain rate of 10^{-12} s^{-1} (Ebert et al. 2007a), then the regional displacement rate was ~1.6 mm/yr. This average slip rate could accommodate the ~12 km of offset estimated for the Saillon cave (Ebert et al. 2007a) in the ~8 ma that the inverted limb of the Morcles nappe was actively deforming (Loup 1992; Kirschner et al. 1999). Using the paleowattmeter (Austin & Evans 2007), the dislocation creep flow laws of Renner et al. (2002) (Rp) or Schmid et al. (1977) (Sdis), and the diffusion creep flow laws of Herwegh et al. (2003) (Hdif) or Schmid et al. (1977) (Sdif), the strain rates calculated at each distance from the contact between the inverted limb of the Morcles nappe and the Triassic cover of the Aiguille Rouge massif are consistent with the shear-zone thicknesses required to accommodate the regional displacement rate (Fig. 9c). Assuming the regional displacement rates remained approximately constant during thrusting of the Morcles nappe, this suggests that, in agreement with Ramsay et al. (1983), with progressive thrusting, the active

zone of intense shear became narrower, and the microstructure is thus recording the peak strain rates at a given position. If temperatures were lower than the peak metamorphic temperatures, lower strain rates would be predicted from the observed microstructure, thus requiring a broader shear zone to accommodate the same displacement rate. For example, at 308 ºC the AE07RpHdif composite flow law predicts similar total strain rates to the AE07SdisSdif composite flow law at 358 ºC (Fig. 9c).

Several key uncertainties will influence this analysis. First, as discussed above, there is significant uncertainty in the absolute values of the temperature estimates for each location, although the relative temperatures appear to be robust (Ebert et al. 2007a). Secondly, the regional displacement rate might have varied over time. Lastly, we do not, at present, have good constraints on the total displacement accommodated by the meso-scale shear zones, so we cannot quantify the fraction of the regional displacement rate that these features accommodated. Despite these uncertainties, the agreement between the predicted distribution of strain rate and that required to explain the tectonic environment during nappe emplacement is striking.

7.5. Implications for the emplacement of the Helvetic nappes

Reduced grain sizes are frequently observed in association with mylonite shear zones, including in deformed limestones throughout the Helvetic zone. For example in the Doldenhorn nappe and Glarus thrust, Herwegh & Pfiffner (2005) and Ebert et al. (2007b), respectively, documented similar grain-size profiles with decreasing distance to the thrust contact as we have observed in the Morcles nappe. However, unlike in the present study on the Morcles nappe where the strongest CPO intensities were found in the finest-grained limestone mylonites closest to the thrust contact, these previous studies documented reduced CPO intensities in the finest-grained rocks closest to the thrust contact in both the Doldenhorn nappe (Herwegh & Pfiffner

2005) and Glarus thrust (Ebert et al. 2007b). Earlier workers have made similar observations on the Glarus thrust (Schmid et al. 1977; Pfiffner 1982). All of these previous studies attributed the correlation between fine grain sizes and weak CPO intensities to a transition from dislocation creep dominated deformation at coarse grain sizes to grain size sensitive diffusion creep and/or dislocation creep accommodated grain boundary sliding at finer grain sizes. However, both along the Glarus thrust (Ebert et al. 2007b) and in the Gellihorn nappe (Herwegh & Kunze 2002; Herwegh et al. 2005) fine-grained layers with a strong CPO are found juxtaposed with layers having a similarly fine grain size and a weak CPO. More detailed work is necessary to quantitatively relate CPO intensity with deformation mechanisms and mechanical properties; however, these observations suggest that the mechanical evolution of limestone mylonites may have differed between the different Helvetic nappes, possibly resulting in variations in the temporal evolution of the distribution of strain. If so, the mechanical history of the various Helvetic nappes may have been markedly different, thus influencing the overall evolution of the Helvetic zone, although much more work is required to quantify this statement.

8. Conclusions

In samples where there is no evidence of second-phases influencing the calcite grain size (Z>500 μm), there is a significant reduction in calcite grain size, and concomitant increase in CPO intensity with decreasing distance to the thrust contact. When second phases are present (Z<500 μm), these poison calcite grain-growth, resulting in a finer calcite grain size.

We have used the paleowattmeter to estimate strain rates within the inverted limb of the Morcles nappe. When the paleowattmeter is applied to samples with Z>500 μm collected previously from several locations along the nappe, the strain-rates predicted using published flow laws are consistent with estimates based on geologic observations. If the grain size along a

transect perpendicular to the thrust contact is interpreted by the paleopiezometers, stresses are predicted to vary, and to be higher closer to the thrust contact. However, due to mechanical considerations, this scenario seems unlikely. If stresses are assumed to be constant along the transect, the paleowattmeter suggests material weakening, which is consistent with theoretical considerations pertaining to strain localization. Such weakening might be associated with the formation of CPO and a strong foliation, both of which are observed close to the thrust contact. Further, our CPO observations suggest that deformation was accommodated by dislocation creep, despite the fine grain size.

To fully understand strain localization in multiphase rocks, more work needs be done investigating the coupling between CPO formation, grain-size evolution, foliation development, and rheological properties. Despite these uncertainties, the deformation conditions predicted using the paleowattmeter and calcite flow laws are in good agreement with both microstructural and regional scale observations along the Morcles nappe.

9. Acknowledgements

We would like to thank Greg Hirth, Louie Kerr, Luc Mehl, and Jessica Warren for assisting us with the EBSD system at WHOI. Dirk Rieke-Zapp was extremely helpful in the field, and Uli Mok provided assistance with image analysis. Reviews by Luigi Burlini, Stefan Schmid, and an anonymous reviewer greatly improved this manuscript, as did discussions with Clark Burchfiel and Peter Kelemen. The thin section lab at the University of Bern kindly prepared the thin sections. This work was supported by NSF grants EAR0510412 and OCE0452787 (BE), GSA student research grant 7586-04 (NA), SNF grants 21-66889.01 and 200020-103720 (MH), and the MIT Student Research Fund (NA).

10. References

Atkinson, H. 1988: Theories of normal grain growth in pure single phase systems. Acta Metallurgica **36**: 469-491.

Austin, N.&Evans, B. 2007: Paleowattmeters: A scaling relation for dynamically recrystallized grain size. Geology **35**(4): 343-346.

Badoux, H. 1972: Tectonique de la nappe de Morcles entre Rhône et Lizerne: Matériaux pour la Carte Géologique de la Suisse. Nouvelle Série **143**: 1–74.

Barber, D.&Wenk, H. 1979: Deformation twinning in calcite, dolomite, and other rhombohedral carbonates. Physics and Chemistry of Minerals **5**(2): 141-165.

Barber, D., Wenk, H., Gomez-Barreiro, J., Rybacki, E.&Dresen, G. 2007: Basal slip and texture development in calcite: new results from torsion experiments. Physics and Chemistry of Minerals **34**(2): 73-84.

Barnhoorn, A., Bystricky, M., Burlini, L.&Kunze, K. 2004: The Role of Recrystallization on the Deformation Behaviour of Calcite Rocks: High Strain Torsion Experiments on Carrara Marble. Journal of Structural Geology **26**: 885–903.

Barnhoorn, A., Bystricky, M., Kunze, K., Burlini, L.&Burg, J. 2005: Strain localisation in bimineralic rocks: Experimental deformation of synthetic calcite–anhydrite aggregates. Earth and Planetary Science Letters **240**(3-4): 748-763.

Bestmann, M., Kunze, K.&Matthews, A. 2000: Evolution of a calcite marble shear zone complex on Thassos Island, Greece: microstructural and textural fabrics and their kinematic significance. Journal of Structural Geology **22**(11-12): 1789-1807.

Bestmann, M.&Prior, D. 2003: Intragranular dynamic recrystallization in naturally deformed calcite marble: diffusion accommodated grain boundary sliding as a result of subgrain rotation recrystallization. Journal of Structural Geology **25**(10): 1597-1613.

Boullier, A.&Quenardel, J. 1981: The Caledonides of northern Norway: relation between preferred orientation of quartz lattice, strain and translation of the nappes. Geological Society London Special Publications **9**(1): 185-195.

Braun, J., Chéry, J., Poliakov, A., Mainprice, D., Vauchez, A., Tomassi, A.&Daignières, M. 1999: A simple parametrization of strain localization in the ductile regime due to grain size reduction: A case study for olivine. Journal of Geophysical Research **104**(B11): 25167-25182.

Bucher, S., Schmid, S., Bousquet, R.&Fugenschuh, B. 2003: Late-stage deformation in a collisional orogen(Western Alps): nappe refolding, back-thrusting or normal faulting? Terra Nova **15**(2): 109-117.

Burg, J. 1999: Ductile structures and instabilities: their implication for Variscan tectonics in the Ardennes. Tectonophysics **309**(1): 1-25.

Burkhard, M. 1988: L'Helvétique de la bordure occidentale du massif de l'Aar(évolution tectonique et métamorphique). Eclogae Geologicae Helvetiae **81**(1): 63-114.

Burkhard, M.&Kerrich, R. 1988: Fluid regimes in the deformation of the Helvetic nappes, Switzerland, as inferred from stable isotope data. Contributions to Mineralogy and Petrology **99**(4): 416-429.

Burkhard, M.&Goy-Eggenberger, D. 2001: Near vertical iso-illite-crystallinity surfaces cross-cut the recumbent fold structure of the Morcles nappe, Swiss Alps. Clay Minerals **36**(2): 159-170.

Burlini, L.&Bruhn, D. 2005: High-strain zones: laboratory perspectives on strain softening during ductile deformation. Geological Society London Special Publications **245**(1): 1.

Covey-Crump, S. 1997: The normal grain growth behaviour of nominally pure calcitic aggregates. Contributions to Mineralogy and Petrology **129**(2): 239-254.

Coward, M.&Dietrich, D. 1989: Alpine tectonics--an overview. Geological Society London Special Publications **45**(1): 1-29.

Crespo-Blanc, A., Masson, H., Sharp, Z., Cosca, M.&Hunziker, J. 1995: A stable and 40 Ar/39 Ar isotope study of a major thrust in the Helvetic nappes (Swiss Alps); evidence for fluid flow and constraints on nappe kinematics. Bulletin of the Geological Society of America **107**(10): 1129-1144.

de Bresser, J.&Spiers, C. 1990: High-temperature deformation of calcite single crystals by r+ and f+ slip. Geological Society London Special Publications **54**(1): 285-298.

de Bresser, J.&Spiers, C. 1993: Slip systems in calcite single crystals deformed at 300–800 C. Journal of Geophysical Research **98**(B4): 6397-6409.

de Bresser, J.&Spiers, C. 1997: Strength characteristics of the r, f, and c slip systems in calcite. Tectonophysics **272**(1): 1-23.

de Bresser, J., Peach, C., Reijs, J.&Spiers, C. 1998: On dynamic recrystallization during solid state flow: Effects of stress and temperature. Geophysical Research Letters **25**(18): 3457-3460.

de Bresser, J., Ter Heege, J.&Spiers, C. 2001: Grain size reduction by dynamic recrystallization: can it result in major rheological weakening? International Journal of Earth Sciences **90**(1): 28-45.

de Bresser, J. 2002: On the mechanism of dislocation creep of calcite at high temperature: inferences from experimentally measured pressure sensitivity and strain rate sensitivity of flow stress. Journal of Geophysical Research **107**(B12): doi:10.1029/2002JB001812.

de Bresser, J., Urai, J.&Olgaard, D. 2005: Effect of water on the strength and microstructure of Carrara marble axially compressed at high temperature. Journal of Structural Geology **27**(2): 265-281.

Derby, B.&Ashby, M. 1987: On Dynamic Recrystallization. Scripta Metallurgica et Materialia **21**(6): 879-884.

Derby, B. 1991: The Dependence of Grain Size on Stress During Dynamic Recrystallization. Acta Metallurgia et Materialia **39**(5): 955-962.

Derby, B. 1992: Dynamic recrystallisation. The steady state grain size. Scripta Metallurgica et Materialia **27**(11): 1581-1586.

Dietrich, D.&Song, H. 1984: Calcite fabrics in a natural shear environment, the Helvetic nappes of western Switzerland. Journal of Structural Geology **6**(1-2): 19-32.

Dietrich, D. 1986: Calcite fabrics around folds as indicators of deformation history. Journal of Structural Geology **8**(6): 655-668.

Dietrich, D.&Durney, D. 1986: Change of direction of overthrust shear in the Helvetic nappes of western Switzerland. Journal of Structural Geology **8**(3-4): 389-398.

Dietrich, D. 1989: Fold axis parallel extension in an arcuate fold and thrust belt: the case of the Helvetic nappes. Tectonophysics **170**: 183–212.

Dietrich, D.&Casey, M. 1989: A new tectonic model for the Helvetic nappes. Geological Society London Special Publications **45**(1): 47-63.

Dresen, G., Evans, B.&Olgaard, D. 1998: Effect of quartz inclusions on plastic flow in marble. Geophysical Research Letters **25**(8): 1245-1248.

Drury, M., Humphreys, F.&White, S. 1989: Effect of dynamic recrystallization on the importance of grain-boundary sliding during creep. Journal of Materials Science **24**(1): 154-162.

Ebert, A., Herwegh, M., Evans, B., Pfiffner, A., Austin, N.&Vennemann, T. 2007a: Microfabrics in carbonate mylonites along a large-scale shear zone (Helvetic Alps). Tectonophysics **444**(1-4): 1-26.

Ebert, A., Herwegh, M.&Pfiffner, A. 2007b: Cooling induced strain localization in carbonate mylonites within a large-scale shear zone (Glarus thrust, Switzerland). Journal of Structural Geology **29**(7): 1164-1184.

Epard, J. 1990: La nappe de Morcles au sud-ouest du Mont-Blanc, Université de Lausanne, Faculté des sciences, Institut de géologie et de paléontologie.

Escher, A., Masson, H.&Steck, A. 1993: Nappe geometry in the Western Swiss Alps. Journal of Structural Geology **15**(3-5): 501-509.

Etheridge, M.&Wilkie, J. 1981: An assessment of dynamically recrystallized grainsize as a palaeopiezometer in quartz-bearing mylonite zones. Tectonophysics **78**: 475-508.

Evans, B., Renner, J.&Hirth, G. 2001: A few remarks on the kinetics of static grain growth in rocks. International Journal of Earth Sciences **90**(1): 88-103.

Exner, H. 1972: Analysis of Grain- and Particle-Size Distributions in Metallic Materials. International Metallurgical Reviews **17**(159): 25-42.

Frey, M., Teichmüller, M., Teichmüller, R., Mullis, J., Künzi, B., Breitschmid, A., Gruner, U.&Schwizer, B. 1980: Very low-grade metamorphism in external parts of the Central Alps: Illite crystallinity, coal rank and fluid inclusion data. Eclogae Geologicae Helvetiae **73**: 173–203.

Gleason, G., Tullis, J.&Heidelbach, F. 1993: The role of dynamic recrystallization in the development of lattice preferred orientations in experimentally deformed quartz aggregates. Journal of Structural Geology **15**(9-10): 1145-1168.

Goy-Eggenberger, D. 1998: Faible métamorphisme de la nappe de Morcles: minéralogie et géochimie, Université de Neuchâtel.

Groshong Jr, R., Pfiffner, O.&Pringle, L. 1984: Strain partitioning in the Helvetic thrust belt of eastern Switzerland from the leading edge to the internal zone. Journal of Structural Geology **6**(1): 5-18.

Guillope, M.&Poirier, J. 1979: Dynamic recrystallization during creep of single-crystalline halite: An experimental study. Journal of Geophysical Research **84**(B10): 5557-5567.

Hall, C.&Parmentier, E. 2003: Influence of grain size evolution on convective instability. Geochemistry, Geophysics, Geosystems **4**(3): doi:10.1029/2002GC000308.

Handy, M. 1990: The solid-state flow of polymineralic rocks. Journal of Geophysical Research **95**(B6): 8647-8661.

Handy, M. 1994: Flow laws for rocks containing two non-linear viscous phases: a phenomenological approach. Journal of Structural Geology **16**(3): 287-301.

Harris, L., Burg, J.&Sauniac, S. 1983: Strain distribution within the Pardailhan Nappe(Montagne Noire, France) and structure of its basal thrust zone: implications for events associated with nappe emplacement. Journal of Structural Geology **5**(3-4): 431-440.

Herwegh, M., Handy, M.&Heilbronner, R. 1997: Temperature-and strain-rate-dependent microfabric evolution in monomineralic mylonite: evidence from in situ deformation of norcamphor. Tectonophysics **280**(1): 83-106.

Herwegh, M. 2000: A new technique to automatically quantify microstructures of fine grained carbonate mylonites: two-step etching combined with SEM imaging and image analysis. Journal of Structural Geology **22**(4): 391-400.

Herwegh, M.&Kunze, K. 2002: The influence of nana-scale second phase particles on deformation of fine-grained calcite mylonites. Journal of Structural Geology **24**: 1463-1478.

Herwegh, M.&Berger, A. 2003: Differences in grain growth of calcite: a field-based modeling approach. Contributions to Mineralogy and Petrology **145**(5): 600-611.

Herwegh, M., Xiao, X.&Evans, B. 2003: The effect of dissolved magnesium on diffusion creep in calcite. Earth and Planetary Science Letters **212**(3-4): 457-470.

Herwegh, M.&Berger, A. 2004: Deformation mechanisms in second-phase affected microstructures and their energy balance. Journal of Structural Geology **26**(8): 1483-1498.

Herwegh, M., de Bresser, J.&ter Heege, J. 2005: Combining natural microstructures with composite flow laws: an improved approach for the extrapolation of lab data to nature. Journal of Structural Geology **27**(3): 503-521.

Herwegh, M.&Pfiffner, O. 2005: Tectono-metamorphic evolution of a nappe stack: A case study of the Swiss Alps. Tectonophysics **404**(1): 55-76.

Hobbs, B., Muhlhaus, H.&Ord, A. 1990: Instability, softening and localization of deformation. Geological Society London Special Publications **54**(1): 143-165.

Humphreys, F.&Hatherly, M. 1995: Recrystallization and related annealing phenomena, Pergamon Tarrytown, NY, USA.

Humphreys, F.&Ardakani, M. 1996: Grain boundary migration and Zener pinning in particle-containing copper crystals. Acta materialia **44**(7): 2717-2727.

Ji, S., Jiang, Z., Rybacki, E., Wirth, R., Prior, D.&Xia, B. 2004: Strain softening and microstructural evolution of anorthite aggregates and quartz-anorthite layered composites deformed in torsion. Earth and Planetary Science Letters **222**(2): 377-390.

Kameyama, M., Yuen, D.&Fujimoto, H. 1997: The interaction of viscous heating with grain-size dependent rheology in the formation of localized slip zones. Geophysical Research Letters **24**(20): 2523-2526.

Karato, S., Toriumi, M.&Fujii, T. 1980: Dynamic recrystallization of olivine single crystals during high-temperature creep. Geophysical Research Letters **7**(9): 649-652.

Kennedy, L.&White, J. 2001: Low-temperature recrystallization in calcite: Mechanisms and consequences. Geology **29**(11): 1027-1030.

Kirschner, D., Sharp, Z.&Masson, H. 1995: Oxygen isotope thermometry of quartz-calcite veins; unraveling the thermal-tectonic history of the subgreenschist facies Morcles Nappe (Swiss Alps). Bulletin of the Geological Society of America **107**(10): 1145-1156.

Kirschner, D., Cosca, M., Masson, H.&Hunziker, J. 1996: Staircase 40 Ar/39 Ar spectra of fine-grained white mica; timing and duration of deformation and empirical constraints on argon diffusion. Geology **24**(8): 747-750.

Kirschner, D., Masson, H.&Sharp, Z. 1999: Fluid migration through thrust faults in the Helvetic nappes (Western Swiss Alps). Contributions to Mineralogy and Petrology **136**(1): 169-183.

Krabbendam, M., Urai, J.&van Vliet, L. 2003: Grain size stabilisation by dispersed graphite in a high-grade quartz mylonite: an example from Naxos (Greece). Journal of Structural Geology **25**(6): 855-866.

Kreemer, C., Haines, J., Holt, W., Blewitt, G.&Lavallee, D. 2000: On the determination of a global strain rate model. Earth Planets Space **52**(10): 765-770.

Kreemer, C., Holt, W.&Haines, A. 2003: An integrated global model of present-day plate motions and plate boundary deformation. Geophysical Journal International **154**(1): 8-34.

Loup, B. 1992: Mesozoic subsidence and stretching models of the lithosphere in Switzerland(Jura, Swiss Plateau and Helvetic realm). Eclogae Geologicae Helvetiae **85**(3): 541-572.

Marquer, D., Petrucci, E.&Iacumin, P. 1994: Fluid advection in shear zones: evidence from geological and geochemical relationships in the Aiguilles Rouges Massif(Western Alps, Switzerland). Schweizerische Mineralogische und Petrographische Mitteilungen **74**(1): 137-148.

Mas, D.&Crowley, P. 1996: The effect of second-phase particles on stable grain size in regionally metamorphosed polyphase calcite marbles. Journal of Metamorphic Geology **14**(2): 155-162.

Mehl, L.&Hirth, G. 2008: Plagioclase recrystallization and preferred orientation in layered mylonited: Evaluation of flow laws for the lower crust. J. of Geophys. Res., **113**(B05202): doi: 10.1029/2007JB005075.

Milton, N.&Williams, G. 1981: The strain profile above a major thrust fault, Finnmark, N Norway. Geological Society London Special Publications **9**(1): 235.

Montesi, L.&Zuber, M. 2002: A unified description of localization for application to large-scale tectonics. J. Geophys. Res **107**(B3): doi: 10.1029/2001JB000465.

Montesi, L.&Hirth, G. 2003: Grain size evolution and the rheology of ductile shear zones- From laboratory experiments to postseismic creep. Earth and Planetary Science Letters **211**(1): 97-110.

Nes, E., Ryum, N.&Hunderi, O. 1985: On the Zener drag. Acta Metallurgica **33**: 11-22.

Olgaard, D.&Evans, B. 1986: Effect of second-phase particles on grain growth in calcite. Journal of the American Ceramic Society **69**(11): 272-277.

Panien, M., Schreurs, G.&Pfiffner, A. 2005: Sandbox experiments on basin inversion: testing the influence of basin orientation and basin fill. Journal of Structural Geology **27**(3): 433-445.

Paterson, M. 1979: Deformation Mechanisms in Carbonate Crystals. Physics of Materials (A festschrift for Dr. Walter Boas), CSIRO and University of Melbourne, Melbourne: 199-208.

Paterson, M. 1995: A theory for granular flow accomodated by material transfer via an intergranular fluid. Tectonophysics **245**(3-4): 135-151.

Pfiffner, O. 1981: Fold-and-thrust tectonics in the Helvetic Nappes (E Switzerland). Geological Society London Special Publications **9**(1): 319-327.

Pfiffner, O. 1982: Deformation mechanisms and flow regimes in limestone from the Helvetic zone fo teh Swiss Alps. Journal of Structural Geology **4**(4): 429-442.

Pfiffner, O. 1993: The structure of the Helvetic nappes and its relation to the mechanical stratigraphy. Journal of Structural Geology **15**(3-5): 511-521.

Pieri, M., Burlini, L., Kunze, K., Stretton, I.&Olgaard, D. 2001a: Rheological and microstructural evolution of Carrara marble with high shear strain: results from high temperature torsion experiments. Journal of Structural Geology **23**(9): 1393-1413.

Pieri, M., Kunze, K., Burlini, L., Stretton, I., Olgaard, D., Burg, J.&Wenk, H. 2001b: Texture development of calcite by deformation and dynamic recrystallization at 1000K during torsion experiments of marble to large strains. Tectonophysics **330**(1): 119-140.

Poirier, J. 1980: Shear localization and shear instability in materials in the ductile field. Journal of Structural Geology **2**(1-2): 135–142.

Ramsay, J. 1981: Tectonics of the Helvetic Nappes. Geological Society London Special Publications **9**(1): 293.

Ramsay, J., Casey, M.&Kligfield, R. 1983: Role of shear in development of the Helvetic fold-thrust belt of Switzerland. Geology **11**(8): 439-442.

Ramsay, J. 1989: Fold and fault geometry in the western Helvetic nappes of Switzerland and France and its implication for the evolution of the arc of the western Alps. Geological Society London Special Publications **45**(1): 33-45.

Renner, J., Evans, B.&Siddiqi, G. 2002: Dislocation creep of calcite. Journal of Geophysical Research **107**: 1-16.

Renner, J., Siddiqi, G.&Evans, B. 2007: Plastic flow of two-phase marbles. Journal of Geophysical Research **112**(B7).

Rutter, E. 1972: The influence of interstitial water on the rheological behaviour of calcite rocks. Tectonophysics **14**: 13-33.

Rutter, E. 1995: Experimental study of the influence of stress, temperature, and strain on the dynamic recrystallization of Carrara marble. Journal of Geophysical Research **100**(B12): 24651-24664.

Rutter, E. 1999: On the relationship between the formation of shear zones and the form of the flow law for rocks undergoing dynamic recrystallization. Tectonophysics **303**(1): 147-158.

Rutter, E. H., Casey, M.&Burlini, L. 1994: Preferred crystallographic orientation development during the plastic and superplastic flow of calcite rocks. Journal of Structural Geology **16**(10): 1431-1446.

Rybacki, E., Paterson, M., Wirth, R.&Dresen, G. 2003: Rheology of calcite-quartz aggregates deformed to large strain in torsion. Journal of Geophysical Research **108**(10.1029).

Sakai, T.&Jonas, J. 1984: Dynamic recrystallization-Mechanical and microstructural considerations. Acta Metallurgica **32**: 189-209.

Schenk, O., Urai, J.&Evans, B. 2005: The effect of water on recrystallization behavior and grain boundary morphology in calcite-observations of natural marble mylonites. Journal of Structural Geology **27**(10): 1856-1872.

Schmid, S., Boland, J.&Paterson, M. 1977: Superplastic flow in fine-grained limestone. Tectonophysics **43**(3-4): 257-291.

Schmid, S., Paterson, M.&Boland, J. 1980: High temperature flow and dynamic recrystallization in Carrara marble. Tectonophysics **65**: 245-280.

Schmid, S., Casey, M.&Starkey, J. 1981: The microfabric of calcite tectonites from the Helvetic Nappes (Swiss Alps). Geological Society London Special Publications **9**(1): 151.

Schmid, S., Panozzo, R.&Bauer, S. 1987: Simple shear experiments on calcite rocks: rheology and microfabric. Journal of Structural Geology **9**(5-6): 747-778.

Shimizu, I. 1998: Stress and temperature dependence of recrystallized grain size: A subgrain misorientation model. Geophysical Research Letters **25**(22): 4237-4240.

Shimizu, I. 1999: A stochastic model of grain size distribution during dynamic recrystallization. Philosophical Magazine A **79**(5): 1217-1231.

Siddans, A. 1983: Finite strain pattern in some Alpine nappes. Journal of Structural Geology **5**(3-4): 441-448.

Skemer, P., Katayama, I., Jiang, Z.&Karato, S. 2005: The misorientation index: Development of a new method for calculating the strength of lattice-preferred orientation. Tectonophysics **411**(1): 157-167.

Smith, C. 1948: Grains, phases, and ainterfaces: as interpretation of microstructure. Transactions of the American Institute of Mining and Metallurgical Engineers **15**(4): 1-37.

Stipp, M., Stunitz, H., Heilbronner, R.&Schmid, S. 2001: Dynamic recrystallization of quartz: correlation between natural and experimental conditions. Geological Society London Special Publications **200**(1): 171-190.

Ter Heege, J., De Bresser, J.&Spiers, C. 2002: The influence of dynamic recrystallization on the grain size distribution and rheological behaviour of Carrara marble deformed in axial compression. Deformation Mechanisms, Rheology and Tectonics Current Status and Future Perspectives, Special Publication-Geological Society of London **200**: 119–136.

Ter Heege, J., De Bresser, J.&Spiers, C. 2004: Composite flow laws for crystalline materials with log-normally distributed grain size: theory and application to olivine. Journal of Structural Geology **26**(9): 1693-1705.

Ter Heege, J., De Bresser, J.&Spiers, C. 2005: Dynamic recrystallization of wet synthetic polycrystalline halite: dependence of grain size distribution on flow stress, temperature and strain. Tectonophysics **396**(1-2): 35-57.

Trümpy, R. 1973: The timing of orogenic events in the Central Alps. Gravity and Tectonics"(De Jong, K. & Scholten, R.).-Wiley, New York: 229-251.

Twiss, R. 1977: Theory and applicability of a recrystallized grain size paleopiezometer. Pure and Applied Geophysics **115**(1): 227-244.

Twiss, R.&Sellars, C. 1978: Limits of applicability of the recrystallized grain size geopiezometer. Geophysical Research Letters **5**(5): 337-340.

Underwood, E. 1970: Quantitative Stereology. Reading, MA, Addison-Wesley Publishing Co.

Urai, J., Means, W.&Lister, G. 1986: Dynamic recrystallization of minerals. AGU Geophysical Monograph **36**: 161-199.

van der Wal, D., Chopra, P., Drury, M.&Fitzgerald, J. 1993: Relationships between dynamically recrystallized grain size and deformation conditions in experimentally deformed olivine rocks. Geophysical Research Letters **20**(14): 1479-1482.

Walker, A., Rutter, E.&Brodie, K. 1990: Experimental study of grain-size sensitive flow of synthetic, hot-pressed calcite rocks. Geological Society London Special Publications **54**(1): 259.

Wang, Z., Bai, Q., Dresen, G., Wirth, R.&Evans, B. 1996: High-temperature deformation of calcite single crystals. Journal of Geophysical Research **101**(B9): 20377-20390.

Warren, J.&Hirth, G. 2006: Grain size sensitive deformation mechanisms in naturally deformed peridotites. Earth and Planetary Science Letters **248**(1-2): 438-450.

Wenk, H., Venkitasubramanyan, C., Baker, D.&Turner, F. 1973: Preferred orientation in experimentally deformed limestone. Contributions to Mineralogy and Petrology **38**(2): 81-114.

Xiao, X.&Evans, B. 2003: Shear-enhanced compaction during non-linear viscous creep of porous calcite-quartz aggregates. Earth and Planetary Science Letters **216**(4): 725-740.

11. Tables

Table 1) (see next page) Sample names; distance from MOG18N1 normal to the thrust contact, which we considered the estimated distance to the thrust contact; average calcite grain size from linear intercept measurements (D_{cc}), including a stereological correction of 3/2; mineralogy of second phases in the given lithology (usual abbreviations, Sh.Sil refers generically to sheet silicates), and the M-Index (Skemer et al. 2005) from crystallographic orientations obtained by EBSD. All samples are from the Saillon cave (Swiss Coordinates 578.950/113.500). Lithology is given in the sample name: MOG refers to the Gault, MOU refers to the upper Urgonian, and MOUg refers to the lower Urgonian. Zones of apparent localization, including the boundaries of the meso-scale shear zones are denoted with “loc”.

Table 1)

Sample	Distance relative to MOG18N1 (m)	D_{cc} (µm)	Z (µm)	Second Phases	M-Index (calcite)
MOG18N1	0.00	4.3-8.9	38-pure	Qtz	0.19-0.49
MOG18N2	0.25	9.5-10.3	43-pure	Qtz+Chl	0.10
MOG18N3	0.75	13.3-15.1	460-pure	Qtz+Chl	0.11
MOG18N4	1.05	6.5	69	Qtz+Chl	0.15
MOG18N5	1.35	10.1-11.1	47-72	Qtz+Chl	0.09
MOG18N6	2.25	11.3-11.4	67-142	Qtz+Chl	
MOG18N7t	2.75	12.0-12.7	146-206	Qtz+Chl	
MOG18N8	4.85	14.5-15.9	73-101	Qtz+Chl	
MOG18N9	5.65	20.6-22.0	pure		0.21
MOG18N10t	7.25	14.3-17.2	778-895	Qtz+Chl	
MOU18N18	7.60	22.4	pure		
MOU18N19	7.63	22.5-24.1	pure		
MOU18N21t	7.95	14.5-21.6	85-pure	Sh.Sil+/-Qtz	
MOU18N22	8.65	19.6-20.8	1776-pure	Sh.Sil+/-Qtz	0.14
MOU18N22 loc	8.65	7.6-9.9	58-441	Sh.Sil+/-Qtz	0.07
MOU18N23	8.65	20.6-24.6	pure		0.14
MOU18N23 loc	8.65	7.5	86	Sh.Sil+/-Qtz	0.04
MOU18N11	8.90	23.2-25.1	pure		0.08
MOU18N25	9.35	21.9	pure		
MOU18N12	9.50	19.2-21.5	pure		
MOU18N14	9.50	15.6-21.8	169-pure	Sh.Sil+/-Qtz	0.16
MOU18N24	9.65	18.1	pure		
MOU18N13t	10.00	15.4-20.8	125-pure	Sh.Sil+/-Qtz	0.09
MOU18N15	10.00	14.6-23.6	236-pure	Sh.Sil+/-Qtz	
MOU18N27t	10.25	21.1-26.5	pure		
MOU18N17t	10.30	14.5-23.2	86-pure	Sh.Sil+/-Qtz	
MOU18N30	11.05	13.9-20.8	110-pure	Sh.Sil+/-Qtz	0.04
MOU18N30 loc	11.05	11.8-14.7	79-pure	Sh.Sil+/-Qtz	
MOU18N28b	11.25	18.5-21.3	272-pure	Sh.Sil+/-Qtz	
MOUg18N29	12.55	18.1-26.2	73-pure	Sh.Sil+/-Qtz	0.16

Table 2) Grain-size evolution relationships and parameters used to model the Morcles nappe. Labels correspond to those used in the text and in figures. K_g, Q_g, and p are the constants in the normal grain-growth equation, γ is the average grain-boundary energy, c is geometrical constant, and λ is the proportion of mechanical work associated with dislocation creep that is not dissipated, and is thus stored in the microstructure.

Label	Grain Size Scaling Relationship	Reference (Scaling Relationship)	Parameters	Reference (Parameters)
AE07	$d_s^{1+p} = \frac{K_g \exp\left(\frac{-Q_g}{RT}\right) p^{-1} c\gamma}{\beta\lambda\sigma\dot{\varepsilon}_{tot}}$	(Austin & Evans 2007)	K_g=2.5e9 ($\mu m^p\ s^{-1}$)	(Covey-Crump 1997)
			Q_g=175 kJ/mol	
	$\beta = \frac{\dot{\varepsilon}_{dis}}{\dot{\varepsilon}_{tot}}$		p=3	
			γ=1 J m^{-2}	(Austin & Evans 2007)
			c=π	
			λ=0.1	
S1980	$d_s = B\sigma^{-q}$	(Twiss 1977)	B=$10^{2.63}$ ($\mu m\ MPa^m$)	(Schmid et al. 1980)
			q=0.9767	
R1995SG	$d_s = B\sigma^{-q}$	(Twiss 1977)	B=$10^{3.31}$ ($\mu m\ MPa^m$)	(Rutter 1995)
			q=1.14	

Table 3) Calcite flow laws and parameters used to model the Morcles nappe. Equation labels correspond to those used in the text and in figures.

Label	Flow Law	Type	Parameters	Reference
Rp	$\dot{\varepsilon}_p = A_p \sigma^2 \exp\left(\frac{\sigma}{\sigma_p}\right) \exp\left(-\frac{Q_p}{RT}\right)$ $\sigma_p = \left[\Sigma_{p,o} + K_p d^{-m_p}\right]\left[T\ m - T\ \right]$	Dislocation Creep (Peierls Law)	A_p=270.4 ($MPa^{-2}\ s^{-1}$) Q_p=200 kJ/mol m_p=0.5 K_p=115 ($MPa\ \mu m^{mp}\ kK^{-1}$) $\Sigma_{p,o}$=7.8 ($MPa\ kK^{-1}$) Tm=1600 (K)	(Renner et al. 2002)
Sdis	$\dot{\varepsilon}_{dis} = A_{dis} \sigma^{n_{dis}} \exp\left(-\frac{Q_{dis}}{RT}\right)$	Dislocation Creep (Power Law)	A_{dis}=2511.9 ($MPa^{-ndis}\ s^{-1}$) n_{dis}=4.7 Q_{dis}=297 kJ/mol	(Schmid et al. 1977)
Sdif	$\dot{\varepsilon}_{dif} = A_{dif} \sigma^{n_{dif}} d^{-m_{dif}} \exp\left(-\frac{Q_{dif}}{RT}\right)$	Diffusion Creep	A_{difs}=19952.6 ($MPa^{-ndifs}\ \mu m^{-mdifs}\ s^{-1}$) n_{difs}=1.66 m_{difs}=-2.5 Q_{difs}=209 kJ/mol	(Schmid et al. 1977)
Wdif	$\dot{\varepsilon}_{dif} = A_{dif} \sigma^{n_{dif}} d^{-m_{dif}} \exp\left(-\frac{Q_{dif}}{RT}\right)$	Diffusion Creep	A_{difw}=79432.8 ($MPa^{-ndifw}\ \mu m^{-mdifw}\ s^{-1}$) n_{difw}=1.7 m_{difw}=-1.9 Q_{difw}=190 kJ/mol	(Walker et al. 1990)
Hdif	$\dot{\varepsilon}_{dif} = A_{dif} \sigma^{n_{dif}} d^{-m_{dif}} \exp\left(-\frac{Q_{dif}}{RT}\right)$	Diffusion Creep	A_{difh}=4.3e7 ($MPa^{-ndifh}\ \mu m^{-mdifh}\ s^{-1}$) n_{difh}=1.1 m_{difh}=-3.3 Q_{difh}=200 kJ/mol	(Herwegh et al. 2003)

12. Figures

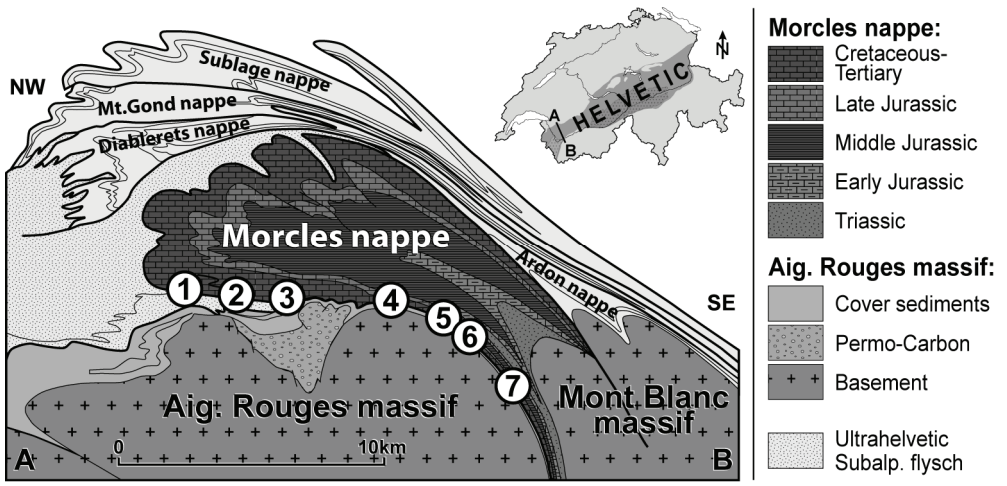


Figure 1) A schematic cross section along transect A-B, from the map in the upper right hand corner, through the Helvetic nappes in southwestern Switzerland (after Escher et al. 1993 and Ebert et al. 2007a). Numbers correspond to sample locations from Ebert et al. (2007a). This study focuses on sample location 5 (Swiss Coordinates 578.950/113.500).

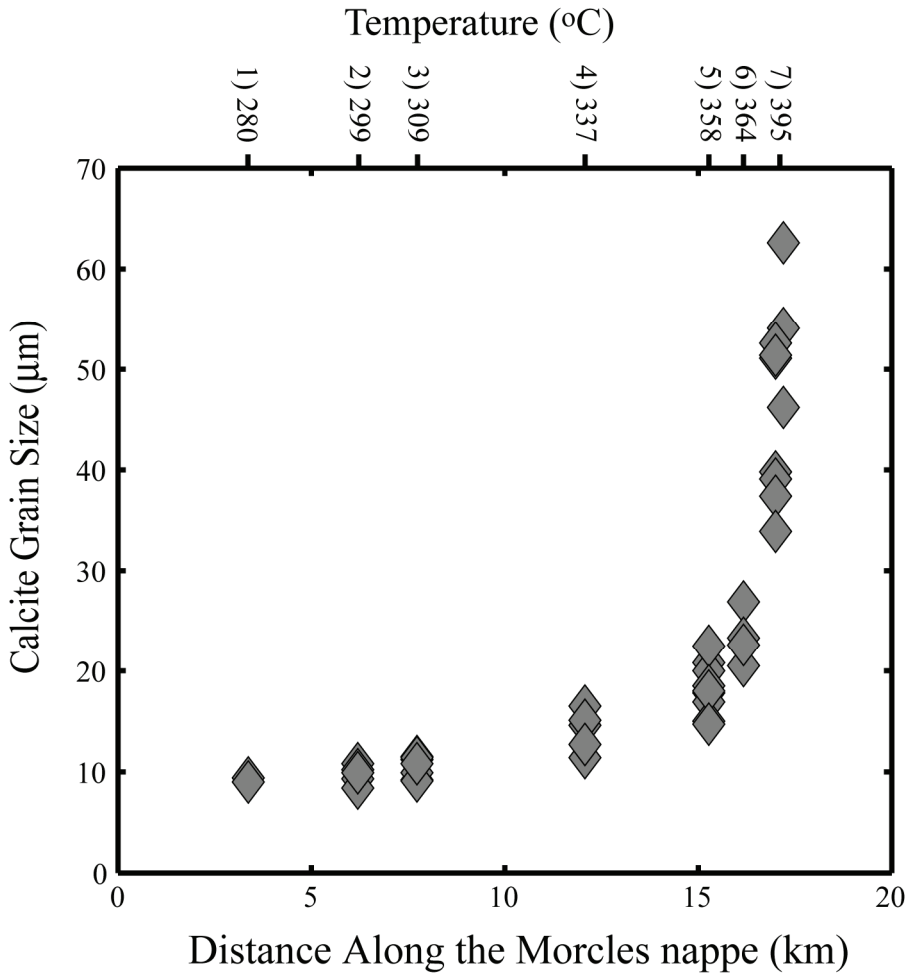
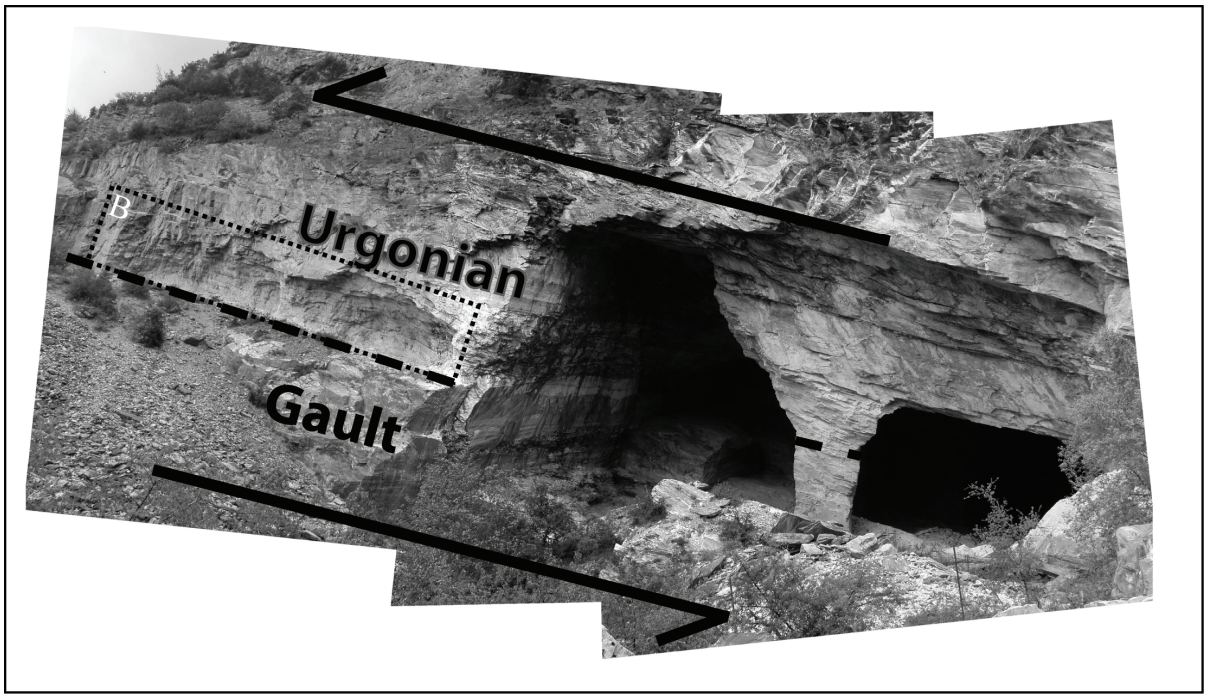
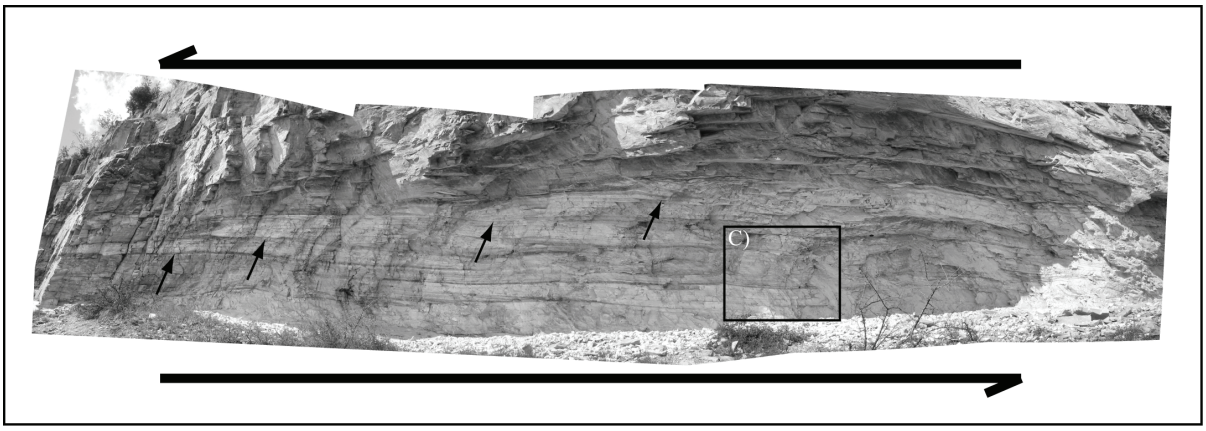


Figure 2) The variation in grain size and temperature along the inverted limb of the Morcles nappe, using data from Ebert et al. (2007a). The numbers preceding temperatures correspond to the locations highlighted in figure 1.

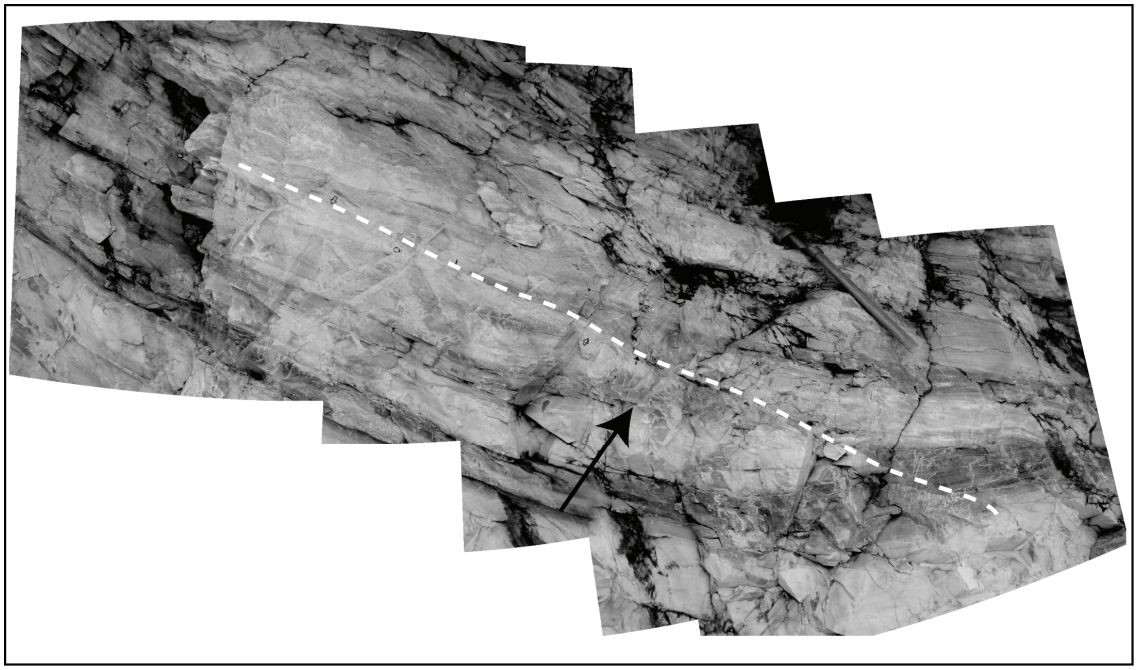
3A)



3B)



3C)



3D)

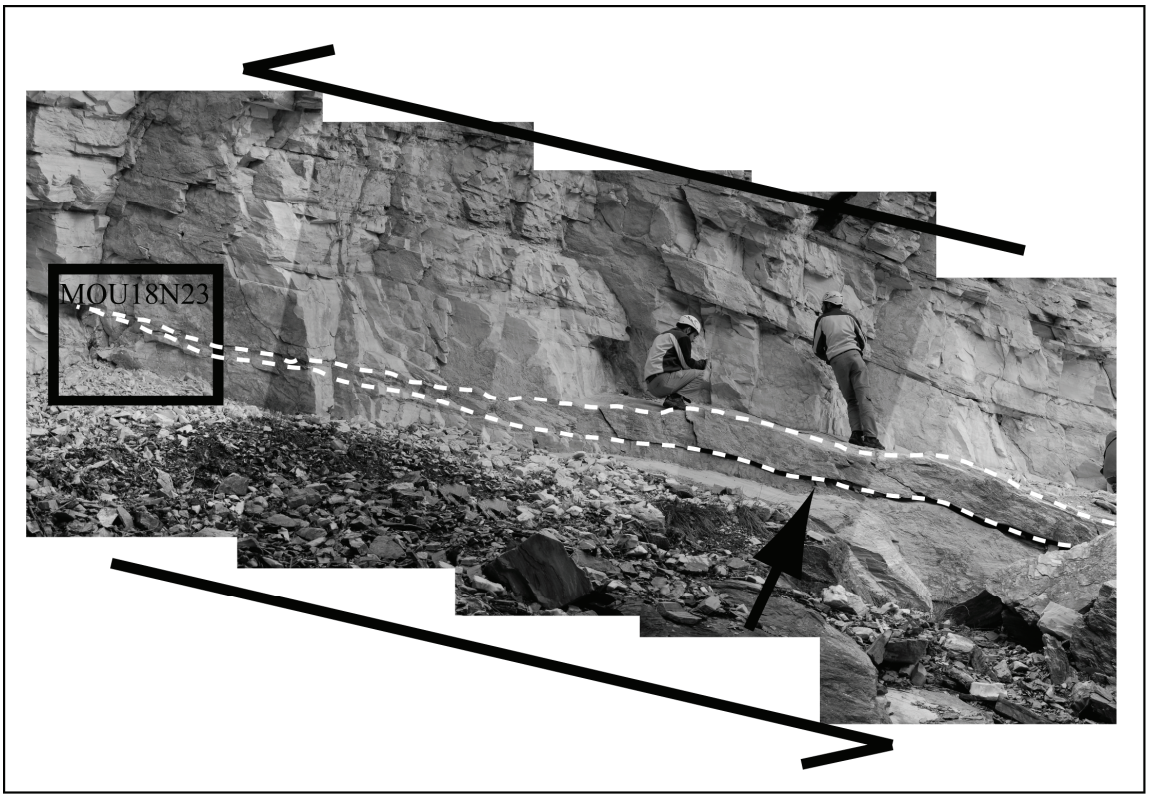


Figure 3) (see next page for caption)

Figure 3) A) The outcrop (location 5 in figure 1) where all the samples were obtained for this study. The lithological contact between the Gault and the Urgonian, which parallels the shear-zone boundary, is highlighted. The lowermost sample (MOG18N1) was taken from the back of the cave, at the lower right of image, and the uppermost sample (MOUg18N29) was taken from the outcrop near the bushes in the upper left of the image. These two locations are separated by a distance of 12.55 m normal to the thrust contact. The dashed box highlights the region shown in figure 3b. B) The contact between the upper Urgonian (white) and the lower Urgonian (grey). Notice the discrete bands of lower Urgonian within the upper Urgonian (highlighted with arrows). The box corresponds to the location of figure 3c. C) Evidence of the contemporaneous activity of folding (see arrow) and localized shear (white dashed line) (hammer for scale). D) A band of Gault (highlighted with white dashed lines) imbricated into the upper Urgonian. The box shows the location of samples MOU18N22 and MOU18N23 (human for scale).

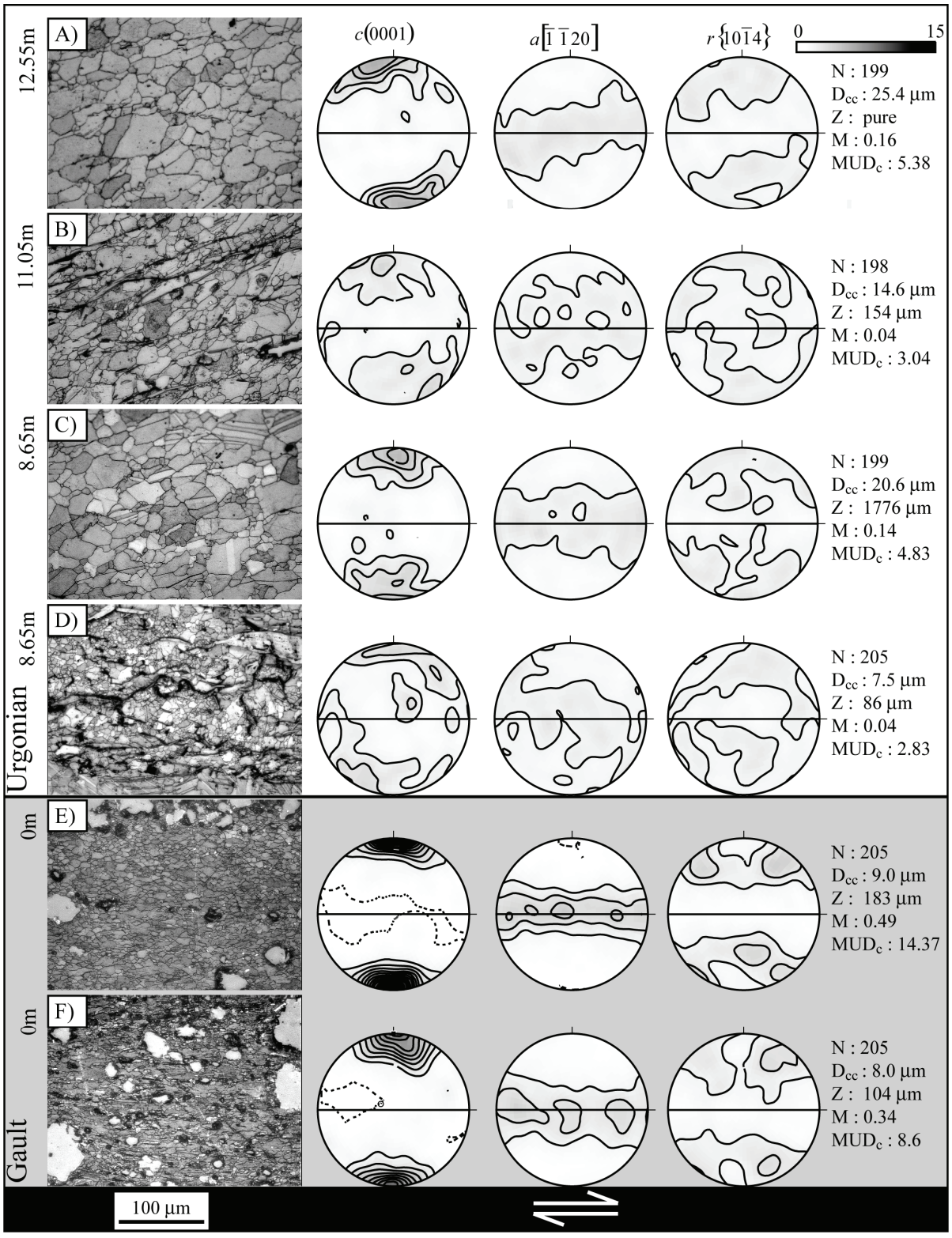


Figure 4) (see next page for caption)

Figure 4) Microstructures and crystallographic orientations for samples: A) MOUg18N29, B) MOU18N30, C) MOU18N23, D) MOU18N23 "loc", E) and F) MOG18N1 ("loc" refers to samples from the meso-scale shear zones). Pole figures are for $c(0001)$, $a[\bar{1}\,\bar{1}20]$, and $r\{10\bar{1}4\}$. All pole figures are contoured to the same scale (upper right), with maximum multiples of a uniform distribution (MUD) of 15 on a linear grey scale, and a contour interval of 1, using Gaussian smoothing of 8.5º. The horizontal line in each pole figure is parallel to the foliation in the direction of the lineation. N refers to the number of grains (with MAD<1.3) used to create the pole figure, M is the M-Index (Skemer et al. 2005), and MUD_c is the maximum MUD value on the c-axis pole figure. The distances (in m) refer to estimated distance from the thrust contact, assuming MOG18N1 is on the thrust contact. D_{cc} and Z refer to the mean calcite grain size and the Zener parameter respectively, for the regions analyzed by EBSD (which are shown in the micrographs). A) is the most distal sample from the thrust contact in our data set, and contains no second phases, B) is a sample from near A), however, it contains a large volume of sheet silicates, C) and D) correspond to the box in figure 3d, at the tip of the imbricated layer of Gault within the upper Urgonian. C) Upper Urgonian, approximately 10 mm away from the imbricated Gault layer, containing a very low proportion of second phases whereas D) is from the sheet-silicate rich contact between the imbricated layer of Gault and the upper Urgonian. E) and F) are from the lowermost sample we collected, which is the nearest sample to the thrust contact (see main text). The dominant second phase in this sample is quartz, and the difference between the images is the proportion of quartz.

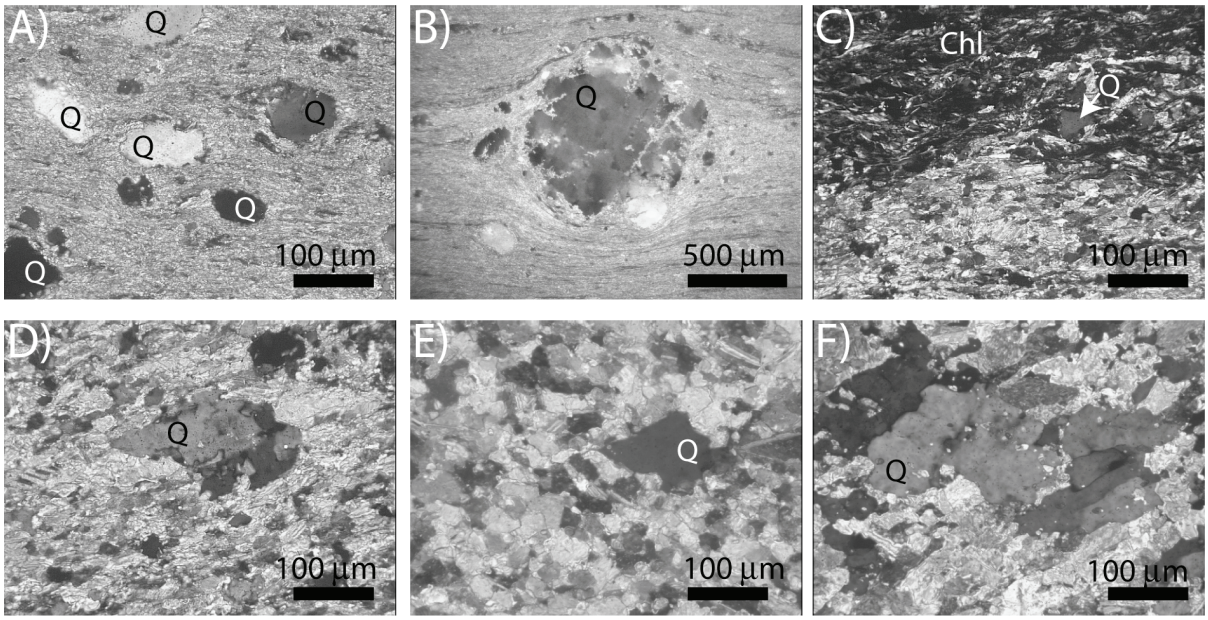


Figure 5) Transmitted light micrographs of second phases within fine-grained, recrystallized calcite, all shown with a top to the right sense of shear. A-B) Quartz (Q) within sample MOG18N1, from closest to the thrust contact, C) Quartz (Q) and chlorite (Chl) within MOG18N2, 0.25 m above MOG18N1, D) Quartz (Q) within MOG18N4, from 1.05 m above MOG18N1, E) Quartz (Q) within MOU18N14, from 9.50 m above MOG18N1, and F) Quartz (Q) within MOU18N17t from 10.30 -m above MOG18N1.

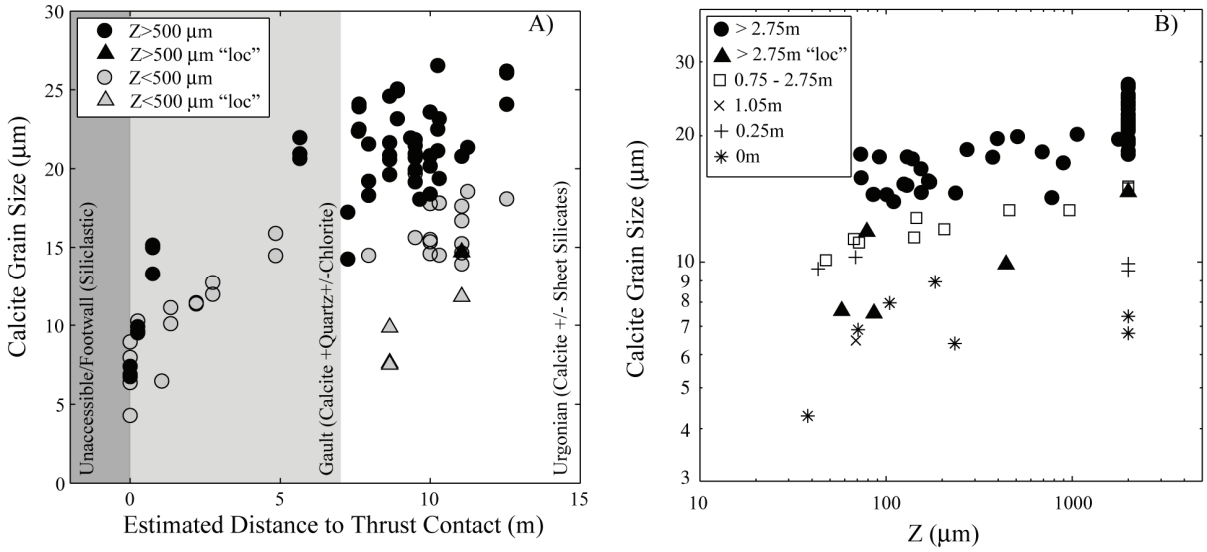


Figure 6) Variations in grain size as a function of A) estimated distance to the thrust contact, and B) Zener parameter (see section 5.2). The shaded boxes in A) represent the lithologic variations, and the corresponding variations in second phase mineralogy. Samples in A) are distinguished based on Z, using a cutoff of Z=500 µm, while in B), distances to the thrust contact are highlighted. In both plots, samples obtained from meso-scale shear zones (labeled "loc"), based on field observations, are also highlighted. Z=2000 µm refers to samples with no second phases visible in the micrographs that were analyzed.

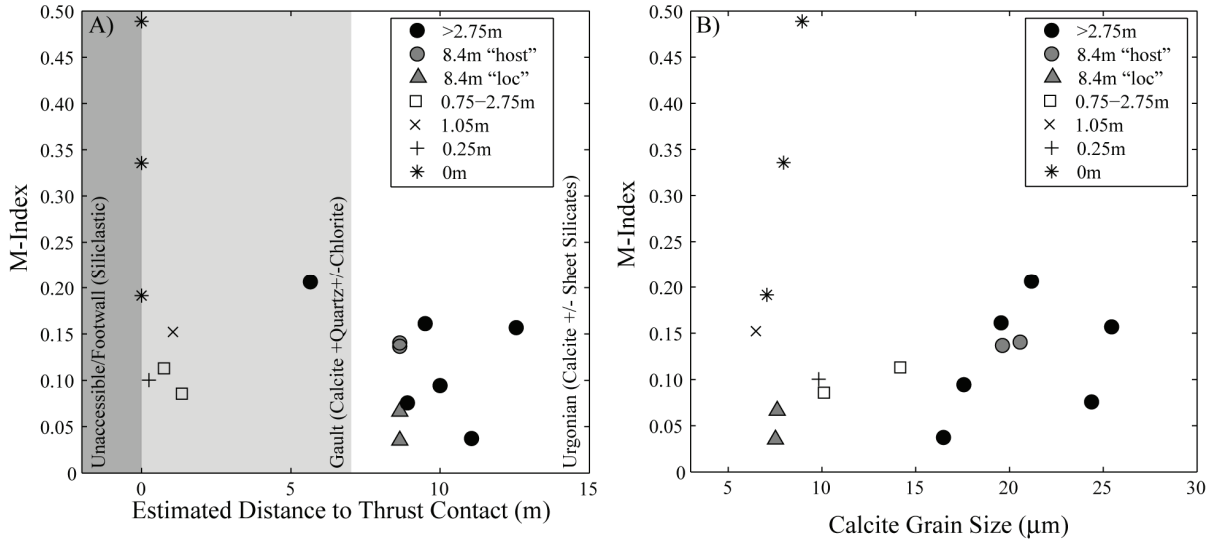


Figure 7) CPO intensity, quantified using the M-Index (Skemer et al. 2005) as a function of A) estimated distance from the thrust contact, B) calcite grain size. The symbols and grey scale are the same as in figure 6b. As in figures 4&6, "loc" refers to samples from the meso-scale shear zones and "host" refers to samples bounding the meso-scale shear zones.

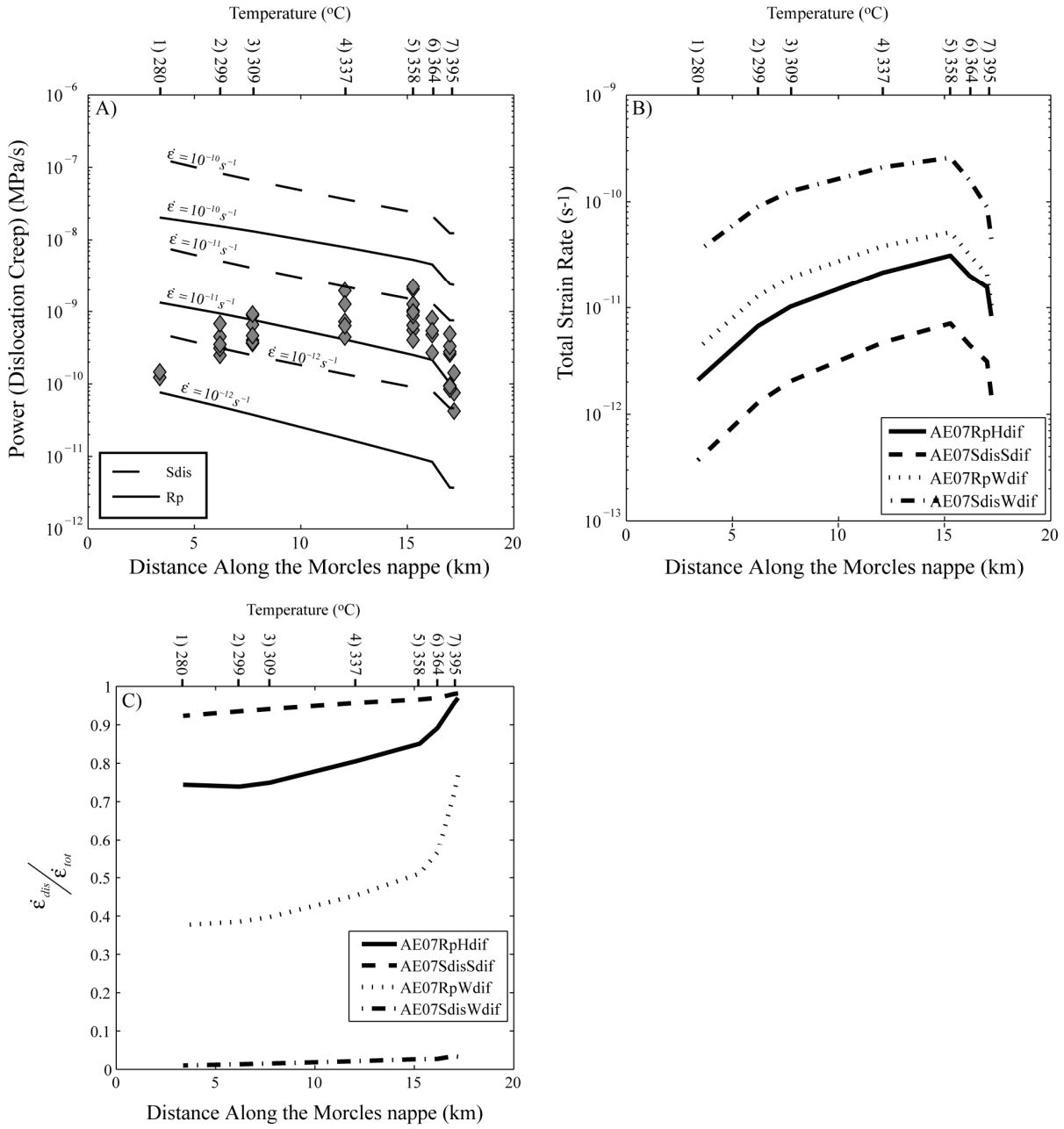


Figure 8) A) Calculated power ($\sigma\dot{\varepsilon}_{dis}$) along the inverted limb of the Morcles nappe, determined using the paleowattmeter (Austin & Evans 2007), based on the peak metamorphic temperatures and measured calcite grain sizes from samples with Z>500 µm from Ebert et al. (2007a), shown in gray diamonds. The contours show predictions for constant dislocation creep strain rates of 10^{-10}, 10^{-11}, and 10^{-12} s^{-1} at all locations, based on the flow laws of Renner et al. (2002) (Rp) and Schmid et al. (1977) (Sdis). B) Total strain rates, predicted along the inverted limb of the Morcles nappe, based on the average $\sigma\dot{\varepsilon}_{dis}$ determined for each location using the paleowattmeter (eq. AE07) and the flow laws listed in the legend (see Tables 2&3). C) The proportion of the total strain rate that is accommodated by dislocation creep along the Morcles nappe, based on the flow laws listed in the legend and in table 3, and the paleowattmeter (AE07).

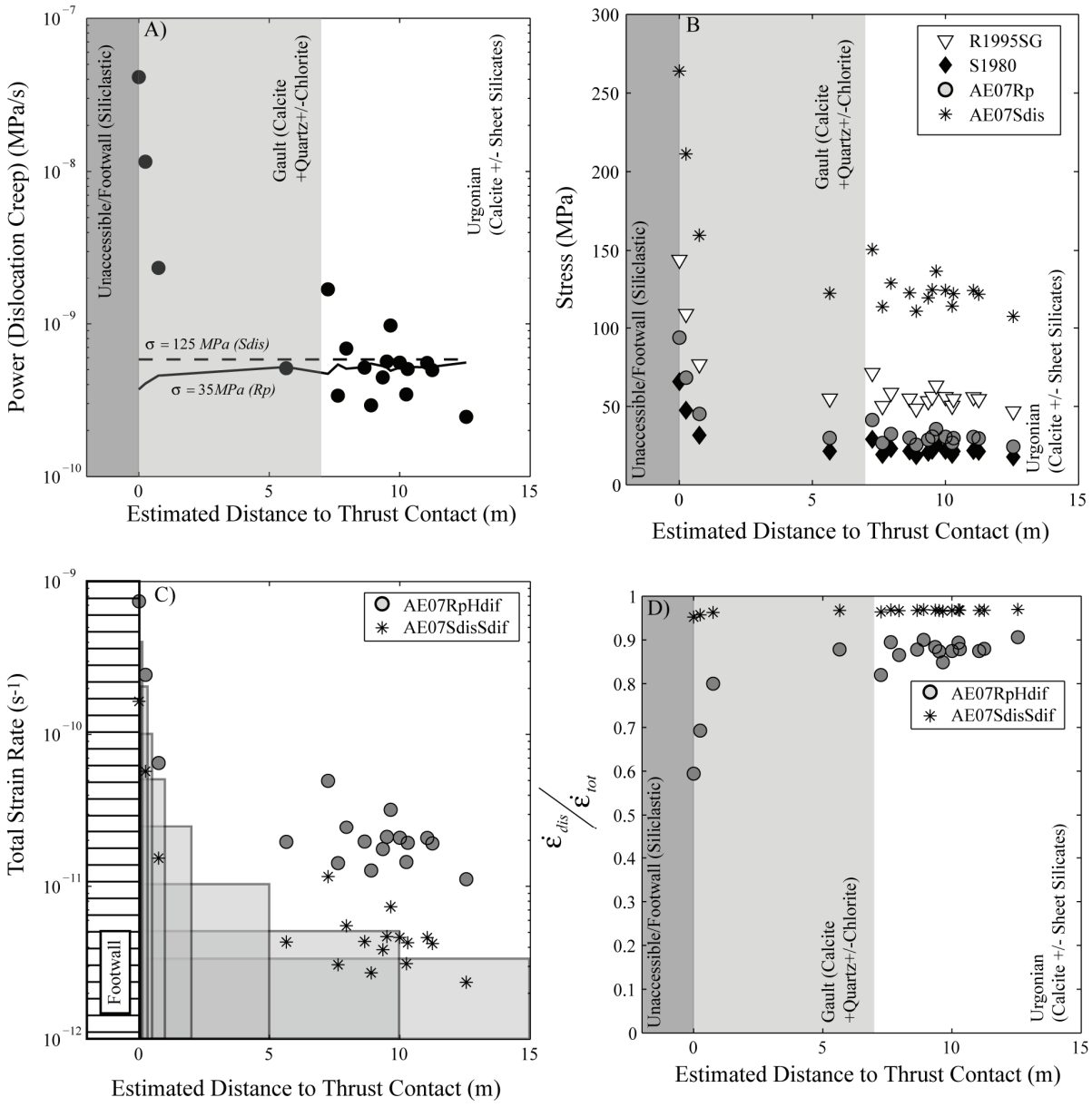


Figure 9) (see next page for caption)

Figure 9) A) Variations in the power associated with dislocation creep ($\sigma\dot{\varepsilon}_{dis}$) perpendicular to the thrust contact, based on predictions from the paleowattmeter (AE07) and the measured calcite grain sizes reported in table 1. The contours show the predictions for constant differential stress (as labeled) normal to thrust contact using the dislocation creep flow laws of Renner et al. (2002) (Rp) and Schmid et al. (1977) (Sdis). B) Differential stress variations normal to the thrust contact, based on the predictions of the relationships in table 2 (AE07, S1980, R1995SG). Stresses were determined from the paleowattmeter (AE07) using the dislocation creep flow laws of Renner et al. (2002) (Rp) and Schmid et al. (1977) (Sdis) and from the paleopiezometers (S1980, R1995SG). The only plausible mechanical explanation for this scenario is a temporal evolution in stress (though see text for a further discussion). C) Strain rate variations normal to the thrust contact based on the paleowattmeter (AE07) and a composite flow law using either the parameters from Renner et al. (2002) (Rp) + Herwegh et al. (2003) (Hdif) or Schmid et al. (1977) (Sdis + Sdif). The grey boxes correspond to the shear-zone thickness required, for the corresponding strain rate, to accommodate the average regional displacement rate while the Morcles nappe was actively deforming. D) The proportion of the total strain rate that is accommodated by dislocation creep perpendicular to the contact between the inverted limb of the Morcles nappe and the Triassic cover of the Aiguille Rouge massif, based on the flow laws listed in the legend and in table 3. All calculations were performed assuming a peak metamorphic temperature of 358 ºC.

Chapter 4

The Kinetics of Microstructural Evolution During Deformation of Calcite

Nicholas Austin
Brian Evans

Abstract

There is a strong coupling between the microstructure and the strength of rocks that is thought to play a key role in the evolution of shear zones and in our ability to interpret the mechanics of natural deformation processes. To investigate the microstructural evolution of calcite-rich rocks, we have performed a series of hydrostatic and deformation experiments on synthetic calcite aggregates at 1023 K and 300 MPa. The mechanical data from our experiments were broadly consistent with a composite flow law for concurrent dislocation and diffusion creep, but there is a systematic misfit between the predicted and measured strain rates that varies directly with strain and with progressive intensification of crystallographic preferred orientation (CPO). Recrystallization rates also responded to the deformation conditions. When the bulk strain rate was dominated by diffusion creep, calcite grains grew at the same rate as occurs by normal grain growth under isostatic conditions. When the dominant deformation mechanism was dislocation creep, the matrix grain size was reduced at a rate that varied directly with product of stress, strain rate, and the square of grain size. Thus, reduction rate was proportional to mechanical work rate. If the stable grain size achieved during deformation depends on the product of stress and strain rate, rather than stress alone, then that grain size is an indication of the work rate, and can be used as a paleowattmeter. Following this line of thought suggests that the gradient of recrystallized grain sizes that is often observed in the highly deformed portions of shear zones would not require a gradient in stress, but could also be explained by material softening, resulting in locally elevated strain rates under constant stresses.

1. Introduction

Shear zone geometry and strength probably evolve in response to variations in loading, thermodynamic conditions (e.g. temperature, pressure etc.), or internal mechanical state variables. Often, geometry and thermodynamic conditions can be deduced from observations of field structure and metamorphic grade. Although the feedback between strength and the evolution of material state variables must be of fundamental importance, and although that coupling has been studied by experiments and calculations, several problems remain at issue, including the kinetics of recrystallization.

Both implicit and explicit state variables have been used to describe the mechanical evolution of rocks. For example, Covey-Crump (1994) used stress relaxation experiments to measure a hardness parameter, which he did not explicitly identify. Based on mechanical experiments on halite, Stone et al. (2004) suggested that the mean and distribution of the sub-grain size could be explicitly identified as a state variable for dislocation creep. Other microstructural elements also investigated as explicit state variables include dislocation density, crystallographic preferred orientation (CPO), and grain size. Because grain size can be easily observed using a conventional light microscope and because it often varies dramatically between deformed and undeformed rocks, there is an extensive database of grain sizes for many rock types, deformed both in the laboratory and in nature.

Numerous theoretical and empirical models have been developed to relate deformation conditions to growth kinetics and steady-state grain size during dynamic recrystallization (Derby & Ashby 1987; Derby 1990, 1991, 1992; Kameyama et al. 1997; De Bresser et al. 1998; Shimizu 1998; Braun et al. 1999; De Bresser et al. 2001; Montesi & Zuber 2002; Hall & Parmentier 2003; Montési & Hirth 2003; Austin & Evans 2007; Shimizu 2008). Such models are

based on a broad collection of measurements of the recrystallized or mean grain size developed during deformation in triaxial compression, simple shear, or torsion. Although the experiments are run until a steady-state microstructure is apparently developed, it is important to note that strains in even the most protracted experiments are orders of magnitude below those often observed in natural shear zones.

The kinetics of changes in grain size (e.g. equations 15 and 24-25) and in grain-size distribution (Montesi & Zuber 2002; Ter Heege et al. 2002; Hall & Parmentier 2003) have important implications for the evolution of mechanical properties (De Bresser et al. 1998), and for understanding the processes that lead to the formation and maintenance of mylonites. Never the less, the kinetics of grain-size evolution during deformation are poorly constrained, as most studies have focused on the steady-state recrystallized grain size. In the triaxial experiments presented here, we examined the evolution of grain size under a range of deformation conditions. Carbonate rocks were chosen because they have been well-studied in experiments and in natural shear zones; because calcite grain size evolves rapidly during experiments, allowing precise rate measurements; and because both dislocation and diffusion creep can be examined.

1.1. Previous Grain Size Evolution Models

The strong correlation between flow stress and recrystallized grain size observed in metals and ceramics (see Twiss 1977), calcite (Schmid et al. 1980; Rutter 1995; Barnhoorn et al. 2004), quartz (Stipp & Tullis 2003), and olivine (Karato et al. 1980; Van Der Wal et al. 1993) is often given as:

$$d_s = A_o \sigma^{-k} \qquad (1)$$

(see Table 1 for a list of symbols). Several workers (Derby & Ashby 1987; Derby 1990) have provided theoretical explanations for this empirical relationship, but there are discrepancies between the theoretical predictions and experimental observations (e.g. De Bresser et al. 1998).

Twiss (1977) proposed that an equilibrium grain size occurs when the boundary energy associated with newly recrystallized grain equals the strain energy of the dislocations within the enclosed volume, assuming:

$$\sigma = \rho^{0.5} \tag{2}$$

(e.g. De Bresser 1996). For the case where all boundaries are tilt walls, and all dislocations are edge dislocations, Twiss (1977) obtained equation 1 where

$$k = \frac{(2\phi - 1)}{\phi} \tag{3}$$

Here ϕ is the ratio of total dislocation length in the boundary to that in the grain interior, which Twiss (1977) argues must be ≥ 1 in order for grain boundaries to form. There are two mechanisms of dynamic recrystallization: sub-grain rotation recrystallization, and grain boundary migration recrystallization (Guillope & Poirier 1979; Rutter 1995), which may occur under different stress, temperature, and strain-rate conditions (Guillope & Poirier 1979), leading to different recrystallized grain size regimes (Rutter 1995). Derby and Ashby (Derby & Ashby 1987; Derby 1990) present a model for the steady-state grain size during migration recrystallization, assuming that a balance between bulge nucleation and grain-boundary migration stabilizes the steady-state grain size:

$$d_s^{\,2} = \frac{Jd^*MF}{\dot{\varepsilon}} \tag{4}$$

where the product of the grain boundary mobility (M) and the driving force (F) may relate to static grain growth rate, although it may also depend on driving forces related to the lattice strain

energy associated with dislocations. If the parameters appropriate for dislocation creep strain rate accommodated by power law creep (n=3) are inserted into equation 4, the apparent k value in eq. 1 is 3/2, although this value will be modified by variations in the dislocation creep stress exponent (n) or if MF is grain size dependent (i.e. is related to the hydrostatic grain growth rate).

If subgrain rotation, rather than migration recrystallization, is dominant, Shimizu (1998, 2008) proposed that subgrains whose boundaries exceed some critical misorientation will become grain nuclei and begin to grow. The steady state grain size will exist when the grain growth rate is balanced by the nucleation rate from subgrains, the latter of which will depend on the flux of dislocations into subgrain boundaries. The result of this analysis is:

$$d_s = A_1 \left(\frac{\dot{N}}{I} \right)^{1/4} \tag{5}$$

(where I is the nucleation rate and $\dot{N}$ is the growth rate of the nuclei) which leads to:

$$\frac{d_s}{b} = A_2 \left(\frac{\sigma}{\mu} \right)^{-k} \left(\frac{D_{gb}}{D_v} \right)^{1/j} \tag{6}$$

when the appropriate nucleation and grain growth rates are substituted. Here, k=5/4 for intracrystalline nucleation and k=4/3 for grain boundary nucleation.

Note that the Derby and Ashby model (Derby & Ashby 1987; Derby 1990) and the Shimizu model (Shimizu 1998, 2008) include a temperature dependence, arising either from the difference in thermal activation energy of grain-boundary migration and that for dislocation creep (Derby & Ashby 1987; Derby 1990), or from that for volume and grain boundary diffusion (Shimizu 1998, 2008). Temperature dependence of steady-state grain size has not been reported in empirical studies of recrystallized grain size on calcite, olivine, or quartz (Karato et al. 1980;

Schmid et al. 1980; Van Der Wal et al. 1993; Rutter 1995; Stipp & Tullis 2003), although a moderate temperature dependence of recrystallized grain size was reported by (De Bresser et al. 1998) during deformation of Mg-Alloys, and by Ter Heege et al. (2005) during deformation of halite, and Austin & Evans (2007) argued that a temperature dependence of recrystallized grain size cannot be ruled out based on experimental data for calcite and quartz.

Along with the mechanistic models discussed above, two classes of scaling relationships for grain size evolution have been proposed, based on the assumption of competing processes of grain growth and grain-size reduction. These scaling relationships are unlike the mechanistic models of Derby and Ashby (Derby & Ashby 1987; Derby 1990) and Shimizu (Shimizu 1998, 2008), in that they are based largely on statistical or thermodynamic concepts of grain-size evolution. Here, we will adopt the terminology of Hall & Parmentier (2003), in referring to these as synchronous or asynchronous relationships.

In these scaling relationships, it is generally assumed that grain growth obeys the same, well established, kinetic relationship as under hydrostatic conditions (see Evans et al. 2001 for a review):

$$d^p - d_o^p = K\ \Delta t \tag{7}$$

where d_o is the average grain size at $t=t_o$, p is a constant, and K is a thermally activated rate constant:

$$K = K_g \exp\left[\frac{-Q_g}{RT}\right] \tag{8}$$

In equation 7, p=2 for intrinsic or interface limited grain growth, and p=3 for liquid film, solute drag, or pore drag mechanisms. Equation 7 may be recast in terms of grain-growth rate:

$$\dot{d} = K_g \exp\left[\frac{-Q_g}{RT}\right] p^{-1} d^{1-p} \qquad (9)$$

The driving forces for grain boundary migration, and hence grain growth, may be modified by variations in dislocation densities between grains, by chemical potential gradients, or by changes in the geometrical relationship between grains (Sato et al. 1990; Kellermann Slotemaker 2006). Consequently, the static grain growth rate may only provide a minimum estimate owing to the driving force for grain growth arising from capillary forces (Evans et al. 2001). Notice that, if pore fluids or second phases are present, grain boundary mobility, and thus grain-growth rate may be inhibited (Smith 1948; Olgaard & Evans 1986, 1988).

The kinetics of grain size reduction during dislocation creep are more poorly constrained than that of grain growth. Derby and Ashby (Derby & Ashby 1987; Derby 1990) have suggested that dynamic recrystallization is a statistical phenomenon where nucleation events are more likely for coarser grains and higher strain rates, assuming that a critical strain for microstructural evolution (Poliak & Jonas 1996) has been reached. Based on these assumptions, the rate of grain size reduction by dynamic recrystallization has been described with the relation

$$\dot{d} = \frac{-\dot{\varepsilon}\, d}{\varepsilon_c} \qquad (10)$$

(Kameyama et al. 1997; Braun et al. 1999; Montesi & Zuber 2002; Hall & Parmentier 2003; Montési & Hirth 2003). Different authors have suggested that the strain rate term might refer to the total strain rate (Kameyama et al. 1997; Braun et al. 1999) or the dislocation creep strain rate (Montesi & Zuber 2002), and that the grain size (d) might refer to either the mean grain size (Hall & Parmentier 2003), or the difference between the stable grain size and current mean grain size (Kameyama et al. 1997; Braun et al. 1999; Montesi & Zuber 2002).

Synchronous and asynchronous relationships differ in the coupling between grain growth or grain boundary migration, and grain size reduction. De Bresser and coworkers (De Bresser et al. 1998; De Bresser et al. 2001) proposed that the recrystallized grain size will tend to balance in a region such that there will be a constant ratio between the contributions to the strain rate from dislocation creep and diffusion creep or grain boundary sliding, which they termed the Field Boundary Hypothesis. When this ratio is too heavily weighted towards dislocation creep, grain size reduction will occur, driving the overall grain size back towards the mechanism boundary. Alternatively, when the ratio is too heavily weighted towards diffusion creep, grain growth will occur, once again driving deformation back towards the boundary between the deformation mechanisms. The stable grain size will be determined by the equilibrium relationship between the contributions to strain rate of dislocation creep and diffusion creep or grain boundary sliding:

$$d_s = X\sigma^{\frac{-(n-1)}{m}} \exp\left[\frac{Q_{dis} - Q_{dif}}{mRT}\right] \tag{11}$$

where

$$X = \left(\frac{A_{dif}}{C_f A_{dis}}\right)^{\frac{1}{m}} \tag{12}$$

and

$$C_f = \frac{\dot{\varepsilon}_{dif}}{\dot{\varepsilon}_{dis}} \tag{13}$$

Montési & Hirth (2003) argued that grain size might be a simple function of stress, potentially obeying equation 1, rather than being determined by a balance between the strain rate contributions from dislocation creep and diffusion creep. With that assumption, they describe the grain size evolution rate using equations 7-10, however, equation 1 is used to describe the stabilized grain size. Both this model and the field-boundary hypothesis (De Bresser et al. 1998) are asynchronous, as either grain-size reduction or growth processes occur exclusively, depending on whether the current grain size is coarser or finer than the stable size.

A second class of synchronous scaling relationships assumes that growth and reduction processes are independent but occur simultaneously. Then, the stable grain size occurs when the two rates are balanced. Hall & Parmentier (2003) proposed a synchronous relationship whereby equations 9 and 10 are summed, resulting in an overall rate of grain-size evolution of

$$\dot{d} = K_g \exp\left[\frac{-Q_g}{RT}\right] p^{-1} d^{1-p} - \frac{\dot{\varepsilon}\, d}{\varepsilon_c} \tag{14}$$

If it is assumed that grain growth and grain size reduction processes are in dynamic equilibrium at the stable grain size, then this stabilized grain size will be defined as the point where the rates of these processes balance (Hall & Parmentier 2003), and

$$d_s^p = \frac{\varepsilon_c K_g \exp\left(\frac{-Q_g}{RT}\right) p^{-1}}{\dot{\varepsilon}} \tag{15}$$

By focusing on migration recrystallization and assuming that a stabilized grain size results from the boundary mobility, the driving pressure, and the duration required to attain steady state, which depends on strain rate, Barnett (2007) obtained:

$$d_s = A_3 \frac{M_o \exp\left(\frac{-Q_m}{RT}\right) \vartheta \sigma^2}{\dot{\varepsilon} \mu} \tag{16}$$

which results in similar stress and temperature dependences of recrystallized grain size as 15, and is consistent with experimental observations on a range of metals

The primary difference between these two classes of models is that, in the synchronous relationships, the equilibrium grain size is specified by the kinetics of grain growth and grain-size reduction, whereas in asynchronous relationships, it is defined by a relationship that is

independent of grain size evolution kinetics, such as the relative contribution of different strain rates (field boundary hypothesis), or a piezometer (modified field boundary hypothesis).

1.2. The Paleowattmeter

Recently, Austin & Evans (2007) proposed a scaling law in which the grain-size reduction rate is controlled by the rate of mechanical work, and the ability of the rock to either dissipate or store this energy. The basic premise for this scaling law, a paleowattmeter, results from conservation of energy and is, to first order, independent of whether the rate-controlling mechanism of recrystallization is sub-grain rotation or grain-boundary migration. The rate of mechanical work per unit volume (power) is:

$$\dot{W} = \sigma\dot{\varepsilon} \tag{17}$$

This input rate must be balanced by the rate of increase in the internal energy of the system plus the rate of dissipation, which is largely related to heat production. Thus:

$$\dot{W} = \dot{E}_{\text{int}} + \dot{\theta}_{irr} \tag{18}$$

(e.g., Poliak & Jonas 1996). Assuming that grain size evolves over time scales less than those for stress variations, and that, consequently, the dislocation structure remains nominally constant (eq. 2) (De Bresser 1996), the rate of increase of internal energy is related to the rate of increase of grain boundary area:

$$\dot{E}_{\text{int}} = \frac{-c\gamma}{d^2}\dot{d}_{red} \tag{19}$$

where c is geometric constant (=π for spherical grains) and γ is the grain boundary energy. Thus,

$$\dot{W}_v = \sigma\dot{\varepsilon} = \frac{-c\gamma}{d^2}\dot{d}_{red} + \dot{\theta}_{irr} \tag{20}$$

The rate of dissipation ($\dot{\theta}_{irr}$) will be determined by the relative partitioning of strain rate between diffusion creep and dislocation creep, and the efficiency of each process. Several authors suggest that grain-growth rates are not modified when deformation is accommodated by diffusion creep (Karato 1989; Walker et al. 1990). Consequently, Austin & Evans (2007) posit that all of the power input during diffusion creep is completely dissipated (λ_{dif}=0). Some portion of the power input during dislocation creep is stored in the material microstructure ($0<\lambda_{dis}<1$) so the rate that energy is dissipated is:

$$\dot{\theta}_{irr} = (1-\beta)\sigma\dot{\varepsilon} + (1-\lambda_{dis})(\beta)\sigma\dot{\varepsilon} \qquad (21)$$

where $\beta = \dot{W}_{dis} / \dot{W}_{tot}$, with $\dot{W}_{tot} = \sigma\dot{\varepsilon}_{tot} = \sigma\dot{\varepsilon}_{dif} + \sigma\dot{\varepsilon}_{dis}$ and $\dot{W}_{dis} = \sigma\dot{\varepsilon}_{dis}$. λ_{dis} is the portion of the power input by dislocation creep strain rate that is responsible for increases in internal energy (also see Poliak & Jonas 1996; Austin & Evans 2007 for more discussion). Laboratory studies on metals suggest that about 90% of all mechanical work is converted to heat (Camacho & Ortiz 1997; Hodowany et al. 2000). However, both experimental observations and theoretical considerations (Chrysochoos et al. 1987; Mason et al. 1994; Kapoor & Nemat-Nasser 1998; Rittel 1999; Hodowany et al. 2000; Rosakis et al. 2000; Wei et al. 2004; Schreyer & Maudlin 2005; Longère & Dragon 2008) suggest that the proportion of energy stored in the microstructure may vary between 0% and 40% (Rosakis et al. 2000), depending on materials, strain, strain rate, and temperature. Because the exact partitioning is unknown, we treat $\lambda_{dis}=\lambda$ as a constant and = 0.1, (cf. Austin & Evans 2007; Austin et al. in press), not 1 as suggested by Shimizu (2008).

Incorporating 19 into 18, yields a relationship for a grain size reduction rate which differs from equation 10:

$$\dot{d}_{red} = \frac{-\beta\lambda\sigma\dot{\varepsilon}d^2}{c\gamma} \tag{22}$$

If grain growth and reduction processes act simultaneously and are linearly independent (i.e., are synchronous), then $\dot{d}_{tot} = \dot{d}_{red} + \dot{d}_{gr}$, (where, as noted above, $\dot{d}_{red}$ is negative).Thus

$$\dot{d}_{tot} = -\frac{\beta\lambda\sigma\dot{\varepsilon}d^2}{c\gamma} + K_g \exp\left(\frac{-Q_g}{RT}\right) p^{-1} d^{1-p} \tag{23}$$

(notice that there is a typo in this equation in Austin & Evans 2007,). By setting the grain size evolution rate to zero, the steady state grain size is

$$d^{1+p} = \frac{K_g \exp\left(\frac{-Q_g}{RT}\right) p^{-1} c\gamma}{\beta\lambda\sigma\dot{\varepsilon}} \tag{24}$$

or equivalently,

$$d^{1+p} = \frac{K_g \exp\left(\frac{-Q_g}{RT}\right) p^{-1} c\gamma}{\lambda\sigma\dot{\varepsilon}_{dis}} \tag{25}$$

If previously published dislocation creep flow laws and grain growth kinetics are used in Eqs. 24 and 25, steady-state grain sizes measured during experiments on quartz, calcite, and olivine are successfully predicted (Austin & Evans 2007). The temperature dependence of recrystallized grain size predicted by equations 23-25 is consistent with published stress-grain size data for these three minerals (Austin & Evans 2007). Consequently, if grain growth and creep activation energies differ, those workers argue that must be taken into account when extrapolating measured stress-grain size data to natural conditions that may be hundreds of degrees colder than the experiments (e.g. Austin et al. in press).

1.3. Comparison of Grain Size Evolution Models

Considering the substantial differences in their formulation, the agreement between the various relations between stress and grain size for calcite, quartz, and olivine is quite remarkable (Fig. 1), particularly with regards to the exponent, *k*. However, for a given grain size, the different relationships predict nearly an order of magnitude difference in stress, which may relate to the significant uncertainty in many of the pre-exponential terms. In particular, the pre-exponential terms of the mechanistic models of Shimizu (Shimizu 1998, 2008) and Derby & Ashby (Derby & Ashby 1987; Derby 1990, 1991, 1992) depend on numerous material and microstructural properties, which are not considered here. More importantly, the different predictions regarding the temperature dependence of recrystallized grain size cause prediction of the relative stresses for a given grain size to differ widely under different conditions. For example, for quartz, the paleowattmeter (Austin & Evans 2007) agrees well with the recrystallized grain sizes obtained in experiments (Stipp & Tullis 2003). But, the paleowattmeter also predicts a temperature dependence of recrystallized grain size. Thus, there is significant discrepancy between stresses predicted by two models for natural shear zones containing quartz (Fig. 1) (Austin & Evans 2007). A similar observation was made by Shimizu (2008). Finally, not all of the relations predict the kinetics of grain size evolution, an important factor in determining if natural shear zones ever attain a steady-state grain size, and if shear zone microstructure will "reset" quickly to new deformation conditions (e.g. Prior et al. 1990).

2. Methodology

2.1. Sample Material and Preparation

The samples used in this study were prepared from two batches of reagent-grade (>99.95% pure) calcite powder, supplied by Malinckrodt (labeled x and b), ensuring that there was no initial lattice preferred orientation and that the impurity content was <0.05%. The powders were cold pressed into copper capsules with an ID of 10 mm, a length of 20 mm, and a wall thickness of 0.3 mm with a uniaxial stress of 10 MPa. The green bodies produced had porosities of 30±5% (Renner et al. 2002). Alumina spacers three millimeters thick were placed at each end; the completed sample assemblies were then heated to 363K for at least 12 hours to drive off adsorbed volatiles. In selected hydrostatic experiments, stacks of three samples, each 10 mm in diameter and ~5 mm long and separated by 3 mm-thick alumina spacers were loaded into the capsules. For all configurations, the sample assemblies were inserted into a second copper jacket, also with a 0.3 mm wall, and loaded between alumina and zirconia pistons.

2.2. Static Grain Growth Experiments

Samples for hydrostatic grain-growth experiments were hot isostatically pressed (HIPed) for 900 to 36900 s, at either 923 or 1023 K, at a confining pressure of 300 MPa (Table 3,4), with the internal pore space vented to the atmosphere, using a servocontrolled, internally heated, gas-medium apparatus (Paterson 1990). The samples were pressurized to 240 MPa, and then heated at a rate of 10 K/min. Temperature is believed to be constant within 3 K along the length of the sample, and the set-point is maintained to better than ±2 K, resulting in total uncertainty of ±5 K. Confining pressure is constant to better than ±5 MPa during an experiment. After 900 s at T≥823

K, the samples have compacted by >25%, no longer contain visible pores, and have measured porosities of ~1%, indicating that complete densification has occurred.

2.3. Deformation Experiments

In deformation experiments, after a hot press of the desired duration, a constant end-load was applied to the sample while holding temperature and confining pressure fixed (Table 4). Loads were chosen such that, for each initial grain size, deformation was either entirely in the diffusion creep regime, near the diffusion creep – dislocation creep boundary, or in the dislocation creep regime, based on the flow laws of Herwegh et al. (2003) and Renner et al. (2002) (Table 2, Fig. 1a). The force was held constant for durations ranging from 600 to 36000 s, after which it was entirely removed prior to quenching, in order to check for load cell drift. In four experiments, the force was changed several times during the course of the experiment (Table 4). Load was measured internally and is believed to be precise to about 20 N, or about 0.03 MPa of axial stress (Renner et al. 2002). Force was converted to stress by dividing by the cross sectional area of the sample, assuming constant volume deformation, and accounting for the stiffness of the apparatus. The strength of the Cu jacket was corrected using published flow laws for Cu (Frost & Ashby 1982), which are in agreement with independent measurements of jacket strength (Renner et al. 2002). Sample dimensions are known to ±0.1 mm. Consequently, we believe stresses are known to within ~5%, although uncertainties may be slightly higher at stresses below 10 MPa (Renner et al. 2002). Displacement was measured with two externally mounted displacement transducers to a precision of ~0.3 μm. Strain is reported as natural strain ($\ln[1+\varepsilon_o]$) determined by back calculating an initial length from the final length and total displacement, after accounting for apparatus stiffness; it is believed to be known to better than ~10% (i.e. .1 millistrain) (Renner et al. 2002). Strain rates are reported as the average over the duration of the

experiment, or by averaging over the final 100 s to minimize noise. Standard deviations associated with averaging are generally greater than measurement uncertainties and are of order 10-20% of the reported strain rate. At the conclusion of all experiments, after load removal, the sample was quenched by shutting off the furnace. Temperature was then dropped to 300K within ~600 s. Once 473 K was reached, the pressure was dropped over ~1800 s.

2.4. Microstructural Analysis

Following each experiment, samples were cut in half lengthwise, embedded in epoxy, polished, and etched in 0.37% hydrochloric acid for approximately 30 s (Herwegh 2000). The polished, etched samples were imaged in reflected light and the grain boundaries were manually traced with one pixel boundaries using a drawing tablet. Thresholded grain-boundary maps were analyzed using NIH Image J® to measure grain area, perimeter, and major and minor axes of the best fit ellipse. Grain areas were corrected by adding half of each boundary pixel to the neighboring grain. Grain size is reported as the equivalent circular diameter (ECD) of the measured grain area, with no correction for converting between the 2D image and the 3D sample (Tables 3,4). To investigate the effect of grain flattening on measured grain sizes, we also used the major and minor axes of the best fit ellipse, coupled with the measured area to calculate an ellipsoid, which was in turn converted to a sphere, from which the diameter was calculated (ie. Equivalent Spherical Diameter or ESD), which removes the effect of grain flattening; however, the ECD and ESD methods produce indistinguishable results. On select samples, we also measured mean intercept lengths from the same images used to obtain grain areas. For these samples, mean intercept lengths are directly comparable to ECD measurements, without using any stereological correction (Figure 2), consistent with previous observations of Rutter et al. (1994).

As there are no significant differences between the ECD, ESD, and mean intercept length methods in our samples, only ECD grain sizes are reported. All measured grain sizes are included in the mean values reported, however, the uncertainties for grains below 1 μm are significant (the theoretical resolution of the microscope is worse than 0.2 μm, and in reality is probably more nearly 0.5 μm). Our aim was to study at least 400 grains in each sample, however, in some of the coarsest samples, only ~100 grains were traced. Uncertainties in grain sizes were estimated by comparing the repeatability of the mean grain size measured in nominally identical experiments. At 923 K, the uncertainty is ±10% of the grain size, whereas at 1023 K, it is less, ±5%.

For select samples, the crystallographic preferred orientation (CPO) was measured on the same samples as grain size, using electron back-scatter diffraction (EBSD). Samples were selected for EBSD in order to investigate the evolution of CPO with varying strain, and to compare the CPO in samples that underwent grain growth with that in samples that underwent grain size reduction. Analyses were performed using a JEOL JSM 840 SEM with HKL Channel 5+ software at the Woods Hole Oceanographic Institution (WHOI), with an accelerating voltage of 15kV, tilt of 70º, and working distance of 23 mm. The beam current was varied between 3e-7 and 3e-8 A. For each region of investigation, >200 individual grains were manually selected by ensuring that the diffraction pattern was significantly different than neighboring analyses. Each analysis was indexed using the HKL software, accepting only fits with MAD<1.3. In addition, each indexed pattern was manually checked. Pole figures were created using the program PFch5 (D. Mainprice, pers. comm., 2007). They are presented as lower hemisphere projections with Gaussian smoothing of 8.5º, and are contoured for each 0.25 multiples of a uniform distribution

(MUD) up to global maximum of 5. The texture intensity is quantified with the J-Index of the c-axis pole figure.

3. Results

3.1. Mechanical Data

Average stress – strain rate data is calculated over A) the duration of each experiment , and B) over the last 100 s of the experiment, except when there are discontinuities in the strain rate – time curves, owing to doglegging or barreling of the sample. In those cases, the final values of stress, strain rate, and strain are taken prior to the discontinuities (Table 4). During experiments at constant load, stress progressively decreased as the cross-sectional area of the sample increased (Table 4). Strain rates also decreased with time (Table 4). The stress-strain rate systematics over the last 100 s of each experiment are consistent with a transition from an apparent stress exponent of <3.0 at low stress to an apparent stress exponent of >4.0 at high stress (Figure 3).

3.2. Static Grain Growth

The results of static grain-growth experiments are listed in table 3 and depicted in figures 4-6. At 923 K (powder x), notable grain growth occurs. In reflected light, the samples exhibit polygonal microstructure, with generally straight grain boundaries, six-sided grains, and numerous triple junctions (Figures 4,5). There is a significant scatter in the distribution of average grain size with time (Figure 6), which we attribute to the presence of sub-micron scale porosity (≤1% in all experiments) that is an inevitable remnant of the sample fabrication process (Walker et al. 1990; Covey-Crump 1997; Renner et al. 2002). At 1023 K, two different powders (x and b), of nominally the same composition, but different initial grain size were used. In both

sets of samples, six-sided polygonal grains with straight grain boundaries are common, and numerous triple junctions are present (Figures 4,5). Average grain size at 1023 K increased systematically with time, owing to increased grain boundary mobility, although porosities are equivalent to those at 923 K. With increasing duration of heat treatment, and consequently increasing mean grain size, the grain size distributions broadened (Figures 4,5).

3.3. Grain-size Evolution during Deformation

3.3.1. Low Stress

Deformation experiments run at 923 K, at differential stresses at or below 22 MPa, showed grain growth consistent with that observed under static conditions (Figure 4, Table 4), and the microstructures strongly resemble those of the static grain-growth experiments (Figure 4). One sample (c-1005), deformed at a differential stress of 10 MPa, has a much coarser grain size than an experiment run for an equivalent time under hydrostatic conditions, however, a duplicate experiment run at a stress of 17 MPa (c-1014) has a grain size consistent with grain sizes from hydrostatic experiments of the same duration.

Samples with "fine" initial grain sizes and those deformed at "low" stresses at 1023 K have microstructures that consist of polygonal grains with straight grain boundaries, and numerous triple or four-grain junctions (Figure 4). The grain-size distributions formed during deformation strongly resemble those produced under static conditions (Figure 4). These samples also have the same average grain size as experiments run for comparable times under static conditions (Table 3,4; Figure 4,6). The only significant exceptions are the two experiments deformed for 36000 s at a differential stress of ~10 MPa, both of which have coarser grain sizes than an experiment run for a comparable duration under hydrostatic conditions (Figure 6), although they have similar grain morphologies. Aside from these experiments, we observe no evidence of any

modification of the grain-growth kinetics or microstructural evolution during "low-stress" experiments at either 923 K or 1023 K.

3.3.2. High Stress

At 1023 K, samples deformed at "high" stresses or with "coarse" starting grain sizes exhibit microstructures that deviate from those observed in static and low-stress experiments (Figures 5,6). For example, samples c-1083, c-1095, c-1096, and c-1097 suggest that with increasing stress, grain-size distributions become skewed towards finer grain sizes. With increasing stress, grain boundaries become more irregular; there are no longer well-defined triple junctions; and with the exception of some finer grains, there are no polygonal grains (Figure 5). Average grain sizes of samples deformed at "high" stress, with "coarse" starting grain size fall below that of samples hot pressed for equivalent total times (Figure 5,6).

3.4. Crystallographic Preferred Orientation

All samples investigated exhibit some degree of Crystallographic Preferred Orientation (CPO) (Figure 7). c-poles are distributed around a small circle within ~30-45 degrees of the compression direction (parallel to the long axis of the sample), and a-axes are broadly distributed in a girdle normal to the c-poles. r-poles have very weak preferred orientation. The intensity of the CPO, quantified using the J-Index of the c-axis pole figure, increases with increasing strain (Figure 7,8). Samples that underwent grain-growth have weaker CPO intensity than those that underwent grain-size reduction (Figure 7,8).

4. Discussion

4.1. Mechanical Evolution

The mechanical data reported in table 4 are roughly consistent with a composite flow law (eq. 26) using the dislocation creep law of Renner et al. (2002), and the diffusion creep law of Herwegh et al. (2003) (Table 2)

$$\dot{\varepsilon}_{tot} = \dot{\varepsilon}_{dif} + \dot{\varepsilon}_{dis} \tag{26}$$

(e.g., Renner et al. 2002; Ter Heege et al. 2002) (Figure 3). Parameters for these flow laws were obtained from experiments on similar materials and at the same thermodynamic conditions as our experiments; and they should accurately represent the mechanical data collected here. By using eq. 26, we implicitly assume that the two mechanisms are linearly independent and that the average grain size may be used in the diffusion creep law. Our results are also consistent with the previous experimental observations of Renner et al. (2002) from strain rate stepping experiments at nominally the same temperature (Figure 3).

There are, however, small discrepancies between total measured strain rates and the sum of those predicted for dislocation creep (Renner et al. 2002) and diffusion creep (Herwegh et al. 2003), which correlate with strain (r=0.74) (Figure 9). As total strain and stress are not correlated (r=0.05), this difference cannot simply be systematic misfit between the flow laws and the data. There is also only a very weak correlation between misfits and grain size (r=0.23), and between the residual misfit after the strain correlation and grain size (r=0.30), suggesting that the grain size dependence of strain rate is adequately accounted for. There is, however, a strain dependence of strain rate that remains. Our data suggest that this weakening may relate to the formation and evolution of CPO (Figures 7,8). If $CPO = f(\varepsilon...)$, then at least two explicit

internal state variables are probably required to describe the creep rate of calcite: grain size (or grain size distribution) and CPO (or the orientation distribution function (ODF) of crystallographic orientations). Evolution equations for both of these state variables may be required to describe the mechanical evolution of shear zones.

Previous authors have suggested that the flow stress during constant strain rate deformation of Carrara marble depends on strain, either in a power-law relationship (Rutter 1999) or in an exponential relationship (Lutton & Sellars 1969; Barnhoorn et al. 2004). None of these studies correlate strain with the evolution of an internal state variable. The exponential relationship (Lutton & Sellars 1969) may correlate with weakening associated with CPO formation for certain loading geometries, where the strength that is asymptotically approached will be that of the easy slip system under a given set of thermodynamic conditions (De Bresser & Spiers 1993; Wang et al. 1996). Although we suspect that CPO is an important variable, our data are not sufficient to relate the evolution of strain with CPO quantitatively.

4.2. Kinetics of coarsening during triaxial and hydrostatic loading

Static grain growth kinetics at both 923 K and 1023 K are well described by equations 7-9 (Figure 6), with a grain growth exponent of 3. Values of K ($=K_g exp[-Qg/RT]$) required to fit each subset of the data are listed in table 5. Due to the limited temperature range of our experiments, we do not calculate the activation enthalpy for grain-growth. However, if grain growth parameters from Covey-Crump (1997) are inserted (K_g=2.5e9 μm^{-p} s^{-1}, p=3, Q_g=174 kJ mol^{-1}), the K value at 1023K (3.26 μm^{-p} s^{-1}) is very close to that observed in our experiments on powder b (3.16 μm^{-p} s^{-1}) at the same temperature, with the same p value.

Static grain-growth kinetics are highly sensitive to porosity (Evans et al. 2001) and chemical impurities (Evans et al. 2001; Freund et al. 2001; Herwegh et al. 2003). The experiments

reported here were performed on reagent-grade calcite powder in an effort to minimize any chemical effects on grain growth kinetics. However, as a consequence of preparing samples from powders, limited porosity is inevitably present, although in all samples reported here porosity is below ~1%. If pore drag is rate-limiting, the grain growth exponent (p) is expected to be between 2 and 4 depending on the mechanism of diffusion across or around the pore (Brook 1976; Covey-Crump 1997; Evans et al. 2001). A grain growth exponent of 3, as observed in the experiments reported here, is predicted if the rate limiting process is either vapor transport across the pore, or lattice diffusion through the growing phase (Brook 1976; Covey-Crump 1997). However, we cannot definitively distinguish the mechanism of grain growth from our experiments.

The reason for the variation in K between the two powders (x and b) at the same temperature is not clear. One possibility is that there are chemical differences at the ppm level, between these samples. Freund et al. (2001) found that increasing Mn content from 10 ppm to 670 ppm resulted in an increase in K_g of over 2 orders of magnitude. The difference in K between the two powders we investigated was less than 1 order of magnitude, and thus could conceivably be related to chemical variations, although the reported chemical analyses show no measureable differences between the two powders. A second, preferred, explanation is that variations in the grain size of the powder prior to cold pressing and HIPing influenced the porosity distribution. The powder with an initially finer grain size (x) has a lower K than that with an initially coarser grain size (b) (Fig. 6). Although there is no measurable or visible difference in porosity in samples prepared from these two powders, subtle differences in porosity distribution might still have a fairly dramatic influence on K.

Previous workers using fine-grained aggregates of calcite (Walker et al. 1990) and olvine (Karato 1989) have reported that the kinetics of coarsening during diffusion creep are equivalent to normal grain growth under hydrostatic conditions, but others posit that dynamic coarsening during diffusion creep might be enhanced owing to grain switching (Sato et al. 1990; Kellermann Slotemaker 2006). Our results suggest that grain-growth kinetics during diffusion creep are equivalent to those observed under hydrostatic conditions, but some uncertainties remain. Three low-stress, creep experiments (c-1005, c-1090, and c-1108, Fig. 6) do show enhanced rates. Although these enhanced growth rates might be caused by boundary switching during creep, faster growth kinetics might also result from small variations in porosity (Wong et al. 1997; Xiao & Evans 2003). Notice that one hydrostatic grain growth experiment (c-1046) is also abnormally fast (Fig. 6).

In all experiments where flow laws predict that diffusion creep is the dominant deformation mechanism, grain coarsening occurs, and mechanical work done on the rock is not stored in the form of grain-boundary energy. We suspect that growth kinetics are completely indifferent to diffusion creep, and can be fit with the same kinetic equation as that for normal grain growth under static conditions (equations 7-9). But, even if coarsening is enhanced by grain switching (Sato et al. 1990; Kellermann Slotemaker 2006), not only is boundary energy not stored, it is removed at a faster rate than during normal grain growth. These results are consistent with the supposition that, absent other retarding forces, grain growth will occur during diffusion creep and will act to reduce the creep rate (c.f. De Bresser et al. 2001).

4.3. Grain-Size Reduction Kinetics

Average grain-size evolution rates during deformation were determined by subtracting the starting grain size (i.e., after HIP) from the average size at the end of the test and dividing by the

elapsed time; negative values indicate reduction rates; positive values coarsening rates. The starting grain sizes were not measured directly but were calculated based on the HIP duration, the grain-growth relation (equations 7 and 8), and *p* and *K* values appropriate for the temperature and starting material (Tables 4,5). The grain-size evolution rate correlates with the product of stress, strain rate, and initial grain size squared (Fig. 10), suggesting that the reduction rate is determined by the rate that mechanical work is done during deformation, or alternatively, the rate that energy is added to the system. The correlation is much weaker if the reduction rate is compared to either stress or strain rate independently (Fig. 10). This result is consistent with a paleowattmeter scaling relationship (Austin & Evans 2007). The transition from grain growth to grain size reduction in these experiments is determined by the relative rates of normal grain growth (equation 9) and dynamic reduction (equation 22), which, in turn, is determined by the value of $\sigma\dot{\varepsilon}d^2$.

We supplemented our data with similar information from compression experiments on Carrara marble (Ter Heege et al. 2002), with a starting grain size of 68 μm, at temperatures of 1103 K, 1173 K, and 1223 K (Fig. 11). The correlation between $\sigma\dot{\varepsilon}d^2$ and grain size evolution rate is clearly seen in that data, too. However, both the slopes and the intercepts of the best fit lines for the Carrara experiments seem to differ from our synthetic aggregates and perhaps also change as a function of temperature.

The intercepts of the rate curves, i.e., the coarsening rate when $\sigma\dot{\varepsilon}d^2 = 0$, which correspond to the rate of normal grain growth, are noticeably larger in Carrara marble than those for the synthetic material (Fig. 11b). The temperature dependence of the intercepts are also greater in Carrara (best fit = -353 kJ/mol) than in synthetic calcite (Fig. 11b). This result is consistent with the higher thermal activation of grain growth observed in Carrara marble (-392 kJ mol^{-1}) as

compared to the activation energies for grain growth observed in several other natural and synthetic fine grained marbles (-99 to -232 kJ mol^{-1}) (Covey-Crump 1997; Freund et al. 2001).

The slopes of the reduction curves $\left(\frac{\partial(\dot{d})}{\partial(\sigma\dot{\varepsilon}d^2)} = \chi\right)$ are also of interest (Fig. 11c) because they indicate the strength of coupling between recrystallization rate and input power. Experiments for Carrara at 1223 and 1173 K (Ter Heege et al. 2002), have approximately the same slope, but χ at 1103 K may be larger. Our experiments at 1023 K on synthetic marble have a more negative slope, suggesting a material difference or a temperature dependence. But because the data are limited, and the uncertainties are quite high, the existence or cause of such an effect is not entirely clear.

If stress, strain rate and grain size are measured directly, four other parameters, c, γ, λ, and β, may influence χ. In the current experiments, we directly calculated the last of these, but for Carrara marble, there is no well-calibrated flow law for diffusion creep, and thus, the partitioning of strain rate, β, has not been directly measured in that rock.

Each of the other three factors can, however, be bounded or estimated. In metals, deformed under conditions where the defect microstructure and strength are changing, the amount of heat dissipated ($1-\lambda$) is known to vary as a function of strain, strain rate, and temperature, and under various conditions, has been shown to vary from 1 to <0.6 (i.e., λ varies from >0.4 to 0) (Chrysochoos et al. 1987; Mason et al. 1994; Camacho & Ortiz 1997; Kapoor & Nemat-Nasser 1998; Rittel 1999; Hodowany et al. 2000; Rosakis et al. 2000; Wei et al. 2004; Schreyer & Maudlin 2005; Longère & Dragon 2008).

Systematic variations in grain morphology could also cause the geometric parameter, *c*, to vary from one set of experiments to another. Such variations might arise owing either to measurement

artifacts or to differences in the actual shape. For example, the shape parameter, c, for nearly spherical grains should approximately = π, but calculating grain size as either ECD or ESD imposes other specific geometric assumptions. Grain boundary energy varies with a number of parameters including the degree of misorientation between grains, crystallographic orientation of the grain boundary in question, and the concentration of impurities segregated to the grain boundaries.

If all three factors are combined to give a single adjustable parameter, under the assumptions above (λ=0.1, c=π, γ=1 J m^{-2}) (Austin & Evans 2007), $\lambda/c\gamma$ would be about 0.03 m^2 J^{-1}. That value, along with published flow laws (Renner et al. 2002; Herwegh et al. 2003) (Table 2) and grain-growth parameters (Covey-Crump 1997) (p=3; Kg=2.5x10^9; Qg=174 kJ mol^{-1}) successfully predicts grain sizes measured during dynamic recrystallization (Schmid et al. 1980; Rutter 1995). The same parameters and flow laws also predict strain rates in the inverted limb of the Morcles nappe of the Swiss Helvetic Alps that are consistent with estimates of shear-zone thickness, offsets, and duration of thrusting (Ebert et al. 2007; Austin et al. in press).

We have also estimated $\lambda/c\gamma$ for each of our experiments. If the grain growth parameters from Covey-Crump (1997) and the flow laws from Renner et al. (2002) and Herwegh et al. (2003) are used, the data suggest a lower value, $0.001<\lambda/c\gamma<0.020$ m^2 J^{-1} (Fig 10b). Alternatively, if the grain growth parameters we obtained for each powder and temperature (Table 5) are used, we calculate $0.001<\lambda/c\gamma<0.009$ m^2 J^{-1}.

There are several explanations for the discrepancy between these values and those estimated previously (Austin & Evans 2007). In addition to systematic variations in $\lambda/c\gamma$, in these experiments, we measured an average grain size evolution rate and compared it to an average stress, average strain rate, and the initial grain size. But, in our experiments, all of these

parameters are varying, and in particular, the grain-size reduction rate slows (approaches zero) as the grain size approaches a stable grain size. Thus, the estimated $\lambda/c\gamma$ values (which are secants to the curve) will be lower than the actual values at a given instant (which are tangents). Future experiments need to be designed to investigate variations in λ, which is important both for understanding grain size evolution kinetics and for understanding viscous shear heating (Kameyama et al. 1997; Kelemen & Hirth 2007)

It is important to emphasize that, despite the complexity of many parameters in the paleowattmeter, the correlation between the rate of grain-size evolution and that of mechanical work is robust and that, by making simplifying assumptions regarding c, γ, and λ, grain sizes measured in the laboratory are successfully predicted, and geologically reasonable strain rates are predicted for natural shear zones (Austin & Evans 2007; Austin et al. in press).

4.4. Grain Size Stabilization During Deformation

Grain-size stabilization has important consequences for the mechanical evolution of shear zones. Using equation 25, along with the Peierls dislocation creep flow law of Renner et al. (2002) (Table 2) and the grain growth parameters from Covey-Crump (1997), which are consistent with the grain growth kinetics of powder b (Table 5), we calculate stabilized grain sizes under specific thermodynamic conditions using the paleowattmeter with the same $\lambda/c\gamma$ values, flow laws, and grain growth parameters as Austin & Evans (2007), and using a $\lambda/c\gamma$ value of 0.0025 $m^2\ J^{-1}$, consistent with our experimental observations (Fig. 12) (note that the predicted grain sizes are quite similar despite the uncertainty in $\lambda/c\gamma$). If the grain growth parameters for powder x are used (Table 5) along with the measured $\lambda/c\gamma$ value of 0.0025 $m^2\ J^{-1}$, the predicted grain size is between that for the two sets of parameters discussed above. We also show the stable grain sizes predicted by the Field Boundary Hypothesis (equation 11-13) (De

Bresser et al. 1998), and the stress-grain size piezometers (Schmid et al. 1980; Rutter 1995). The samples where we observe either grain growth or grain size reduction are compared to each of these predictive relationships (Fig. 12). While none of the relationships are consistent with all of the observations, the transition from grain growth to grain size reduction is consistent with the predictions of the paleowattmeter (eq. 25), however neither the Schmid et al. (1980) piezometer nor the mechanism boundary (De Bresser et al. 1998; De Bresser et al. 2001) can be ruled out.

4.5. Microstructural Evolution and Rheological Weakening

An inherent assumption in our analysis has been that low strain flow laws are sufficient to quantify the rheology of highly strained rocks, such as those that occur in many natural shear zones. This assumption has been questioned by Barnhoorn et al. (2004), based on high strain torsion experiments on Carrara marble. As with Barnhoorn's torsion experiments (Barnhoorn et al. 2004), the data presented here exhibit a strain dependence of strain rate. Part of this increased rate of deformation may be due to a transition to grain size sensitive deformation (e.g. Lee et al. 2002), however Rutter (Rutter 1995; Rutter 1999) argued that the observed weakening in his experiments could not be related to a switch in deformation mechanism, and our observations do not suggest a strong correlation between weakening and grain size. Our observations, along with torsion experiments on both calcite (Pieri et al. 2001a; Pieri et al. 2001b; Barnhoorn et al. 2004) and olivine (Bystricky et al. 2000) suggest that weakening may be associated with formation and intensification of a crystallographic preferred orientation (CPO). Thus, it may be important to consider the role of CPO when analyzing the mechanical properties of highly strained rocks. If, through processes of dynamic recrystallization and CPO formation, significant weakening is possible within the dislocation creep regime, then the value of $\dot{\varepsilon}_{dis}$ in equation 25 will increase under constant stress conditions, and the stabilized grain size will decrease. If a shear zone is

deforming everywhere under constant stress, then the mechanically weakest regions will have the finest grain size (equations 24 and 25). This provides a possible explanation for reduced grain sizes in highly deformed shear zones, without calling upon elevated stresses in regions of apparent strain localization, which may be in contradiction to localization theory (Hobbs et al. 1990). At least two explicit state variables are required to explain the mechanical evolution of shear zones: grain size and CPO intensity.

5. Conclusions

During deformation at elevated temperature, where the bulk strain rate is determined by the relative contributions of dislocation creep and diffusion creep, the experimentally measured grain size evolution rate of calcite is controlled by stress, strain rate, and grain size. When stresses are "low" and grain sizes are "fine," grains grow; the kinetics of which are indistinguishable from under static conditions. At "high" stresses or for "coarse" grained samples, grain size reduction occurs at a rate determined by $\sigma\dot{\varepsilon}d^2$, and when grain size evolution rates from different calcite rocks deformed at different temperatures are compared, systematic variations in rate of grain size evolution are observed. The transition from grain growth to grain size reduction observed in deformation experiments is closely predicted by the paleowattmeter.

Grain size evolution during deformation in calcite, thus, appears to be controlled by a competition between grain growth, which is determined by the static growth rate, and grain size reduction, which is dictated by the rate work is done during deformation ($\sigma\dot{\varepsilon}$), and the partitioning of energy between the microstructure and heat production. Where these grain growth and grain size reduction processes balance, grain size is stabilized.

With increasing strain in our experiments, systematic weakening is observed, which is likely related to the formation of CPO, and the evolution of internal state variables. Progressive strain

weakening, at constant stress provides a mechanism for strain localization, and will result in grain size reduction in the most deformed rocks without requiring elevated stresses.

There are several key advantages to the paleowattmeter over existing grain size evolution relationships. First, it is consistent with laboratory measurements of both stabilized grain size and grain size evolution rates. Secondly, by providing information regarding grain size evolution rates as well as the stabilized grain size, it allows for estimation of the time necessary to reach the stabilized grain size for a given material under given conditions. Third, it provides an explanation for highly-strained, fine-grained mylonites, without calling for elevated stresses in the most highly deformed portions of shear zones, by predicting finer grain sizes at higher strain rates, even under constant stress conditions. The paleowattmeter, thus, is consistent with laboratory observations, and provides an explanation for the grain size variations observed in shear zones that is consistent with localization theory.

6. Acknowledgements

We would like to thank Uli Mok, Xiaohui Xiao, and Jock Hirst for their assistance in the laboratory. Discussions with Greg Hirth, Lili Xu, Bill Durham, Georg Dresen, Joerg Renner, and David Kohlstedt greatly improved this manuscript. Louie Kerr, Luc Mehl, and Jessica Warren kindly assisted us with the EBSD system. This work was funded by NSF grants EAR0309510, EAR0510412, and OCE0452787.

7. References

Austin, N.&Evans, B. 2007: Paleowattmeters: A scaling relation for dynamically recrystallized grain size. Geology **35**(4): 343.

Austin, N., Evans, B., Herwegh, M.&Ebert, A. in press: Strain Localization in the Morcles Nappe (Helvetic Alps, Switzerland). Swiss Journal of Geosciences.

Barnett, M. 2007: A practical condition for migration dynamic recrystallization. Acta Materialia **55**(9): 3271-3278.

Barnhoorn, A., Bystricky, M., Burlini, L.&Kunze, K. 2004: The role of recrystallisation on the deformation behaviour of calcite rocks: large strain torsion experiments on Carrara marble. Journal of Structural Geology **26**(5): 885-903.

Braun, J., Chéry, J., Poliakov, A., Mainprice, D., Vauchez, A., Tomassi, A.&Daigniéres, M. 1999: A simple parameterization of strain localization in the ductile regime due to grain size reduction: A case study for olivine. Journal of Geophysical Research-Solid Earth **104**(B11).

Brook, R. 1976: Controlled grain growth. Treatise on Materials Science and Technology **9**: 331-364.

Bystricky, M., Kunze, K., Burlini, L.&Burg, J. 2000: High Shear Strain of Olivine Aggregates: Rheological and Seismic Consequences. Science. **290:** 1564-1567.

Camacho, G.&Ortiz, M. 1997: Adaptive Lagrangian modelling of ballistic penetration of metallic targets. Computer Methods in Applied Mechanics and Engineering **142**(3-4): 269-301.

Chrysochoos, A., Maisonneuve, O., Martin, G., Caumon, H.&Chezeaux, J. 1987: Plastic and Dissipated Work and Stored Energy. Nucl. Eng. Des. **114**(3): 323-333.

Covey-Crump, S. 1994: The application of Hart's state variable description of inelastic deformation to Carrara marble at T less than 450 C. Journal of Geophysical Research **99**(B10): 19,793-19,808.

Covey-Crump, S. J. 1997: The normal grain growth behaviour of nominally pure calcitic aggregates. Contributions to Mineralogy and Petrology **129**(2-3): 239-254.

de Bresser, J.&Spiers, C. 1993: Slip systems in calcite single crystals deformed at 300–800 C. Journal of Geophysical Research **98**(B4): 6397-6409.

de Bresser, J. 1996: Steady state dislocation densities in experimentally deformed calcite materials: Single crystals versus polycrystals. Journal of Geophysical Research **101**(B10): 22189-22202.

de Bresser, J., Peach, C., Reijs, J.&Spiers, C. 1998: On dynamic recrystallization during solid state flow: Effects of stress and temperature. Geophys. Res. Lett **25**(18): 3457–3460.

de Bresser, J., Ter Heege, J.&Spiers, C. 2001: Grain size reduction by dynamic recrystallization: can it result in major rheological weakening? International Journal of Earth Sciences **90**(1): 28-45.

Derby, B.&Ashby, M. 1987: On Dynamic Recrystallization. Scr. Metall. **21**(6): 879-884.

Derby, B. 1990: Dynamic recrystallization and grain size. Deformation Processes in Minerals, Ceramics and Rocks: 354–64.

Derby, B. 1991: The Dependence of Grain Size on Stress During Dynamic Recrystallization. Acta Metallurgia et Materialia **39**(5): 955-962.

Derby, B. 1992: Dynamic recrystallisation. The steady state grain size. SCR METALL MATER. **27**(11): 1581-1586.

Ebert, A., Herwegh, M., Evans, B., Pfiffner, A., Austin, N.&Vennemann, T. 2007: Microfabrics in carbonate mylonites along a large-scale shear zone (Helvetic Alps). Tectonophysics **444**(1-4): 1-26.

Evans, B., Renner, J.&Hirth, G. 2001: A few remarks on the kinetics of static grain growth in rocks. International Journal of Earth Sciences **90**(1): 88-103.

Freund, D., Rybacki, E.&Dresen, G. 2001: Effect of impurities on grain growth in synthetic calcite aggregates. Physics and Chemistry of Minerals **28**(10): 737-745.

Frost, H.&Ashby, M. 1982: Deformation-Mechanism Maps: The Plasticity and Creep of Metals and Ceramics, Pergamon Press.

Guillope, M.&Poirier, J. 1979: Dynamic recrystallization during creep of single-crystalline halite: An experimental study. Journal of Geophysical Research **84**(B10): 5557-5567.

Hall, C.&Parmentier, E. 2003: Influence of grain size evolution on convective instability. Geochemistry, Geophysics, Geosystems **4**(3): 1.

Herwegh, M. 2000: A new technique to automatically quantify microstructures of fine grained carbonate mylonites: two-step etching combined with SEM imaging and image analysis. Journal of Structural Geology **22**(4): 391-400.

Herwegh, M., Xiao, X.&Evans, B. 2003: The effect of dissolved magnesium on diffusion creep in calcite. Earth and Planetary Science Letters **212**(3-4): 457-470.

Hirth, G., Teyssier, C.&Dunlap, J. 2001: An evaluation of quartzite flow laws based on comparisons between experimentally and naturally deformed rocks. International Journal of Earth Sciences **90**(1): 77-87.

Hobbs, B., Muhlhaus, H.&Ord, A. 1990: Instability, softening and localization of deformation. Geological Society London Special Publications **54**(1): 143.

Hodowany, J., Ravichandran, G., Rosakis, A.&Rosakis, P. 2000: Partition of plastic work into heat and stored energy in metals. Experimental Mechanics **40**(2): 113-123.

Kameyama, M., Yuen, D.&Fujimoto, H. 1997: The interaction of viscous heating with grain-size dependent rheology in the formation of localized slip zones. Geophysical Research Letters **24**(20): 2523-2526.

Kapoor, R.&Nemat-Nasser, S. 1998: Determination of temperature rise during high strain rate deformation. Mechanics of Materials **27**(1): 1-12.

Karato, S., Toriumi, M.&Fujii, T. 1980: Dynamic recrystallization of olivine single crystals during high-temperature creep. Geophysical Research Letters **7**(9): 649-652.

Karato, S. 1989: Grain growth kinetics in olivine aggregates. Tectonophysics **168**: 255-273.

Kelemen, P. B.&Hirth, G. 2007: A periodic shear-heating mechanism for intermediate-depth earthquakes in the mantle. **446**(7137): 787-790.

Kellermann Slotemaker, A. 2006: Dynamic recrystallization and grain growth in olivine rocks, Utrecht University**:** 187.

Lee, K., Jiang, Z.&Karato, S. 2002: A scanning electron microscope study of the effects of dynamic recrystallization on lattice preferred orientation in olivine. Tectonophysics **351**(4): 331-341.

Longère, P.&Dragon, A. 2008: Plastic work induced heating evaluation under dynamic conditions: Critical assessment. Mechanics Research Communications **35**(3): 135-141.

Lutton, M.&Sellars, C. 1969: Dynamic Recrystallization in Ni and Ni-Fe Alloys During High Temperature Deformation. Acta Metall **17**: 1033-1043.

Mason, J., Rosakis, A.&Ravichandran, G. 1994: On the strain and strain-rate dependence of plastic work converted to heat-an experimental study using high-speed infrared detectors and the kolsky bar. Mechanics of Materials **17**: 135-145.

Montesi, L.&Zuber, M. 2002: A unified description of localization for application to large-scale tectonics. J. Geophys. Res **107**(10.1029).

Montési, L.&Hirth, G. 2003: Grain size evolution and the rheology of ductile shear zones: from laboratory experiments to postseismic creep. Earth and Planetary Science Letters **211**(1-2): 97-110.

Olgaard, D.&Evans, B. 1986: Effect of second-phase particles on grain growth in calcite. J. Am. Ceram. Soc **69**(11): 272-277.

Olgaard, D.&Evans, B. 1988: Grain growth in synthetic marbles with added mica and water. Contributions to Mineralogy and Petrology **100**(2): 246-260.

Paterson, M. 1990: Rock deformation experimentation. AGU Geophysical Monograph **56**: 187-194.

Pieri, M., Burlini, L., Kunze, K., Stretton, I.&Olgaard, D. 2001a: Rheological and microstructural evolution of Carrara marble with high shear strain: results from high temperature torsion experiments. Journal of Structural Geology **23**(9): 1393-1413.

Pieri, M., Kunze, K., Burlini, L., Stretton, I., Olgaard, D., Burg, J.&Wenk, H. 2001b: Texture development of calcite by deformation and dynamic recrystallization at 1000K during torsion experiments of marble to large strains. Tectonophysics **330**(1-2): 119-140.

Poliak, E.&Jonas, J. 1996: A one-parmenter approach to determining the critical conditions for the initiation of dynamic recrystallization. Acta Materialia **44**(1): 127-136.

Prior, D., Knipe, R.&Handy, M. 1990: Estimates of the rates of microstructural changes in mylonites. Geological Society London Special Publications **54**(1): 309.

Renner, J., Evans, B.&Siddiqi, G. 2002: Dislocation creep of calcite. J. Geophys. Res **107**: 1-16.

Rittel, D. 1999: On the conversion of plastic work to heat during high strain rate deformation of glassy polymers. Mechanics of Materials **31**(2): 131-139.

Rosakis, P., Rosakis, A., Ravichandran, G.&Hodowany, J. 2000: A thermodynamic internal variable model for the partition of plastic work into heat and stored energy in metals. Journal of the Mechanics and Physics of Solids **48**(3): 581-607.

Rutter, E. 1999: On the relationship between the formation of shear zones and the form of the flow law for rocks undergoing dynamic recrystallization. Tectonophysics **303**(1): 147-158.

Rutter, E.&Brodie, K. 2004: Experimental intracrystalline plastic flow in hot-pressed synthetic quartzite prepared from Brazilian quartz crystals. Journal of Structural Geology **26**(2): 259-270.

Rutter, E. H., Casey, M.&Burlini, L. 1994: Preferred crystallographic orientation development during the plastic and superplastic flow of calcite rocks. Journal of Structural Geology **16**(10): 1431-1446.

Rutter, E. H. 1995: Experimental study of the influence of stress, temperature, and strain on the dynamic recrystallization of Carrara Marble. Journal of Geophysical Research, B, Solid Earth and Planets **100**(12): 24,651-24,663.

Sato, E., Kuribayashi, K.&Horiuchi, R. 1990: A Mechanism of Superplastic Deformation and Deformation Induced Grain Growth Based on Grain Switching. Superplasticity in Metals, Ceramics, and Intermetallics: 27-32.

Schmid, S., Paterson, M.&Boland, J. 1980: High temperature flow and dynamic recrystallization in Carrara marble. Tectonophysics **65**(3): 4.

Schreyer, H.&Maudlin, P. 2005: Thermodynamically consistent relations involving plasticity, internal energy and thermal effects. Philosophical Transactions: Mathematical, Physical and Engineering Sciences **363**(1836): 2517-2541.

Shimizu, I. 1998: Stress and temperature dependence of recrystallized grain size: A subgrain misorientation model. Geophysical Research Letters **25**(22): 4237-4240.

Shimizu, I. 2008: Theories and applicability of grain size piezometers: The role of dynamic recrystallization mechanisms. Journal of Structural Geology: doi:10.1016/j.jsg.2008.03.004.

Smith, C. 1948: Grains, phases, and ainterfaces: as interpretation of microstructure. Transactions of the American Institute of Mining and Metallurgical Engineers **15**(4): 1-37.

Stipp, M.&Tullis, J. 2003: The recrystallized grain size piezometer for quartz. Geophysical Research Letters **30**(21).

Stone, D., Plookphol, T.&Cooper, R. 2004: Similarity and scaling in creep and load relaxation of single-crystal halite(NaCl). Journal of Geophysical Research. B. Solid Earth **109**.

Ter Heege, J., De Bresser, J.&Spiers, C. 2002: The influence of dynamic recrystallization on the grain size distribution and rheological behaviour of Carrara marble deformed in axial compression. Geological Society London Special Publications **200**(1): 331.

Ter Heege, J., De Bresser, J.&Spiers, C. 2005: Dynamic recrystallization of wet synthetic polycrystalline halite: dependence of grain size distribution on flow stress, temperature and strain. Tectonophysics **396**(1-2): 35-57.

Twiss, R. 1977: Theory and applicability of a recrystallized grain size paleopiezometer. Pure and Applied Geophysics **115**(1): 227-244.

van der Wal, D., Chopra, P., Drury, M.&Fitzgerald, J. 1993: Relationships between dynamically recrystallized grain size and deformation conditions in experimentally deformed olivine rocks. Geophysical Research Letters **20**(14): 1479-1482.

Walker, A., Rutter, E.&Brodie, K. 1990: Experimental study of grain-size sensitive flow of synthetic, hot-pressed calcite rocks. Geological Society London Special Publications **54**(1): 259.

Wang, Z., Bai, Q., Dresen, G., Wirth, R.&Evans, B. 1996: High-temperature deformation of calcite single crystals. Journal of Geophysical Research **101**(B9): 20377-20390.

Wei, Q., Kecskes, L., Jiao, T., Hartwig, K., Ramesh, K.&Ma, E. 2004: Adiabatic shear banding in ultrafine-grained Fe processed by severe plastic deformation. Acta Materialia **52**(7): 1859-1869.

Wong, T., David, C.&Zhu, W. 1997: The transition from brittle faulting to cataclastic flow in porous sandstones: Mechanical deformation. Journal of Geophysical Research **102**(B2): 3009-3026.

Xiao, X.&Evans, B. 2003: Shear-enhanced compaction during non-linear viscous creep of porous calcite–quartz aggregates. Earth and Planetary Science Letters **216**(4): 725-740.

8. Tables

Table 1a) List of symbols.

Symbol	Description
d_s	Stabilized grain size
d_o	Initial grain size
d	Present grain size
σ	Differential Stress
ρ	Dislocation density
ϕ	Ratio of dislocation length in the grain boundary to that in the grain interior
J	Constant relating to subgrain distribution and material properties
d*	Limiting subgrain size
M	Grain boundary mobility $=M_o\exp(-Q_m/RT)$
F	Driving force for grain boundary migration
$\dot{N}$	Growth rate of a grain nuclei
I	Grain Nucleation rate
b	Burgers vector
A	Constant
$\dot{\varepsilon}$	Strain rate
μ	Shear modulus
D	Diffusivity $= D_o\exp(-Q_D/RT)$
p	Grain-Growth exponent
K	Grain-Growth pre-exponential
Q	Activation ethalpy
R	Gas Constant (8.314 J K^{-1} mol^{-1})
T	Temperature (K)
ε_c	Critical strain for microstructural evolution
n	Stress exponent
m	Grain size exponent in flow laws
φ	Average subgrain boundary misorientation
$\dot{E}_{\text{int}}$	Time derivative of internal energy
$\dot{\theta}_{irr}$	Time derivative of dissipated energy
γ	Grain boundary energy
λ	Proportion of the energy associated with dislocation creep stored in the microstructure
β	Fraction of the total mechanical work rate accommodated by dislocation creep
c	Geometric constant
$\dot{W}$	Rate mechanical work is done

Table 1b) List of subscripts.

Subscript	Description
gb	Grain boundary diffusion
v	Volume diffusion
dis	Dislocation creep
p	Peierls creep
dif	Diffusion creep
g	Growth
red	Reduction
tot	Total

Table 2) Calcite flow laws used in this study.

Flow Law	Type	Parameters	Reference
$\dot{\varepsilon}_p = A_p \sigma^2 \exp\left(\frac{\sigma}{\sigma_p}\right) \exp\left(-\frac{Q_p}{RT}\right)$ $\sigma_p = \left[\Sigma_{p,o} + K_p d^{-m_p}\right]\left[T\, m - T\right]$	Dislocation Creep (Peierls Law)	A_p=270.4 (MPa^{-2} s^{-1}) Q_p=200 kJ/mol m_p=0.5 K_p=115 (MPa μm^{mp} kK^{-1}) $\Sigma_{p,o}$=7.8 (MPa kK^{-1}) Tm=1600 (K)	(Renner et al. 2002)
$\dot{\varepsilon}_{dif} = A_{dif} \sigma^{n_{dif}} d^{-m_{dif}} \exp\left(-\frac{Q_{dif}}{RT}\right)$	Diffusion Creep	A_{dif}=4.3e7 (MPa^{-ndif} μm^{-mdif} s^{-1}) n_{dif}=1.1 m_{dif}=-3.3 Q_{dif}=200 kJ/mol	(Herwegh et al. 2003)

Table 3) Data from hydrostatic experiments. Standard deviation (1 sigma) represents the measured distribution of grain sizes in each sample. The starting material is shown in parantheses (b or x).

Experiment	T(K)	Total Duration (s)	Mean d (ECD) (µm)	Standard Deviation (µm)
c-1091 (b)	1023	900	16.9	7.2
c-1093 (b)	1023	9900	32.9	15.8
c-1109 (b)	1023	18900	39.0	17.4
c-1094 (b)	1023	36900	51.4	27.4
c-1046 (x)	1023	4500	24.5	11.4
c-1060t (x)	1023	4500	12.7	5.7
c-1073t (x)	1023	18900	16.6	7.5
c-1044 (x)	1023	18900	20.1	9.9
c-1013 (x)	923	900	4.4	2.5
c-1018 (x)	923	4500	10.0	5.0
c-1064t (x)	923	4500	8.0	3.8
c-1067t (x)	923	18900	10.8	4.9
c-1008 (x)	923	36900	18.7	8.9
c-1066t (x)	923	36900	15.3	6.9

Table 4) Data from deformation experiments. The starting powder is labeled in parantheses (b or x). For experiments which underwent multiple deformation and annealing steps (c-1048, c-1049, c-1051, and c-1052) these steps are listed sequentially, and a zero value for stress and strain rate denotes an annealing step. Average strain rate and average stress values are calculated over the duration of the experiment, while the strain rate and stress at maximum strain are average values over the last 100s of the experiment (see text for a more detailed explanation). A) are experiments run at 1023K whereas B) are experiments run at 923K.

4a) T=1023K

Experiment	Total Duration (s)	HIP time (s)	Duration at Target Stress (s)	Average Strain Rate (s^{-1})	Average Stress (MPa)	Strain Rate at End (s^{-1})	Stress at End (MPa)	Mean d (ECD) (μm)	Strain
c-1090 (b)	36900	900	36000	7.7E-06	10.5	7.2E-06	9.2	94.0	0.277
c-1108 (b)	36900	900	36000	2.6E-06	10.9	2.7E-06	10.4	62.8	0.098
c-1095 (b)	11700	9900	1800	3.1E-05	24.1	2.6E-05	23.7	32.1	0.060
c-1089 (b)	20700	18900	1800	1.0E-04	27.1	8.4E-05	25.8	27.2	0.220
c-1096 (b)	11700	9900	1800	9.3E-05	29.5	7.3E-05	28.2	23.9	0.176
c-1107 (b)	2700	900	1800	9.6E-05	30.2	6.8E-05	28.7	19.6	0.186
c-1092 (b)	1500	900	600	3.9E-04	36.6	2.1E-04	35.0	14.9	0.293
c-1097 (b)	10500	9900	600	2.1E-04	38.7	2.4E-04	38.6	25.4	0.180
c-1056 (x)	18900	900	18000	2.5E-06	9.4	1.5E-06	9.4	20.4	0.042
c-1057 (x)	4500	900	3600	7.1E-06	10.7	5.3E-06	10.8	13.4	0.027
c-1045 (x)	4500	900	3600	2.5E-05	20.6	2.1E-05	20.1	13.3	0.089
c-1085 (x)	20700	18900	1800	2.4E-05	22.9	2.1E-05	22.7	22.0	0.050
c-1086 (x)	38700	36900	1800	2.3E-05	23.7	1.9E-05	23.5	24.5	0.041
c-1048 (x)	10500	4500	1800	1.4E-04	32.9	1.1E-04	30.6		0.227
			3600	3.9E-06	10.0	4.2E-06	9.9		0.259
			600	9.3E-05	28.5	9.3E-05	28.5	13.9	0.306
c-1049 (x)	10500	4500	1800	1.2E-04	47.6	1.1E-04	45.9		0.119
			3600	0.0E+00	0.0	0.0E+00	0.0		0.172
			600	8.0E-05	44.5	8.0E-05	44.5	15.7	
c-1050 (x)	5699	4500	1199	1.2E-04	31.7	1.0E-04	30.8	13.5	0.131
c-1051 (x)	9900	4500	1800	9.5E-05	29.0	7.1E-05	27.7		0.163
			3600	1.9E-06	9.0	1.8E-06	9.0	17.0	0.182
c-1052 (x)	9900	4500	1800	1.1E-04	32.4	7.9E-05	30.9		0.180
			3600	0.0E+00	0.0	0.0E+00	0.0	16.1	
c-1053 (x)	6300	4500	1800	9.5E-05	29.5	7.6E-05	28.1	14.6	0.161
c-1084 (x)	2700	900	1800	7.6E-05	31.1	7.1E-05	29.8	12.4	0.121
c-1047 (x)	5400	4500	900	2.8E-04	39.1	2.6E-04	38.1	11.5	0.250

4b) T=923K

Experiment	Total Duration (s)	HIP time (s)	Duration at Target Stress (s)	Average Strain Rate (s^{-1})	Average Stress (MPa)	Strain Rate at End (s^{-1})	Stress at End (MPa)	Mean d (ECD) (μm)	Strain
c-1005 (x)	18900	900	18000	2.8E-06	11.4	2.8E-06	11.1	20.4	0.053
c-1007 (x)	36900	900	36000	8.6E-07	10.9	1.8E-06	10.6	17.6	0.035
c-1017 (x)	4500	900	3600	2.5E-06	9.7	4.0E-06	9.3	8.1	0.006
c-1014 (x)	18900	900	18000	3.2E-06	17.1	2.5E-06	16.9	15.3	0.061
c-1015 (x)	36900	900	36000	2.7E-06	21.6	2.8E-06	20.7	18.1	0.103
c-1016 (x)	4500	900	3600	3.3E-06	22.1	2.7E-06	22.1	8.0	0.014

Table 5) K and p values ($d^p - d_o^p = K\ \Delta t$) which best fit the hydrostatic grain growth kinetics for each sample material (b or x) at each temperature investigated in this study.

Temperature (K)	Powder	K ($\mu m^{-p} s^{-1}$)	p
1023	b	3.16	3
1023	x	0.338	3
923	x	0.126	3

9. Figures

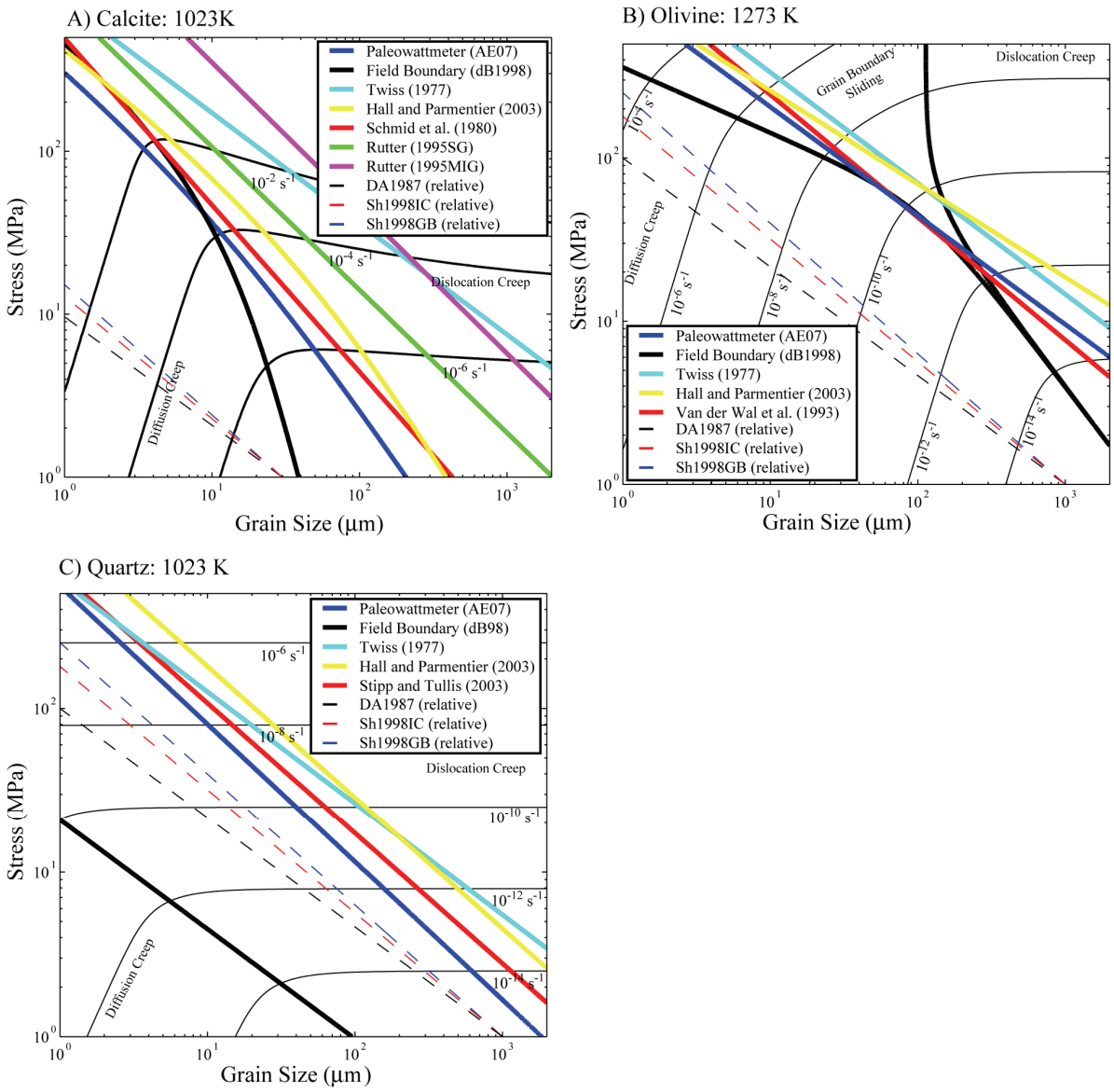


Figure 1) (see next page for caption)

Figure 1) Deformation mechanism maps for A) Calcite (T=1023), B) Olivine (T=1273K), and C) Quartz (T=1023K), showing the stabilized grain sizes predicted by the various grain size evolution relationships discussed, as well as those predicted by empirical piezometers. For the paleowattmeter (eq. 25), the same values for each parameter are used as by Austin and Evans (2007) (λ=0.1, c=π, and γ=1 J m^{-2}). The field boundary is the stable grain size predicted by de Bresser et al. (1998, 2001) (dB1998) (eq. 11). The Derby and Ashby (1989) (DA1989) (eq. 4), Shimizu (1998) intracrystalline nucleation (Sh1998IC) (eq. 6), and Shimizu (1998) grain boundary nucleation (Sh1998GB) (eq. 6) relationships are shown in terms of their apparent k values; the absolute values of the pre-exponential terms in each of these relationships are not calculated. Empirically calibrated stress-grain size relationships are also shown for each mineral: A) Calcite: Schmid et al. (1980) and Rutter (1995), B) Olivine: Van der Wal et al. (1993), and C) Quartz: Stipp and Tullis (2003), along with the relationship predicted by Twiss (1977) (eq. 1-3). Flow laws used to construct the deformation mechanism maps and to calculate the strain rate for each stress and grain size are: A) dislocation creep: Renner et al. (2002) and diffusion creep: Herwegh et al. (2003), B) Hirth and Kohlstedt (2003) for dislocation creep, grain boundary sliding, and diffusion creep, and C) Hirth et al. (2001) for dislocation creep and Rutter & Brodie (2004) for diffusion creep, all assuming a composite flow law (eq. 26).

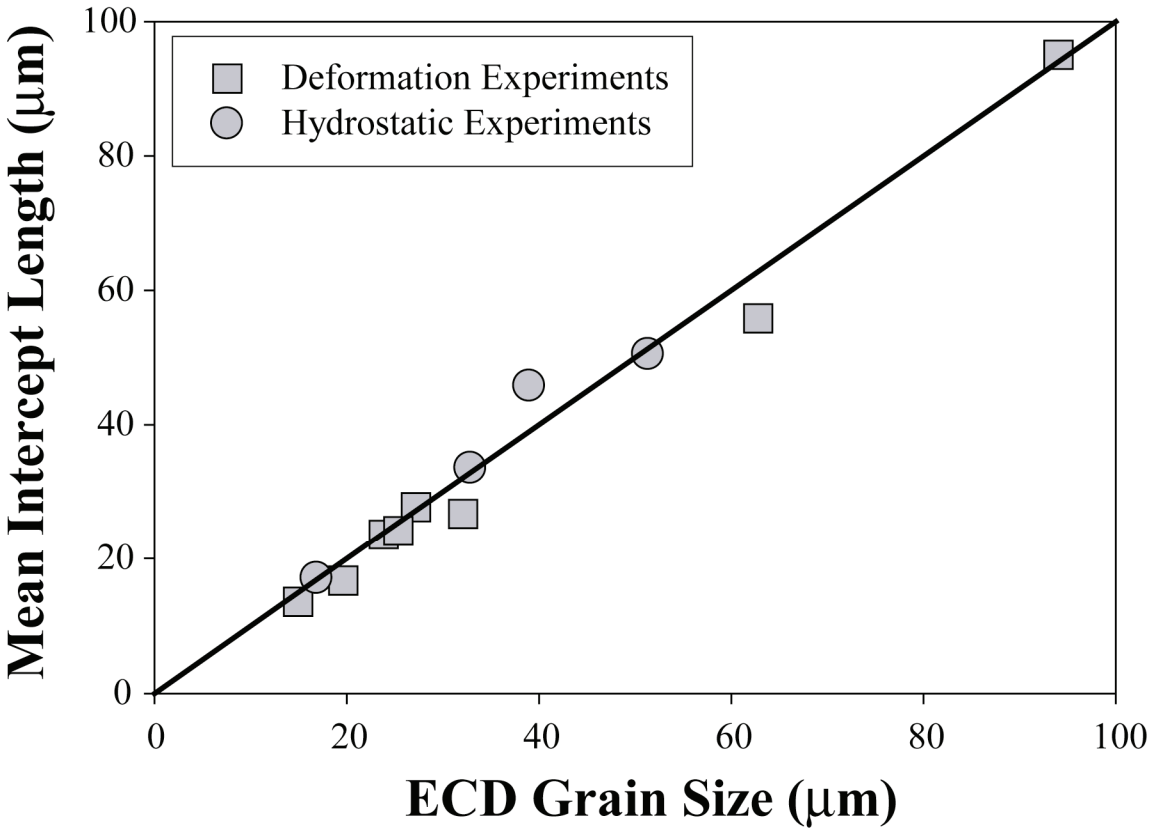


Figure 2) A comparison of the equivalent circular diameters from measured grain areas (ECD) and mean intercept lengths (powder b). The heavy black line is a 1:1 correlation. For each sample, both measurements were made on the same image. Samples which were deformed are distinguished from those heat-treated hydrostatically.

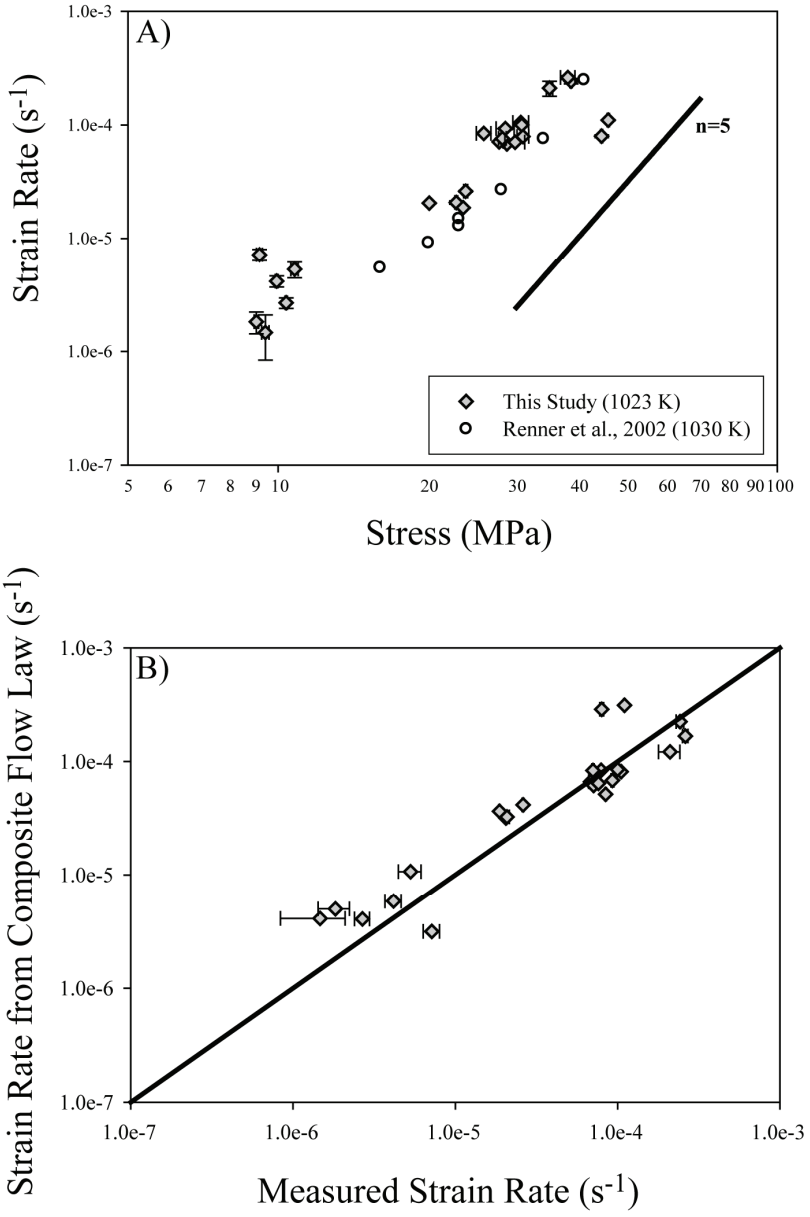


Figure 3) A) Stress – strain-rate data over the last 100s of each experiment, for deformation experiments at 1023 K. The heavy line corresponds to a stress exponent (*n*) of 5. Data from Renner et al. (2002) on a similar starting material at T=1030K are also shown. B) Comparison between our measured final strain-rates, and those predicted by a composite flow law (eq. 26) using the Renner et al. (2002) dislocation creep flow law and the Herwegh et al. (2003) diffusion creep flow law (Table 2). The stress over the 100 s and the final, measured grain size for each of our 1023K experiments are used to calculate the composite flow law strain rate. The solid line is a 1:1 correlation.

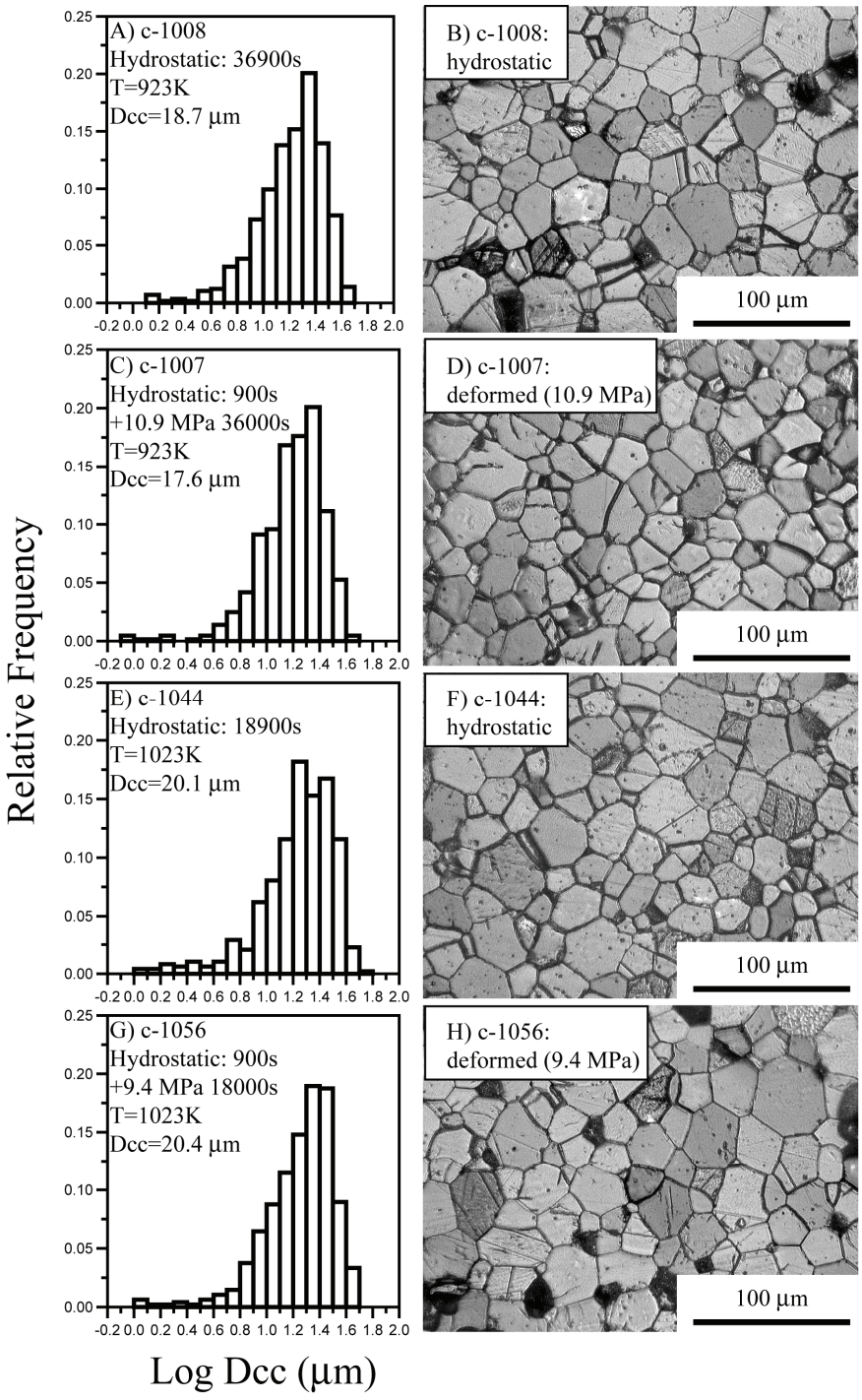


Figure 4) (see next page for caption)

Figure 4) Grain size distributions (A,C,E,G) and the corresponding reflected light micrographs of polished, etched samples (B,D,F,H respectively) for both hydrostatic experiments and samples deformed at a differential stress of ~10 MPa at both 923 K and 1023 K. The experimental conditions for each experiment are listed in tables 3 and 4, and are summarized in the figure. D_{cc} is the mean calcite grain size (ECD) in μm. For deformed samples, the average stress over the experiment is shown, along with the duration of HIP prior to deformation (hydrostatic) and the duration of the deformation step (both in s). A) and B) are a hydrostatic experiment, run for 36900 s on powder x at 923 K, whereas C) and D) are from a sample of powder x HIPed for 900 s after which it was deformed at a differential stress of 10.9 MPa for 36000 s to a strain of 0.035 at 923 K. E) and F) are a hydrostatic experiment run on powder x for 18900 s at 1023 K, whereas G) and H) are from a sample of powder x HIPed for 900 s after which it was deformed at a differential stress of 9.4 MPa for 18000 s to a strain of 0.042 at 1023 K. In all micrographs, the loading direction was vertical.

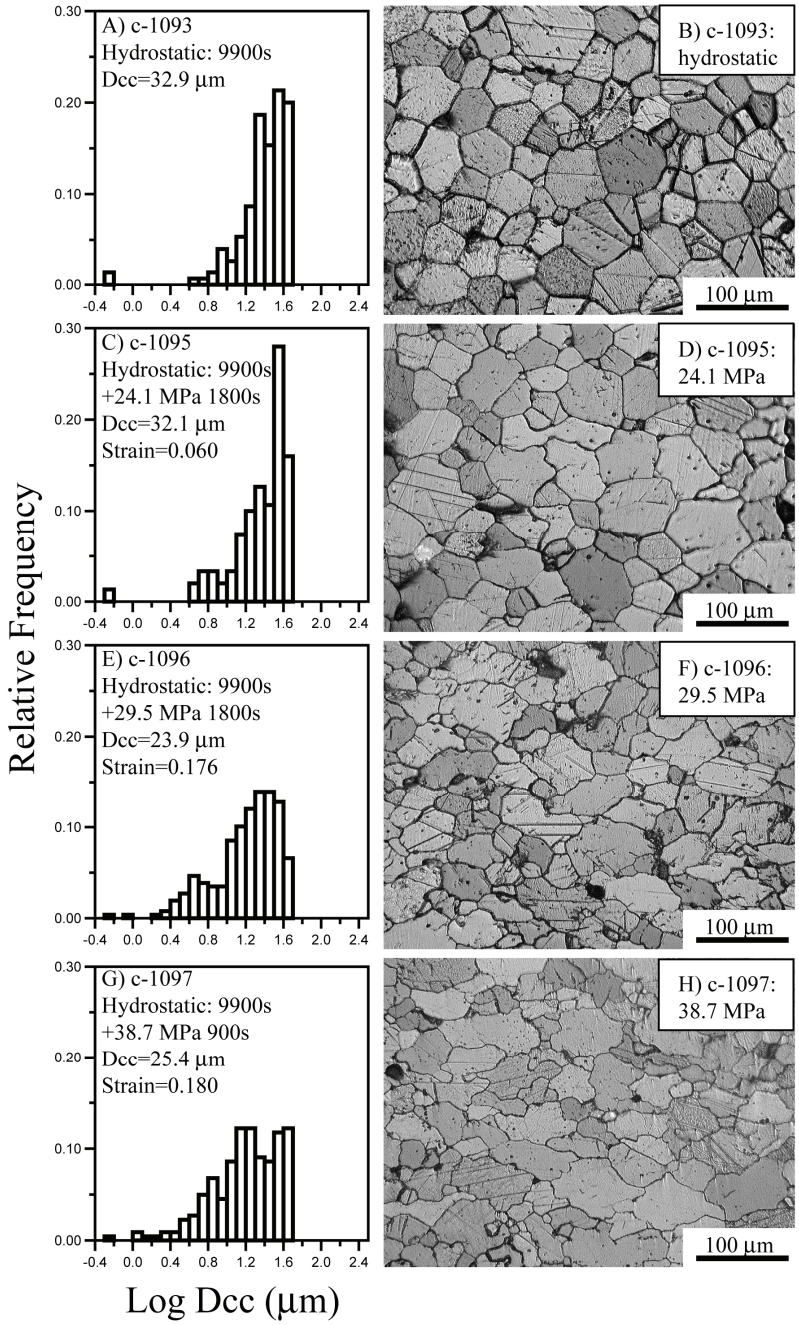


Figure 5) Grain size distributions and reflected light micrographs of samples of powder b, all at 1023 K. Details of the experimental conditions are listed in tables 3 and 4. A) and B) were HIPed for 9900 s at 1023 K. This is the starting material for samples shown in C)-F), which were deformed at progressively higher stresses (in all micrographs, the loading direction was vertical). C) and D) A sample HIPed for 9900 s at 1023 K, after which it was deformed at a differential stress of 24.1 MPa for 1800 s, to a strain of 0.060. E) and F) A sample that was HIPed for 9900 s at 1023 K after which it was deformed at a differential stress of 29.5 MPa for 1800 to a strain of 0.176. G) and H) A sample that was HIPed for 9900 s at 1023 K after which it was deformed at a differential stress of 38.7 MPa for 900 s to a strain of 0.180.

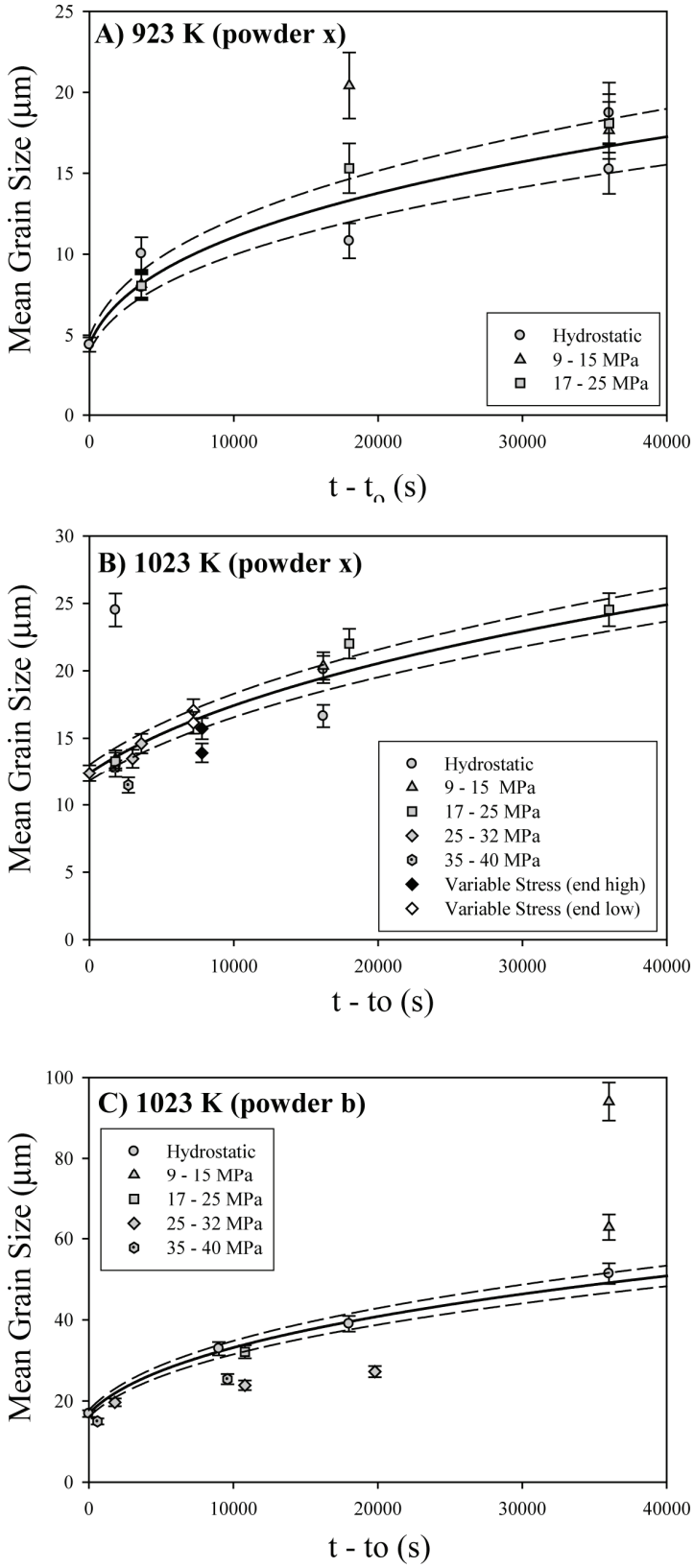


Figure 6) (see next page for caption)

Figure 6) Grain size vs. time for experiments run at A) 923 K on powder x, B) 1023 K on powder x, and C) 1023 K on powder b. Symbols are the same in each plot, and correspond to the differential stress conditions of the experiment. The solid curve is the best fit to the hydrostatic grain growth data (Table 5) for the appropriate temperature and powder, and the dashed lines are the uncertainty (10% at 923 K and 5% at 1023 K). In (B), variable stress experiments are distinguished by whether the final step was i) "low stress" or hydrostatic (expts. C-1051 and c-1052) or ii) high stress (expts. C-1048 and c-1049).

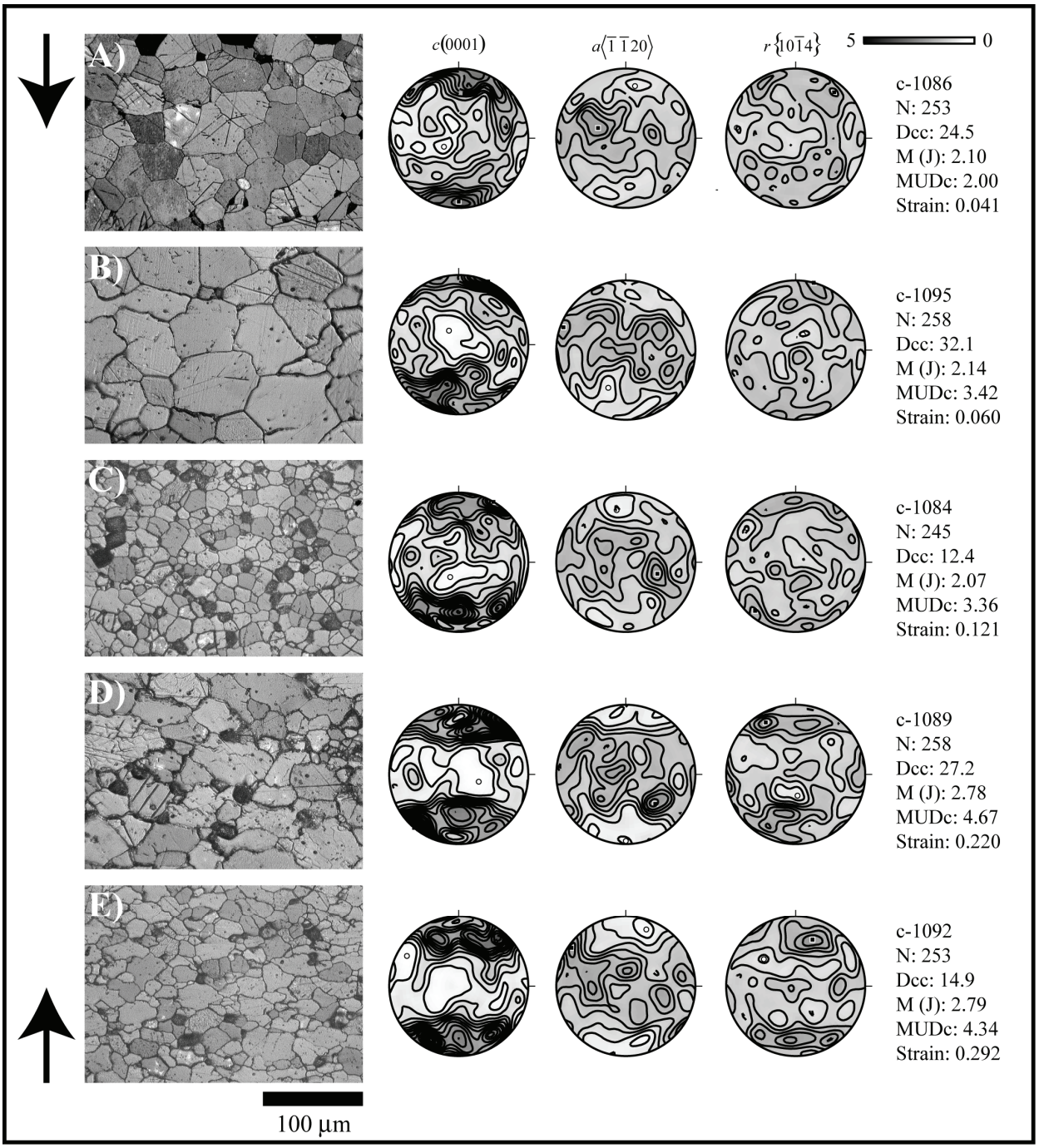


Figure 7) Reflected light micrographs and pole figures of samples deformed at 1023 K. All micrographs are to the same scale, and the compression direction during the experiments was aligned with the arrows. Pole figures are contoured at each 0.25 multiples of a uniform distribution (MUD) to a maximum MUD of 5. N is the number of grains analyzed, D_{cc} is the calcite grain size (in µm), J is the J-Index of the c-axis pole figure MUDc is the maximum MUD of the c-axis pole figure. Strain is the total strain reached in the experiment. Stress and strain-rate conditions of each experiment are listed in table 4.

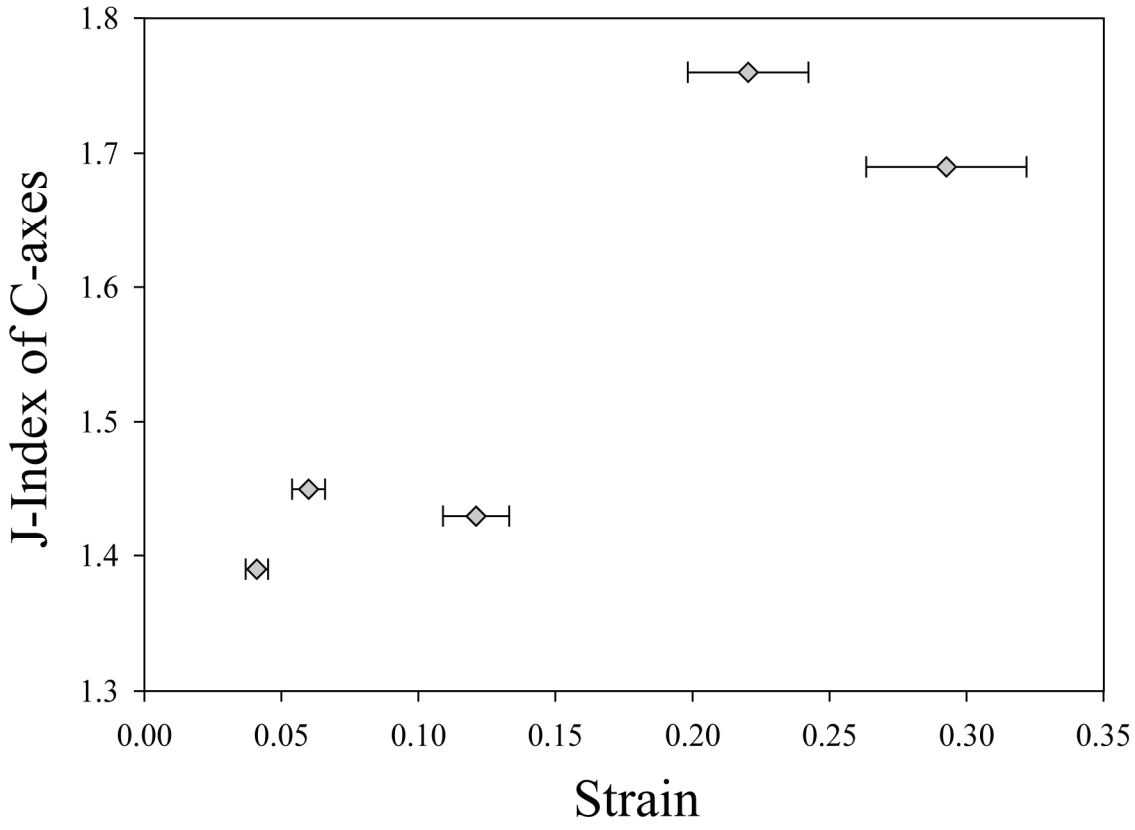


Figure 8) A plot of the J-index of the c-axis pole figure against the maximum strain reached in that experiment.

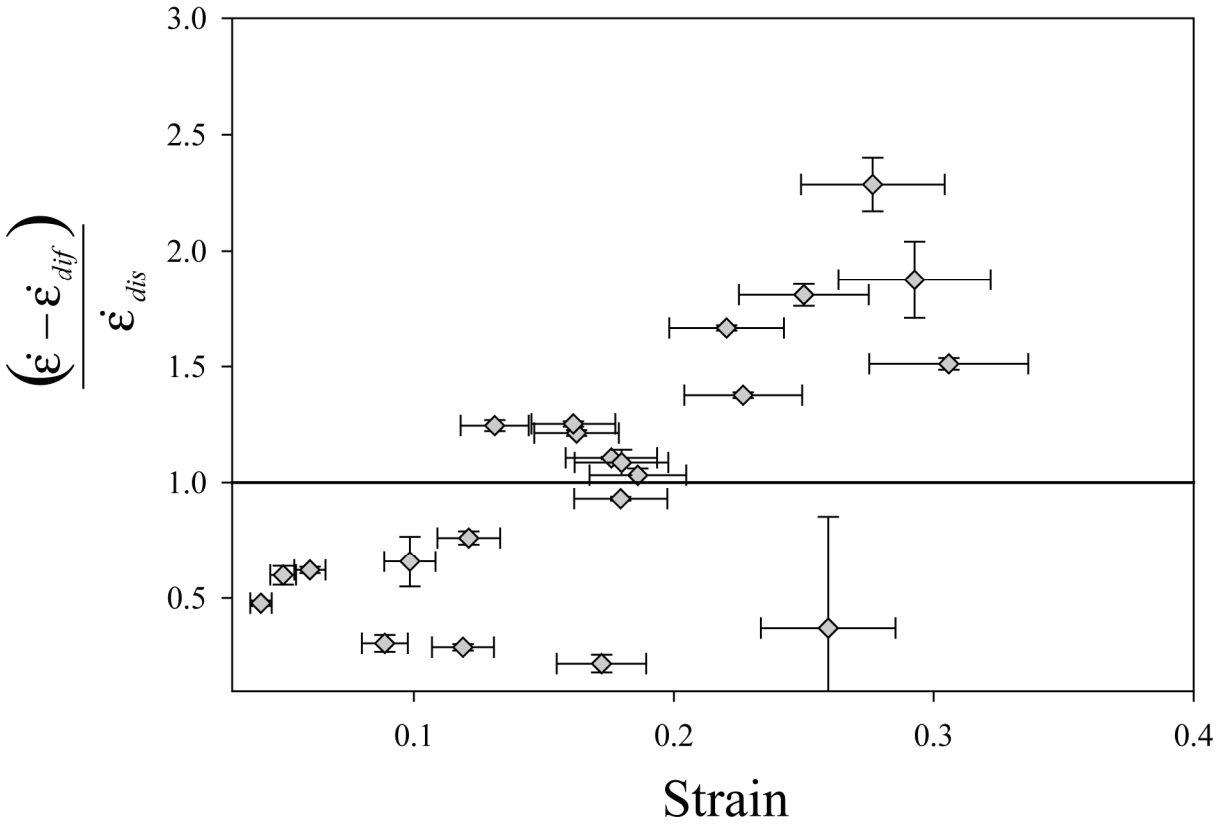


Figure 9) Measured strain-rate – diffusion creep strain rate (using the Herwegh et al. (2003) flow law) is representative of the contribution of dislocation creep to the measured strain rate. Thus dividing this value by the predicted dislocation creep rate (using the Renner et al. (2002) dislocation creep flow law) gives the relative measured dislocation creep strain rate compared the predicted rate. Values less than 1 are stronger than predicted, and values greater than 1 are weaker than predicted. Notice the progressive weakening with increasing strain.

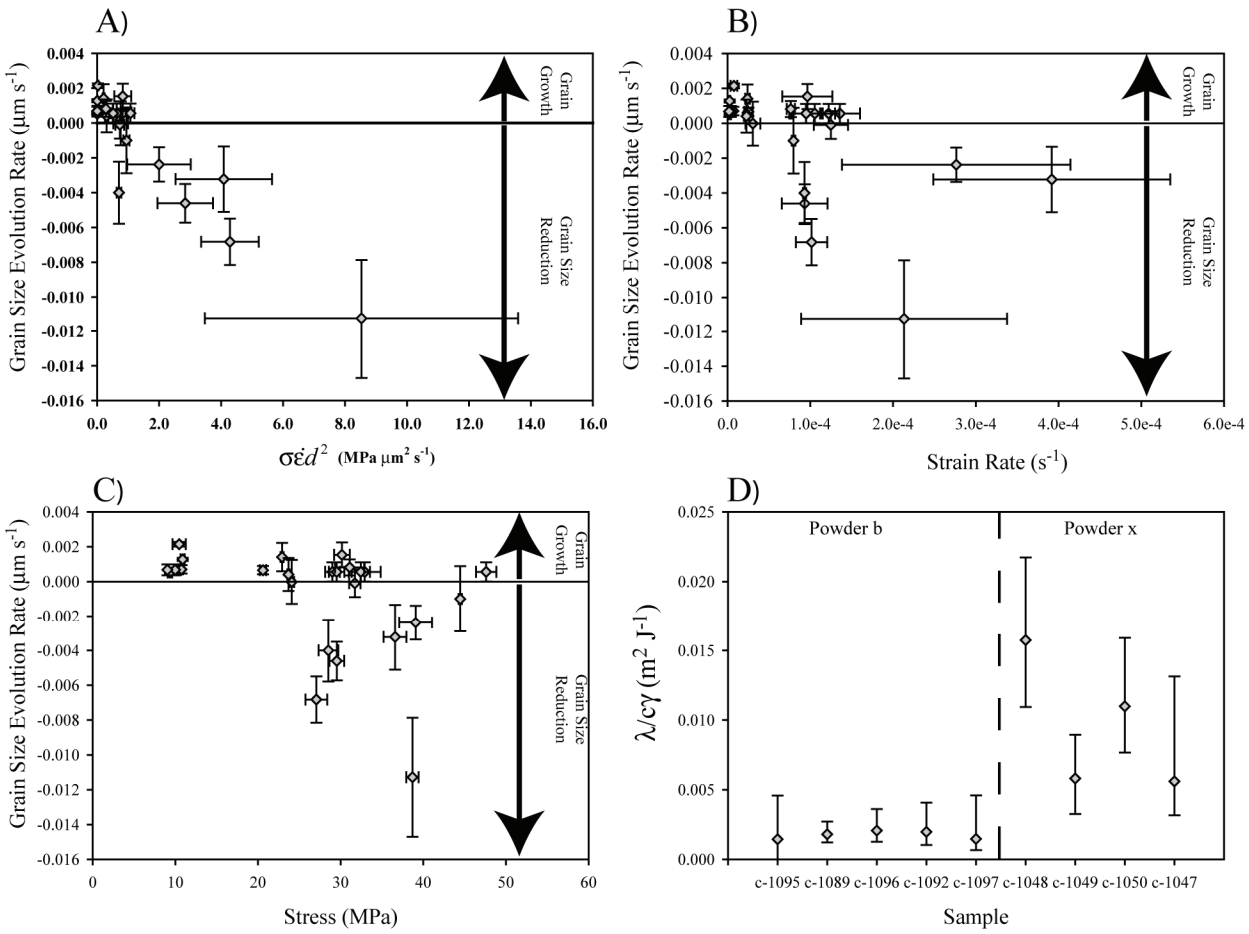


Figure 10) A) Average grain size evolution rate during our deformation experiments, obtained by comparing the initial grain size after HIPing with the final measured grain size, plotted against the product of average stress, average strain rate, and initial grain size squared. Positive grain size evolution rates correspond to grain growth, and negative values correspond to grain size reduction. B) The same grain size evolution rate plotted against the measured strain rate. C) Grain size evolution rate plotted against the measured stress. D) Estimated $\lambda/c\gamma$ values for each of the experiments where we observed grain size reduction. These were obtained using the same stress, strain rate, and grain size values as in (A), along with the grain growth parameters from Covey-Crump (1997) and a β value calculated using the dislocation creep flow law of Renner et al. (2002) and the diffusion creep flow law from Herwegh et al. (2002). Samples from the two powder are distinguished.

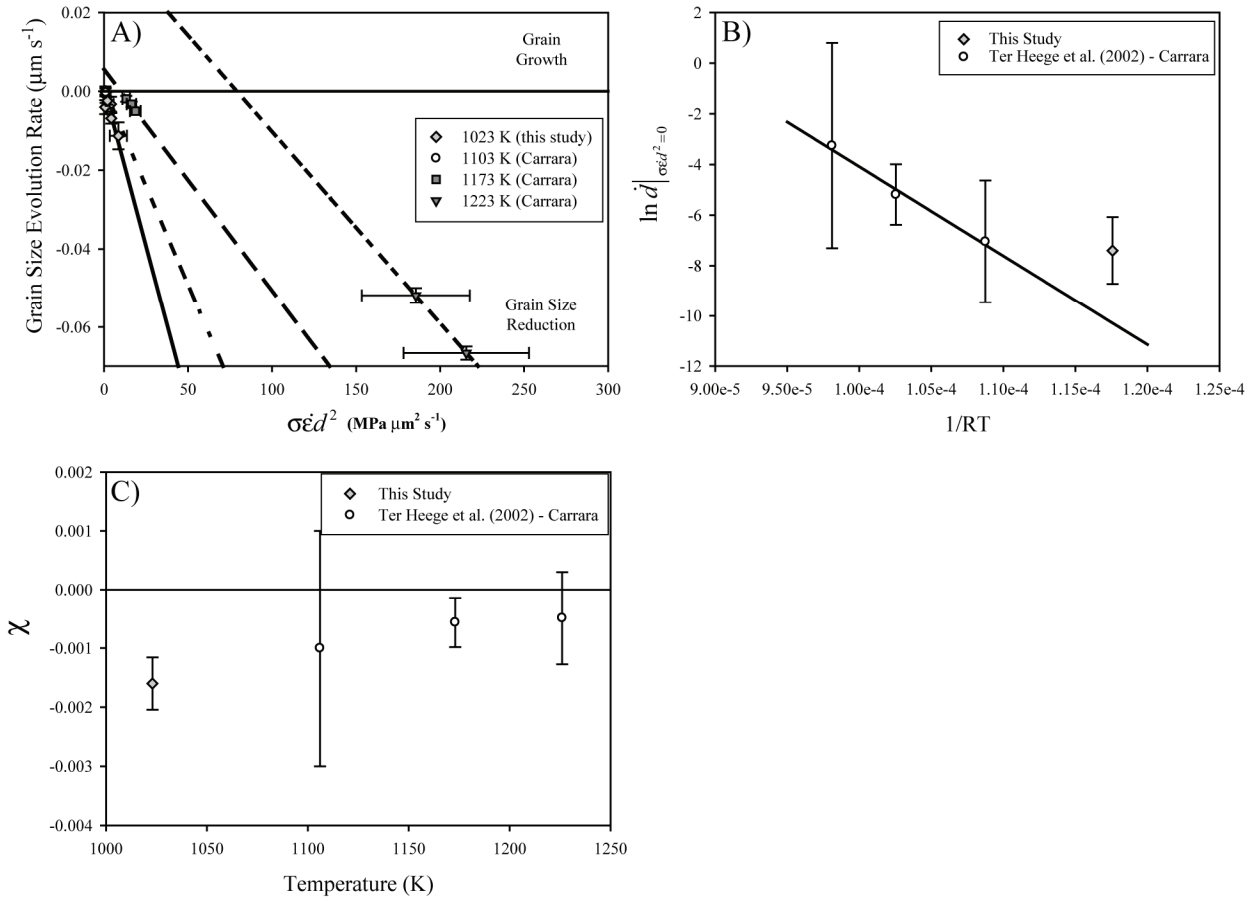


Figure 11) A) The same plot as Figure 9a, however, we have supplemented our data with that of Ter Heege et al. (2002) from deformation experiments on Carrara marble at 1103 K, 1173 K, and 1223 K. The lines plotted are the best linear fits to the data at each temperature. B) Variation in $\ln \dot{d}\big|_{\sigma\dot{\varepsilon}d^2=0}$ as a function of material and temperature. The solid line is a best fit to the Carrara data from Ter Heege et al. (2002) and corresponds to an activation energy of -352 kJ mol^{-1}. The uncertainties are significant due to the limited number of data points in (A). C) Variation in χ, also as a function of material and temperature. Uncertainties are similar to those in (B).

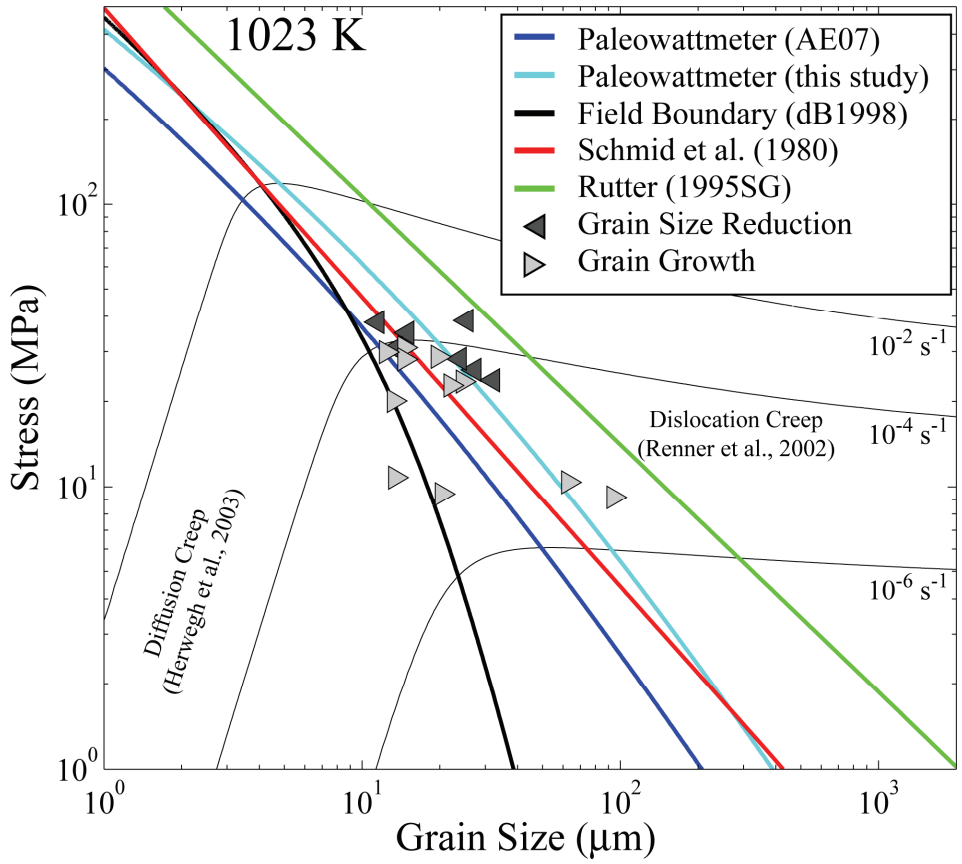


Figure 12) A calcite deformation mechanism map, constructed for our experimental conditions of 1023 K using the dislocation creep flow law from Renner et al. (2002) and the diffusion creep flow law from Herwegh et al. (2003). Our final grain sizes are plotted, indicating whether the grain size increased or decreased during the course of the experiment. Also plotted are the stress – grain-size trends for the paleowattmeter (Austin and Evans, 2007), the field boundary hypothesis (de Bresser et al., 1998&2001), the Twiss piezometer (Twiss, 1977), the Rutter (1995) piezometer, and the Schmid et al. (1980) piezometer. As in figure 1, diffusion creep strain rates are calculated using the flow law from Herwegh et al. (2003) and dislocation creep strain rates are calculated using the dislocation creep flow law from Renner et al. (2002) (Table 2).

Chapter 5

Strength Evolution and the Development of Crystallographic Preferred Orientation During Deformation of Poly-Phase Marbles

Nicholas Austin
Brian Evans
Erik Rybacki
Georg Dresen

Abstract

Deformed rocks commonly consist of more than one mineral phase, which may have dramatically different mechanical properties. In naturally deformed rocks, the deformation mechanisms of these polyphase aggregates, and in turn the strength, is commonly investigated by studying crystallographic preferred orientation (CPO) of the constituent phases. Here, we investigate the influence of varying volume fractions and geometries of rigid second phases on the strength and CPO evolution of calcite rocks using compression and torsion deformation experiments at a temperature of 1023 K, at equivalent strain rates between ~2e-6 and 1e-3 s^{-1}. The second phases are rigid carbon spheres or splinters, which are chemically inert at our experimental conditions, have a known particle size distribution, and known particle geometry. The addition of 1 vol.% spheres to calcite has little effect on either the strength or CPO development. The strength of these samples is consistent with the strength of slip in $f\langle 10\bar{1}1\rangle$ in calcite. 10 vol.% splinters increases the strength at low strains and low strain rates although has little effect on the strength at high strains and/or high strain rates, compared to pure samples. At high strains, the strength of these samples is also consistent with the strength of $f\langle 10\bar{1}1\rangle$. A similar CPO to that in pure samples is observed, although the intensity is reduced in samples containing 10 vol.% splinters. When 10 vol.% spheres are added to calcite, the strength of the aggregate is reduced, and a distinct and strong CPO develops. The strength of this material is consistent with the weaker $r\langle\bar{1}2\bar{1}0\rangle$ or $c\langle\bar{1}2\bar{1}0\rangle$ calcite slip systems. Viscoplastic self consistent calculations were used to model the evolution of CPO in these materials, and suggest that $f\langle 10\bar{1}1\rangle$ and $c\langle\bar{1}2\bar{1}0\rangle$ are necessary to produce the CPO's in pure samples, whereas $r\langle\bar{1}2\bar{1}0\rangle$ must be dominant if CPO's of samples containing 10 vol.% spheres are to be reproduced, consistent with our measured strengths. If phase and/or grain boundary sliding accommodates more strain in samples containing 10 vol.% spheres compared to other samples we investigated, then it may explain the lack of activity of the strong $f\langle 10\bar{1}1\rangle$ slip system.

1. Introduction

In order to understand lithospheric dynamics, it is essential to understand the rheology of polyphase aggregates. For example, the mid-crustal calcite mylonites of the Swiss Helvetic Alps contain between 0 and ~50% non-calcite phases, most commonly sheet silicates, quartz, or dolomite (e.g. Herwegh & Berger 2004; Ebert et al. 2007; Austin et al. in press), that latter two being mechanically much stronger than the calcite host. In the lower crust, shear zones commonly form in gabbros consisting of relatively weak plagioclase with varying proportions of much stronger clinopyroxene (e.g. Mehl & Hirth 2008), and in the lithospheric mantle, olivine is the dominant, and relatively weaker phase, containing varying proportions of stronger orthpyroxene and clinopyroxene (e.g. Warren & Hirth 2006), to cite a few examples.

The interpretation of naturally deformed mylonites is frequently complicated as, in highly deformed and recrystallized ultramylonites, it is rare to have precise constraints on the finite strain (though see Ramsay 1981; Warren et al. 2008). Further, fine-grained ultramylonites with a microstructure affected by second phases may have a crystallographic preferred orientation (CPO) that is stronger (e.g. Austin et al. in press) or weaker (e.g. Warren & Hirth 2006; Ebert et al. 2007; Mehl & Hirth 2008) than coarser grained mylonites and protomylonites.

Laboratory deformation experiments may be used to gain insight into the relationship between mechanical strength, CPO, grain size, and mineralogy in poly-phase rocks. However, it is not possible to systematically investigate every relevant, naturally occurring combination of phases and phase distributions. Further, the relative strengths of the constituent phases may vary as a function of deformation conditions (e.g. Tullis & Wenk 1994). It is, therefore, common practice to predict the mechanical behavior of the polyphase aggregate based on the properties and volume fractions of the constituent phases. Theoretical considerations usually indicate that the

strength of the aggregate is constrained between the end-member strengths of the constituent phases (Eshelby 1957; Hashin & Shtrikman 1963; Tullis et al. 1991; Ji & Zhao 1993); a conclusion which has been supported by experimental studies on a range of geologic materials (Dresen et al. 1998; Xiao et al. 2002; Rybacki et al. 2003; Dimanov & Dresen 2005; Renner et al. 2007). However, debate still exists regarding whether and/or under what circumstances, the presence of relatively stronger second phases may inhibit grain growth, thus driving deformation of the primary phase into the diffusion creep or grain boundary sliding regime leading to bulk weakening (e.g. Olgaard 1990), as opposed to acting as load supporting grains resulting in bulk strengthening (e.g. Dimanov & Dresen 2005). If, as a result of the presence of second phases, different deformation mechanisms are activated (e.g. Wheeler 1992; Mcdonnell et al. 2000), or if geometric effects are significant (Handy 1990, 1994; Ji et al. 2004; Barnhoorn et al. 2005; Holyoke & Tullis 2006a, b), then the strength of the end-member phases may be different in polyphase rocks. For example, Bruhn et al. (1999) and Ji et al. (2004) both found that the strength of polyphase aggregates may be weaker than either end-member phase. If chemical reaction occurs during deformation, the mechanical properties of the aggregate may be substantially different than predicted by end-member mixing models (e.g. White & Knipe 1978; Rutter & Brodie 1988; Stünitz & Tullis 2000; De Ronde et al. 2005; Holyoke & Tullis 2006c).

Here, our aim is to investigate the influence of shape and volume fraction of chemically inert, rigid, second phases on the mechanical properties and CPO evolution of calcite rocks by performing compression and torsion deformation experiments on synthetically prepared mixtures of calcite and rigid, glassy-carbon spheres or splinters. We suggest that this system is applicable specifically to lower green-schist facies sheer zones, where calcite deforms by crystal-plastic mechanism while quartz, dolomite, and feldspars remain brittle, and also more

generally to any scenario where a mechanically weak phase contains a relatively low volume fraction of a chemically inert, mechanically much stronger phase.

2. Methodology of Laboratory Experiments

2.1. Sample Materials

The samples used in this study were prepared from reagent-grade (>99.95% pure) synthetic calcite powder, supplied by Malinckrodt (powder (b) from Chapter 4.) The second phases are Alfa Aesar type II glassy carbon spheres (mean particle size of 4μm) and glassy carbon splinters (mean particle size of 5μm) (Fig. 1). These were chosen as they are chemically inert to a temperature of 3273 K, have known particle size distributions and particle geometries, and do not deform at the stresses and temperatures of our experiments (Young's Modulus = 35 GPa). The calcite powder was either studied as supplied, or was mixed with volume fractions of 0.011±0.002 spheres or 0.110±0.010 spheres or splinters, resulting in four different sample materials. Calcite powder was mixed with the rigid second phases by smearing known masses of each constituent on a glass platen. This approach was selected in order not to modify the particle size or shapes of the calcite or carbon powders.

The powders were cold pressed into copper capsules with an ID of 10 mm and a length of 20 mm, and a wall thickness of 0.3 mm, with a uniaxial stress of 10 MPa, producing green bodies with a porosity of 30±5% (Renner et al. 2002). 3 mm thick alumina spacers were inserted at each end of the sample assembly, which was then heated to 363 K for at least 12 hours to drive off adsorbed volatiles.

2.2. Deformation Experiments

2.2.1. Compression

Compression experiments were performed at a temperature of 1023 K and a confining pressure of 300 MPa using a Paterson-type, servocontrolled, internally heated, gas medium apparatus at

the Massachusetts Institute of Technology (MIT) (Paterson 1990; Renner et al. 2002). The samples were first pressurized to 240 MPa, and then heated at a rate of 15 K/min to the experimental temperature of 1023 K. Temperature is believed to be constant within 3 K along the length of the sample, and the set point is maintained to better than ±2 K, resulting in a total uncertainty of ±5 K. Confining pressure is constant to better then ±5 MPa during an experiment. Samples were hot isostatically pressed for a prescribed duration, usually 8100 s (Table 1, Fig. 2), with the internal pore space vented to the atmosphere in order to ensure complete densification and to control the starting grain size. Unlike when quartz is mixed with calcite aggregates, the presence of 1 vol.% or 10 vol.% glassy carbon spheres or splinters does not appear to influence the final porosity after HIPing. After 900 s at T≥823 K, the samples have compacted by >25% and no longer contain visible pores, indicating that complete densification had occurred.

After the HIP, each sample was deformed at a constant axial displacement rate until a prescribed strain was reached (Table 1). During deformation, load was measured internally, and is believed to be precise to about 20 N, or about 0.03 MPa of axial stress (Renner et al. 2002). Force was converted to stress by dividing by the cross sectional area of the sample, assuming constant volume deformation and accounting for the stiffness of the apparatus. The strength of the Cu jacket was removed from the measured load using published flow laws for Cu (Frost & Ashby 1982), which are in agreement with independent measurements of jacket strength (Renner et al. 2002). Sample dimensions are known to ±0.1 mm. We thus believe stresses are known to within 5%. Displacement is measured with two externally mounted displacement transducers to a precision of 0.3 μm. Strain is reported as natural strain ($\ln[1+\varepsilon_o]$) determined by back calculating an initial length from the final length and total displacement, after accounting for apparatus distortion. Strain is believed to be known to better than 10%. At the conclusion of all

experiments, the load was first removed to check for load cell drift. The sample was then quenched by shutting off the furnace, resulting in a temperature drop to 300 K within ~ 600 s. Once 473 K was reached, the pressure was dropped over ~1800 s.

Two sets of compression experiments were run. First, we ran a series of displacement rate - stepping experiments. Each step was run until an apparent flow stress was reached, which usually occurred at a strain of ~0.03, although in some cases, strains <0.02 or >0.09 were required (Table 1). Between each step, load was removed in order to check for load cell drift. In all stepping experiments, the displacement rate was systematically increased, until the last step, when a lower displacement rate was revisited to check for mechanical evolution of the material. Additional tests were run at constant displacement rate to a strain >0.25 in order to investigate the mechanical and microstructural evolution during deformation.

2.2.2. Torsion

Torsion experiments were run on a Paterson-type gas medium apparatus at the Geo-Forschungs-Zentrum (GFZ) in Potsdam, previously described by (Rybacki et al. 2003). This machine is similar to the one used for compression experiments, but is equipped with a torsion actuator. A detailed description of the torsion method has previously been given by (Paterson & Olgaard 1999). During the experiment, torque was measured using an internal, strain gauge-based load cell, and twist was controlled by an externally mounted transducer. No additional axial load was applied during the experiments. Due to similar calibration procedures, the uncertainties on temperature and pressure are believed to be consistent with those on the apparatus used for compression experiments at MIT (T±5 K, P±5 MPa).

Torsion experiments were run on each specimen at a temperature of 1023 K and a pressure of 400 MPa, at a constant twist rate $\left(\dot{\theta}\right)$ of either 1.73e-3 rad/s for ~18000 s or 1.21e-4 rad/s for ~259200 s. During torsion experiments, the local strain and strain rate within the sample vary

linearly from zero in the center of the specimen to a maximum at its outer edge. The maximum shear strain rate $(\dot{\gamma})$ at the outer surface of the specimen is obtained from the relation:

$$\dot{\gamma} = \dot{\theta}\left(\frac{D}{2L}\right) \tag{1}$$

Similarly, the strain at the outer surface of the specimen is given by

$$\gamma = \theta\left(\frac{D}{2L}\right) \tag{2}$$

Here, D is the sample diameter and L is the length. While shear strain rate varies linearly throughout the sample, shear stress varies non-linearly. For material creeping at steady state by power-law flow, the sensitivity of strain rate on stress (n) is

$$n = \frac{\Delta \ln \dot{\gamma}}{\Delta \ln \tau} \tag{3}$$

where τ is the shear stress. For n>>1, the majority of the torque (M) is supported by the outer-most portion of the sample, so the measured torque may be related to the torque on the outer-most portion of the sample, which corresponds to the maximum shear strain rate determined using equation 1. The (maximum) shear stress on the outer-most portion of the sample may be calculated using the relationship

$$\tau = M\frac{4\left(3 + 1/n\right)}{\pi D^3} \tag{4}$$

n=5 was used to determine shear stress from the measured torque in our experiments, consistent with the experiments described in Chapter 4 on the same material, at the same temperature.

If a von Mises constitutive relationship applies to creep deformation of rocks (e.g. Odqvist 1966; Schmid et al. 1987; Paterson & Olgaard 1999), then equivalent creep rates would be expected for equivalent values of the von Mises equivalent stress (σ_{eq})

$$\sigma_{eq} = \sqrt{\frac{1}{2}\left\{(\sigma_1 - \sigma_2)^2 + (\sigma_2 - \sigma_3)^2 + (\sigma_3 - \sigma_1)^2\right\}} \quad (5)$$

Further, creep rates under different states of stress may be compared through the relationship

$$\dot{\varepsilon}_{eq} = \sqrt{\frac{2}{9}\left\{(\dot{\varepsilon}_1 - \dot{\varepsilon}_2)^2 + (\dot{\varepsilon}_2 - \dot{\varepsilon}_3)^2 + (\dot{\varepsilon}_3 - \dot{\varepsilon}_1)^2\right\}} \quad (6)$$

As with stress, $\dot{\varepsilon}_{eq}$ is the von Mises equivalent strain rate. Thus, shear strain rate and shear stress measured in torsion experiments can be converted to equivalent stress and equivalent strain rate using the relationships $\sigma_{eq} = \sqrt{3}\tau$ and $\dot{\varepsilon}_{eq} = \dot{\gamma}/\sqrt{3}$ (Schmid et al. 1987; Paterson & Olgaard 1999; Barnhoorn et al. 2004). For samples deformed in triaxial compression, $\sigma_{eq} = \sigma_d = \sigma_1 - \sigma_3$ and $\dot{\varepsilon}_{eq} = \dot{\varepsilon}_1$.

Samples for torsion tests were initially HIPed for a prescribed duration (Table 1, Fig. 2), at T=1023 K, P=300 MPa on the apparatus at MIT, following the procedure described above. The samples were then removed from the jacket and machined into right cylinders with a diameter of 7 mm and a length of 7 mm. Two torsion samples were machined from each HIPed sample. The machined samples were inserted into a Cu jacket, with a wall thickness of 0.2 mm, and loaded between zirconia pistons. Pressure was first increased to ~320 MPa, after which temperature was increased. The furnace stabilized at the target temperature of 1023 K ~3600 s after we initially began to heat the sample, at which point the torque zero was established through repeatedly twisting the sample in both the clockwise and counterclockwise directions.

The prescribed, constant twist rate was then applied, in a counterclockwise sense, for approximately 5 full rotations, which for our sample size results in a maximum shear strain at the outer edge of the sample of ~16. During torsion experiments, slight misalignments in the sample column may lead to oscillations in the measured torque, which have a wavelength corresponding to one rotation of the sample column (Barnhoorn et al. 2004). We make no correction for this oscillation in our data set, although the amplitude of this oscillation limits the accuracy of the measurement. Measured torque was corrected for the strength of the Cu jacket using the same flow law parameters as in the compression tests. At the conclusion of each experiment, the furnace was quenched prior to unloading the specimen.

2.3. Grain-Size Analysis

Following each experiment, with the exception of the strain rate stepping experiments and one torsion experiment, the specimen was cut lengthwise, polished, and etched in 0.37% hydrochloric acid for approximately 30 s in order to enhance grain boundaries (Herwegh 2000). The polished, etched samples were imaged in reflected light. Linear intercept lengths were measured both parallel and perpendicular to the long axis of the sample, from which a mean value was calculated. No stereological correction was applied. Previous studies (Rutter et al. 1994; Chapter 4) have shown that, in their experiments, the grain size determined by mean linear intercept length is directly comparable to that determined by the mean equivalent circular diameter method.

2.4. Crystallographic Preferred Orientation

Crystallographic orientations and crystallographic preferred orientation (CPO) were determined for the samples deformed in torsion, on the same polished sections used for measuring grain size, using electron back scatter diffraction (EBSD). These sections were

prepared within 200-300 μm of the outer edge of the sample. As strain rate varies linearly through the sample, the strain and strain rate at the point of analysis were within 10% of the reported, maximum values, and the stress is believed to have been within 2% of the reported maximum stress (for n=5).

Analyses were performed using a JEOL JSM 840 SEM with HKL Channel 5+ software at the Woods Hole Oceanographic Institution, using the same working conditions described by Austin et al. (in press). In each sample >200 individual grains were manually selected by ensuring that the diffraction pattern was significantly different than neighboring analyses. Each analysis was indexed using the HKL software, accepting only fits with mean angular deviation (MAD)<1.3, and then each indexed pattern was also manually checked. Pole figures were created with the program PFch5 and inverse pole figures were created with the program IPFch5 (D. Mainprice, pers. Comm., 2007). The overall CPO intensity is quantified with the M-Index (Skemer et al. 2005).

3. Laboratory Results

3.1. Mechanical Results

3.1.1. Compression

The results of all deformation experiments are listed in table 1 and shown in figures 3 and 4. Pure samples, samples containing 1 vol.% spheres, and samples containing 10 vol.% spheres, have indistinguishable strengths during compression experiments (Figure 3,4), and the apparent stress exponent (n) in these samples is ~5 (also see Chapter 4). Within experimental uncertainty, there was no variation in strength when the initial conditions were revisited at the end of strain-rate stepping experiments. During constant displacement rate tests, pure samples continually hardened up to a strain of 0.25-0.35, whereas samples containing 1 vol.% spheres underwent a slight weakening and samples containing 10 vol.% spheres maintained an approximately

constant flow stress. At low strain rates in all compression experiments, samples containing 10 vol.% splinters are significantly stronger than any other samples investigated (Fig. 3,4), however, at these low stresses and strain rates, they have a dramatically higher apparent stress exponent (>9.0), and approach a similar strength to pure samples, or those containing 1 or 10 vol.% spheres at higher strain rates (~1e-4 s^{-1}). Upon revisiting a strain rate of 1e-5 s^{-1} at the end of the experiment, the same stress as obtained during the second step was measured. During constant displacement rate tests on samples containing 10 vol.% splinters, no work hardening or softening was observed.

3.1.2. Torsion

During torsion experiments on pure samples, a slight hardening was observed over the course of each experiment, run at shear strain rates of 8.7e-4 s^{-1} and 6.1e-5 s^{-1} (samples c-1087:1t and c-1087:2t), to shear strains of ~16. Samples containing 1 vol.% spheres had a higher yield than the pure samples at both strain rates, after which both samples underwent a period of minor weakening, followed by the onset of hardening which began at shear strains greater than ~5, resulting in samples containing 1 vol.% spheres being slightly stronger than pure samples after a shear strain of ~16.

Samples containing 10 vol.% spheres (c-1192:1t and c-1192:2t) are weaker than pure samples, or those containing 1 vol.% spheres. These samples undergo minor hardening throughout the experiment. On the other hand, samples containing 10 vol.% splinters (c-1193:1t and c-1193:2t) are initially stronger than either the pure material, or samples containing 1 vol.% spheres, however, these samples both undergo progressive weakening with increasing strain, and after a shear strain of ~16, have a strength similar to the pure materials at both strain rates investigated (6.1e-5 s^{-1} and 8.7e-4 s^{-1}).

3.1.3. Strength Comparison: Compression vs. Torsion

To compare mechanical data from axial compression experiments to that from torsion experiments, we convert all axial stresses and strain rates from compression experiments and shear stresses and strain rates from torsion experiments into equivalent stresses and strain rates using equations 5 and 6. Figure 4 shows a direct comparison between the mechanical data obtained from compression experiments at MIT and that obtained from torsion experiments at the GFZ.

The measured strengths of pure calcite, or samples containing 1 vol.% spheres, obtained from strain rate stepping experiments and compression experiments run to equivalent strains of 0.25 to 0.35 are indistinguishable from the equivalent stresses measured at similar equivalent strain rates in torsion experiments on the same materials, after a similar equivalent strain (Fig. 4). However, at the higher strains reached in torsion experiments, both of these materials are significantly stronger than the strengths measured at lower strains in compression experiments (Fig. 4).

Samples containing 10 vol.% splinters deformed in compression, both in strain rate stepping experiments and at constant displacement rate to equivalent strains of 0.23 to 0.30 also have similar strengths to samples deformed in torsion at similar equivalent strain rates to similar equivalent strains. However, samples containing 10 vol.% splinters, deformed in torsion continue to harden up to an equivalent strain of between 1 and 2, after which they progressively weaken until the maximum equivalent strain of 9.0 (Fig. 4), at which point they again have similar strengths to samples deformed in compression.

Finally, samples containing 10 vol.% spheres are initially much weaker when deformed in torsion than when deformed in compression (Fig. 4), although with increasing strain, the

strengths of these samples, deformed in torsion, approach the strengths of those deformed in compression.

Rybacki et al. (2003) compared data from torsion and compression experiments on Solnhofen limestone and on calcite-quartz aggregates, at the same nominal strain rate, and found that samples deformed in torsion had a lower flow stress than samples deformed in compression, similar to our observation on samples containing 10 vol.% spheres. They suggested that one reason for this discrepancy might be variations in the formation and evolution of CPO in torsion and compression.

The similar strengths obtained in compression and in torsion of our pure samples, samples containing 1 vol.% spheres, and 10 vol.% splinters suggest that the results of compression experiments and torsion experiments may be directly related using equivalent stresses and strain rates, and that inter-laboratory variations are small. The discrepancy between samples containing 10 vol.% spheres, deformed in compression and in torsion at the same equivalent strain may relate to differences in the yield surface and/or to other micromechanical variations between these loading geometries. For the remainder of this paper, all stresses and strain rates will be presented as equivalent stresses and equivalent strain rates, to facilitate comparison of data from compression experiments with that from torsion experiments.

3.2. Microstructural Evolution During Torsion Deformation

Twinning is apparent in all pure samples, deformed in torsion (Fig. 2), and a foliation develops at an angle of ~30º-35º to the shear plane. Samples containing 1 vol.% spheres develop a similar foliation although twinning is less apparent. There is no readily apparent difference in the distribution of the carbon spheres in any samples containing 1 vol.% spheres, when compared to the starting materials.

In samples containing 10 vol.% spheres, deformed in torsion, the carbon spheres are more homogeneously mixed throughout the samples after deformation than in the starting materials. In the sample deformed at an equivalent strain rate of 5.0e-4 s^{-1}, many more carbon spheres are found in grain interiors, and a similar, albeit weaker, foliation at ~35º to the shear plane is also observed. Twins are rare in these samples

In samples containing 10 vol.% splinters, deformed in torsion, the carbon splinters become aligned at ~30º to the shear plane (Fig. 2). Unlike in the samples containing spheres, the splinters are seldom found within grain interiors, remaining exclusively on grain boundaries. As in the samples containing 10 vol.% spheres, twins are rare in these samples.

3.3. Crystallographic Preferred Orientation

In samples deformed in torsion to an equivalent strain of ~9.0 at a temperature of 1023 K, two distinct CPO's develop as a function of the shape and volume fraction of the rigid inclusions (Fig. 5,6). One CPO is characteristic of pure samples, and is also observed in samples containing 1 vol.% spheres deformed at an equivalent strain rate of 5.0e-4 s^{-1}. This CPO is distinguished by a strong c-axis maxima normal to the shear plane (maxima 1 from Schmid et al., 1987), a secondary peak back rotated ~30º from the shear direction (maxima 3 from Schmid et al., 1987), and a-axes that are distributed approximately normal to the c-axis maxima (Fig. 5). The inverse pole figure for these samples shows concentrations of the sample axis along the crystallographic c-axis, r-poles, and f-poles (Fig. 6). The shear direction is preferentially aligned with either the $\langle 20\bar{2}1 \rangle$ direction, or normal to the c-axis, between the a-axis and $\langle 10\bar{1}0 \rangle$ direction (Fig. 6). The characteristics of this CPO are similar to those observed by Barnhoorn et al. (2004) in torsion experiments run on Carrara marble at 773 and 873 K, at equivalent strain rates between 1.7e-3 and 2.9e-5 s^{-1} to an equivalent strain >5. This CPO is composed of

$r\langle\bar{2}021\rangle^{\pm}$ and $c\langle\bar{1}2\bar{1}0\rangle^{\pm}$ orientation components (Fig. 5,6) (Barnhoorn et al. 2004). Samples containing 10 vol.% splinters develop a similar, albeit weaker, CPO to the pure samples (Fig. 5), although the sample deformed at a strain rate of 5.0e-4 s^{-1} has developed an additional c-axis maxima (maxima 2 from Schmid et al., 1987).

The second, distinct, CPO develops in samples containing 10 vol.% spheres (c-1192:1t and c-1192:2t), at both strain rates investigated (Fig. 5,6). These samples develop a single, strong, c-axis maximum normal to the shear direction and slightly inclined to the shear plane. The a-axes produce three distinct poles, separated by ~60º, with the strongest concentration aligned with the shear direction. There is no apparent alignment of $\langle 20\bar{2}1\rangle$ with the shear direction or of f-poles perpendicular to the shear plane. In the inverse pole figures (Fig. 6), there is a strong concentration of the sample axes between the r-poles and c-pole and a strong alignment of the shear direction with the a-axes. The sample deformed at an equivalent strain rate of 5.0e-4 s^{-1} (c-1192:1t) has a stronger CPO intensity, quantified using the M-Index, than the sample deformed to the same strain at an equivalent strain rate of 3.4e-5 s^{-1} (c-1192:2t). This CPO has the same characteristics as those observed in torsion experiments on Carrara marble at 1000 K to equivalent strains >2.9, with orientation components between $c\langle\bar{1}2\bar{1}0\rangle^{\pm}$ and $r\langle\bar{1}2\bar{1}0\rangle^{\pm}$ (Pieri et al. 2001a; Pieri et al. 2001b; Barnhoorn et al. 2004). There are also qualitative similarities with this pattern and that observed by Schmid et al. (1987) during deformation of Carrara Marble in the grain boundary migration regime.

Sample c-1189:2t, containing 1 vol.% spheres, deformed at an equivalent strain rate of 3.5e-5 s^{-1}, to an equivalent strain of 9.0, has a CPO intermediate between the end-member cases of the pure sample and those containing 10 vol.% spheres (Figs. 5,6). This sample has a weak

alignment of the $\langle 20\bar{2}1 \rangle$ direction in the shear plane, and has a secondary c-axis maxima back rotated from the shear direction (maxima 3) similar to the pure samples, however, the r-poles, f-poles, and a-axes resemble the patterns from samples containing 10 vol.% spheres.

4. Polycrystalline CPO Calculations

Viscoplastic self-consistent (VPSC) models have often been used to simulate the formation of CPO in calcite rocks (Lebensohn & Tome 1993; Lebensohn et al. 1998; Wenk 1999; Pieri et al. 2001b; Barber et al. 2007), and thus, we performed a series of calculations to compare with our experiments. The premise of such models is that intracrystalline deformation is accommodated by slip on a limited number of discrete planes, with defined burgers vectors. Rigid bounds in strength are defined by two end-member model types: Taylor (iso-strain) and Sachs (iso-stress) models. Taylor models (e.g. Taylor, 1938) are upper bounds for strength, in which all grains undergo the same deformation, and grain boundaries do not slip. For iso-volumetric deformation, slip on five independent systems is required (von Mises criterion). The lower-bound (Sachs) (e.g. Chastel et al., 1993) models require fewer slip systems; but do not require displacement continuity across the grain boundaries. Consequently, grains oriented for easy slip will be preferentially deformed.

Intermediate between Taylor and Sachs models are *n-site* visco-plastic self consistent models (Molinari et al. 1987; Wenk et al. 1991; Lebensohn & Tome 1993; Lebensohn et al. 1998); here, we used a "one-site" model (Molinari et al. 1987; Tommasi et al. 2000). Specifying the correct slip- or twin- systems and accurate values for the CRSS to activate each is a critical part of the simulation. Some studies of calcite deformation have also included dynamic recrystallization (Lebensohn et al. 1998; Pieri et al. 2001b), while others have not (Barber et al. 2007).

The VPSC technique considers each grain as an inclusion in a homogeneous (but anisotropic) equivalent medium (HEM) with properties defined by the average of the aggregate. As the inclusion deforms, it maintains both strain compatibility and stress equilibrium with the HEM, but interactions between neighboring grains are not considered. The interaction problem is solved using an Eshelby formulation (1957), which relates the local stresses and strain rates to the macroscopic quantities.

$$\dot{e}_{ij} - \dot{E}_{ij} = -\alpha \tilde{M}_{ijkl}\left(s_{ij} - S_{ij}\right) \tag{11}$$

where M is the Eshelby tensor, $\dot{e}$ and s refer to the microscopic von Mises equivalent strain rate and stress, and $\dot{E}$ and S are the macroscopic von Mises equivalent strain rate and stress. For all the calculations described here, α=1 (note that α=0 corresponds to the Taylor (iso-strain) model, and α=∞ corresponds to the Sachs (iso-stress) model). Following Tommasi et al. (2000), we supposed that numerical convergence had been achieved when the relative difference between the macroscopic and the average microscopic Von Mises equivalent stress and strain rate was less than 0.03. The time step is chosen such that each increment results in an equivalent strain of 0.02.

The primary, high temperature, dislocation slip systems in calcite are $r\langle\bar{2}021\rangle^{\pm}$, $c\langle\bar{1}2\bar{1}0\rangle^{\pm}$ $f\langle 10\bar{1}1\rangle^{\pm}$, $f\langle 20\bar{2}1\rangle^{-}$ (Griggs 1938; Turner et al. 1954; Griggs et al. 1960; Turner & Heard 1965; Weiss & Turner 1972; Braillon & Serughetti 1976; Paterson 1979; Spiers & Wenk 1980; De Bresser & Spiers 1990, 1993; Wang et al. 1996; Barber et al. 2007) and, only recently observed, $r\langle\bar{1}2\bar{1}0\rangle^{\pm}$ (De Bresser 2008). Bestmann et al. (2000) have suggested that $c\langle\bar{1}2\bar{1}0\rangle^{\pm}$ slip may be accommodated by duplex slip in the basal plane, consisting of components in both

the positive and negative *a* directions, although we do not consider that possibility in these calculations. At lower temperatures, slip on $f\langle 10\bar{1}1\rangle^{\pm}$ and $c\langle \bar{1}2\bar{1}0\rangle^{\pm}$ are believed to be replaced by e-twinning and $f\langle \bar{2}201\rangle^{-}$ slip (e.g. De Bresser & Spiers 1993) . For the conditions of our experiments, based on the work of de Bresser and Spiers (1990; 1993), we assume that $r\langle \bar{2}021\rangle^{\pm}$ is the easy slip system; $c\langle \bar{1}2\bar{1}0\rangle^{\pm}$ and $r\langle \bar{1}2\bar{1}0\rangle^{\pm}$ are slightly stronger, and $f\langle 10\bar{1}1\rangle^{\pm}$ is the hardest. Slip on $r\langle \bar{2}021\rangle^{\pm}$ may involve work hardening, and thus at high strains, its significance may be reduced (De Bresser & Spiers 1997). At 1023 K, the CRSS for $f\langle 20\bar{2}1\rangle^{-}$ is higher than that for $f\langle 10\bar{1}1\rangle^{\pm}$ (De Bresser & Spiers 1997). Although some twins are observed in our samples (Fig. 2), strain from that mechanism is thought to contribute little to the overall strain at high temperatures (De Bresser & Spiers 1997). Thus, we excluded it from our calculations.

Four distinct sets of CRSS values were used in our calculations, but the stress exponent for each was held constant at 5.0, consistent with our experimental observations on polycrystalline aggregates (Table 2). This value was chosen as the stress exponents for individual calcite slip systems are presently poorly constrained. Neither work hardening nor dynamic recrystallization were considered in our calculations. In all simulations, we started with 1000 randomly oriented grains and deformed the aggregate to a total equivalent strain of 2.0 (Fig. 7). Some assumptions in VPSC calculations may break down at strains >1.0 (Blackman et al. 2002), however, in our calculations, many aspects of the CPO do not stabilize until strains >1.0. Our results, at a strain of 2.0, are consistent with those of Pieri et al.(2001b) (Fig. 7) and Barber et al. (2007) (not shown) when the appropriate CRSS values are chosen.

The crystallographic orientations we obtain from VPSC using the CRSS values from De Bresser & Spiers (1997) (dB1997), either with or without $r\langle\bar{1}2\bar{1}0\rangle^{\pm}$ closely reproduce those we observe in our pure samples (Figs. 6,7). The primary difference between the calculated and observed crystallographic orientations is that, when $r\langle\bar{1}2\bar{1}0\rangle^{\pm}$ is inhibited, calculated a-axis orientations more closely reproduce those in our experiments, whereas when $r\langle\bar{1}2\bar{1}0\rangle^{\pm}$ is allowed, the f-pole and $\langle 20\bar{2}1\rangle$ patterns are matched better. Varying the strength of $r\langle\bar{1}2\bar{1}0\rangle^{\pm}$ slip did not reconcile these two observations.

On the other hand, CPO's calculated using the values of Pieri et al. (2001b), where the weak slip systems are $r\langle\bar{1}2\bar{1}0\rangle^{\pm} \pm c\langle\bar{1}2\bar{1}0\rangle^{\pm}$, more closely reproduced the pattern observed in samples containing 10 vol.% spheres (Figs. 5,7). Dynamic recrystallization was not required to produce this pattern. In our calculations, with increasing strain, the CPO does not transition from the pattern observed in pure samples to that observed at the end of the experiments in samples containing 10 vol.% spheres (Figs. 5,7). The primary difference that results from including $c\langle\bar{1}2\bar{1}0\rangle^{\pm}$ as a weak system is that, if $c\langle\bar{1}2\bar{1}0\rangle^{\pm}$ is included, the a-axes are more strongly aligned in the shear direction, and the c-axes are concentrated nearer the shear plane normal. At an equivalent strain of 2, none of our calculated crystallographic orientations produced c-axis maxima 2, and thus none reproduced the pattern of c-1193:1t, containing 10 vol.% splinters, deformed at an equivalent strain rate of 5.0e-4 s^{-1}.

5. Slip System activity and the strength of two-phase marbles

For each sample deformed in torsion, we have A) determined which slip systems were favorably oriented for slip in each grain, based on the measured crystallographic orientations and

the final applied stress in each experiment (Fig. 8), and B) estimated the strength of the sample if deformation was limited by slip on each slip system, assuming the average schmid factor for that slip system over all grains is representative of the aggregate (Fig. 9). The critical resolved shear stress for slip on each slip system discussed above was determined from the equations provided by De Bresser & Spiers (1997) which are valid for a strain rate of ~2.0e-4 to 2.0e-5 s^{-1} at our experimental temperature of 1023 K (Table 2). The CRSS of $r\langle\bar{1}2\bar{1}0\rangle^{\pm}$ slip was taken to be the same as that for $c\langle\bar{1}2\bar{1}0\rangle^{\pm}$ slip, consistent with the observations of De Bresser et al. (2008) and with our VPSC calculations (Table 2).

Presently, the stress exponent for slip on individual slip systems in calcite is poorly constrained, so we only compare the predicted shear stress to our experiments performed in torsion at a similar equivalent strain rate of ~3.5e-5 s^{-1} (Figs. 8,9). Unfortunately, the pure sample deformed in torsion at this equivalent strain rate (c-1087:2t) broke while being removed from the jacket, so we cannot calculate schmid factors for this sample.

5.1. Pure Samples and 1 vol.% Spheres

The CPO's of our pure samples or those containing 1 vol.% spheres, deformed in torsion to an equivalent strain of 9.0, at equivalent strain rates of either 5.0e-4 s^{-1} or 3.5e-5 s^{-1} are consistent with deformation accommodated by intracrystalline dislocation creep with contributions from the experimentally studied, high temperature calcite slip systems (Fig. 5,7). In the sample containing 1 vol.% spheres deformed at an equivalent strain rate of 3.5e-5 s^{-1}, most grains are oriented such that >3 slip systems are favorably oriented for slip at the measured flow stress. These are most commonly $r\langle\bar{1}2\bar{1}0\rangle^{\pm}$, $r\langle20\bar{2}1\rangle^{-}$, $c\langle\bar{1}2\bar{1}0\rangle^{\pm}$ and $f\langle10\bar{1}1\rangle^{\pm}$ (Fig. 8). The strength of this sample is consistent with the shear stress required for slip on an f plane in either

the $\langle 20\bar{2}1\rangle^{-}$ or $\langle 10\bar{1}1\rangle^{\pm}$ direction (Fig. 9). Previous authors (Goetze & Kohlstedt 1977; Paterson 1979; De Bresser & Spiers 1997) have suggested that the strength of calcite, deforming by dislocation creep, is determined by slip on $f\langle 10\bar{1}1\rangle^{\pm}$, consistent with the measured strength of this sample.

5.2. 10 vol.% Splinters

The CPO's for samples containing 10 vol.% splinters are similar to those for pure samples (Figs. 5,6). At the measured flow stresses, as in samples containing 1 vol.% spheres, >3 slip systems are favorable oriented for slip, again most commonly $r\langle\bar{1}2\bar{1}0\rangle^{\pm}$, $r\langle\bar{2}021\rangle^{\pm}$, $c\langle\bar{1}2\bar{1}0\rangle^{\pm}$ and $f\langle 10\bar{1}1\rangle^{\pm}$ (Fig. 8). Based on the average schmid factor for each slip system, and similar to the sample containing 1 vol.% spheres, the strengths of samples containing 10 vol.% splinters appear to be determined by slip on an f plane in either the $\langle 20\bar{2}1\rangle^{-}$ or $\langle 10\bar{1}1\rangle^{\pm}$ direction. At high strains, we do not detect any substantial hardening associated with the addition of rigid second phases to a calcite matrix, as would be expected by mechanical mixing models, although samples containing 10 vol.% spheres are stronger at low strains and low strain rates.

5.3. 10 vol.% Spheres

The CPO's of samples containing 10 vol.% spheres are consistant with slip on $r\langle\bar{1}2\bar{1}0\rangle^{\pm}$ and $c\langle\bar{1}2\bar{1}0\rangle^{\pm}$ accommodating most of the intracrystalline strain. These samples deform at flow stresses at which <3 slip systems are favorably oriented for slip, most commonly $r\langle\bar{1}2\bar{1}0\rangle^{\pm}$, $r\langle\bar{2}021\rangle^{\pm}$ and $c\langle\bar{1}2\bar{1}0\rangle^{\pm}$ (Fig. 8), and slip on $r\langle\bar{1}2\bar{1}0\rangle^{\pm}$ or $c\langle\bar{1}2\bar{1}0\rangle^{\pm}$ appears to be rate limiting (Fig. 9). If $r\langle\bar{2}021\rangle^{\pm}$ does not accommodate significant strain, as suggested by both

VPSC (Fig. 7) and measured crystallographic orientations for this material (Figs. 5,6) then only two slip systems can be active ($r\langle \bar{1}2\bar{1}0\rangle^{\pm}$ and $c\langle \bar{1}2\bar{1}0\rangle^{\pm}$) (Figs. 8,9).

6. Discussion

All of the experiments performed as part of this study plot near the deformation mechanism boundary between dislocation creep and diffusion creep (Renner et al. 2002; Herwegh et al. 2003) (Fig. 10). The mechanical data and the crystallographic orientations provide insight as to which slip systems were active in each sample during deformation (Fig. 8,9). When used as input into VPSC calculations, the relative slip system strengths obtained empirically by De Bresser & Spiers (1997) successfully reproduce the CPO's observed in our pure sample, in samples containing 1 vol.% spheres, and the sample containing 10 vol.% splinters deformed at an equivalent strain rate of 3.4e-5 s^{-1} (Fig. 5-7). The strengths of these samples at high strain are also consistent with slip on the (hard) $f\langle 10\bar{1}1\rangle^{\pm}$ or $f\langle \bar{2}201\rangle^{-}$ slip systems (Fig. 9), consistent with von Mises criterion (Goetze & Kohlstedt 1977; Paterson 1979; De Bresser & Spiers 1997), and in the majority of samples, at the measured flow stress, >3 families of slip systems are favorably oriented for slip (Fig. 8). Along with the measured apparent stress exponent of ~5 in pure samples and in samples containing 1 vol.% spheres, these observation suggest that deformation was accommodated by intracrystalline dislocation creep, and the slip system strengths obtained by De Bresser & Spiers (1997) appear to be consistent with our observations.

In samples containing 10 vol.% carbon spheres or splinters, some hardening associated with the addition of a strong phase to a weaker matrix is expected (Tullis et al. 1991). In the case of samples containing 10 vol.% carbon splinters, at low strain rates and low strains, this hardening is observed (Figs. 3,4), although at high strains in torsion experiments, the strengths of these samples are similar to those of pure samples (Fig. 3) and are again consistent with the stress

required for slip on $f\langle 10\bar{1}1\rangle^{\pm}$ or $f\langle\bar{2}201\rangle^{-}$. These samples containing 10 vol.% splinters also have a much higher apparent stress exponent (n>9.0) than pure samples (n~5.0), particularly at low stresses and strain rates. As a result, samples containing 10 vol.% splinters are stronger than pure samples at low strain rates, but this hardening is diminished at higher strain rates, and the apparent stress exponent of samples containing 10 vol.% splinters approaches that of pure samples as the strengths converge (Fig. 4). This decrease in the apparent n with increasing stress and strain rate in samples containing 10 vol.% splinters is opposite to the common observation of increased n with increasing stress and strain rate (Rutter 1974; Schmid et al. 1980; Schmid et al. 1987). Presently the reason for this discrepancy is not clear, although it must somehow relate to the geometry of the rigid second phase as samples containing 10 vol.% spheres have an apparent stress exponent of ~5.

Samples containing 10 vol.% spheres do not exhibit any strengthening associated with the presence of rigid inclusions, and in fact, when this material is deformed in torsion it is weaker than the pure material or that containing 10 vol.% splinters. However, again the measured strengths and measured crystallographic orientations produce a consistent picture. The measured strengths of these samples are consistent with the strength of the weaker $c\langle\bar{1}2\bar{1}0\rangle^{\pm}$ and $r\langle\bar{1}2\bar{1}0\rangle^{\pm}$ slip systems (Fig. 9), both of which VPSC calculations suggest must be active in order to reproduce the measured CPO, which is dominated by $c\langle\bar{1}2\bar{1}0\rangle^{\pm}$ and $r\langle\bar{1}2\bar{1}0\rangle^{\pm}$ orientation components (Fig. 5-7). Further, the crystallographic orientations and measured flow stress in these samples suggest that <3 families of slip systems could be active: at the applied flow stress, very few grains are suitably oriented for slip on either $f\langle 10\bar{1}1\rangle^{\pm}$ or $f\langle\bar{2}201\rangle^{-}$ (Fig.

8), and there is no $\langle 20\bar{2}1\rangle$ component in the CPO (Fig. 6). Thus, unlike in pure samples, where the strength is determined by the stress required for slip on the "hard" $f\langle 10\bar{1}1\rangle^{\pm}$ or $f\langle\bar{2}201\rangle^{-}$ slip system, in samples containing 10 vol.% spheres deformed in torsion, the strength is determined by the stress required for slip on the "easy" $r\langle\bar{1}2\bar{1}0\rangle^{\pm}$ or $c\langle\bar{1}2\bar{1}0\rangle^{\pm}$ slip systems.

If the relative slip system strengths do not change with varying second phase particle shape, which seems unlikely, then the number of slip systems required to accommodate strain must be reduced (e.g. von Mises criterion is relaxed). This may occur if deformation is heterogeneous, if there is strain incompatibility (such as dilation), or if an additional strain accommodating mechanism becomes active. While the first two possibilities cannot be ruled out, the microstructures of samples containing 10 vol.% spheres do not suggest anomalously heterogeneous deformation, nor is there any evidence of dilation in these samples (Fig. 2). Chemical effects associated with the presence of the glassy carbon particles, such as enhanced diffusion along calcite-carbon boundaries (e.g. Mcdonnell et al. 2000) or changes in vacancy concentration in the calcite, also seem unlikely, due to the dramatically different behavior as a function of the shape of the carbon particles at the same volume fraction (10%), for chemically identical materials. Therefore, we consider the possibility that an additional strain accommodating mechanism is active in samples containing 10 vol.% spheres.

One possible mechanism is dislocation creep accommodated phase boundary sliding on the weak calcite-carbon boundaries, coupled with grain-boundary sliding on calcite-calcite boundaries. Schmid et al. (1980) and Rutter (1995) both observed shear displacements on grain boundaries after deformation experiments on Carrara marble, which may have accommodated up to 50% of the total strain, and a grain boundary sliding mechanism has also been proposed for

calcite based on mechanical data (Walker et al. 1990; Rutter et al. 1994). The switch from a strength close to the "hard" $f\langle 10\bar{1}1\rangle^{\pm}$ or $f\langle \bar{2}201\rangle^{-}$ slip systems in pure samples to a strength close to the "easy" $r\langle \bar{1}2\bar{1}0\rangle^{\pm}$ and/or $c\langle \bar{1}2\bar{1}0\rangle^{\pm}$ slip systems in samples containing 10 vol.% spheres may also be consistent with a grain boundary sliding mechanism contributing to strain in these samples. For example, during dislocation creep accommodated grain boundary sliding in olivine, the strength appears to be controlled by slip on the "easy" (010)[100] slip system, whereas when strain is accommodated by intracrystalline dislocation creep, the strength is closer to the "hard" (010)[001] slip system (Hirth & Kohlstedt 2003).

If grain boundary sliding is active in samples containing 10 vol.% spheres, it is inhibited in samples containing 10 vol.% splinters. These samples also have a weaker CPO than any other samples investigated, despite their fine grain size and elevated strength. The lower CPO intensities may result from dislocation pile-ups around the carbon splinters, which act to increase the effective size of the rigid inclusion, thus inhibiting CPO formation (Humphreys & Kalu 1990), although detailed TEM work is required to quantify this. Also, pinning of grain boundaries by the carbon splinters will inhibit grain rotations, thus slowing CPO formation. Elongate particles exert a greater pinning force than spherical particles (Ryum et al. 1983), consistent with both the weaker CPO's and greater strengths in samples containing carbon splinters than in samples containing a similar volume fraction of carbon spheres.

Notwithstanding any speculation regarding additional deformation mechanisms, it is important to emphasize that in all of the samples studied here, the measured strengths are consistent with the measured crystallographic orientations in the respective experiments and the slip system strengths obtained empirically by De Bresser & Spiers (1997), suggesting that the strength of calcite rocks is determined by the stress required for slip on the strongest slip system required to

accommodate strain. A transition in strength and in CPO occurs as a function of both the volume fraction and shape of the rigid second phase after a similar strain at constant temperature and strain rate. The shape of rigid second phases thus plays a significant role in both the strength and CPO evolution of calcite rocks. The geometry as well as the mechanical properties of all phases, must be considered when estimating the strength of poly-phase rocks.

7. Conclusions

Several conclusions may be drawn from this study:

1) The von Mises equivalent stress measured during torsion experiments on synthetic calcite rocks is directly comparable to that from compression experiments at the same equivalent strain rate.
2) Samples containing 10 vol.% splinters are stronger than pure samples at low strain rates, but have a higher apparent stress exponent, which decreases with increasing strain rate, resulting in similar strength of these two materials at high strain rates. On the other hand, in torsion experiments samples containing 10 vol.% spheres are weaker than pure samples.
3) VPSC calculations using the relative CRSS values proposed by De Bresser & Spiers (1997) successfully reproduce CPO's in pure synthetic limestones that have deformed by intracrystalline dislocation creep. The importance of $r\langle\bar{1}2\bar{1}0\rangle^{\pm}$ slip during intracrystalline dislocation creep cannot be determined, although $c\langle\bar{1}2\bar{1}0\rangle^{\pm}$ and $r\langle20\bar{2}1\rangle^{\pm}$ slip are necessary to reproduce experimentally obtained CPO's. The bulk strength of these samples is well explained by the stress required for slip on $f\langle10\bar{1}1\rangle^{\pm}$ or $f\langle\bar{2}201\rangle^{-}$. Samples containing 1 vol.% spheres have similar mechanical characteristics to pure samples, and develop a similar CPO.

4) Samples containing 10 vol.% spheres, deformed at the same temperature and strain rate, and to the same strain as pure samples develop a distinct CPO, that is characterized by $r\langle\bar{1}2\bar{1}0\rangle^{\pm}$ and $c\langle\bar{1}2\bar{1}0\rangle^{\pm}$ orientation components. VPSC calculations suggest that $r\langle\bar{1}2\bar{1}0\rangle^{\pm}$ slip must be operative to produce this CPO. The strength of these samples is also well explained by slip on $c\langle\bar{1}2\bar{1}0\rangle^{\pm}$ or $r\langle\bar{1}2\bar{1}0\rangle^{\pm}$.

5) In samples containing 10 vol.% spheres, the strength is determined by slip on the "easy" slip system, whereas, in pure samples the strength is determined by slip on the "hard" slip system. This transition apparently suggests that von Mises criterion has been relaxed, which may require an additional strain accommodating mechanism. One possibility is that grain- or phase- boundary sliding is enhanced by the presence of spherical particles, although many more experiments are required to identify any additional deformation mechanism.

6) The strength and CPO of poly-phase rocks are sensitive to both the volume fraction of rigid second phases, and the geometry of these second phases. Both of these parameters must be considered when estimating the strength of naturally deformed rocks.

8. Acknowledgements

We would like to thank Michael Naumann, Uli Mok, and Xiaohui Xiao for their extensive help in the laboratory. Jock Hirst and the machine shop at the GFZ helped with sample preparation. Discussions with Greg Hirth, William Durham, Peter Kelemen, and Timothy Grove greatly improved this manuscript. This work was funded by the National Science Foundation grants EAR0309510, EAR0510412, and OCE0452787and by the MIT student research fund.

9. References

Austin, N., Evans, B., Herwegh, M.&Ebert, A. in press: Strain Localization in the Morcles Nappe (Helvetic Alps, Switzerland). Swiss Journal of Geosciences.

Barber, D., Wenk, H., Gomez-Barreiro, J., Rybacki, E.&Dresen, G. 2007: Basal slip and texture development in calcite: new results from torsion experiments. Physics and Chemistry of Minerals **34**(2): 73-84.

Barnhoorn, A., Bystricky, M., Burlini, L.&Kunze, K. 2004: The role of recrystallisation on the deformation behaviour of calcite rocks: large strain torsion experiments on Carrara marble. Journal of Structural Geology **26**(5): 885-903.

Barnhoorn, A., Bystricky, M., Kunze, K., Burlini, L.&Burg, J. 2005: Strain localisation in bimineralic rocks: Experimental deformation of synthetic calcite–anhydrite aggregates. Earth and Planetary Science Letters **240**(3-4): 748-763.

Bestmann, M., Kunze, K.&Matthews, A. 2000: Evolution of a calcite marble shear zone complex on Thassos Island, Greece: microstructural and textural fabrics and their kinematic significance. Journal of Structural Geology **22**(11-12): 1789-1807.

Blackman, D., Wenk, H.&Kendall, J. 2002: Seismic anisotropy of the upper mantle: 1. Factors that affect mineral texture and effective elastic properties. Geochem. Geophys. Geosyst **3**(9): 8601.

Braillon, P.&Serughetti, J. 1976: Mechanical twinning in calcite. Phys. Status Solidi A **33**: 405-413.

Bruhn, D. F., Olgaard, D. L.&Dell'Angelo, L. N. 1999: Evidence for enhanced deformation in two-phase rocks; experiments on the rheology of calcite-anhydrite aggregates. Journal of Geophysical Research, B, Solid Earth and Planets **104**(1): 707-724.

Chastel, Y., Dawson, P., Wenk, H.&Bennett, K. 1993: Anisotropic convection with implications for the upper mantle. Journal of Geophysical Research **98**(B10): 17,757-17,771.

de Bresser, J.&Spiers, C. 1990: High-temperature deformation of calcite single crystals by r+ and f+ slip. Geological Society London Special Publications **54**(1): 285-298.

de Bresser, J.&Spiers, C. 1993: Slip systems in calcite single crystals deformed at 300–800 C. Journal of Geophysical Research **98**(B4): 6397-6409.

de Bresser, J. 2008: Evidence for r< a> slip in calcite. European Union of Geosciences conference.

de Bresser, J. H. P.&Spiers, C. J. 1997: Strength characteristics of the r, f, and c slip systems in calcite. Tectonophysics **272**(1): 1-23.

de Ronde, A., Stünitz, H., Tullis, J.&Heilbronner, R. 2005: Reaction-induced weakening of plagioclase–olivine composites. Tectonophysics **409**(1-4): 85-106.

Dimanov, A.&Dresen, G. 2005: Rheology of synthetic anorthite-diopside aggregates: Implications for ductile shear zones. Journal of Geophysical Research **110**(B7).

Dresen, G., Evans, B.&Olgaard, D. 1998: Effect of quartz inclusions on plastic flow in marble. Geophysical Research Letters **25**(8): 1245-1248.

Ebert, A., Herwegh, M., Evans, B., Pfiffner, A., Austin, N.&Vennemann, T. 2007: Microfabrics in carbonate mylonites along a large-scale shear zone (Helvetic Alps). Tectonophysics **444**(1-4): 1-26.

Eshelby, J. 1957: The Determination of the Elastic Field of an Ellipsoidal Inclusion, and Related Problems. Proceedings of the Royal Society of London. Series A, Mathematical and Physical Sciences (1934-1990) **241**(1226): 376-396.

Frost, H.&Ashby, M. 1982: Deformation-Mechanism Maps: The Plasticity and Creep of Metals and Ceramics, Pergamon Press.

Goetze, C.&Kohlstedt, D. 1977: The dislocation structure of experimentally deformed marble. Contributions to Mineralogy and Petrology **59**(3): 293-306.

Griggs, D., Turner, F.&Heard, H. 1960: Deformation of rocks at 500 to 800 C. Geol. Soc. Am. Mem **79**: 39-104.

Griggs, D. T. 1938: Deformation of single calcite crystals under high confining pressures. American Mineralogist **23**(1): 28-33.

Handy, M. 1990: The solid-state flow of polymineralic rocks. Journal of Geophysical Research **95**(B6): 8647-8661.

Handy, M. 1994: Flow laws for rocks containing two non-linear viscous phases: a phenomenological approach. Journal of Structural Geology **16**(3): 287-301.

Hashin, Z.&Shtrikman, S. 1963: A variational approach to the theory of the elastic behavior of multiphase materials. J. Mech. Phys. Solids **11**(2): 127-140.

Herwegh, M. 2000: A new technique to automatically quantify microstructures of fine grained carbonate mylonites: two-step etching combined with SEM imaging and image analysis. Journal of Structural Geology **22**(4): 391-400.

Herwegh, M., Xiao, X.&Evans, B. 2003: The effect of dissolved magnesium on diffusion creep in calcite. Earth and Planetary Science Letters **212**(3-4): 457-470.

Herwegh, M.&Berger, A. 2004: Deformation mechanisms in second-phase affected microstructures and their energy balance. Journal of Structural Geology **26**(8): 1483-1498.

Hirth, G.&Kohlstedt, D. 2003: The rheology of the upper mantle and the mantle wedge: A view from the experimentalists. Inside the Subduction Factory. Eiler, J., American Geophysical Union. **138:** 83-105.

Holyoke, C.&Tullis, J. 2006a: Mechanisms of weak phase interconnection and the effects of phase strength contrast on fabric development. Journal of Structural Geology **28**(4): 621-640.

Holyoke, C.&Tullis, J. 2006b: Formation and maintenance of shear zones. Geology **34**(2): 105-108.

Holyoke, C.&Tullis, J. 2006c: The interaction between reaction and deformation: an experimental study using a biotite+ plagioclase+ quartz gneiss. Journal of Metamorphic Geology **24**(8): 743-762.

Humphreys, F.&Kalu, P. 1990: The Plasticity of Particle-Containing Polycrystals. Acta Metall. Mater. **38**(6): 917-930.

Ji, S.&Zhao, P. 1993: Flow laws of multiphase rocks calculated from experimental data on the constituent phases. Earth and Planetary Science Letters **117**(1-2): 181-187.

Ji, S., Jiang, Z., Rybacki, E., Wirth, R., Prior, D.&Xia, B. 2004: Strain softening and microstructural evolution of anorthite aggregates and quartz–anorthite layered composites deformed in torsion. Earth and Planetary Science Letters **222**(2): 377-390.

Lebensohn, R.&Tome, C. 1993: A Self-Consistent Anisotropic Approach for the Simulation of Plastic Deformation and Texture Development of Polycrystals. Acra Metnll. Mater **41**: l-2624.

Lebensohn, R., Wenk, H.&Tomé, C. 1998: Modelling deformation and recrystallization textures in calcite. Acta Materialia **46**(8): 2683-2693.

McDonnell, R., Peach, C., van Roermund, H.&Spiers, C. 2000: Effect of varying enstatite content on the deformation behavior of fine-grained synthetic peridotite under wet conditions. J Geophys Res **105**: 13535-13553.

Mehl, L.&Hirth, G. 2008: Plagioclase preferred orientation in layered mylonites: Evaluation of flow laws for the lower crust. J. Geophys. Res **113**.

Molinari, A., Canova, G.&Azhy, S. 1987: A self-consitent approach of the large deformation polycrystal viscoplasticity. Acta Metallurgica **35**: 2983-2994.

Odqvist, F. 1966: Mathematical Theory of Creep and Creep Rupture, Oxford University Press.

Olgaard, D. 1990: The role of second phase in localizing deformation. Geological Society London Special Publications **54**(1): 175.

Paterson, M. 1979: Deformation Mechanisms in Carbonate Crystals. Physics of Materials (A festschrift for Dr. Walter Boas), CSIRO and University of Melbourne, Melbourne: 199-208.

Paterson, M. 1990: Rock deformation experimentation. AGU Geophysical Monograph **56**: 187-194.

Paterson, M. S.&Olgaard, D. L. 1999: Rock deformation tests to large shear strains in torsion. Journal of Structural Geology **22**(9): 1341-1358.

Pieri, M., Burlini, L., Kunze, K., Stretton, I.&Olgaard, D. L. 2001a: Rheological and microstructural evolution of Carrara Marble with high shear strain; results from high temperature torsion experiments. Journal of Structural Geology **23**(9): 1393-1413.

Pieri, M., Kunze, K., Burlini, L., Stretton, I., Olgaard, D. L., Burg, J. P.&Wenk, H. R. 2001b: Texture development of calcite by deformation and dynamic recrystallization at 1000 K during torsion experiments of marble to large strains. Tectonophysics **330**(1-2): 119-140.

Ramsay, J. 1981: Tectonics of the Helvetic Nappes. Geological Society London Special Publications **9**(1): 293.

Renner, J., Evans, B.&Siddiqi, G. 2002: Dislocation creep of calcite. J. Geophys. Res **107**: 1-16.

Renner, J., Siddiqi, G.&Evans, B. 2007: Plastic flow of two-phase marbles. Journal of Geophysical Research **112**(B7).

Rutter, E. 1974: The influence of temperature, strain rate and interstitial water in the experimental deformation of calcite rocks. Tectonophysics **22**(3-4): 311-334.

Rutter, E.&Brodie, K. 1988: Experimental approaches to the study of deformation/metamorphism relationships. Mineralogical Magazine **52**(364): 35-42.

Rutter, E. 1995: Experimental study of the influence of stress, temperature, and strain on the dynamic recrystallization of Carrara marble. Journal of Geophysical Research **100**(B12): 24651-24664.

Rutter, E. H., Casey, M.&Burlini, L. 1994: Preferred crystallographic orientation development during the plastic and superplastic flow of calcite rocks. Journal of Structural Geology **16**(10): 1431-1446.

Rybacki, E., Paterson, M., Wirth, R.&Dresen, G. 2003: Rheology of calcite-quartz aggregates deformed to large strain in torsion. Journal of Geophysical Research **108**(10.1029).

Ryum, N., Hunderi, O.&Nes, E. 1983: On grain boundary drag from second phase particles. Scripta Metallurgica **17**(11): 1281-1283.

Schmid, S., Paterson, M.&Boland, J. 1980: High temperature flow and dynamic recrystallization in Carrara marble. Tectonophysics **65**(3): 4.

Schmid, S., Panozzo, R.&Bauer, S. 1987: Simple shear experiments on calcite rocks: rheology and microfabric. Journal of Structural Geology **9**(5-6): 747-778.

Skemer, P., Katayama, I., Jiang, Z.&Karato, S. 2005: The misorientation index: Development of a new method for calculating the strength of lattice-preferred orientation. Tectonophysics **411**(1): 157-167.

Spiers, C.&Wenk, H. 1980: Evidence for slip on r and f in the positive sense in deformed calcite single crystals. EOS Trans. Am. Geophys. Union **61**: 1128.

Stünitz, H.&Tullis, J. 2000: Weakening and strain localization produced by syn-deformational reaction of plagioclase. International Journal of Earth Sciences **90**(1): 136-148.

Taylor, G. 1938: Plastic strain in metals. J. Inst. Metals **62**(1).

Tommasi, A., Mainprice, D., Canova, G.&Chastel, Y. 2000: Viscoplastic self-consistent and equilibrium-based modeling of olivine lattice preferred orientations: Implications for the upper mantle seismic anisotropy. J. Geophys. Res. Solid Earth **105**: 7893–7908.

Tullis, J.&Wenk, H. 1994: Effect of muscovite on the strength and lattice preferred orientation of experimentally deformed quartz aggregates. Materials science & engineering. A, Structural materials: properties, microstructure and processing **175**(1-2): 209-220.

Tullis, T., Horowitz, F.&Tullis, J. 1991: Flow laws of polyphase aggregates from end-member flow. Journal of Geophysical Research **96**(B5): 8081-8096.

Turner, F., Griggs, D.&Heard, H. 1954: Experimental deformation of calcite crystals. Bulletin of the Geological Society of America **65**(9): 883-933.

Turner, F.&Heard, H. 1965: Deformation in calcite crystals at different strain rates. Geol. Sci. Publ. Univ. Calif. Los Angeles **46**: 103-126.

Walker, A., Rutter, E.&Brodie, K. 1990: Experimental study of grain-size sensitive flow of synthetic, hot-pressed calcite rocks. Geological Society London Special Publications **54**(1): 259.

Wang, Z., Bai, Q., Dresen, G., Wirth, R.&Evans, B. 1996: High-temperature deformation of calcite single crystals. Journal of Geophysical Research **101**(B9): 20377-20390.

Warren, J.&Hirth, G. 2006: Grain size sensitive deformation mechanisms in naturally deformed peridotites. Earth and Planetary Science Letters **248**(1-2): 438-450.

Warren, J., Hirth, G. Kelemen, P.B. 2008: Evolution of olivine lattice preferred orientation during simple shear in the mantle. Earth and Planetary Science Letters doi: 10.1016/j.epsl.2008.03.063

Weiss, L.&Turner, F. 1972: Some observations on translation gliding and kinking in experimentally deformed calcite and dolomite. Geophys Monograph **7**: 95-107.

Wenk, H., Bennett, K., Canova, G.&Molinari, A. 1991: Modelling plastic deformation of perioditite with the self-consistent theory. Journal of Geophysical Research **96**(B5): 8337-8349.

Wenk, H. 1999: Voyage through the deformed Earth with the self-consistent model. Modelling and Simulation in Materials Science and Engineering **7**(5): 699-722.

Wheeler, J. 1992: Importance of pressure solution and coble creep in the deformation of polymineralic rocks. Journal of Geophysical Research **97**(B4): 4579-4586.

White, S.&Knipe, R. 1978: Transformation-and reaction-enhanced ductility in rocks. Journal of the Geological Society **135**(5): 513-516.

Xiao, X., Wirth, R.&Dresen, G. 2002: Diffusion creep of anorthite-quartz aggregates. Journal of Geophysical Research **107**: 2279.

10. Tables

Table 1a) Data from compression experiments. Stress and strain rate values are taken at the reported, maximum strain. In strain rate stepping experiments, each step is listed sequentially, along with the total strain at the end of each step. All experiments were run at constant axial displacement rate during each step.

Experiment	Material	Stress (MPa)	Strain Rate (s^{-1})	Strain	Mean Intercept Length (μm)
c-1221	Pure	37.9	7.3E-04	0.35	16.2
c-1220	Pure	25.8	4.7E-05	0.25	26.8
c-1229	Pure	17.7	1.1E-05	0.04	
		50.7	1.2E-03	0.33	
		20.4	1.6E-05	0.38	
c-1188	Pure	17.4	4.9E-06	0.03	
		19.6	9.7E-06	0.05	
		28.7	5.6E-05	0.10	
		33.5	1.1E-04	0.16	
		45.8	5.3E-04	0.23	
		53.6	1.1E-03	0.32	
		15.4	1.5E-05	0.36	
c-1225	1%sph	26.0	4.7E-05	0.25	18.3
c-1223	1%sph	34.0	7.0E-04	0.30	14.6
c-1190	1%sph	19.5	7.2E-06	0.03	
		21.2	1.1E-05	0.07	
		27.1	6.0E-05	0.10	
		31.5	1.3E-04	0.15	
		40.9	5.3E-04	0.21	
		48.6	1.1E-03	0.28	
		16.6	1.5E-05	0.33	
c-1230	1%sph	16.7	1.1E-05	0.03	
		42.5	1.5E-03	0.35	
		14.7	1.7E-05	0.43	

Table 1a) (continued)

Experiment	Material	Stress (MPa)	Strain Rate (s^{-1})	Strain	Mean Intercept Length (μm)
c-1228	10%sph	23.5	4.9E-05	0.30	6.6
c-1222	10%sph	41.5	7.3E-04	0.35	6.5
c-1194	10%sph	16.0	5.6E-06	0.03	
		21.3	1.1E-05	0.06	
		28.5	5.7E-05	0.09	
		34.8	1.2E-04	0.13	
		47.7	5.6E-04	0.17	
		54.5	1.0E-03	0.24	
		22.2	1.4E-05	0.29	
c-1231	10%sph	13.4	1.2E-05	0.03	
		47.3	1.5E-03	0.40	
		15.7	1.7E-05	0.46	
c-1226	10%splint	39.0	4.7E-05	0.23	7.1
c-1224	10%splint	60.3	6.8E-04	0.30	6.3
c-1232	10%splint	58.6	6.6E-04	0.30	4.9
c-1195	10%splint	28.1	2.4E-06	0.02	
		29.7	1.1E-05	0.06	
		35.5	5.6E-05	0.10	
		39.0	1.1E-04	0.14	
		50.8	5.3E-04	0.17	
		57.6	1.0E-03	0.25	
		31.7	1.3E-05	0.30	

Table 1b) Data from torsion experiments. Mechanical data is reported as shear stress, shear strain rate, and shear strain. Shear stresses and shear strain rates are reported at the given shear strain. All experiments were run at constant twist rate.

Experiment	Material	Shear Stress (MPa)	Shear Strain Rate (s^{-1})	Shear Strain	Mean Intercept Length (μm)
c-1087:1t	Pure	20.6	8.7E-04	0.61	12.1
		27.1	8.7E-04	15.59	
c-1087:2t	Pure	14.4	6.1E-05	0.43	
		18.8	6.1E-05	15.59	
c-1189:1t	1%sph	23.1	8.7E-04	0.56	10.8
		31.3	8.7E-04	15.59	
c-1189:2t	1%sph	13.6	6.1E-05	0.43	19.5
		20.9	6.1E-05	15.59	
c-1192:1t	10%sph	15.4	8.7E-04	0.61	9
		18.4	8.7E-04	15.59	
c-1192:2t	10%sph	6.3	6.0E-05	0.52	12.3
		11.9	6.0E-05	15.59	
c-1193:1t	10%splint	25.6	8.7E-04	0.52	7.7
		25.8	8.7E-04	15.59	
c-1193:2t	10%splint	19.9	5.9E-05	0.43	5.5
		20.7	5.9E-05	15.31	

Table 2) Absolute and relative values of the critical resolved shear stresses (CRSS) necessary for slip on each calcite slip system, used in this study. Values labeled dB1997 are based on the experimental data of De Bresser and Spiers (1997), extrapolated to a temperature of 1023 K, and +r<a> denotes the inclusion of $r\langle\bar{1}2\bar{1}0\rangle^{\pm}$ with the same CRSS as $c\langle\bar{1}2\bar{1}0\rangle^{\pm}$, after De Bresser et al. (2008). P2003 refers to the CRSS values used by Pieri et al. (2003), and +c<a> is a scenario where $c\langle\bar{1}2\bar{1}0\rangle^{\pm}$ is given the same CRSS as $r\langle\bar{1}2\bar{1}0\rangle^{\pm}$, after De Bresser et al. (2008). The absolute values are used to compare measured strengths to the individual slip systems, whereas the relative strengths are used for VPSC calculations.

	Absolute	Relative			
Slip System	**dB1997+r<a> (MPa)**	**dB1997**	**dB1997 +r<a>**	**P2003**	**P2003 +c<a>**
$f\langle 20\bar{2}1\rangle^{+}$	infinity	9	9	1.5	1.5
$f\langle 20\bar{2}1\rangle^{-}$	15.1	4.5	4.5	1.5	1.5
$f\langle 10\bar{1}1\rangle^{+}$	10.5	3.2	3.2	1.5	1.5
$f\langle 10\bar{1}1\rangle^{-}$	10.5	3.2	3.2	1.5	1.5
$r\langle\bar{2}021\rangle^{+}$	3.3	1	1	1.5	1.5
$r\langle\bar{2}021\rangle^{-}$	3.3	1	1	1.5	1.5
$r\langle\bar{1}2\bar{1}0\rangle^{+}$	6.3	9	1.9	1	1
$r\langle\bar{1}2\bar{1}0\rangle^{-}$	6.3	9	1.9	1	1
$c\langle\bar{1}2\bar{1}0\rangle^{+}$	6.3	1.9	1.9	1.5	1
$c\langle\bar{1}2\bar{1}0\rangle^{-}$	6.3	1.9	1.9	1.5	1

11. Figures

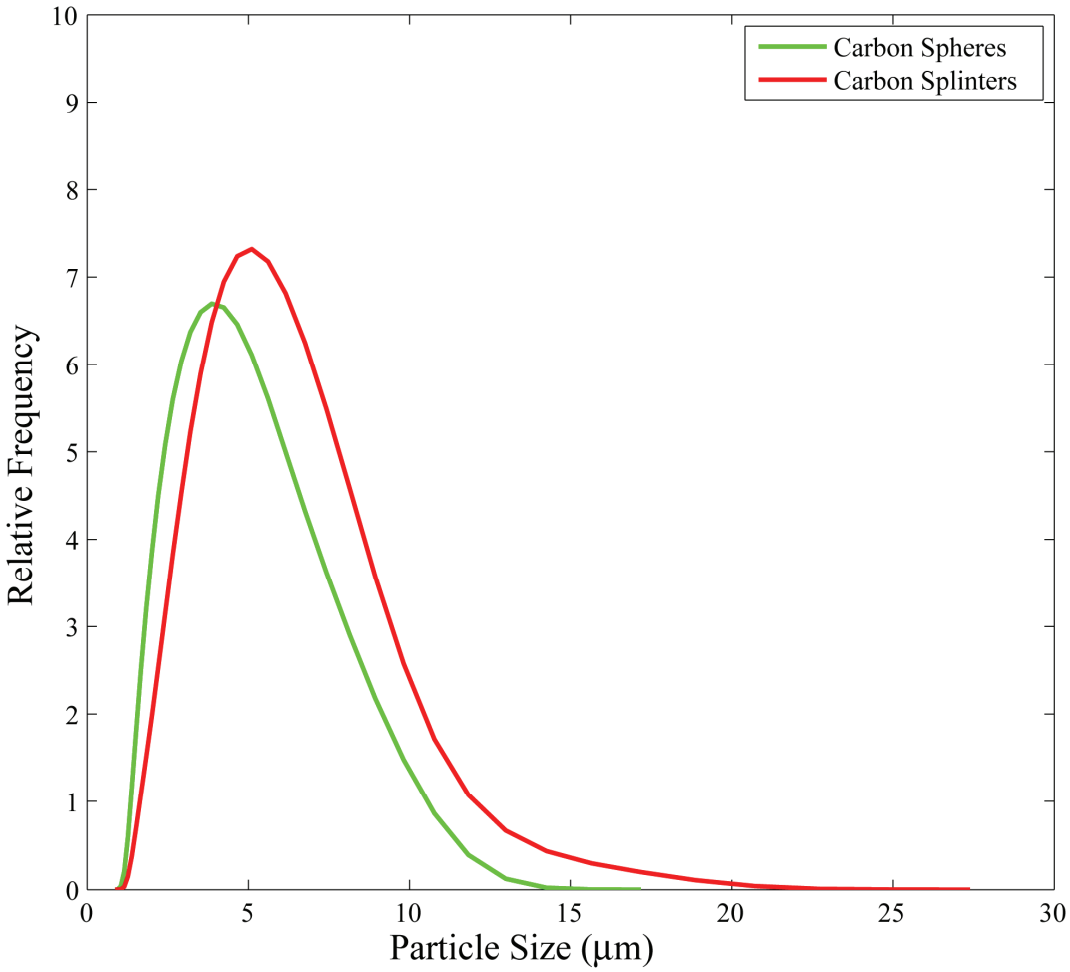


Figure 1) Carbon particle size distributions. The green curve is for the carbon spheres, and red curve is for the carbon splinters.

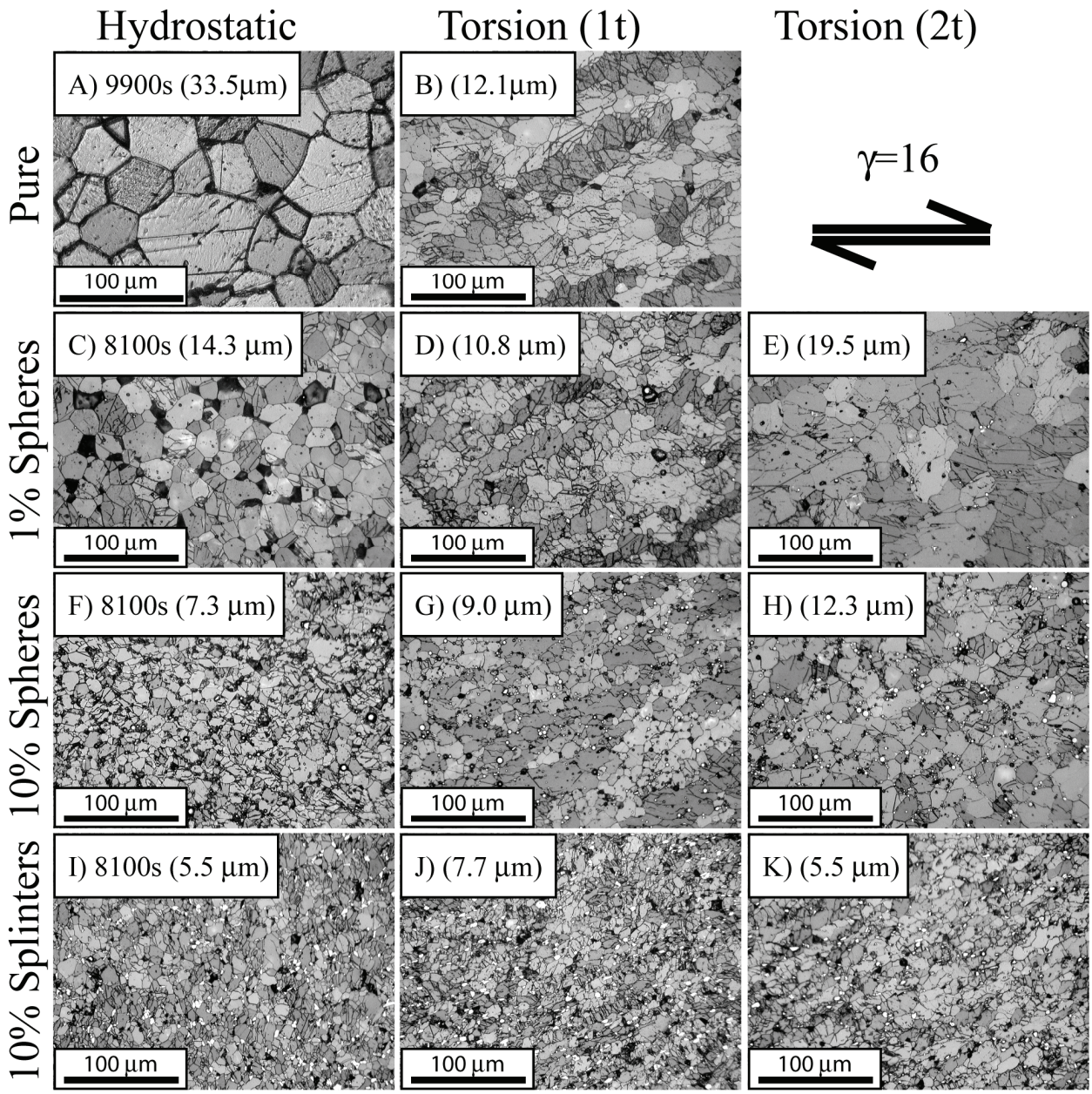


Figure 2) Reflected light micrographs of etched samples of our 4 sample materials. The carbon spheres or splinters are white in color, whereas the calcite is grey. A), C), F), and I) are from samples HIPed for between 8100 s and 9900 s (labeled), which are similar to the starting materials for the samples deformed in torsion shown in B), D), E), G), H), J), and K). All torsion experiments were run to a shear strain of ~16, and the images are taken between 200 and 300 μm of the outer surface of the sample. Torsion(1t) refers to samples deformed at a shear strain rate of 8.7e-4 s^{-1} and Torsion(2t) refers to samples deformed at a shear strain rate of ~6.0e-5 s^{-1} with the sense of shear as shown in the upper right, and a horizontal shear plane. In each micrograph, the mean intercept length is labeled. The foliation at ~30º to the shear plane is apparent in B) and D) and to a lesser extent in G).

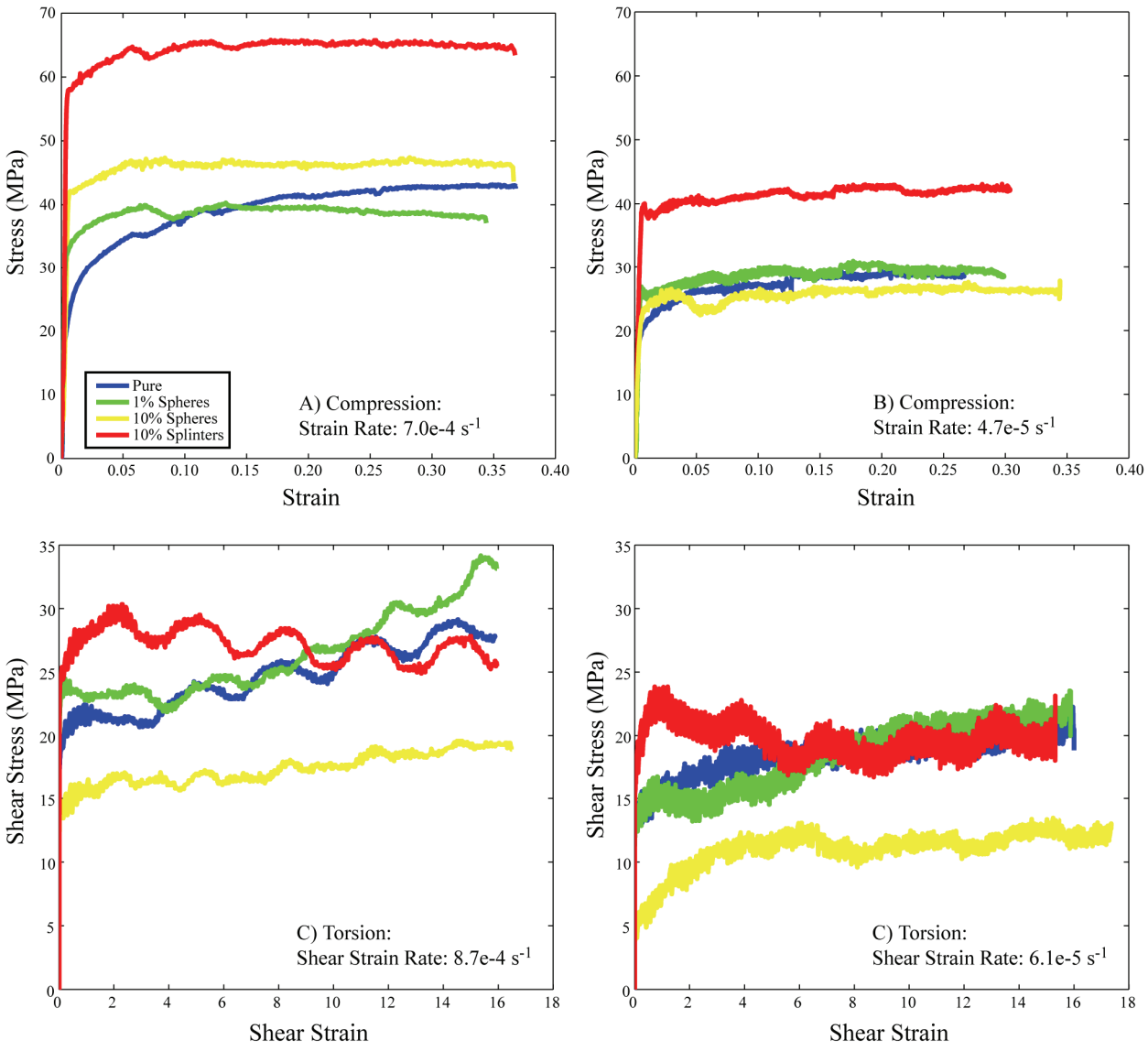


Figure 3) Stress strain curves for the constant displacement rate (compression) and constant twist rate (torsion) experiments run in this study. The colors are the same in each plot (which will be used throughout this study), and are shown in A). Blue curves are pure samples, green curves are samples containing 1 vol.% spheres, yellow curves are samples containing 10 vol.% spheres, and red curves are samples containing 10 vol.% splinters. A) and B) are plots from compression experiments, run at MIT, of differential stress vs. axial strain, whereas C) and D) are plots from torsion experiments run at the GFZ of shear stress vs. shear strain. A) is for compression tests run at an axial strain rate of 7.0e-4 s^{-1}, B) is for compression tests run at an axial strain rate of 4.7e-5 s^{-1}, C) is for torsion tests run at a shear strain rate of 8.7e-4 s^{-1}, and D) is for torsion tests run at a shear strain rate of 6.1e-5 s^{-1}.

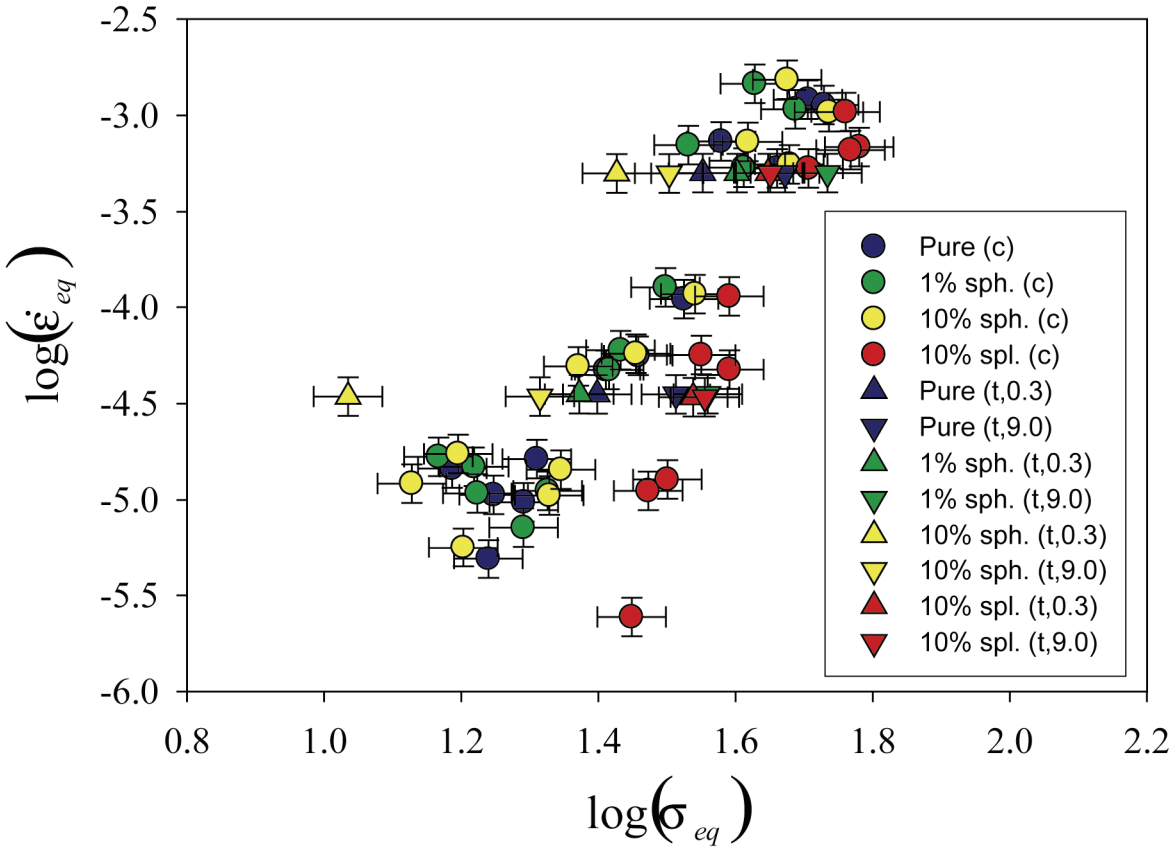


Figure 4) Equivalent stress (σ_{eq}) vs. equivalent strain rate $\left(\dot{\varepsilon}_{eq}\right)$ for all the compression and torsion experiments listed in table 1, calculated as described in the text. The colors are the same as in figure 3: pure samples are blue, samples containing 1 vol.% spheres are green, samples containing 10 vol.% spheres are yellow, and samples containing 10 vol.% splinters are red. Mechanical data from compression experiments (c) is distinguished from that obtained in torsion experiments at "low" strain (t,0.3) (ε_{eq}=0.3), and from the strength of torsion experiments at "high" strain (t,9.0) (ε_{eq}=9.0) (Table 1).

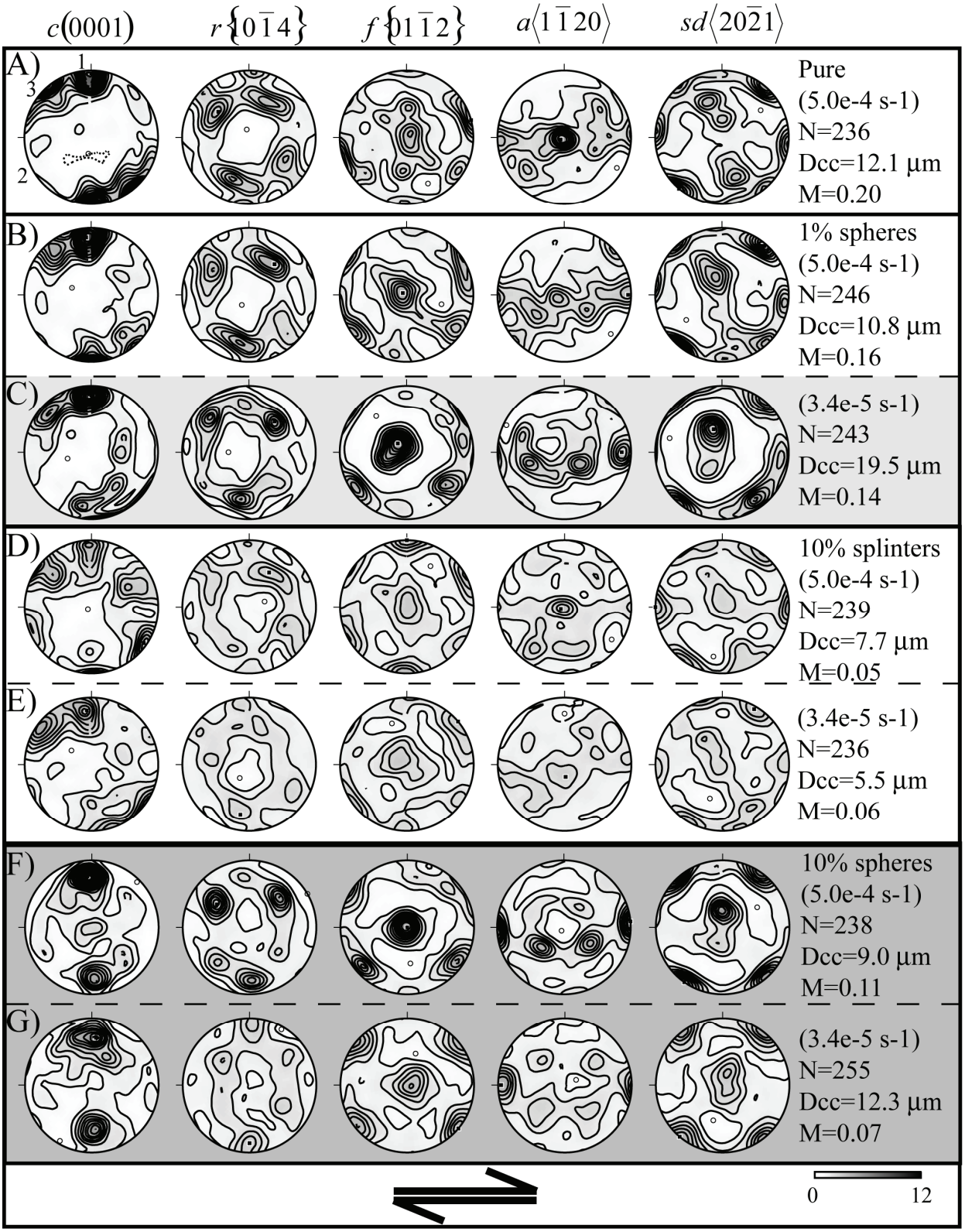


Figure 5) (caption on next page)

Figure 5) Pole figures for samples deformed to an equivalent strain of 9.0 (shear strain of 16) in torsion at T=1023K. The equivalent strain rate on the outer surface of each sample is listed, along with the material, number of grains analyzed by EBSD (N), the mean intercept length (D_{cc}) and the M-Index (after Skemer et al., 2005). Pole figures were created with the program PFch5 (D. Mainprice, pers. comm., 2007). These are lower hemisphere projections with a Gaussian smoothing of 8.5º. The contour interval of 0.5 multiples of a uniform distribution (MUD) is constant in all pole figures, as is the maximum shading. All pole figures are plotted with a dextral sense of shear. Shading is used to denote the two distinct CPO's we observe. White background refers to the pole figures which are similar to that observed in pure samples, whereas dark gray shading refers to the pole figures observed in samples containing 10 vol.% spheres. Light gray shading is for the sample containing 1 vol.% spheres, deformed at an equivalent strain rate of 3.4e-5 s^{-1} which has a CPO intermediate between the two end-members. Numbers on the c-axis pole figure in A) correspond to the three c-axis maxima from Schmid et al. (1987). A) is a pure sample; B) and C) are samples containing 1 vol.% spheres; D) and E) are samples containing 10 vol.% splinters; F) and G) are samples containing 10 vol.% spheres.

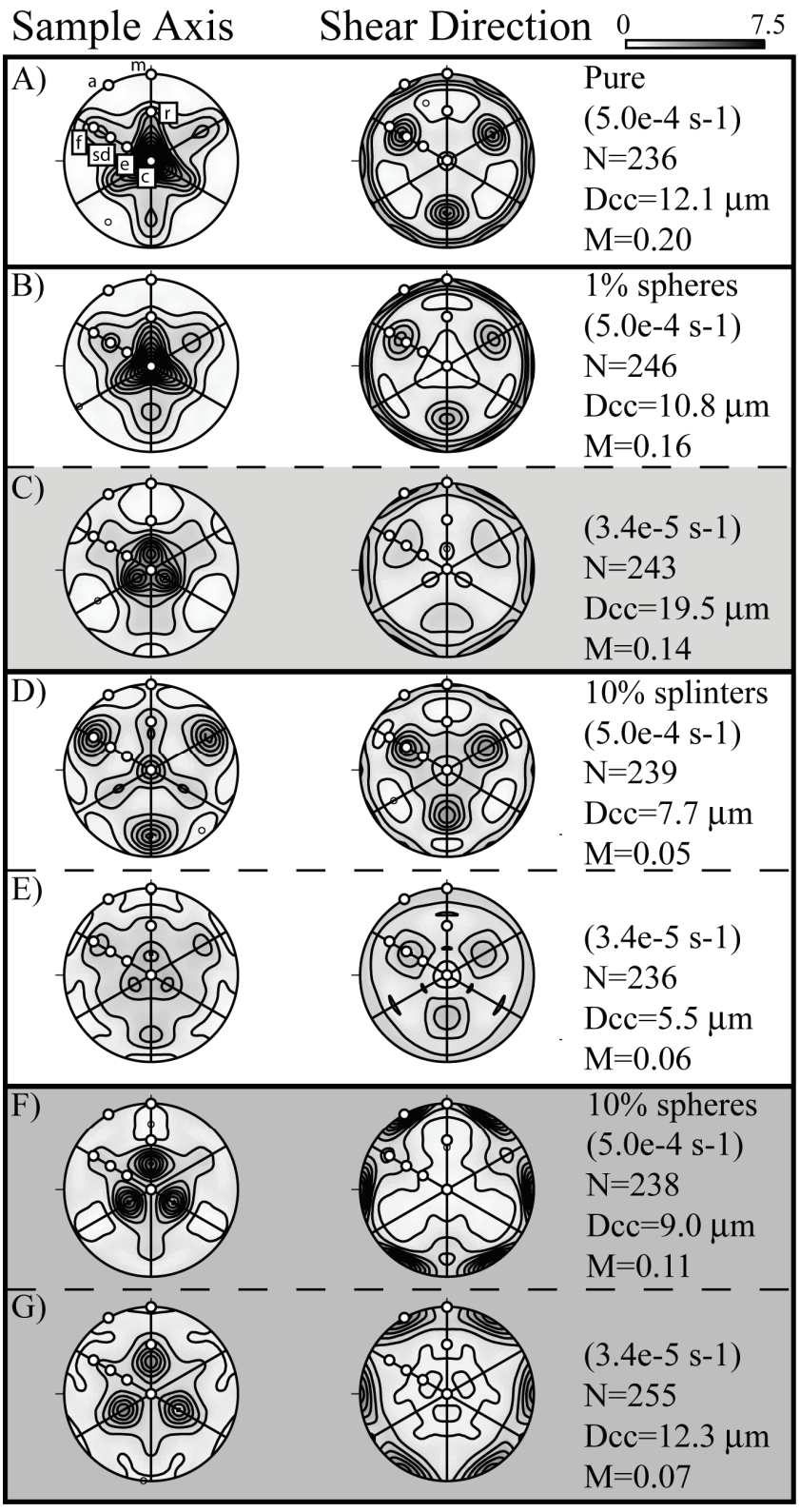


Figure 6) (caption on next page)

Figure 6) Inverse pole figures (IPFs) for the same samples deformed in torsion as figure 5. The sample material, equivalent strain rate (in parantheses), number of grains analyzed by EBSD (N), mean linear intercept length (D_{cc}) and M-Index of each sample are listed. More details of each experiment are listed in table 1. IPFs are plotted for the direction parallel to the long axis of the sample, and for the shear direction. Plots are upper hemisphere projections, with Gaussian smoothing of 8.5º, and are contoured for each 0.5 MUD up to a global maximum of 7.5. Important crystallographic directions in calcite are marked in each IPF, and are labeled in (A). a is $\langle 11\bar{2}0 \rangle$, m is $\langle 10\bar{1}0 \rangle$, r is $\{10\bar{1}4\}$, c is (0001), e is $\{01\bar{1}8\}$, sd is $\langle 02\bar{2}1 \rangle$, and f is $\{01\bar{1}2\}$. The gray shading is the same as in figure 5. A) is a pure sample; B) and C) are samples containing 1 vol.% spheres; D) and E) are samples containing 10 vol.% splinters; and F) and G) are samples containing 10 vol.% spheres.

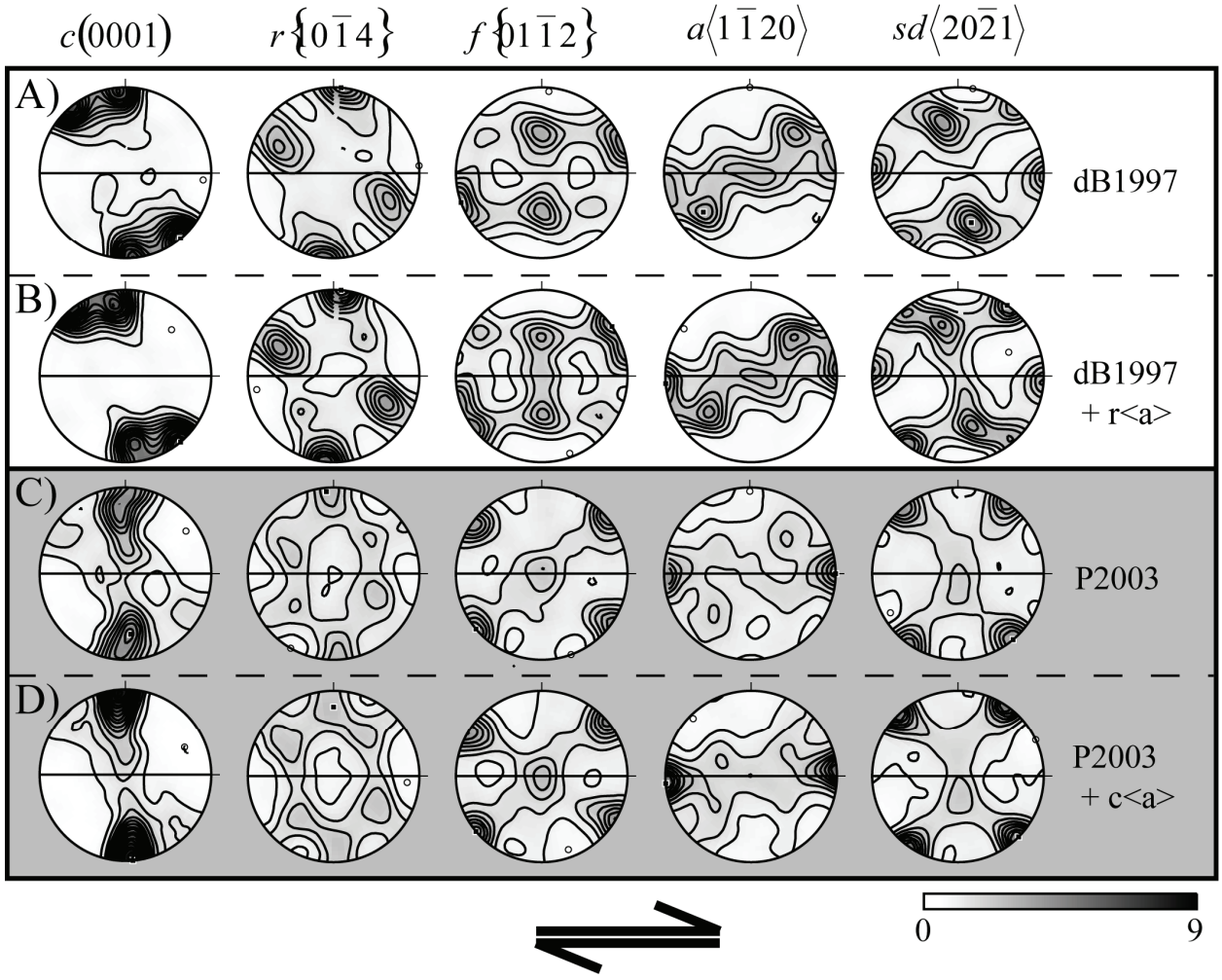


Figure 7) Pole figures from VPSC calculations, all plotted at an equivalent strain of 2.0, with a dextral sense of shear. The horizontal line denotes the shear plane. Contours are for each 0.5 MUD up to a global maximum of 9. The CRSS values used to calculate each pole figure are as in table 2. A) dB1997 are CRSS values from De Bresser and Spiers (1997); B) dB1997+r<a> are the same as in A), except $r\langle\bar{1}2\bar{1}0\rangle^{\pm}$ is included with the same CRSS as $c\langle\bar{1}2\bar{1}0\rangle^{\pm}$; C) P2003: CRSS values from Pieri et al. (2003), and D) P2003+c<a>: the same as C) except $c\langle\bar{1}2\bar{1}0\rangle^{\pm}$ is included with the same CRSS as $r\langle\bar{1}2\bar{1}0\rangle^{\pm}$.

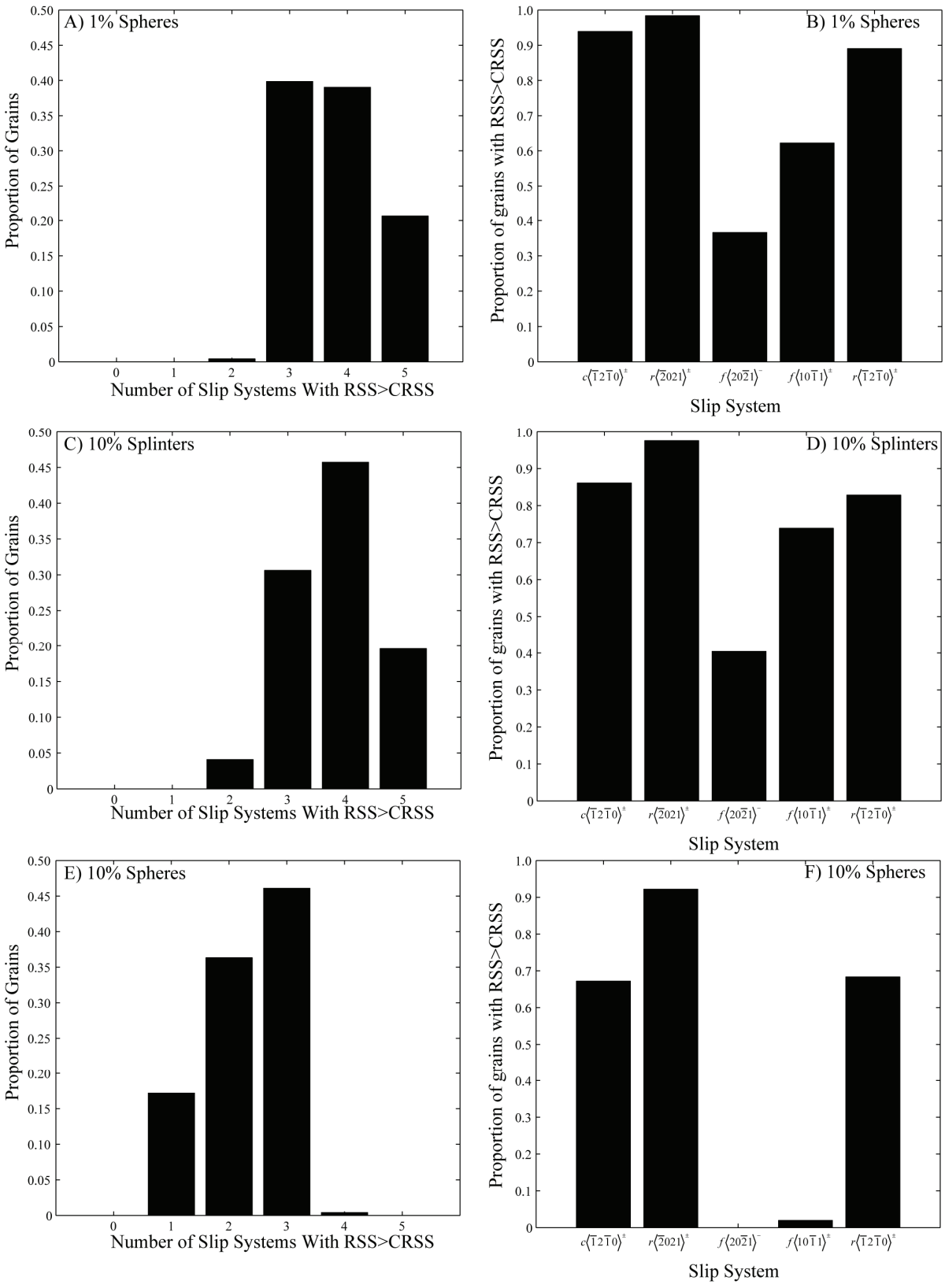


Figure 8) (caption on next page)

Figure 8) Histograms of the number of active slip systems (e.g. with a resolved shear stress greater than the critical resolved shear stress) in each grain (A,C,E), assuming only one strain component from each family of symmetrically equivalent slip systems; and which slip systems are favorably oriented for slip (B,D,F), based on the grain orientations measured by EBSD, and the applied shear stress at the maximum strain in the experiment (Table 1). Plots are for samples deformed in torsion at an equivalent strain rate of 3.4e-5 s^{-1}, using the CRSS values from De Bresser and Spiers (1997) (Table 2). A) and B) are sample c-1189:2t containing 1 vol.% spheres (τ=20.9 MPa); C) and D) are sample c-1193:2t containing 10 vol.% splinters (τ=20.7 MPa); and E) and F) are sample c-1192:2t containing 10 vol.% spheres (τ=11.9 MPa).

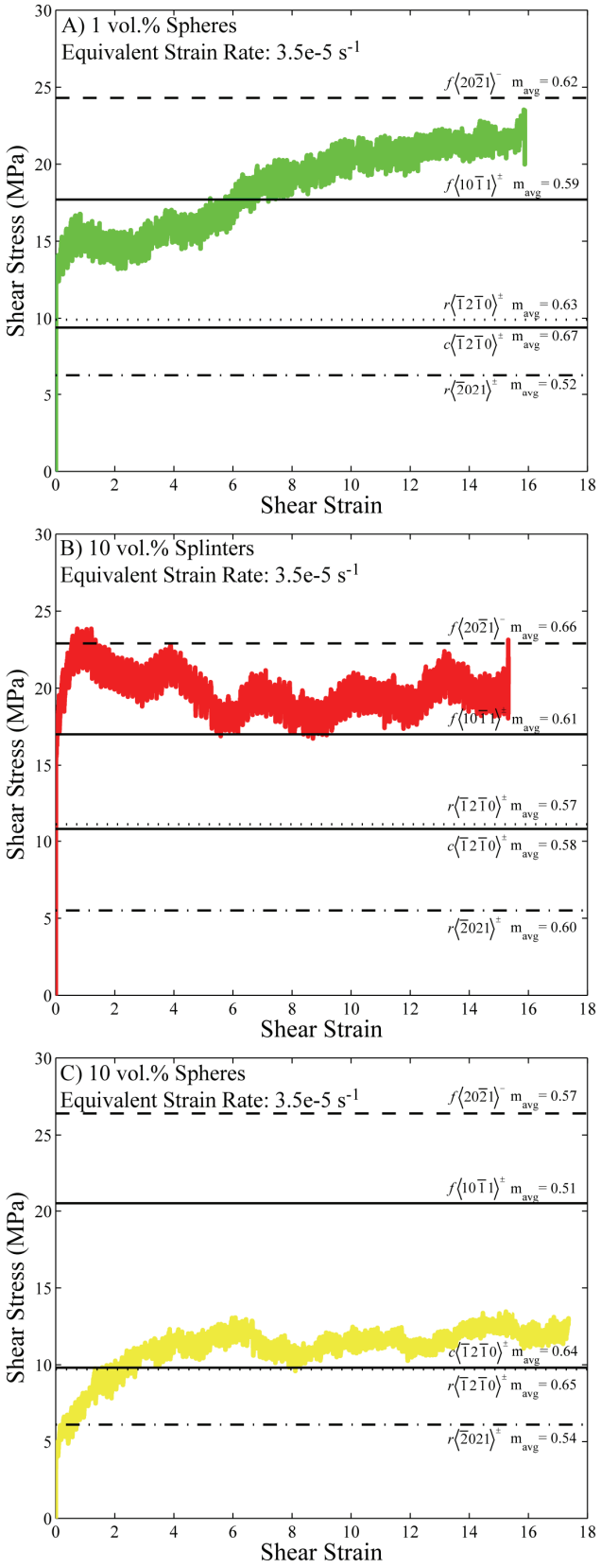


Figure 9) (caption on next page)

Figure 9) Shear stress vs. shear strain curves for samples deformed in torsion at an equivalent strain rate of 3.4e-5 s^{-1} (the same as in figure 3D). Also shown are the shear stresses required for the resolved shear stress on each slip system to exceed the critical resolved shear stress, based on the values of De Bresser and Spiers (1997) (Table 2), and the average schmid factor for each slip system (m_{avg}), from our measured crystallographic orientations. Samples containing A) 1 vol.% spheres (c-1189:2t) or B) 10 vol.% splinters (c-1193:2t) have strengths between the stresses required for slip on $f\langle 10\bar{1}1\rangle^{\pm}$ and $f\langle 20\bar{2}1\rangle^{-}$, whereas samples containing C) 10 vol.% spheres have a strength closer to the stress required for slip on either $r\langle \bar{1}2\bar{1}0\rangle^{\pm}$ or $c\langle \bar{1}2\bar{1}0\rangle^{\pm}$.

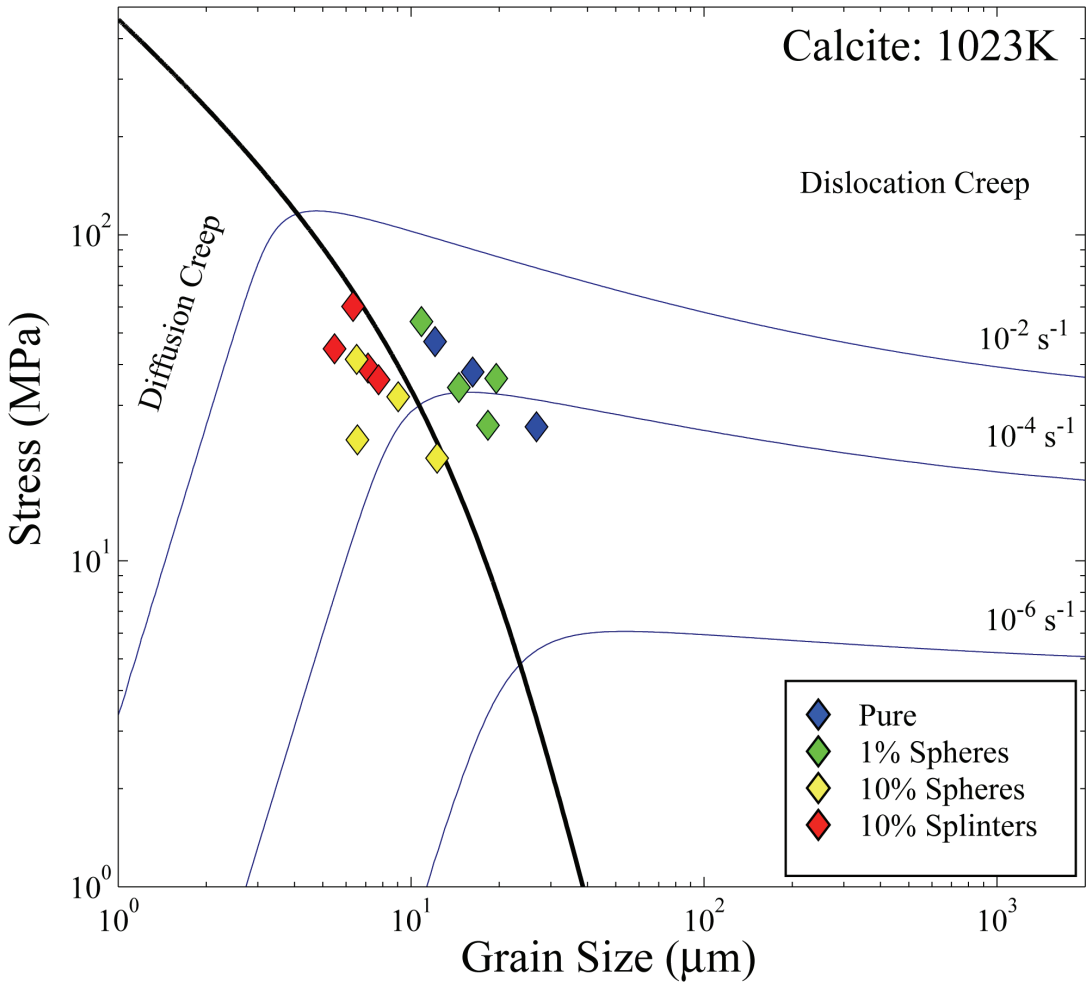


Figure 10) A deformation mechanism map for calcite at 1023K, calculated from the diffusion creep flow law from Herwegh et al. (2003) and the dislocation creep flow law (Peierls creep) from Renner et al. (2002). Our experimental samples are shown, using the equivalent stress at maximum equivalent strain. Grain size is the measured mean intercept length. As in previous plots, blue symbols are pure samples, green symbols are samples containing 1 vol.% spheres, yellow symbols are samples containing 10 vol.% spheres, and red symbols are samples containing 10 vol.% splinters. The black curve is where the dislocation creep and diffusion creep contribute equally to the total strain rate.

Chapter 6

Grain Size Evolution During Deformation of Poly-Phase Marbles

Nicholas Austin
Brian Evans
Erik Rybacki
Georg Dresen

Abstract

The microstructures of deformed rocks are frequently influenced by interactions between the constituent phases. To investigate the nature of these interactions, we have analyzed microstructures from compression and torsion experiments, performed at 1023 K, on calcite rocks containing between 1 and 10 vol.% rigid carbon spheres or splinters, which were deformed to equivalent strains between 0.25 and 9.0. The resulting microstructures are compared with those from samples which have been hot isostatically pressed (HIPed) for similar durations. Under hydrostatic conditions, the addition of as little as 1 vol.% carbon spheres poisons normal grain growth. Shape is also important: for an equivalent volume fraction and grain dimension, carbon splinters result in a finer calcite grain size than carbon spheres. In samples deformed at "high" strain rates, or which have "large" mean free spacing of the pinning phase, the final recrystallized grain size is well explained by competing grain growth and grain size reduction processes, where the grain-size reduction rate is determined by the rate that mechanical work is done during deformation. In these samples, the final grain size is finer than in samples heat treated hydrostatically for equivalent durations. At lower strain rates or in samples with a smaller mean free spacing of the pinning phase, the grain size after deformation is equivalent to that after a hydrostatic heat treatment of the same duration, suggesting that, in these samples, the grain size is determined by the mean free spacing of the pinning phase. The grain sizes from naturally deformed rocks in the Morcles nappe also suggest a similar transition between a pinned grain size and a dynamically recrystallized grain size.

1. Introduction

The microstructure of polyphase materials, including many mylonites, is influenced by the interaction of the constituent phases. The interaction between migrating boundaries of a matrix phase and particles of a second phase has been extensively investigated theoretically (e.g. Smith 1948; Gladman 1966; Haroun & Budworth 1968; Anand & Gurland 1975; Hellman & Hillert 1975; Flowers 1979; Haroun 1980; Louat 1983; Ryum et al. 1983; Nes et al. 1985), in the laboratory (Olgaard & Evans 1986; Lange & Hirlinger 1987; Olgaard & Evans 1988; Stearns & Harmer 1996), and in naturally deformed rocks (Mas & Crowley 1996; Herwegh & Kunze 2002; Krabbendam et al. 2003; Ebert et al. 2007a). The maximum grain size reached during normal grain growth under hydrostatic conditions is related to the mean free spacing of the pinning phase:

$$D_{\max} = A\frac{d_p}{f_p^m} \tag{1}$$

where A is a geometric constant and m varies depending on the distribution, size, and shape of the pinning phase (Smith 1948; Gladman 1966; Haroun & Budworth 1968; Anand & Gurland 1975; Hellman & Hillert 1975; Louat 1983).

During deformation, grain size also evolves in response to some combination of stress, strain rate, and temperature through the process(es) of dynamic recrystallization (Sakai & Jonas 1984; Urai et al. 1986; Drury & Urai 1990; Humphreys & Hatherly 1995; Shimizu 2008). In single phase rocks, a stable grain size is often produced (Twiss 1977; Guillope & Poirier 1979; Karato et al. 1980; Schmid et al. 1980; Van Der Wal et al. 1993; Rutter 1995; Stipp & Tullis 2003; Barnhoorn et al. 2004; Ter Heege et al. 2005; Stipp et al. 2006). The relationship between deformation conditions and the steady-state recrystallized grain size has often been used to infer

the deformation conditions under which natural shear zones formed (White 1979; Christie & Ord 1980; Kohlstedt & Weathers 1980; Etheridge & Wilkie 1981; Ord & Christie 1984; Zulauf 2001; Herwegh et al. 2005b; Warren & Hirth 2006; Mehl & Hirth 2008; Austin et al. in press).

A similar interpretation of the microstructures in rocks containing more than one mineral constituent would require understanding not just the processes of dynamic recrystallization, but also the nature of the interaction between the phases (Herwegh et al. 2005a; Herwegh et al. 2005b; Holyoke & Tullis 2006; Ebert et al. 2007a; Austin et al. in press). Such interactions might well influence both the steady state microstructure (e.g. eq. 1), and the kinetics of microstructural evolution. For example, the drag force on a migrating boundary associated with the presence of a pinning phase is

$$F = X\gamma d_p \tag{2}$$

(Smith 1948; Gladman 1966; Ryum et al. 1983; Nes et al. 1985) where γ is the interfacial energy and X may depend on the angle between the pinned boundary and its unpinned orientation (Evans et al. 2001) or on the shape of the pinning phase (Ryum et al. 1983). This pinning force will influence boundary migration rates, even if it does not completely inhibit grain boundary migration. Since F, A, and m, in equations 1 and 2, all depend on the geometric distribution of the pinning phase, the interpretation of microstructures in polyphase rocks requires an understanding of how grain size and the geometric distribution of phases changes during deformation, and how dynamic recrystallization is effected by the presence of a pinning phase.

To address these questions, we have analyzed the microstructures from deformation experiments performed on synthetic calcite samples containing rigid carbon spheres and splinters, reported in Chapters 4 and 5. We have also performed a series of hydrostatic

experiments for similar durations on the same materials to allow for quantification of the effects of deformation on the resulting microstructure. This system was chosen as the geometry and volume fraction of the pinning phase can be carefully controlled, and there are no chemical reactions between the phases. We suggest that this system is applicable to any situation where a low volume fraction of a chemically inert pinning phase influences the microstructural evolution of a deforming rock.

2. Experimental Methodology

2.1. Sample Materials

The samples used in this study are the same material as those described in Chapter 5. To summarize, these were prepared from reagent-grade (>99.95% pure) synthetic calcite powder, supplied by Malinckrodt (powder (b) from Chapter 4), which was either investigated pure, or mixed with a volume fraction of 0.011±0.002 or 0.110±0.010 Alfa Aesar type II glassy carbon spheres (mean particle size of 4μm) or 0.110±0.010 Alfa Aesar type II glassy carbon splinters (mean particle size of 5μm) as described in Chapter 5. In hydrostatic experiments, samples were hot isostatically pressed (HIPed) for 900 s to 36900 s at a temperature of 1023 K and a confining pressure of 300 MPa (Table 1). The procedure for hydrostatic experiments was identical to that described in Chapter 4. In addition to these hydrostatic experiments, we will also examine the microstructures from compression experiments run at constant axial displacement rate and from torsion experiments run at constant twist rate on the same starting materials, previously described in Chapter 5. In Chapter 5 we showed that the mechanical data from the compression tests could be directly compared to that from torsion tests using von Mises equivalent stresses and strain rates. For the remainder of this paper, unless otherwise noted, all mechanical data is reported in this way.

2.2. Grain-Size Analysis

Each sample was cut lengthwise, polished, and etched in 0.37% hydrochloric acid for approximately 30 s in order to enhance grain boundaries (Herwegh 2000). The polished, etched samples were imaged in reflected light (Figs. 2,4). Samples from torsion experiments were imaged between 200 and 300 μm of the outer surface of the sample. At this position, strains and strain rates are within 10% of the reported maximum value, and stresses are within 2% of the maximum value (for n=5) (Paterson & Olgaard 1999; Chapter 5). Mean linear intercept lengths were determined based on measurements both parallel and perpendicular to the long axis of the sample. No stereological correction was applied. Previous studies (e.g. Rutter et al. 1994; Chapter 4) have shown that, in their experiments, the grain size determined by mean linear intercept length is directly comparable to that determined by the mean equivalent circular diameter method.

3. Microstructural Observations

3.1. Hydrostatic Grain Growth

Under hydrostatic conditions, the grain growth kinetics of the pure synthetic calcite were well explained by the conventional, parabolic growth equation (Fig. 3):

$$d^p - d_o^p = K_g \exp\left(\frac{-Q_g}{RT}\right)\Delta t \qquad (3)$$

where $K = K_g \exp\left(\frac{-Q_g}{RT}\right) = 3.16$ ($\mu m^{-p}\ s^{-1}$) and p=3 (see Chapter 4). In these pure samples, grains systematically coarsen, while maintaining a polygonal microstructure. The addition of 1 vol.% carbon spheres has a dramatic influence on the matrix grain size although the effect on grain shape is much less pronounced (Figs. 1,2). Samples containing 1 vol.% spheres generally

have polygonal grain boundaries, similar to pure samples (Fig. 1), however, the mean grain size is systematically finer than in pure samples after a heat treatment of an equivalent time (Fig 2). The carbon spheres are predominantly concentrated on grain boundaries, although some are found in grain interiors (Fig. 1). No agglomeration of the carbon spheres was observed.

Samples containing 10 vol.% spheres have yet a finer grain size than those containing 1 vol.% spheres (Fig. 2). While some polygonal grains are present in these samples, there are also more grains with irregular grain boundaries, which appear to be associated with inhibited grain boundary migration due to the presence of the carbon spheres (Fig. 1). The carbon spheres themselves are predominantly along grain boundaries, and exhibit some agglomeration along certain boundaries (e.g. Fig. 1). There are very few carbon spheres within grain interiors, suggesting that boundaries are not able to "break free" from the pinning carbon.

Samples containing 10 vol.% carbon splinters have the finest grain size of the samples tested (Fig. 1,2). The carbon splinters also appear to be more homogeneously distributed throughout the sample than the carbon spheres; little agglomeration of the splinters is observed after any hydrostatic experiment (Fig. 1). As with the spheres, the carbon splinters are almost exclusively found on grain boundaries, suggesting that the grain boundaries were effectively pinned. Qualitatively, the splinters do not have any preferred orientation after hydrostatic experiments.

Samples containing any volume fraction of carbon spheres or splinters exhibit similarly slow grain growth rates after times greater than ~900 s, and the stable grain sizes are nearly reached during heating and furnace stabilization. It appears grain growth follows the hydrostatic curve until the grain boundaries interact with the carbon spheres or splinters. The stable grain sizes in this study are comparable to those observed by (Olgaard & Evans 1986) in synthetic calcite aggregates containing alumina particles with similar volume fractions and particle size

distribution as the second phases in this present study. However, the rate that the stable grain size is reached is much faster in our study than observed by (Olgaard & Evans 1986).

3.2. Microstructural Evolution During Deformation

In pure samples, grain size reduction was observed during deformation (Fig. 3-5) at all of the strain rates investigated. A pure sample deformed in compression at a strain rate of 7.3e-4 s^{-1} to a strain of 0.35 (c-1221) has a finer grain size that that deformed at a lower strain rate (c-1220). c-1087:1t, deformed in torsion at an equivalent strain rate of 5.0e-4 s^{-1} to an equivalent strain of 9.0, has a finer grain size than a sample deformed at a similar strain rate to a lower strain in compression. Both samples (c-1221 and c-1087:1t) have similar grain morphologies. Samples deformed in torsion also develop a foliation at ~30-35º to the shear plane (Fig. 4) (Chapter 5).

Samples containing 1 vol.% spheres, deformed in compression at a strain rate 7.0e-4 s^{-1} (c-1223) and in torsion at an equivalent strain rate of 5.0e-4 s^{-1} (c-1189:1t) have similar grain sizes to pure samples deformed under similar conditions (Fig. 3-5). Particularly at high strains, these samples have a finer grain size than samples which have been heat treated hydrostatically for an equivalent duration. On the other hand, samples containing 1 vol.% spheres, deformed at equivalent strain rates between 3.0 and 5.0e-5 s^{-1} have similar grain sizes to samples that were heat treated hydrostatically for an equivalent time, and finer grain sizes than pure samples deformed under similar conditions. There is no readily apparent difference in the distribution of the carbon spheres in any samples containing 1 vol.% spheres. Samples containing 1 vol.% spheres, deformed in torsion, develop a similar foliation to pure samples (Fig. 4).

All samples containing 10 vol.% spheres and 10 vol.% splinters, deformed at all of the strain rates investigated in either torsion or compression have similar grain sizes to samples that were heat treated hydrostatically for equivalent durations. However, in both cases, there are other

microstructural differences between samples deformed in compression, and samples deformed in torsion. In samples containing 10 vol.% spheres, deformed in compression to equivalent strains between 0.30 and 0.35 (c-1222 and c-1228), there is some agglomeration of the carbon spheres, which are found predominantly along grain boundaries. In samples deformed in torsion to an equivalent strain of 9.0 (c-1192:1t, c-1192:2t), the carbon spheres are more homogeneously mixed throughout the samples, and in the sample deformed at an equivalent strain rate of 5.0e-4 s^{-1}, many more carbon spheres are found in grain interiors (Fig. 4). The foliation that develops in both pure samples and those containing 1 vol.% spheres when deformed in torsion is not as apparent in samples containing 10 vol.% spheres.

Samples containing 10 vol.% splinters, deformed in compression to an equivalent strain of 0.23-0.30 also develop a similar grain morphology and second phase distribution as under hydrostatic conditions (Figs. 1,3). However, in samples deformed in torsion to equivalent strains of 9.0 or 8.8 respectively (c-1193:1t, c-11932t), the carbon splinters become aligned at ~30º to the shear plane (Fig. 4). Unlike in the samples containing spheres, however, the splinters are seldom found within grain interiors, remaining exclusively on grain boundaries.

4. Discussion

4.1. Pinning of Grain Boundaries by Second Phases

During the hydrostatic heat treatments, pure calcite aggregates undergo normal grain growth, but the addition of as little as 1 vol.% rigid second phases pins grain boundaries, and inhibits grain growth, consistent with a wealth of previous laboratory, field, and theoretical studies. Shape is important too: oblate particles exert a greater drag force than prolate or spherical particles (Ryum et al. 1983). In these experiments, samples containing 10 vol.% splinters had finer grain sizes than those with 10 vol.% spheres, even though the average nominal grain size of the two powders were similar. However, the growth rate at t>900 s is similar for samples with

both shapes. The exponent, *m,* in Eq. 1 probably depends on the shape of the pinning phase, its distribution, and its size relative to the growing phase, and, therefore, a different pinned grain size would be predicted for elongate and spherical particles (Smith 1948; Gladman 1966; Haroun & Budworth 1968; Anand & Gurland 1975; Hellman & Hillert 1975; Louat 1983). Unfortunately, we were unable to quantify *m* or *A* from our experiments due to a limited range of volume fractions and second phase particle sizes, as well as due to agglomeration of the pinning phase.

4.2. Recrystallized vs. Pinned Grain Sizes

During crystal-plastic deformation, grain size evolves in response to variations in stress, strain rate, and/or temperature (De Bresser et al. 1998; Braun et al. 1999; Austin & Evans 2007; Chapter 4). In previous work, we suggested that the rate of evolution of grain size during deformation is related to the rate of mechanical work ($\sigma\dot{\varepsilon}$) and the efficiency of storage of internal energy. If grain growth and grain size reduction processes are simultaneous and independent, and if production of new grain boundaries is the dominant method for storing internal energy, then the stable grain size (d) is

$$d^{1+p} = \frac{K_g \exp\left(\frac{-Q_g}{RT}\right) p^{-1} c\gamma}{\beta\lambda\sigma\dot{\varepsilon}} \qquad (4)$$

Where, as before, K_g, p, and Q_g are the constants in the grain growth equation (eq. 3), β is the proportion of the total work rate owing to dislocation creep, λ is the proportion of the work due to dislocation creep that is stored, c is a geometric constant ($=\pi$ for spherical grains), and γ is the specific grain boundary energy (Austin & Evans 2007).

Here, we compare the final measured grain sizes in each of our experiments with the initial grain size, and with the stable grain size predicted by equation 4 using values of $K_g \exp\left[\frac{-Q_g}{RT}\right] = 3.16$ (μm^p s^{-1}), p=3, and $\lambda/c\gamma = 0.0025$ (m^2 J^{-1}), obtained empirically (Chapter 4) (Figs. 2,5). We use the measured equivalent stresses and strain rates, assuming the total strain rate is accommodated by dislocation creep (β=1,) (Fig. 6), consistent with apparent stress exponents (n) >5 in all of our experiments. If some portion of the total strain rate is accommodated by mechanisms other than dislocation creep, the grain size predicted by equation 4 will be a minimum value of the stabilized grain size. In Chapter 5, we suggested that an additional strain accommodating mechanism may have been active in samples containing 10 vol.% spheres, which would increase the stable grain size predicted by equation 4, although we do not account for that here.

In figure 6, samples which have reached their stable grain size (from equation 4), should plot at d/d_{pred}=1 if the assumptions discussed above are valid. Samples in which the grain size has been reduced, but which have grains coarser than the stable grain size (e.g. incomplete dynamic recrystallization) plot in the upper left-hand quadrant, whereas samples which have undergone grain growth, but which still have a finer grain size than the predicted stable value lie in the lower right-hand quadrant. We do not expect grain sizes in the upper right-hand or lower left-hand quadrants, because the grain size would be evolving away from the stabilized size. Aside from two outliers, we do not observe any samples in these quadrants (Fig. 6).

In all pure samples, grain size reduction occurs during deformation. The sample deformed in torsion to an equivalent strain of 9.0 at an equivalent strain rate of 5.0e-4 s^{-1} has a grain size very nearly equal to that predicted (eq. 4), whereas a sample deformed in compression at a similar equivalent strain rate, but to an equivalent strain of only 0.35 has an average grain size coarser

than the torsion sample or that predicted. Equivalent strains greater than 0.35 but less than 9.0 are required for the stable grain size to be reached, consistent with the results of torsion experiments on Carrara marble (Pieri et al. 2001; Barnhoorn et al. 2004).

In a sample containing 1 vol.% spheres, deformed at an equivalent strain rate of 7.0e-4 s^{-1} to an equivalent strain of 0.32, the grain size did change significantly (Figs. 5,6), but, grain size reduction did occur in the same material deformed under similar conditions in torsion to an equivalent strain of 9.0 The average grain size at the end of that experiment was consistent with Eq. 4. Again, it appears that an equivalent strain >0.35 and <9.0 is required for the stable grain size to be reached. When the same material was deformed at a lower equivalent strain rate (3.5 to 4.8e-5 s^{-1}) slight grain growth occurred, however, the measured grain size remains below the grain size predicted by equation 4, even to equivalent strains of 9.0. The measured average grain sizes in these samples are similar to those obtained during hydrostatic experiments run for similar durations, suggesting a transition from a deformation controlled grain size at high strain rates to a second phase (e.g. pinned) grain size at low strain rates. In samples deformed at "high" strain rate, or with a "large" mean free spacing of the pinning phase, grain size is indicative of the deformation conditions, and is well explained by equation 4, as long as the sample has undergone sufficient strain for complete recrystallization.

In samples containing 10 vol.% spheres or 10 vol.% splinters, the grain size following deformation is always finer than the predicted recrystallized grain size (eq. 4), or that measured in pure samples deformed under similar conditions, and is not significantly different from that measured in samples with the same second phase content, heat treated hydrostatically for similar durations (Figs. 5,6). In these samples, the grain size reflects the distribution of the pinning phase rather than the deformation conditions. More spheres are found in the interior of grains

after an equivalent strain of 9.0 in samples containing 10 vol.% spheres compared to hydrostatic experiments, which suggests that the grain size is greater than the mean free spacing of the particles. The lack of a measurable difference in grain size may relate to the lack of agglomeration of the spheres after deformation compared to after HIPing, which will decrease the effective particle size, thus decreasing the effective mean free spacing of the pinning phase, although this has not been quantified. Possible variations to β that result from an additional strain accommodating mechanism in samples containing 10 vol.% spheres (e.g. Chapter 5) do not influence this analysis, as, regardless of β, the final grain sizes remain below those predicted by equation 4.

4.3. Comparison to Natural Data

In our experiments, we observed a transition from grain sizes controlled by deformation conditions when strain rates and stresses were high, to those controlled by second phase distributions when strain rates and stresses were low. The grain size at which the transition occurs is set by the mean free spacing of the pinning phase. Such a transition has been observed in natural calcite mylonites (Herwegh & Jenni 2001; Herwegh & Berger 2004; Herwegh et al. 2005a; Herwegh & Pfiffner 2005; Ebert et al. 2007a; Ebert et al. 2007b) as well as in other petrologic systems (Warren & Hirth 2006; Mehl & Hirth 2008). Herwegh and coworkers suggested that the transition grain size is a function of temperature and the mean free spacing of the pinning phase (Herwegh & Jenni 2001; Herwegh & Kunze 2002; Herwegh et al. 2005b; Herwegh & Pfiffner 2005; Ebert et al. 2007a; Ebert et al. 2007b). Our results suggest that, at constant temperature and mean free spacing, the transition from a pinned microstructure to a recrystallized microstructure will also be strain rate and/or stress dependent. Under all conditions, the stable grain size should be the minimum of the grain sizes predicted by equations

1 and 4. Thus, as strain rate or stress increases, the transition from a recrystallized microstructure to a pinned microstructure will require a smaller mean free spacing, $\frac{d_p}{f_p^m}$ (Fig. 7). The value of the exponent, *m*, is constrained by stereology and by pinning conditions. For example, *m*=0.5 is predicted if the each pinned boundary contains one second phase particle, whereas *m*=0.33 if the pinning phase lies on grain triple junctions (Haroun & Budworth 1968; Anand & Gurland 1975; Haroun 1980; Olgaard & Evans 1986).

If pinning occurred during deformation along the Morcles nappe, the maximum possible grain size would be defined by the mean free spacing of the pinning phase. Finer stable grain sizes might occur if the dynamically recrystallized grain size was smaller than the mean free spacing (for example, see Austin et al. in press). To test this hypothesis and constrain *m*, we re-examined grain-size data from one location in the Morcles nappe (Swiss Helvetic Alps) (Fig. 8a), where the peak metamorphic temperature was 631 K (Austin et al., in press), and from a range of locations along the Morcles nappe (Ebert et al. 2007a) where temperature varied systematically from 572 to 668 K (Fig. 8b). Indeed, both data sets are bounded by $\frac{d_p}{f_p^m}$ where *m*=0.55-0.56 (Fig. 9). Because strain rates are believed to be approximately constant along the nappe (Ebert et al. 2007a), the value of $\frac{d_p}{f_p^m}$ for a transition from pinned to unpinned is probably determined by temperature or stress (Fig. 9b), although at one location, where the temperature is believed to be roughly constant, this transition may be determined by strain rate and/or stress (Fig. 9a) (Austin et al., in press). If the data from each location along the Morcles Nappes are fit independently, *m* is approximately 0.33 (Ebert et al. 2008), but those authors suggest that that value is not closely constrained.

Values for A also vary somewhat: A=0.42 (Austin et al., in press) or 1.12 (Ebert et al. 2007a). The primary uncertainty in these fits arises from determining which samples are indicative of a pinned microstructure vs. those with grain sizes determined by the deformation conditions. Differences in the A values may also result from variations in the technique used for measuring grain size (cf. Ebert et al. 2007a). Based on our selection criteria, m is a maximum value and A is a minimum value.

Theories suggest that A should vary between 0.08 and >2 depending on the value of m and the distribution and shape of the pinning phase (Smith 1948; Gladman 1966; Haroun & Budworth 1968; Anand & Gurland 1975; Hellman & Hillert 1975; Haroun 1980; Louat 1983). Thus the A values for grain sizes observed in the Morcles nappe do fall in the admissible range. For comparison, Mehl and Hirth (2008) obtained m=0.41 and A=1.26 for a best fit to data from deformed gabbros on the SW India ridge.

Finally, we note that this analysis does not consider Ostwald ripening of the pinning phase. Such a process would tend to increase the mean free spacing of the pinning phase, to increase $\frac{d_p}{f_p^m}$, at constant f_p, and to favor coarser pinned grain sizes at higher temperatures (Voorhees 1985, 1992; Herwegh et al. 2005a; Ebert et al. 2008). If ripening also resulted in a change in the geometrical distribution or the shape of the pinning phase, it is possible that that process might also lead to variations in m or A. Ostwald ripening did not occur in our experiment, and they do not shed light on this process. We also assumed that the stable recystallized grain size was obtained in the Morcles nappe. Our experiments and previous high strain experiments on calcite rocks (Pieri et al. 2001; Barnhoorn et al. 2004), suggest steady state sizes are achieved at equivalent strains $1<\varepsilon<10$, well below those reached in many natural shear zones, including the Morcles nappe (e.g. Ramsay 1981). Based on microstructural arguments, Herwegh and

coworkers (Herwegh et al. 2005b; Ebert et al. 2007a; Austin et al. in press) also argued that all the grain sizes those authors reported were indicative of the deformation conditions. Thus, the transition from a pinned grain size to a recrystallized grain size observed in experiments is consistent with field observations.

5. Conclusion

In our experiments, the addition of as little as 1 vol.% carbon spheres has a dramatic influence on the stable grain size of synthetic calcite aggregates. At the same volume fraction and for similar particle sizes, splinters result in a finer pinned grain size than spheres. During deformation, the grain size evolves towards the finer of the pinned grain size or the recyrstallized grain size, and the recrystallized grain size is well explained by equation 4. The stable recrystallized grain size is reached between strains of 0.5 and 9.0.

A similar transition between a pinned grain size and dynamically recrystallized grain size is observed within the Morcles nappe. In the Morcles nappe, the recrystallized grain size is interpreted to vary as a function temperature, strain rate, and/or stress.

Both experimental and field observations suggest that, in poly-phase rocks where one phase acts as a pinning phase, the maximum grain size is related to the mean free spacing of that pinning phase. When the recrystallized grain size due to deformation is finer than the pinned grain size, this grain size is indicative of the deformation conditions.

6. Acknowledgements

We would like the thank Michael Naumann, Uli Mok, and Xiaohui Xiao for their help in the laboratory, and Jock Hirst and the machine shop at the GFZ for help with sample preparation. This manuscript benefited greatly from discussions with Marco Herwegh, Andreas Ebert, Greg Hirth, William Durham, Peter Kelemen, and Timothy Grove. This research was funded by the

National Science Foundation grants EAR0309510, EAR0510412, and OCE0452787, and by the MIT student research fund.

7. References

Anand, L.&Gurland, J. 1975: The relationship between the size of cementite particles and the subgrain size in quenched-and-tempered steels. Metallurgical and Materials Transactions A **6**(3): 928-931.

Austin, N.&Evans, B. 2007: Paleowattmeters: A scaling relation for dynamically recrystallized grain size. Geology **35**(4): 343.

Austin, N., Evans, B., Herwegh, M.&Ebert, A. in press: Strain Localization in the Morcles Nappe (Helvetic Alps, Switzerland). Swiss Journal of Geosciences.

Barnhoorn, A., Bystricky, M., Burlini, L.&Kunze, K. 2004: The role of recrystallisation on the deformation behaviour of calcite rocks: large strain torsion experiments on Carrara marble. Journal of Structural Geology **26**(5): 885-903.

Braun, J., Chéry, J., Poliakov, A., Mainprice, D., Vauchez, A., Tomassi, A.&Daigniéres, M. 1999: A simple parameterization of strain localization in the ductile regime due to grain size reduction: A case study for olivine. Journal of Geophysical Research-Solid Earth **104**(B11).

Christie, J.&Ord, A. 1980: Flow stress from microstructures of mylonites: example and current assessment. Journal of Geophysical Research **85**(B11): 6253-6262.

De Bresser, J., Peach, C., Reijs, J.&Spiers, C. 1998: On dynamic recrystallization during solid state flow: Effects of stress and temperature. Geophys. Res. Lett **25**(18): 3457–3460.

Drury, M.&Urai, J. 1990: Deformation-related recrystallization processes. Tectonophysics **172**: 235-253.

Ebert, A., Herwegh, M., Evans, B., Pfiffner, A., Austin, N.&Vennemann, T. 2007a: Microfabrics in carbonate mylonites along a large-scale shear zone (Helvetic Alps). Tectonophysics **444**(1-4): 1-26.

Ebert, A., Herwegh, M.&Pfiffner, A. 2007b: Cooling induced strain localization in carbonate mylonites within a large-scale shear zone (Glarus thrust, Switzerland). Journal of Structural Geology **29**(7): 1164-1184.

Ebert, A., Herwegh, M., Berger, A.&Pfiffner, A. 2008: Grain coarsening maps for polymineralic carbonate mylonites: A calibration based on data from different Helvetic nappes (Switzerland). Tectonophysics: doi:10.1016/j.tecto.2008.05.007.

Etheridge, M.&Wilkie, J. 1981: An assessment of dynamically recrystallized grainsize as a palaeopiezometer in quartz-bearing mylonite zones. Tectonophysics **78**: 475-508.

Evans, B., Renner, J.&Hirth, G. 2001: A few remarks on the kinetics of static grain growth in rocks. International Journal of Earth Sciences **90**(1): 88-103.

Flowers, J. 1979: Grain growth inhibition by spherical particles with a distribution of sizes. Magnetics, IEEE Transactions on **15**(6): 1601-1603.

Gladman, T. 1966: On the Theory of the Effect of Precipitate Particles on Grain Growth in Metals. Proceedings of the Royal Society of London. Series A, Mathematical and Physical Sciences (1934-1990) **294**(1438): 298-309.

Guillope, M.&Poirier, J. 1979: Dynamic recrystallization during creep of single-crystalline halite: An experimental study. Journal of Geophysical Research **84**(B10): 5557-5567.

Haroun, N.&Budworth, D. 1968: Modifications to the Zener formula for limitation of grain size. Journal of Materials Science **3**(3): 326-328.

Haroun, N. 1980: Theory of inclusion controlled grain growth. Journal of Materials Science **15**(11): 2816-2822.

Hellman, P.&Hillert, M. 1975: Effect of Second-Phase Particles on Grain Growth. Scandinavian Journal of Metallurgy **4**(5): 211-219.

Herwegh, M. 2000: A new technique to automatically quantify microstructures of fine grained carbonate mylonites: two-step etching combined with SEM imaging and image analysis. Journal of Structural Geology **22**(4): 391-400.

Herwegh, M.&Jenni, A. 2001: Granular flow in polymineralic rocks bearing sheet silicates: new evidence from natural examples. Tectonophysics **332**(3): 309-320.

Herwegh, M.&Kunze, K. 2002: The influence of nano-scale second-phase particles on deformation of fine grained calcite mylonites. Journal of Structural Geology **24**(9): 1463-1478.

Herwegh, M.&Berger, A. 2004: Deformation mechanisms in second-phase affected microstructures and their energy balance. Journal of Structural Geology **26**(8): 1483-1498.

Herwegh, M., Berger, A.&Ebert, A. 2005a: Grain coarsening maps: A new tool to predict microfabric evolution of polymineralic rocks. Geology **33**(10): 801-804.

Herwegh, M., de Bresser, J.&ter Heege, J. 2005b: Combining natural microstructures with composite flow laws: an improved approach for the extrapolation of lab data to nature. Journal of Structural Geology **27**(3): 503-521.

Herwegh, M.&Pfiffner, O. 2005: Tectono-metamorphic evolution of a nappe stack: A case study of the Swiss Alps. Tectonophysics **404**(1): 55-76.

Holyoke, C.&Tullis, J. 2006: The interaction between reaction and deformation: an experimental study using a biotite+ plagioclase+ quartz gneiss. Journal of Metamorphic Geology **24**(8): 743-762.

Humphreys, F.&Hatherly, M. 1995: Recrystallization and related annealing phenomena, Pergamon Tarrytown, NY, USA.

Karato, S., Toriumi, M.&Fujii, T. 1980: Dynamic recrystallization of olivine single crystals during high-temperature creep. Geophysical Research Letters **7**(9): 649-652.

Kohlstedt, D.&Weathers, M. 1980: Deformation-induced microstructures, paleopiezometers, and differential stresses in deeply eroded fault zones. Journal of Geophysical Research **85**(B11): 6269-6285.

Krabbendam, M., Urai, J.&van Vliet, L. 2003: Grain size stabilisation by dispersed graphite in a high-grade quartz mylonite: an example from Naxos (Greece). Journal of Structural Geology **25**(6): 855-866.

Lange, F.&Hirlinger, M. 1987: Grain Growth in Two-Phase Ceramics: Al2O3 Inclusions in ZrO. Journal of the American Ceramic Society **70**(11): 827-830.

Louat, N. 1983: The inhibition of grain-boundary motion by a dispersion of particles. Philosophical Magazine A **47**(6): 903-912.

Mas, D.&Crowley, P. 1996: The effect of second-phase particles on stable grain size in regionally metamorphosed polyphase calcite marbles. Journal of Metamorphic Geology **14**(2): 155-162.

Mehl, L.&Hirth, G. 2008: Plagioclase preferred orientation in layered mylonites: Evaluation of flow laws for the lower crust. J. Geophys. Res **113**.

Nes, E., Ryum, N.&Hunderi, O. 1985: On the Zener drag. Acta Metallurgica **33**: 11-22.

Olgaard, D.&Evans, B. 1986: Effect of second-phase particles on grain growth in calcite. J. Am. Ceram. Soc **69**(11): 272-277.

Olgaard, D.&Evans, B. 1988: Grain growth in synthetic marbles with added mica and water. Contributions to Mineralogy and Petrology **100**(2): 246-260.

Ord, A.&Christie, J. 1984: Flow stresses from microstructures in mylonitic quartzites of the Moine Thrust zone, Assynt area, Scotland. Journal of Structural Geology **6**(6): 439-654.

Paterson, M. S.&Olgaard, D. L. 1999: Rock deformation tests to large shear strains in torsion. Journal of Structural Geology **22**(9): 1341-1358.

Pieri, M., Burlini, L., Kunze, K., Stretton, I.&Olgaard, D. L. 2001: Rheological and microstructural evolution of Carrara Marble with high shear strain; results from high temperature torsion experiments. Journal of Structural Geology **23**(9): 1393-1413.

Ramsay, J. 1981: Tectonics of the Helvetic Nappes. Geological Society London Special Publications **9**(1): 293.

Rutter, E. 1995: Experimental study of the influence of stress, temperature, and strain on the dynamic recrystallization of Carrara marble. Journal of Geophysical Research **100**(B12): 24651-24664.

Rutter, E. H., Casey, M.&Burlini, L. 1994: Preferred crystallographic orientation development during the plastic and superplastic flow of calcite rocks. Journal of Structural Geology **16**(10): 1431-1446.

Ryum, N., Hunderi, O.&Nes, E. 1983: On grain boundary drag from second phase particles. Scripta Metallurgica **17**(11): 1281-1283.

Sakai, T.&Jonas, J. 1984: Dynamic recrystallization-Mechanical and microstructural considerations. Acta Metallurgica **32**: 189-209.

Schmid, S., Paterson, M.&Boland, J. 1980: High temperature flow and dynamic recrystallization in Carrara marble. Tectonophysics **65**(3): 4.

Shimizu, I. 2008: Theories and applicability of grain size piezometers: The role of dynamic recrystallization mechanisms. Journal of Structural Geology.

Smith, C. 1948: Grains, phases, and ainterfaces: as interpretation of microstructure. Transactions of the American Institute of Mining and Metallurgical Engineers **15**(4): 1-37.

Stearns, L.&Harmer, M. 1996: Particle-Inhibited Grain Growth in AI2O3-SiC: I, Experimental Results. Journal of the American Ceramic Society **79**(12): 3013-3019.

Stipp, M.&Tullis, J. 2003: The recrystallized grain size piezometer for quartz. Geophysical Research Letters **30**(21).

Stipp, M., Tullis, J.&Behrens, H. 2006: Effect of water on the dislocation creep microstructure and flow stress of quartz and implications for the recrystallized grain size piezometer. Journal of Geophysical Research **111**(B4).

Ter Heege, J., De Bresser, J.&Spiers, C. 2005: Dynamic recrystallization of wet synthetic polycrystalline halite: dependence of grain size distribution on flow stress, temperature and strain. Tectonophysics **396**(1-2): 35-57.

Twiss, R. 1977: Theory and applicability of a recrystallized grain size paleopiezometer. Pure and Applied Geophysics **115**(1): 227-244.

Urai, J., Means, W.&Lister, G. 1986: Dynamic recrystallization of minerals. AGU Geophysical Monograph **36**: 161-199.

van der Wal, D., Chopra, P., Drury, M.&Fitzgerald, J. 1993: Relationships between dynamically recrystallized grain size and deformation conditions in experimentally deformed olivine rocks. Geophysical Research Letters **20**(14): 1479-1482.

Voorhees, P. 1985: The theory of Ostwald ripening. Journal of Statistical Physics **38**(1): 231-252.

Voorhees, P. 1992: Ostwald Ripening of Two-Phase Mixtures. Annual Reviews in Materials Science **22**(1): 197-215.

Warren, J.&Hirth, G. 2006: Grain size sensitive deformation mechanisms in naturally deformed peridotites. Earth and Planetary Science Letters **248**(1-2): 438-450.

White, S. 1979: Grain and sub-grain size variations across a mylonite zone. Contributions to Mineralogy and Petrology **70**(2): 193-202.

Zulauf, G. 2001: Structural style, deformation mechanisms and paleodifferential stress along an exposed crustal section: constraints on the rheology of quartzofeldspathic rocks at supra-and infrastructural levels (Bohemian Massif). Tectonophysics **332**(1): 211-237.

8. Tables

Table 1) Data from hydrostatic experiments. The sample material is listed, along with the duration of the HIP (total time). Standard deviation is the 1 sigma variation in the measured intercept lengths, and does not relate to measurement uncertainty.

Experiment	Material	Total Time (s)	Mean Intercept Length (μm)	Standard Deviation (μm)
c-1283t	10% Spl	36900	8.8	4.7
c-1185t	10% Spl	36900	5.7	3.4
c-1183t	10% Spl	18900	6.5	3.6
c-1227t	10% Spl	8100	5.5	3.5
c-1193	10% Spl	9900	8.2	4.3
c-1186t	10% Spl	900	4.9	2.8
c-1283c	10% Sph	36900	9.2	4.6
c-1185c	10% Sph	36900	9.1	5.0
c-1183c	10% Sph	18900	10.4	5.4
c-1184	10% Sph	8100	8.3	4.5
c-1227c	10% Sph	8100	7.3	3.8
c-1186c	10% Sph	900	7.3	3.9
c-1283b	1% Sph	36900	15.1	6.9
c-1185b	1% Sph	36900	9.8	5.0
c-1183b	1% Sph	18900	15.2	6.8
c-1184b	1% Sph	8100	13.8	6.3
c-1227b	1% Sph	8100	14.3	7.0
c-1186b	1% Sph	900	13.0	6.1
c-1191	Pure	8100	24.5	10.8
c-1109	Pure	18900	45.8	19.0
c-1094	Pure	36900	50.5	23.0
c-1093	Pure	9900	33.5	15.5
c-1091	Pure	900	17.0	7.5
c-1087	Pure	0	9.6	4.6

Table 2a) Data from compression experiments. Duration is the total duration of the experiment, and HIP time is the duration of the heat treatment prior to deformation, which controls the initial grain size. Stress and strain rate are reported at the maximum strain (shown).

Experiment	Material	Duration (s)	HIP Time (s)	Stress (MPa)	Strain Rate (s^{-1})	Strain	Mean Intercept Length (μm)
c-1221	Pure	8880	8100	37.9	7.3E-04	0.35	16.2
c-1220	Pure	14340	8100	25.8	4.7E-05	0.25	26.8
c-1225	1%sph	14760	8100	26.0	4.7E-05	0.25	18.3
c-1223	1%sph	8700	8100	34.0	7.0E-04	0.30	14.6
c-1228	10%sph	15780	8100	23.5	4.9E-05	0.30	6.6
c-1222	10%sph	8760	8100	41.5	7.3E-04	0.35	6.5
c-1226	10%splint	15480	8100	39.0	4.7E-05	0.23	7.1
c-1224	10%splint	8760	8100	60.3	6.8E-04	0.30	6.3

Table 2b) Data from torsion experiments. HIP time is the total HIP time, including both the duration of heat treatment prior to machining the sample, and an 1800 s HIP during heating and furnace stabilization prior to the beginning of the torsion experiment. The total duration includes the entire HIP time and the duration of deformation. Shear stress and shear strain rate are reported at the maximum shear strain (shown).

Experiment	Material	Duration (s)	HIP Time (s)	Shear Stress (MPa)	Shear Strain Rate (s^{-1})	Shear Strain	Mean Intercept Length (μm)
c-1087:1t	Pure	19718	1800	27.1	8.7E-04	15.59	12.1
c-1189:1t	1%sph	27818	9900	31.3	8.7E-04	15.59	10.8
c-1189:2t	1%sph	264435	9900	20.9	6.1E-05	15.59	19.5
c-1192:1t	10%sph	27922	9900	18.4	8.7E-04	15.59	9.0
c-1192:2t	10%sph	271910	9900	11.9	6.0E-05	15.59	12.3
c-1193:1t	10%splint	27818	9900	25.8	8.7E-04	15.59	7.7
c-1193:2t	10%splint	269413	9900	20.7	5.9E-05	15.31	5.5

9. Figures

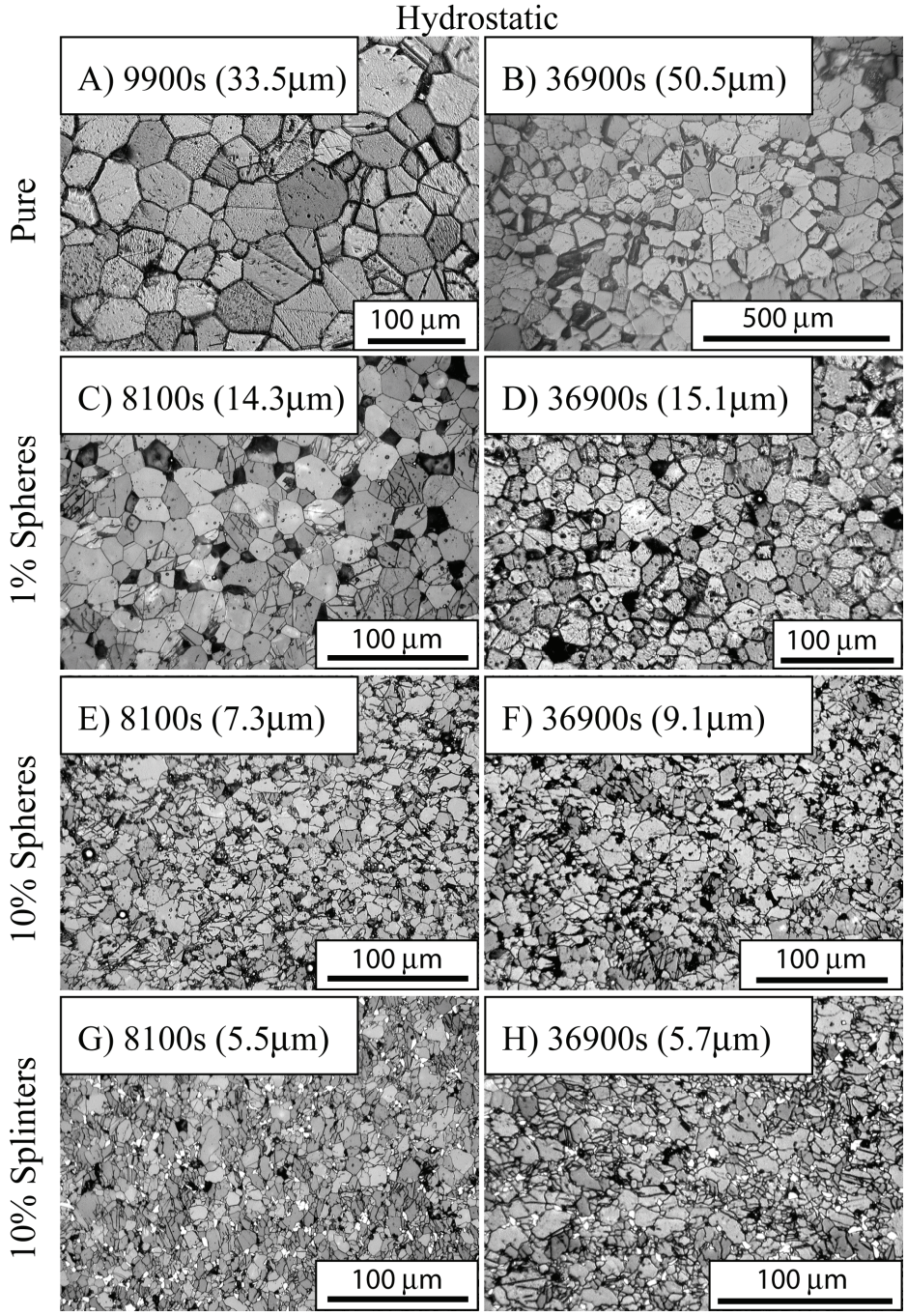


Figure 1) (caption on next page)

Figure 1) Reflected light micrographs of etched samples from hydrostatic experiments, run at 1023 K, on the four sample materials being investigated. The duration of the HIP and the mean linear intercept length are both listed. Carbon spheres and splinters are white in these images, and the calcite is gray. The experiment numbers for each micrograph are: A) c-1093, B) c-1094, C) c-1227b, D) c-1283b, E) c-1227c, F) c-1185c, G) c-1227t, H) c-1185t.

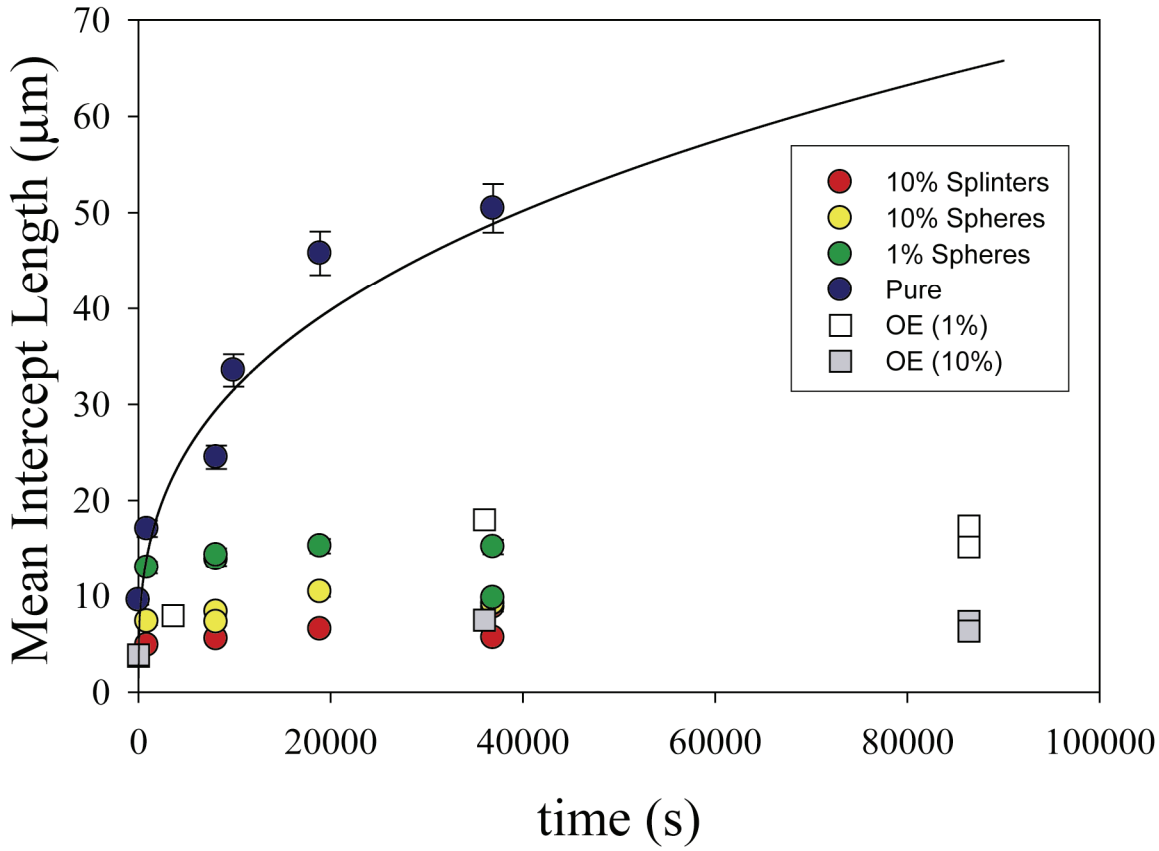


Figure 2) Mean intercept lengths, measured on samples heat treated hydrostatically as a function of time. The black curve is the hydrostatic growth rate (eq. 3) for the pure material (K=3.16 μm^p s^{-1}) (see Chapter 4). Symbol colors represent the different starting materials (see legend). Experiments performed by Olgaard and Evans (1986) (OE) on synthetic calcite containing 1 or 10 vol.% alumina with a similar size distribution to our carbon particles (grit 9.5/4.73) are included for comparison. Olgaard and Evans (1986) used a stereological correction of 3/2 to correct their mean intercept lengths, which has been removed.

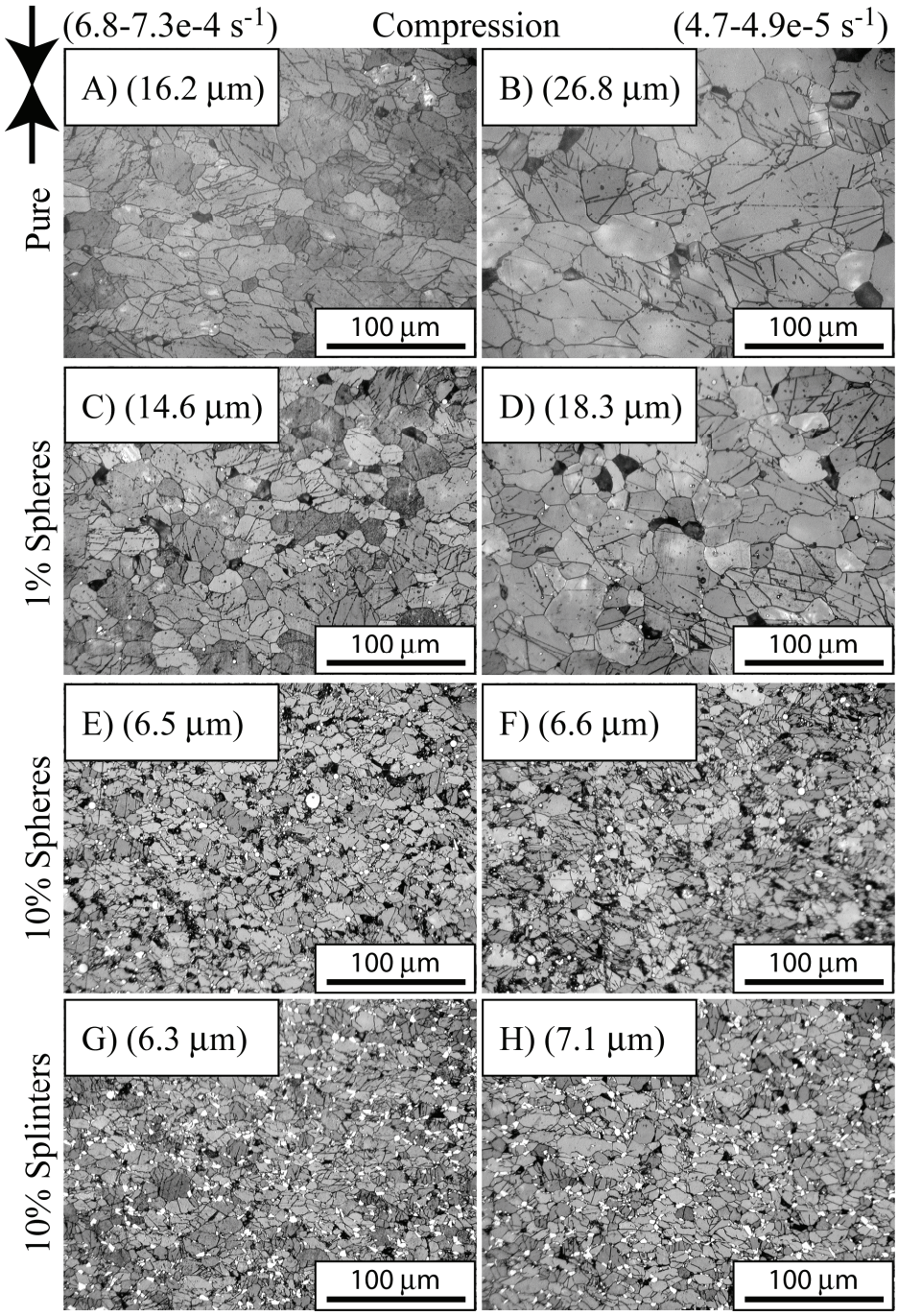


Figure 3) Reflected light micrographs of etched samples after deformation in compression at constant axial displacement rate, corresponding to strain rates of 6.8-7.3e-4 s^{-1} (A,C,E,G) or 4.7-4.9e-5 s^{-1} (B,D,F,H), on each of our four starting materials (as labeled). The loading direction was vertical, as shown. The mean linear intercept length, used to determine grain size, obtained from each sample is shown (see Table 1). As in figure 1, carbon particles are white and calcite is gray. The experiment numbers for each sample are: A) c-1221, B) c-1220, C) c-1223, D) c-1225, E) c-1222, F) c-1228, G) c-1224, H) c-1226.

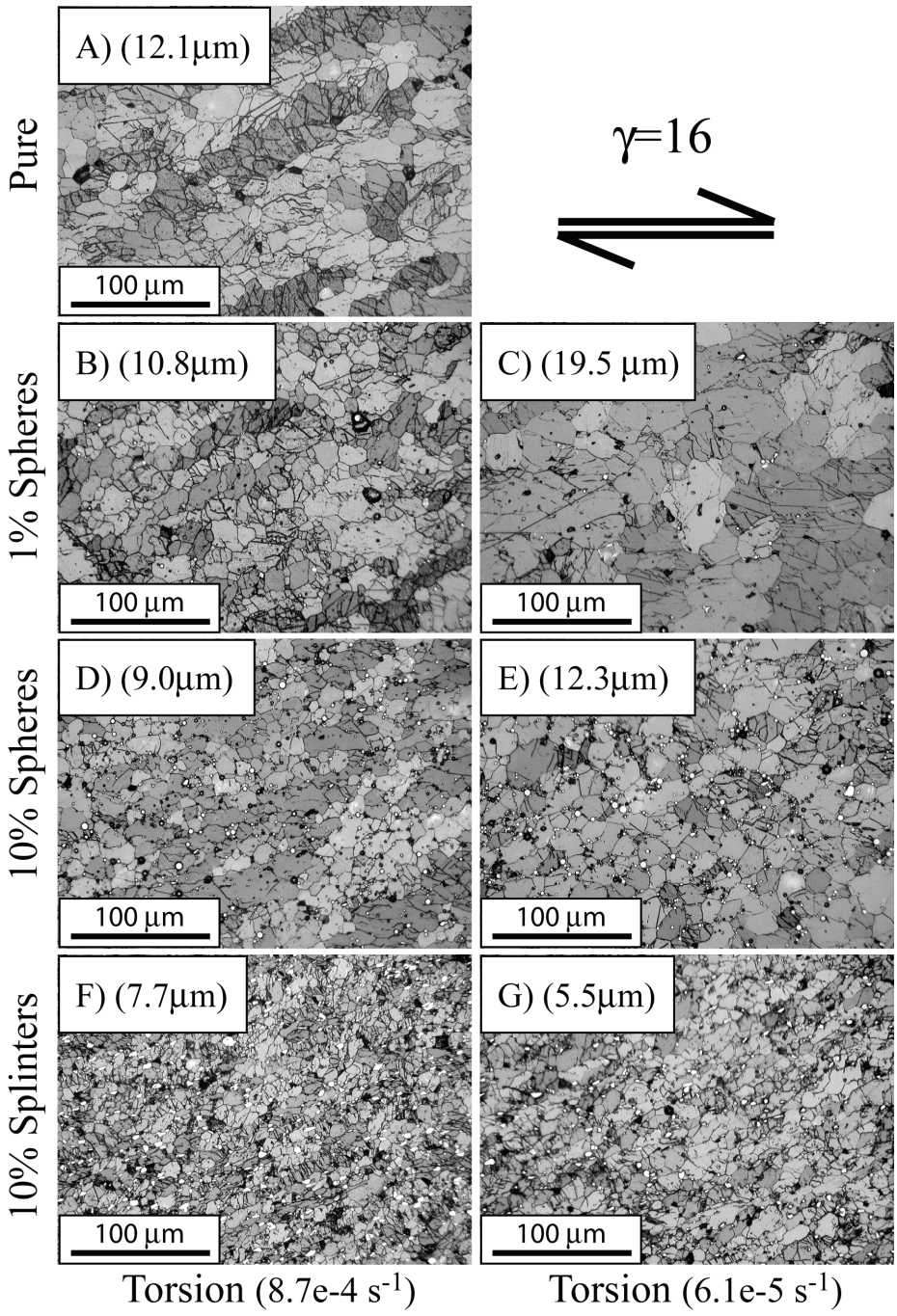


Figure 4) Reflected light micrographs of etched samples, deformed in torsion to a shear strain of 16, at shear strain rates of 8.7e-4 s^{-1} (A,B,D,F) or 6.1e-5 s^{-1} (C,E,G). Sense of shear is dextral, as shown. The mean intercept length of each sample is listed in parentheses. As in figures 1 and 3, carbon particles are white and calcite is gray. A foliation at approximately 30º to the shear plane is apparent in A) and B) and to a lesser extent, D) and E). Alignment of the carbon splinters in a similar orientation is also apparent in F) and G). The experiment numbers corresponding to each micrograph are: A) c-1087:1t, B) c-1189:1t, C) c-1189:2t, D) c-1192:1t, E) c-1192:2t, F) c-1193:1t, and G) c-1193:2t.

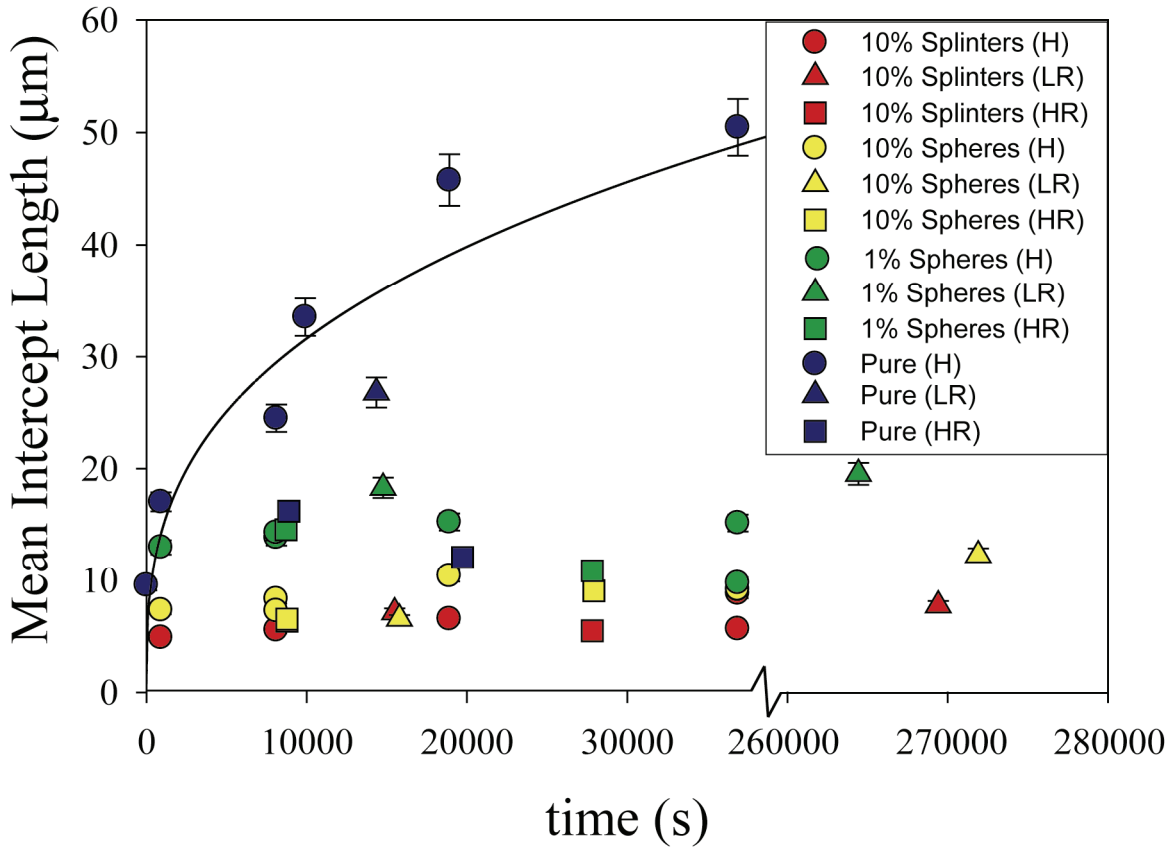


Figure 5) The same plot as in figure 2, however, mean intercept lengths from deformation experiments are included. The color scheme is also the same as figure 4. In the legend, H denotes hydrostatic experiments, "LR" denotes experiments run at an equivalent strain rate of 3.5-4.9e-5 s^{-1} and "HR" denotes experiment run at an equivalent strain rate of 5.0-7.3e-4 s^{-1}. The x-axis is broken at 45000 s in order to plot samples deformed for >260000 s in torsion, although the scale remains the same.

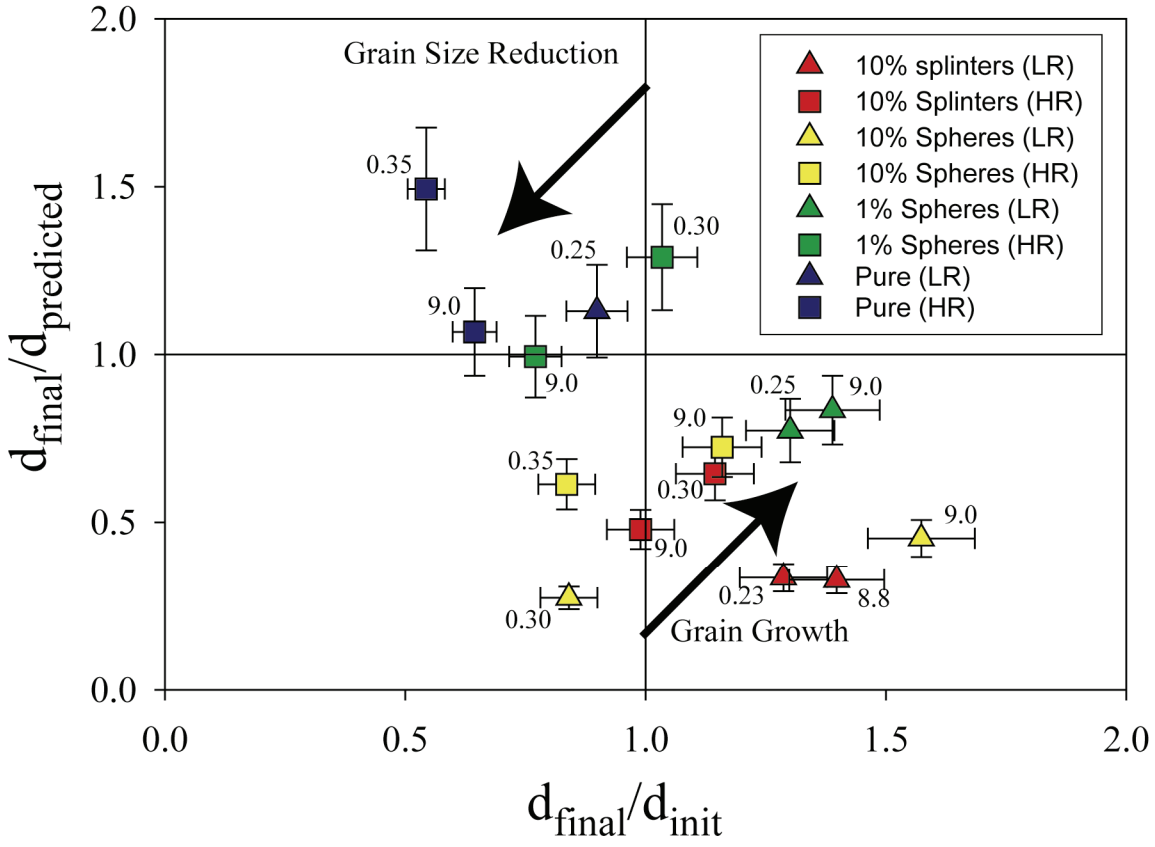


Figure 6) A comparison of the final measured grain size (d_{final}) (mean intercept length) with the initial grain size in each experiment (d_{init}), and the stable grain size predicted by eq. 4 ($d_{predicted}$), using the grain growth kinetics of the pure material (K=3.16 μm^p s^{-1}, p=3), the $\lambda/c\gamma$ value obtained in Chapter 4 (0.0025 m^2 J^{-1}), and assuming that deformation was completely accommodated by dislocation creep (β=1, see text for discussion). As in figure 5, "LR" refers to samples deformed at an equivalent strain rate between 3.5-4.9e-5 s^{-1} and "HR" denotes experiment run at an equivalent strain rate of 5.0-7.3e-4 s^{-1}. The color scheme is shown in the legend, and is the same as in previous figures, and the maximum equivalent strain reached in each experiment is labeled. The initial grain size is estimated based on measured grain sizes from samples HIPed for an equivalent duration. Samples which initially have a coarser grain size than their stable grain size, and undergo grain size reduction during deformation should plot in the upper left hand quadrant, following a trajectory qualitatively similar to the arrow in that quadrant. Samples which initially have a finer grain size than the stable grain size predicted by the deformation conditions, and which grow during deformation, plot in the lower right hand quadrant, following a trajectory qualitatively similar to the arrow in that quadrant. Samples in which the grain size does not evolve will plot on the line d_{final}/d_{init}=1.

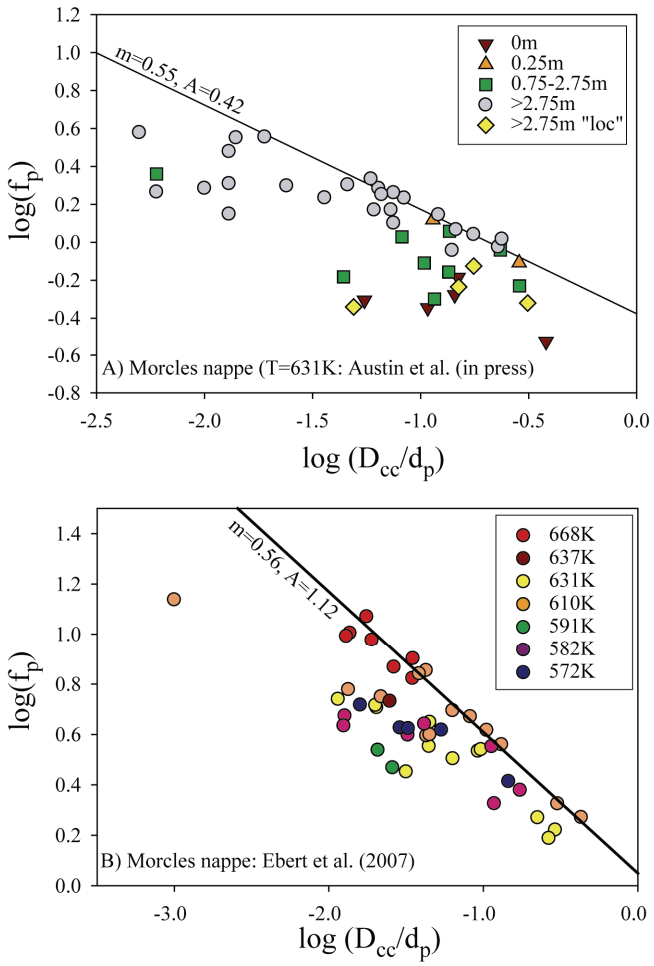


Figure 7) Plots of $\log(D_{cc}/d_p)$ vs $\log(f_p)$ for samples from the Morcles nappe, from A) Austin et al. (in press) and B) Ebert et al. (2007). D_{cc} is the calcite grain size, d_p is the grain size of the pinning phase(s), and f_p is the volume fraction of pinning phase(s). These plots allow for estimation of *A* and *m* in equation 1. In A), Austin et al. (in press) measured D_{cc} by multiplying mean intercept lengths by a stereological correction of 3/2, whereas in B), Ebert et al. (2007a) measured D_{cc} by calculating the area weighted average of equivalent circular diameters. In A), symbols represent the estimated distance to the thrust contact (in m) (see Chapter 3 or Austin et al. (in press) for a more detailed explanation). "loc" denotes samples which have undergone localized deformation at the outcrop scale. In B) sample symbols denote different location along the Morcles nappe, which had different peak metamorphic temperatures (Ebert et al., 2007a): the nose of the nappe had a peak metamorphic temperature of 572 K whereas the peak temperature in the root zone was 668 K. A) is a more detailed transect of the location labeled "631K" in B). The *m* and *A* values were obtained by determining what values bound the upper end of the data, which is a different approach than that taken by Ebert et al. (2008) on the same data set (see text).

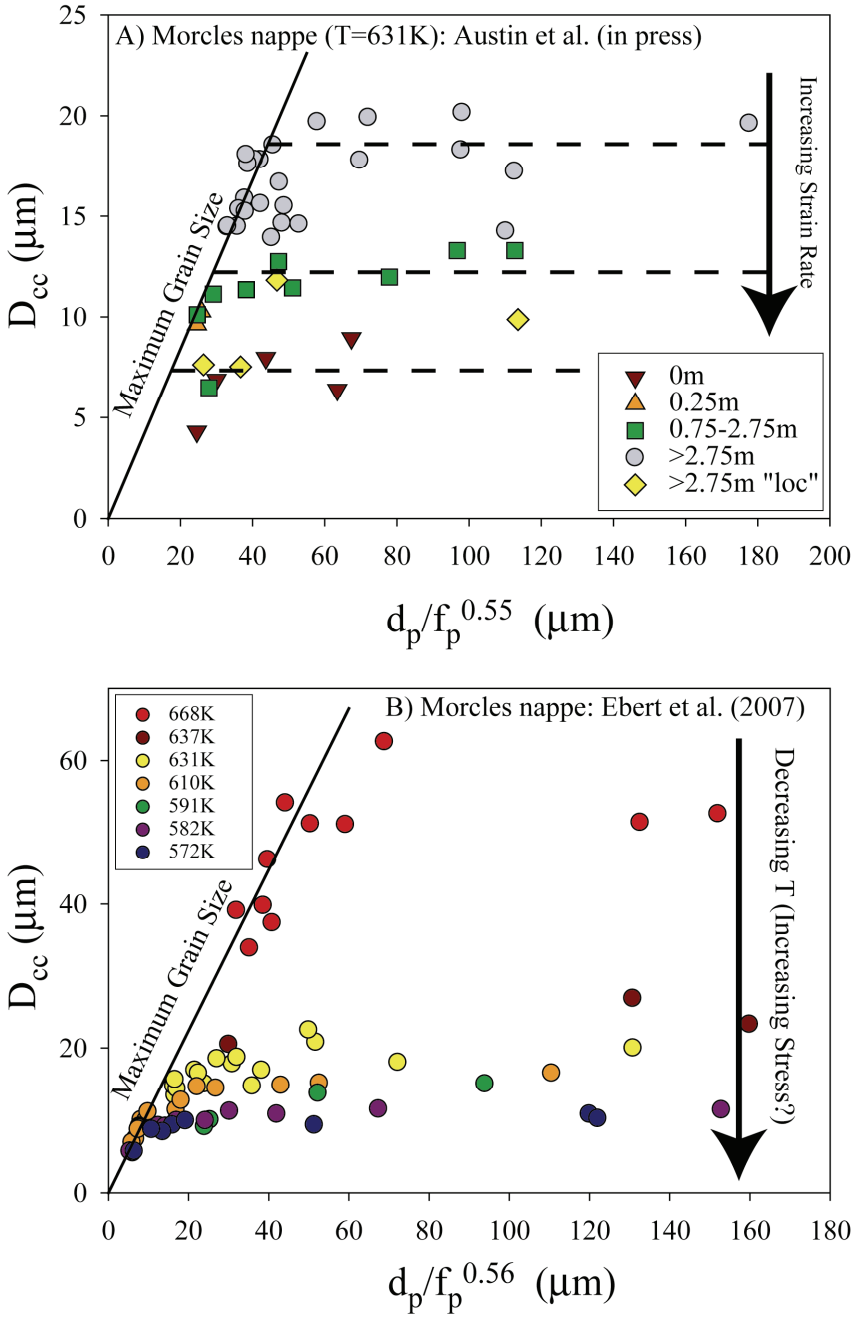


Figure 8) Plots of equation 1 for samples from the Morcles nappe: A) using data from Austin et al. (in press) (Chapter 3), and B) using data from Ebert et al. (2007a). Symbols are the same as in figure 7. *m* values were obtained from figure 7. The maximum grain size corresponds to the *A* values from figure 7. At one location within the Morcles nappe (A) the calcite grain size is reduced with decreasing distance to the thrust contact, possibly correlating with increasing strain rate, whereas in (B), at a range of locations along the Morcles nappe, the calcite grain size is finer at lower temperatures, which may correspond to increasing stresses. As in figure 7, the maximum grain size appears to be well explained by equation 1.